# TOWARD ENHANCED SUPERCAPACITORS BY MUTUALLY ADAPTING ELECTROLYTES AND NANOPOROUS CARBONS

Edurne Redondo Negrete
Universidad Autónoma de Madrid
CIC Energigune

Directors:
Roman Mysyk and Eider Goikolea
Tutor:
Pilar Ocón

# Table of contents

Abstract

Electrochemical capacitors are energy storage systems able to be fully charged and discharged within seconds. Because of their high power density and long cyclability, they are interesting devices for implementing them in many modern applications including the electric vehicle. They are most commonly made of high surface area carbonaceous active materials.

This work presents the use of microporous carbons derived from olive pits, an abundant natural waste material in Spain, in order to produce active materials for electric double layer capacitors (EDLCs) and lithium and sodium ion capacitors (LICs and NICs, respectively). The synthesis conditions of the chemical activation process (temperature and KOH amount) have been adapted to prepare activated carbons (ACs) with improved electrochemical performance. Therefore, in aqueous 6M KOH electrolyte, the maximum gravimetric and volumetric capacitance values achieved are 260 F $g^{-1}$ and 140 F $cm^{-3}$ and in organic 1.5M $(C_2H_5)_4NBF_4$ organic electrolyte, the values are 150 F $g^{-1}$ and 65 F $cm^{-3}$, respectively. Furthermore, the relationship between capacitance and the complex interplay of the accessible specific surface area, the accessible average pore size and the effective dielectric permittivity have been studied, suggesting that moderately solvated ions enhance the high-rate capability in pores that slightly exceed the solvated ion size.

These ACs have also been used as active materials in more exploratory type of electrolytes, such as, aqueous neutral salts and ionic liquids (ILs). ACs working in 6M LiCl electrolyte have demonstrated to be able to provide a capacitance value of 160 F $g^{-1}$ in a voltage window of 1.6 V with very low resistance thanks to the high conductivity of the electrolyte at high salt concentration values. Similarly, when these mesopore-free ACs operate in neat EMITFSI IL, they are able to give gravimetric and volumetric capacitance values as high as 180 F $g^{-1}$ and 150 F $cm^{-3}$ within a cell voltage of 3V, respectively, due to the adaptation of the pore size to the ion size.

Finally, LIC and NIC devices have also been built using the hard carbon directly obtained from the pyrolysis of the olive pits in the negative electrode and previously mentioned ACs in the positive electrode. These LIC and NIC devices overcome their EDLC counterpart in terms of energy density throughout the studied power density range while keeping the cyclability exhibited by EDLCs, which opens up the range of possible applications for these devices.

# 1 STRUCTURE OF THE THESIS

This Doctoral Thesis consists of an Introduction, Objectives, and Results and Discussion. A Summary of the work is included, highlighting the most relevant aspects. Lastly, the Conclusions are presented.

The aim of the **Introduction** is to describe electrochemical capacitors or supercapacitors, by explaining the characteristics of their components and the different types of electrical energy storage mechanisms they are based on, as well as to capture the state-of-the-art concerning the characterisation techniques used to study the process of charge and discharge. The active materials used in electrical double-layer capacitors are of special relevance, in particular microporous carbons, which is the material studied in this Doctoral Thesis. For that reason, the understanding of the structure and properties of microporous carbons is essential, especially parameters such as the specific surface area and the pore size distribution, which play the main role for the adaptability with the ions of the electrolyte.

The **Objectives** part of this dissertation lays out the motivation and objectives of the Doctoral Thesis elaborated as a result of the critical survey of the state--of-the-art in supercapacitors, as presented in the Introduction.

The **Results and Discussion** part is a compilation of the scientific contributions derived from the research work done in the course of this Doctoral Thesis. These are presented in the form of scientific articles published in international peer-reviewed journals.

**Article I:** "Effect of pore texture on performance of activated carbon supercapacitor electrodes derived from olive pits" E. Redondo, J. Carretero-Gonzalez, E. Goikolea, J. Segalini, R. Mysyk, Electrochimica Acta 160 (2015) 178-184.

This article gathers the results from the activation parameters, such as the temperature and the amount of activating agent, and their effect on the properties of the resulting activated carbons, their porous features and their suitability to supercapacitors in aqueous 6M KOH electrolyte. Furthermore, the performance of the positive and the negative electrode are separately studied to show a more fundamental analysis of the permittivity of each electrode with regard to the pore size, into an attempt to better understand, through the electrochemical techniques, the mechanism and characteristics of the electrosorption process.

**Article II:** "Relation between texture and high-rate capacitance of oppositely charged microporous carbons from biomass waste in acetonitrile-based supercapacitors" E. Redondo, J. Segalini, J. Carretero-Gonzalez, E. Goikolea, R. Mysyk, Electrochimica Acta 293 (2019) 496-503.

This publication is focused on the use of the previously described olive pits derived activated carbons in organic 1.5M $(C_2H_5)_4NBF_4$ in acetonitrile electrolyte electrochemical capacitors. The supercapacitor performance is evaluated based on the porosity of the materials taking into account capacitance values and rate capability results. As in the first article, herein also positive and negative electrodes are recorded simultaneously in order to assess their own capacitance values. This study is done at different applied current densities, to determine the capacitance fading depending on the pore size.

**Article III:** "The decisive role of electrolyte concentration in the performance of aqueous chloride-based carbon/carbon supercapacitors with extended voltage window" E. Redondo, E. Goikolea, R. Mysyk, Electrochimica Acta 221 (2016) 177-183.

This article is about the exploratory research on the use of neutral salts as alternative electrolytes for supercapacitors, since switching from conventional aqueous-based electrolytes (KOH or $H_2SO_4$) to neutral salt-based electrolytes permits increasing the voltage, and ultimately the energy storage capability of the system. The concentration of LiCl, NaCl and KCl aqueous electrolytes is set at the

concentration providing the highest electrical conductivity value, which turns out to be the concentration giving the best electrochemical performance. More precisely, improved capacitance retention and the lower cell resistance are enabled by the electrolyte concentration optimization. Moreover, as a result of the small size of chloride anions, even mildly activated ultramicroporous carbons can be coupled with this type of aqueous electrolytes with high capacitive performance.

**Article IV:** "Outstanding room-temperature capacitance of biomass-derived microporous carbons in ionic liquid electrolyte" E. Redondo, W.-Y. Tsai, B. Daffos, P.-L. Taberna, P. Simon, E. Goikolea, R. Mysyk, Electrochemistry Communications 79 (2017) 5-8.

This paper deals with the application of ionic liquids as electrolytes for microporous-based supercapacitors. The use of ILs may allow higher energy density owing to their wider voltage window compared to traditional electrolytes. Specifically, it was found that, in neat 1-ethyl-3-methylimidazolium bis(trifluoromethylsulfonyl)imide, the olive pits derived activated carbons (developed in article I) exhibit outstanding high capacitance values in comparison with other microporous carbons previously reported in the literature. Purportedly, this is due to the exceptional match between pore- and ion-sizes together with a high electrolyte-accessible specific surface area of the material. Most importantly, from the applications standpoint, the moderate pore volume of the carbons resulted in a high volume-based capacitance in neat ionic liquids electrolyte.

**Article V:** "Lithium and sodium ion capacitors with high energy and power densities based on carbons from recycled olive pits" J. Ajuria, E. Redondo, M. Arnaiz, R. Mysyk, T. Rojo, E. Goikolea, Journal of Power Sources 359 (2017) 17-36.

This publication focuses on the use of olive pits derived hard carbon and activated carbon as active materials for negative and positive electrodes, respectively, both in lithium ion capacitors and sodium ion capacitors. The voltage of hybrid supercapacitor cells is extended in comparison to symmetric electric double layer capacitor cells due to the low insertion/de-insertion potential $Li^+$ or $Na^+$ into hard carbon. The developed asymmetric cells also allow the activated carbon electrode to operate in an extended potential range, and, consequently, to get higher capacity values than those reached in symmetric systems. Thus, lithium ion and sodium ion capacitor cells entirely based on a low-cost recycled bio-waste demonstrate a remarkable energy and power density enhancement over their electric double layer capacitor counterpart while maintaining good cycle life.

Finally, the **Conclusions** summarise the original contributions from this doctoral thesis.

# 2 INTRODUCTION

## 2.1 Supercapacitors among other electrochemical energy storage technologies

Supercapacitors, ultracapacitors or electrochemical capacitors, all of them are terms used interchangeably to name the energy storage systems that in terms of energy-to-power density balance perform between batteries and electrolytic capacitors (1). Depending on the charge storage mechanism and the configuration of the electrochemical storage cells, supercapacitors can be classified as electric double-layer capacitors (EDLCs), pseudocapacitors and hybrid supercapacitors. This classification of electrochemical capacitors and related hybrid storage cells can be made according to the electrolyte, the active electrode materials and the cell configurations, as shown in Figure 1 (2). Electrode materials can be divided into two main categories according to the charge storage mechanism: materials for EDLCs (non-Faradic capacitors) and pseudocapacitors (Faradic capacitors). Both types of materials can be combined together and/or with battery-type materials, and various types of asymmetric and hybrid cells can be proposed (3; 4)

Historically, EDLCs were the first type of supercapacitors and are still the main type of commercial supercapacitors on the market today. EDLCs can provide high power density of up to 10 kW $kg^{-1}$ and energy density of 10 W h $kg^{-1}$. One of their main characteristics is that they are able to charge and discharge below 10 s.

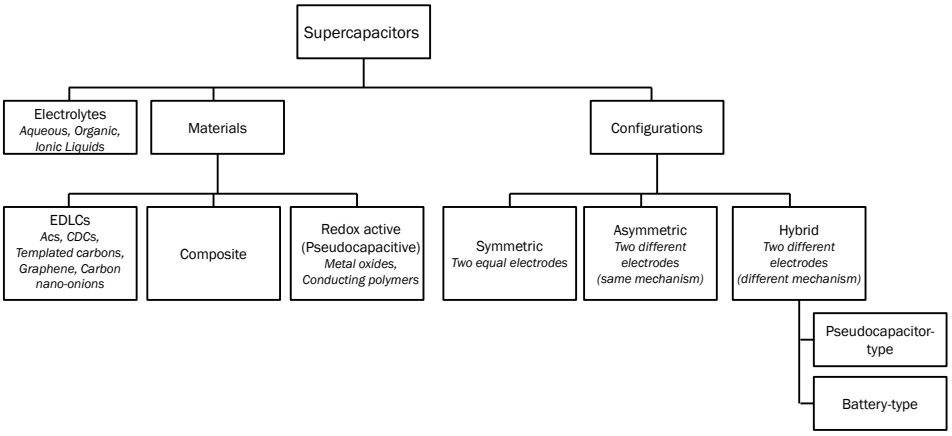


Figure 1. Taxonomy of materials, configurations and electrolytes for supercapacitors (2). ©

### 2.1.1. History of capacitors.

The Leyden jar is an early capacitor invented by Ewald Georg von Kleist in 1745 and firstly produced by Pieter van Musschenbroek in 1746. Figure 2 shows its schematics, which consists of a glass jar coated inside and outside with a thin layer of metal foil (5). The outer foil is grounded and the inner foil is connected to a source of electricity. The Leyden jar can be electrostatically charged producing a strong electrical discharge (6). At that time, scientists thought that the jar must be filled with alcohol or water in order to work. However, Benjamin Franklin concluded that the glass acted as the dielectric in the 1740s and 1750s, and he called a battery to the connection in parallel of several Leyden jars. In 1776, Alessandro Volta found the law of capacitance, which says that for a given object the voltage (V) and the charge (Q) are proportional (7):

$$C = \frac{Q}{V} \qquad \text{Equation 1}$$

In the 1830s, Michael Faraday discovered that the material between the plates has an effect on the quantity of charge on the capacitor plates. William Whewell was the first to use the term “dielectric”. Until the late 1800s, Leyden jars and capacitors were used for spark gap transmitters and medical

electrotherapy equipment. After that period, different types of capacitors started emerging: mica and ceramic capacitors, aluminium and tantalum electrolytic capacitors, polymer film capacitors and EDLCs.

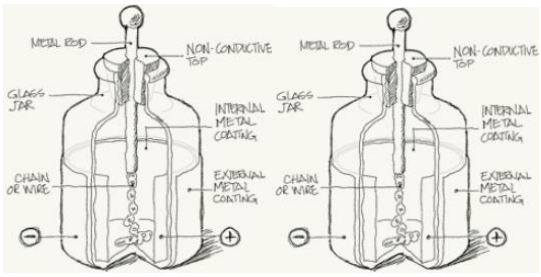


Figure 2. Schematics of a Leyden jar (8).

The mica capacitor was invented by William Dubilier in 1909 (9). This capacitor is composed of a layer of mica and copper foils clamped together, but oxidation and corrosion occurred at the early stages, due to the air gaps between the mica and the foils, which alter the capacitance. In the 1920s, other ceramic capacitors were developed, using for example titanium oxide (rutile) as a substitute of the mica and it was found that the capacitance of this material depends on the temperature. Barium titanate was also used, increasing the permittivity 10 times, but with less stable electrical parameters. In 1961, the multi-layer ceramic capacitor was launched. In the 1890s, Charles Pollak found that an oxide layer is stable on an aluminium anode in a neutral or alkaline solution and, in 1897, he patented a borax electrolyte aluminium capacitor. “Wet” electrolytic capacitors appeared in the 1920s, which are composed of a metal anode immersed in a solution of borax or other electrolyte dissolved in water with the outside of the container acting as the cathode. The modern “dry” electrolytic capacitor was patented by Samual Ruben in 1925, in which a gel-like electrolyte is sandwiched between an oxide coated anode and a metal foil with a paper separator. In 1936, roughening of the anode surface was introduced to increase capacitance. The rapid development of the radio and the television demanded large production and improvements regarding leakage currents, the equivalent series resistance (ESR), the operational temperature range and lifespans, which were achieved by using new organic based electrolytes. Between the 1970s and 1990s lower leakage currents and further reduction in ESR and higher temperatures were achieved. Between the years 2000 and 2005, the “capacitor plague” happened which lead to many capacitors failing prematurely, possibly due to a faulty electrolyte composition.

In the 1930s, tantalum electrolytic capacitors were firstly manufactured, which are composed by wound tantalum foils and a non-solid electrolyte. In the 1950s Bell Laboratories used manganese dioxide as solid electrolyte, by grounding tantalum to the powder and sintering it as a cylinder. In 1954, the Sprague Electric Company did the first commercially viable tantalum solid electrolyte capacitors. In 1975 conductive polymers replaced the manganese dioxide because of their higher conductivity that lead to lower ESR. Polymer tantalum capacitors for surface mount devices (SMDs) were released by NEC, in 1995, and by Sanyo in 1997. 1980 and 2000/2001 tantalum prices suffer two shocks that led to the development of the niobium electrolytic capacitors with manganese dioxide electrolyte.

In 1900, the metalized paper capacitor was patented, which consisted of a coated paper with a binder filled with metal particles. Bosch coated the paper with lacquer by vacuum deposition of metal during the World War II. The first polymer film capacitor was made around 1954 by Bell Labs, which had a 2.5 μm-thick metalized lacquer film separated from the paper. In 1952, Dupont trademarked the mylar capacitor, which had a very strong polyethylene terephthalate (PET). In 1954, 12 μm-thick metalised mylar film capacitor was produced and by 1959 also with polyethylene, polystyrene, polytetrafluoroethylene, PET and polycarbonate. In 1970, electric utilities used film-foil capacitors without paper.

In the early 1950s, General Electric experimented with capacitors with porous carbon electrodes to patent "low voltage electrolytic capacitor with porous carbon electrodes". Standard Oil of Ohio developed and licensed the supercapacitor in the 1970s and NEC commercialised it. It had 5.5 V and up to 1 F in 5 $cm^3$ size, used as backup power for computer memory. These capacitors employed activated carbon (AC) as an electrode active material, which have high specific surface area (SSA) in order to increase the amount of stored charge and thus the capacitance by 6 orders of magnitude. Brian Evans Conway worked on ruthenium oxide electrochemical capacitors from 1975 to 1980. Transition metal oxides or conductive polymers are pseudocapacitive materials that rely on rapid redox events on their surface or subsurface layer (10). Their charge storage capability is much higher, while the electric response is similar to that of electrical double layer capacitance (1). In 1991, he described the difference between supercapacitors and batteries. In 1982, pinnacle Research Institute (PRI) developed the first supercapacitor with low internal resistance. Lithium-ion capacitors have recently appeared on the market with a greater charge storage capacity.

### 2.1.2. Batteries and electrochemical capacitors.

Batteries are also another type of energy storage systems. The difference between these two systems is established on their charge storage mechanism: a physical process in electrochemical capacitors and chemical reactions in batteries (11). Unlike supercapacitors, batteries rely on the slow electrochemical redox processes, which limit the energy storage by the diffusion during the charge transfer. Supercapacitors, on the contrary, use the rapid electrosorption processes onto the surface of highly divided porous materials and pseudocapacitors use fast electrochemical reactions that are not limited by diffusion.

Table 1 Comparison of some important characteristic of state of the arte electrochemical capacitors and lithium-ion batteries (12).

| Characteristic | State of the arte Lithium Ion Battery | Electrochemical Capacitor |
|---|---|---|
| Charge time | ~ 3-5 mins | ~ 1 second |
| Discharge time | ~ 3-5 mins | ~ 1 second |
| Cycle life | <5,000 at 1C rate | >500,000 |
| Specific Energy (Wh/kg) | 70-100 | 5 |
| Specific Power (kW/kg) | 0.5-1 | 5-10 |
| Cycle efficiency (%) | <50% to >90% | <75% to >95% |
| Cost/Wh | 1-2 €/Wh | 10-20 €/Wh |
| Cost/kW | 75-150 €/kW | 25-50€/kW |

Table 1 shows the comparison of some important characteristics of the lithium ion batteries (LIBs) and electrochemical capacitors. The properties of energy storage systems are a consequence of the governing storing mechanisms (12). Batteries have greater power limitations, ruled by the reaction kinetics and mass transport, while supercapacitors have less power limitations, based on fast transport of the ions from the electrolyte within the pore networks. Likewise, batteries can store higher amounts of energy using the bulk of the material, while supercapacitors are limited by surface storage (11).

The Ragone plot, shown in Figure 3, reflects the fact that electrochemical capacitors are below the energy storing capacity of batteries, but have higher power density (13). In spite of this plot being broadly used for locating energy storage systems in terms of power and energy, it does not gather other advantages of EDLCs in comparison with batteries (10).

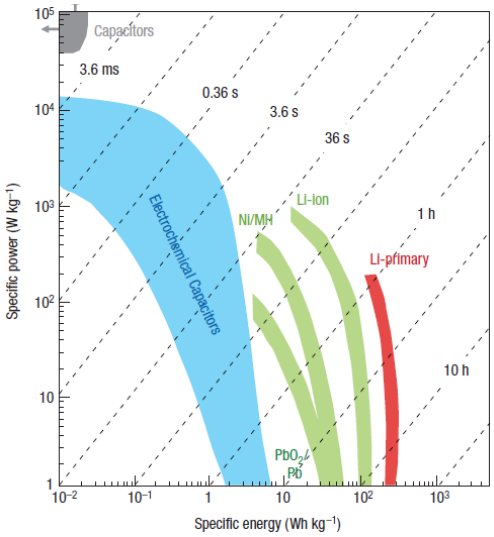


Figure 3. Ragone plot (13) ©.

For instance, the cycle life is longer for supercapacitors than for batteries, because, in the case of supercapacitors, it is only limited by side reactions, while the lifespan of batteries is affected by the mechanical stability of electrodes and the chemical reversibility of the main reactions (11). Another benefit of supercapacitors is the broad operational temperature range, typically between -40 and 60 °C, even up to 100 °C with new electrolyte developments that can insure stability in long-term operation (14). Increasing the temperature decreases the viscosity and increases the ionic mobility, which results in the decrease of the resistance and the increase of the capacitance (15). The reason for that is the electrode and electrolyte material choice. Batteries cannot work at low temperature because they would be kinetically hindered, the reactions would not occur, and at higher temperatures degradation processes would take place. In supercapacitors, non-reactive species are used while the typical electrode materials for batteries involve highly reactive compounds made of alkali metals, which have to be assembled in the presence of highly flammable electrolytes. Linked with this, safety is another important parameter. Batteries have the risk of thermal runaways and fires, because they use alkali–metal based materials that are typically converted into powders of 100 nm. This leads to an increase in their effective surface in contact with the electrolyte, which can be the cause of a safety problem (16). Supercapacitors don not heat as much due to their internal resistance. However, when a fully charged supercapacitor short circuits the energy stored is quickly released, which can cause an electrical arc and damage the divide. Other advantages of supercapacitors are the lower cost per cycle. This is based on their high efficiency to quickly charge and discharge, since energy reversibility is a very important factor in stablishing the value of an energy storage technology together with the cycle life (17). Supercapacitors offer a long operational life, extremely high cycle life and high cycle efficiency. Therefore, in applications where fast charge is required they are more cost effective than batteries, because not only they do not need to be oversized to avoid degradation but also can function over a longer period of time (18).

## 2.2 Applications

Supercapacitor applications are in accordance with their main advantages, *i.e.* the high pulse power capability and almost infinite cycle life. Nowadays, there are several companies developing, manufacturing and marketing energy storage and power delivery solutions, which produce commercial electrochemical capacitors and they have targeted many more applications than at the early stages of the capacitors. Table 2 summarizes some of the most important supercapacitor manufacturers and cells. Moreover, the present commercial supercapacitor packs have increased their voltage from 10 V at power levels below 1 W to 1000 V at power levels above 100kW.

Table 2. Commercial supercapacitors

| Manufacturer | Cell voltage (V) | Capacitance (F) | Specific Energy ($Whkg^{-1}$) | Specific Power ($kWkg^{-1}$) | ESR (mΩ) | Mass (g) |
|---|---|---|---|---|---|---|
| Maxwell (19) | 2.70 | 3000 | 6.0 | 5.9 | 0.29 | 510 |
| Yunasko (20) | 2.7 | 3000 | 6.2 | 7.1 | 0.14 | 490 |
| Nippon Chemi-Pon (21) | 2.5 | 1400 | 4.6 | - | 1.1 | 280 |
| Ioxus (22) | 2.7/2.85 | 3000 | 6.2 | 10.1 | 0.17 | 510 |
| JM energy (23) | 3.8-2.2 | 3300 | 13 | - | 0.7 | 350 |
| Wima (24) | 2.5 | 3000 | 4.7 | - | 0.7 | 615 |
| Skeleton (25) | 2.85 | 3200 | 6.8 | 42 | 0.13 | 533 |

When looking for an application of an energy storage system one can consider three main types: *dc*, pulse or bidirectional. *Dc* energy storage systems are meant to only deliver power when they are in use and they have to be charged eventually, for example, batteries in a mobile phone. An example that uses several 100 F electrochemical capacitors to switch light through diodes is a flashlight. The use of supercapacitors enables quickly recharging the flashlight and prolonging its life (26).

Pulse energy storage systems deliver power intermittently, in a single pulse or in a chain of repetitive pulses. An example is the Starting-Lighting-Ignition (SLI) battery of a conventional internal-combustion-engine automobile, which allows the engine to start working by a high-power pulse which lasts less than 1 s. Moreover, the SLI battery also provides lighting and ignition. Another example can be found in rock crushers that combine internal combustion engines with electrochemical capacitors in a hybrid power system. Therefore, the engine supplies power at low frequency and at *dc*, while supercapacitors are utilised at very high power demanding peaks, thus reducing the fuel consumptions by 30%.

A bidirectional energy storage system delivers and receives power, so the energy flows from storage during the positive power and to storage during the negative power. Examples of this are a diesel electric hybrid bus or a mining shovel. The regenerative energy storage takes place together with change from acceleration to deceleration or from upwards to downwards movements, enabling 25% of fuel saving (11)

The most important applications of supercapacitors are automotive, heavy transportation, trains and trams, heavy duty machinery, forklifts, port cranes, utility grid and microgrid and voltage sag mitigation, UPS and day night storage. They can also be used in small equipment such as screwdrivers or power tubing cutter and back up memories (11; 12).

In vehicles, the use of electrochemical capacitors improves the efficiency and value, because of their high power performance and resiliency (27). They can be used in several parts of the vehicle: as start-stops, in the regenerative energy recovery system, in the power assistance for hybrid electric vehicles, in the short term power backups and in the peak power assistance for high power functions.

Since vehicles need to fulfil present regulations, incorporating storing systems is a solution for saving fuel and lowering the $CO_2$ emissions. When a vehicle uses more than one form of energy for propulsion is considered a hybrid. Thus, a hybrid has a traditional internal combustion engine with a fuel tank, and one or more electric motors with a battery pack. There are different degrees of hybridisation: if the electric motor adds thrust to the combustion engine, but purely electric driving is not possible that would be a mild hybrid, while a full hybrid permits the purely electric driving. Supercapacitors are not sufficient to power the vehicles by their own, but they can be used in mild and full hybrid vehicles to decrease the fuel consumption and to reduce the battery drain and lengthen battery life, respectively (28). The trains, trams, buses and medium- and heavy-duty tracks must be adapted to the regulations on the emissions of $CO_2$ as well as the heavy transportation. Therefore, using supercapacitors helps to reduce the cost and save energy in the hybridisation and electrification

process of these means (29). Figure 4 shows the picture of a 100% electric bus. The Irizar ie tram is an example of a bus which uses lithium ion technology in its batteries with a nominal voltage of 600V/650V and a total capacity of 90-150 kWh. The charge can be carried out with a 125 A plug in 3 h and it also has the ability to quickly charge by pantograph in 5 minutes a maximum power of 500 kW (30).

The start-stop system is one of the parts that is used by automobile manufactures to meet fuel economy standards in conventional and hybrid-electric vehicles, while it also prevents idling, saves fuel and reduces emissions. It is based on turning off the engine when the car is stopped and restarting it when the foot is taken off the brake (31). When supercapacitors are used in this start-stop engine together with batteries they can deliver the power to re-start the engine, which protects the batteries from high current and repetitive cycling to save their life. By using supercapacitors, the starter can be separated from the 12-V boardnet, eliminating the drop on voltage during high power demands and improving the energy efficiency. Thus, supercapacitors promote fast, smooth engine starts and reduce engine vibration, improving driver experience. Moreover, supercapacitors have a high cycling life, operate from -40 to 65 ° C and allow energy storage modules to be small and light. Similarly, in rail applications, EDLCs can be by themselves or in combination with batteries for starting the engine, helping to reduce the size of the batteries and extending their lifetime.


Figure 4. Full electric bus (32)

The regenerative energy recovery is another part that can be adapted in hybrid vehicles. It consists in capturing the energy from the vehicle when it brakes and reusing it later to accelerate. Supercapacitors are very efficient in this technology because they can recapture and store energy when there are bursts. Since the braking lasts only a few seconds, an energy storing device with high power density, such as EDLCs, are the most effective to absorb as much energy as possible (33). Furthermore, LIBs with high power are possible, but this would need of more battery materials and electrolyte to provide low changes in the state of charge. The charge rate and the depth of discharge in battery fabrication are usually limited by the oversizing in order to extend battery life and avoid replacements. For this reason, using EDLCs improve energy recuperation efficiency and eliminate the need for battery oversizing, which reduces the weight and the cost of the entire system. EDLCs are also implemented in rail applications for recovering the energy during braking and helping with the propulsion, for bridge power, for stabilising grid voltage. Buses, as vehicles, also incorporate supercapacitors to their regenerative braking systems.

In the case of trains and trams, energy storing devices must be robust and reliable, have a long operational lifetime and require low maintenance. Moreover, they must be able to manage peak currents, high duty cycles and frequent deep discharge/charge cycles.

Similarly, supercapacitors can also be used in the heavy duty machinery, for example, in cranes, straddle-carries, stackers, forklifts and more earth moving or mining equipment, because they can provide high power density and handle deep discharge cycles. Additionally, they allow minimising the diesel engine because peak power is no longer required. In forklifts supercapacitors are used to lift the

electric forklifts, because in large warehouse operations, batteries have limitations (34). In the harbour cranes and construction/mining deep discharge cycling with high duty cycle are required. When supercapacitors are used up to a 20 % of the diesel consumption can be saved by the braking/drop energy recovery, decreasing the $CO_2$ emissions up to 35 % (35).

Furthermore, EDLCs can be used in generators, because of their high power, fast response and long lifetime and in short-term back-up power, such as automatic gearbox backup systems, automatic crash response systems and x-by-wire controllers (36). Supercapacitors can also be used in back-up for video and audio equipment (cameras, telephones, printers, data terminals, rice cookers and intelligent remote controls), backup of data, for solar battery operated circuits (road guidance flasher), quick charging motor drivers (toy car), back-up power supplies (UPS), backup power supply of E-meter, driver assist of motors, actuators, backups for power supply of drive recorder, emergency brake, door lock releasing devices (37).

Together with the change of energy production model, from the traditional thermal based coal and nuclear energy to the renewables, solar and wind energy, there is the need to deliver quality and reliable power to the modern grid. Supercapacitors alone or integrated with batteries can meet the voltage and power quality requirements for grids and microgrids. Since renewable power can suddenly decrease to half, the EDLCs can respond to these fluctuations to enhance the stability of the grid, so they mitigate the inherent variations of the solar and wind generation (38).

Voltage sags are caused due to distribution line faults, large load additions within a utility service area and load additions from motor starting (39).

## 2.3 Principles of electrochemical capacitors

Figure 5 shows the schematic representation of the components inside an electrochemical capacitor cell and its basic charge/discharge process. Supercapacitor cells are composed of two electrodes (one positive and one negative), the separator and the electrolyte. The electrodes are made of electrically conductive materials in which the charge is accumulated. Upon the charge process the positive electrode is positively polarised, so electrons are removed from the same this electrode and the negative electrode is negatively polarised, electrons are accumulated into the electrode material. Commercial electrodes for electrochemical capacitors are made of the active material, a conductive additive and a binder, which are typically coated onto a current collector. The electrodes are the same in symmetric supercapacitors and different ones in asymmetric cells. The separator is a dielectric, that is soaked with the electrolyte, to allow ion permeability while avoiding the direct electrical contact between both electrodes. Therefore, the use of separators also allows minimizing the size of supercapacitor cells, because it allows bringing the positive and negative electrodes closer without short circuiting. The ability of the electrodes to accommodate electrolyte ions on their surface or in their structure determines the capacitance and capacity, and the electrolyte/electrode interface dictates the cell voltage through its breakdown potentials. Furthermore, the electrolyte greatly influences the total resistance of supercapacitors through its conductivity.

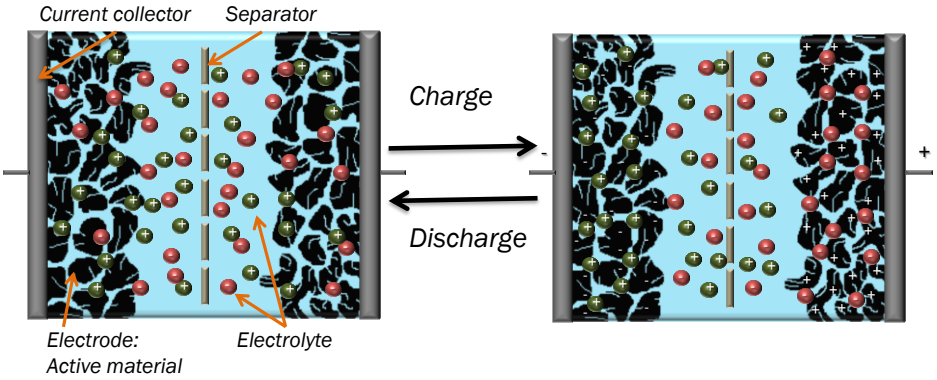


Figure 5 Schematic of the composition and basic charge/discharge mechanism of a type of electrochemical capacitors.

Capacitance, voltage and resistance are the three key parameters to optimise governing electrochemical capacitor performance capacitors. Capacitance (*C*) can be described as the charge (*Q*) stored by unit of voltage (*V*), according to Equation 1. Electrical double-layer capacitance does not involve charge transfer between the electrode material and the ions from the electrolyte and this is the basis of operation of most supercapacitor devices manufactured and used industrially. For plane surfaces, it can be simply and quite accurately described with a parallel-plate capacitor model (the Helmholtz model). According to this model, capacitance is proportional to the effective surface area ($S_a$) of the electrodes, the vacuum permittivity ($\varepsilon_0 = 8.854 \cdot 10^{-12}$ F m$^{-1}$) and the relative permittivity ($\varepsilon_r$) of the dielectric electrolyte in the double-layer, and inversely proportional to the interfacial distance between the electrode and the ions (*d*), as expressed in Equation 2.

$$C = S_a \frac{\varepsilon_0 \varepsilon_r}{d} \qquad \text{Equation 2}$$

Therefore, increasing the SSA of the electrodes, minimising the distance between pore walls and ions and using electrolytes with high relative permittivity would lead to high capacitance values. Therefore, double-layer capacitance requires materials with high surface area per mass or volume to provide sizeable amounts of charge storage.

On the one hand, it is important to have high values of capacitance in order to have high energy, but the voltage contributes more significantly, as energy (*E*) is calculated as:

$$E = \frac{CV^2}{2} \qquad \text{Equation 3}$$

Energy of an electrochemical system, the deliverable energy can be calculated according to Equation 4:

$$\mathrm{E} = -\int_0^{\mathrm{Q}} \mathrm{Vdq} \qquad \text{Equation 4}$$

The discharge energy for an electrochemical capacitor can therefore be calculated as:

$$\mathrm{E} = -\int_0^{\mathrm{Q}} \mathrm{Vdq} = -\int_{\mathrm{V_{max}}}^{\mathrm{V_{min}}} \mathrm{VdCV} = -\mathrm{C}\int_{\mathrm{V_{max}}}^{\mathrm{V_{min}}} \mathrm{VdV} = \mathrm{C}\frac{(\mathrm{V_{max}^2} - \mathrm{V_{min}^2})}{2} \qquad \text{Equation 5}$$

Equation 5 implies that capacitance is constant with potential (or voltage), which is not exactly the case for various electrochemical capacitor systems, but is approximately true for double-layer capacitors. Therefore, the equation based on capacitance should only be used for potential-independent capacitance. In a more general case, the integral of voltage over potential provides the

correct value of energy, which can be especially important for hybrid electrodes and cells systems that are in part based on Faradaic reactions.

On the other hand, power can be calculated from either Equation 6 or Equation 7. This means that high power involves having high energy at short discharge time ($\Delta t$) and it can be optimised by increasing the cell voltage while minimising the resistance ($R$). Power for a specific value of energy density can be obtained according to Equation 6:

$$P = \frac{E}{\Delta t} \qquad \text{Equation 6}$$

Whereas the maximum power of a device can also be calculated by as:

$$P = \frac{V^2}{4R} \qquad \text{Equation 7}$$

The equivalent series resistance (ESR) of a device is also another very important parameter to take into account, and it is influenced by resistive components, such as, the inherent resistivity of the active material, the resistance of the electrolyte and separator, the electrode spacing, etc. and it can be calculated by:

$$\mathrm{ESR} = \frac{\Delta \mathrm{V_{IR}}}{\Delta \mathrm{i}} \qquad \text{Equation 8}$$

where $\Delta V_{IR}$ is the voltage drop and $\Delta i$ is the total change in the applied current.

### 2.3.1. Models of electrical double layer capacitance

Most of the materials used in supercapacitors have pores comprised in the microporous range, with pore widths below 2 nm. Thus, ions cannot be understood as being adsorbed on a single interface, but being confined between two surfaces (pore walls) instead. Therefore, classical theories of electrical double-layer cannot describe the capacitance in such electrodes.

Several treatments were proposed to approach capacitance in the pores. The Helmotz model is the most basic approach to explain the special charge distribution on double-layer interfaces (Figure 6a). The charge of the solid electronic conductor is countered by the ions of the opposite charge at a distance, $d$, from the solid. These neutralising charges are considered to be rigid layers, represented as a simple parallel plate capacitor model.

The Gouy-Chapman or diffuse model considers that counter ions concentrate in the vicinity of the charged solid, without ions being rigidly attached to the surface (Figure 6b). The diffusion of ions into the solution occurs, but it is limited by the counter potential. The thickness of the diffuse layer is determined by the kinetic energy of the ions and its ion concentration is ruled by Boltzmann distribution. This model cannot represent highly charge double-layer, since the experimentally measured thickness is larger than the calculated one. Although the Gouy-Chapman model is more realistic than the Helmotz model, it is not quantitatively accurate and it does not consider the restricted access of ions to the surface.

The Stern model advances by considering that ions can be specifically adsorbed in the surrounding of the electrode surface (Figure 6c). The ions form a compact layer in which they are strongly specifically adsorbed, forming the outer Helmotz plane (OHP). In this model, the internal Stern layer (IHP and OHP) and an outer diffuse layer (e.g. the Gouy-Chapman layer) are combined. (40)

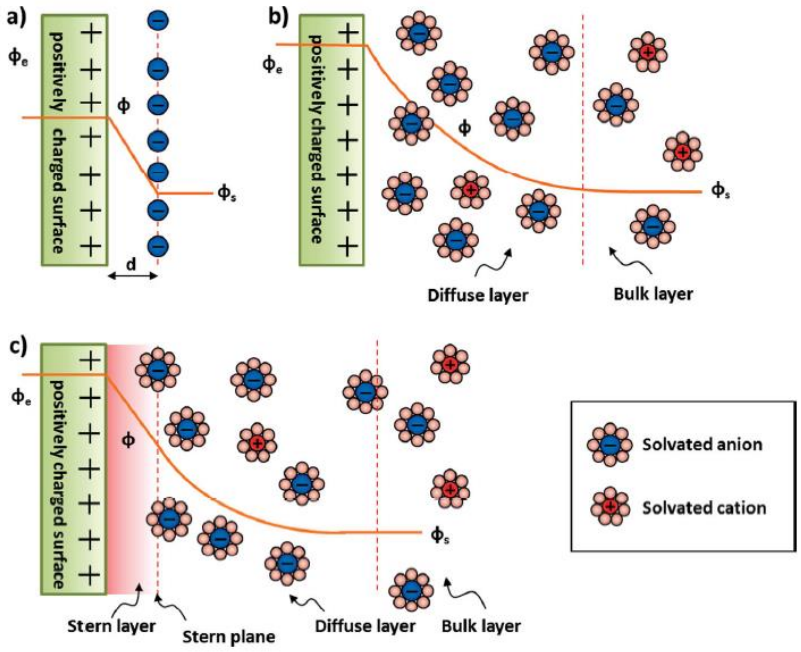


Figure 6 © (40)

All these models are applicable for electrical double-layer on a plane surface, but no so much for the real electrosorption in nanoporous electrodes, which still is lacking of a complete understanding. One of the factors that was not contemplated in the previous model is the effect of surface curvature, which can be significant, since nanoporous material can have various pore shapes, such as cylindrical, slit and spherical. Therefore, when pores are cylindrical, an electrical double-cylinder capacitor (EDCC) can be formed (41; 42).

$$C = \frac{2\pi\varepsilon_r\varepsilon_0 L}{\ln(\frac{b}{a})}$$ Equation 9

where *L* is the pore length and *b* and *a* are the radii of the outer and inner cylinders, respectively.

This model assumes, similarly as in the Helmholtz model, that the counter ions on the inner cylinder completely counter the charges on the pore walls; and that the space charge layer contribution to the overall double-layer capacitance is neglectable because of the high conductivity of the carbon materials.

If this model is driven towards narrower pores, ions may end up entering the cilindrical pores forming an electric wire-in-cylinder capacitor (EWCC). Even if the charge is not evenly distributed among the ions geometry, the pore walls can suffer an average counter charge, because of the transaction and rotation of the ions over the pore axis. In this case the radius of the inner cylinder in micropores would correspond to the effective size of the ions, $a_0$.

### 2.3.2. Pseudocapacitance

The so called pseudocapacitance is an energy storage mechanism that not only is still not fully understood but also is often misused. Pseudocapacitance is claimed to be a different type of capacitance, which can be collectively described with the same capacitance equations as above. Thus, the state-of-charge is proportional to the potential, but is not electrostatic in nature, and is supposedly related to rapid charge transfer (redox process) on the surface or in the near-surface region of electrode materials. Only a limited number of redox processes can be formally described with the capacitance-like equation, so in order to be considered pseudocapacitive, materials should be able to

rapidly provide discharge energy at the same timescale as double-layer capacitance. Thus, it is misleading to use nanostructured battery materials in electrochemical capacitor cells, which are supposed to be high power devices, and carrying out the electrochemical test under low rates and without probing the long cyclability The misuse of the term pseudocapacitance comes from the misunderstanding that pseudocapacitance involves some kind of faradaic process, so often it has been misused to describe battery-type materials. Battery materials clearly have a different electrochemical signature by showing faradaic redox peaks in their cyclic voltammograms as well as plateaus in their constant current charge discharge profiles (43), as shown in Figure 7. However, battery materials can be combined with capacitive materials to build asymmetric cells. When one of the electrodes consists of a capacitive material and the other one of a faradaic material, the resulting hybrid cell performs as a capacitor electrochemically, but this is not a pseudocapacitor. Pseudocapacitance should only be used to describe the mechanism that one material undergoes when it is charged/discharged at the material level (43), not at the cell level. Therefore, redox materials should not be named incorrectly as pseudocapacitive materials, because faradaic and capacitive electrodes show different electrochemical behaviour and their description should be done accordingly to avoid misunderstanding and misnaming of the electrode materials (44).

On top of that, it is still to probe how the pseudocapacitive mechanism actually works. It is believed that pseudocapacitance is due to the superposition of several overlapping redox couples. However, according to empirical calculations, surface faradaic processes show peaks only, which can be more or less broadened depending on the interaction between the reactants, but capacitive response cannot be obtained through that mechanism (45). Surface faradaic peaks can also add to the capacitive double layer charging in proportion to the scan rate (υ). Even for $MnO_2$, which is one of the most referred as pseudocapacitive material, the CV is quasi rectangular.

In a charge process the electron transfer at the interface is accompanied by the insertion of the counter ion. When a diffusion limited interfacial reaction occurs (in battery type materials), while the concentration of the ions is kept constant, the response is proportional to $\upsilon^{1/2}$, and when the diffusion of the counterion matches that of the interfacial electron transfer (in capacitive or pseudocapacitive materials), thus the counterion and the electron transport is fast, the response is proportional to υ. Therefore, the magnitude of the scan rate rules the transition from diffusion control to surface reaction behaviour. The proportion to the scan rate should be used to differentiate the faradaic response from that of a double layer charging/discharging response, instead of the singular response at a scan rate.

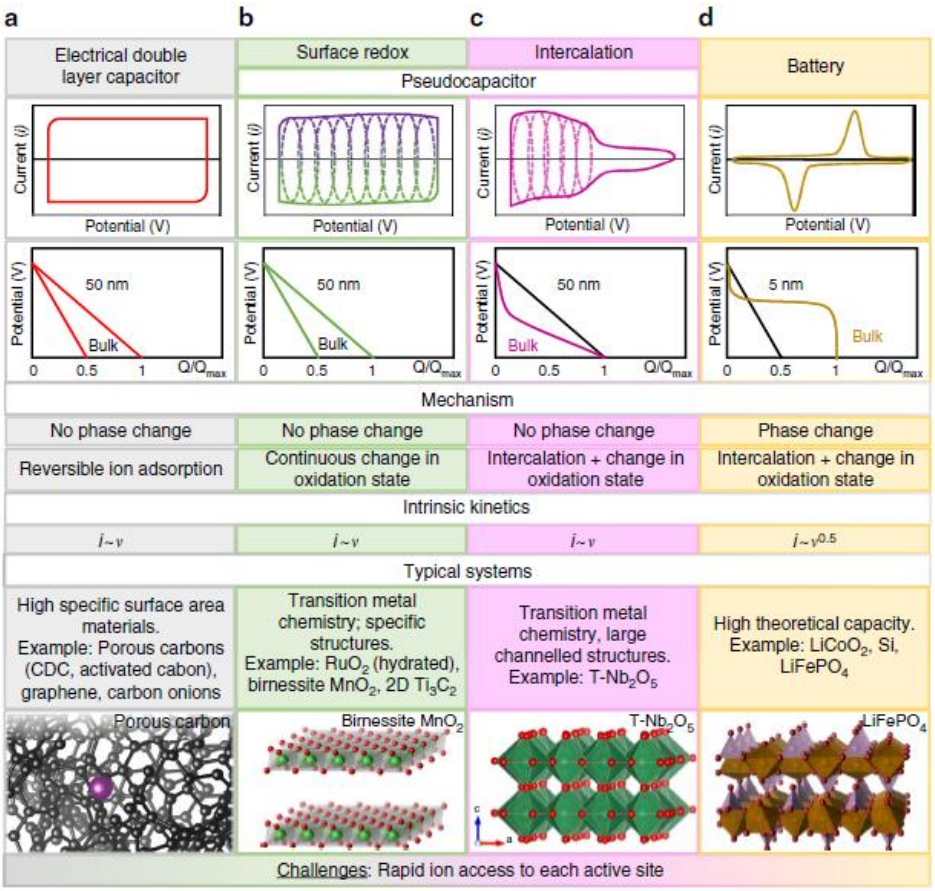


Figure 7. Faradaic and capacitive energy storage (46).

## 2.4 Carbon materials for electrochemical capacitors

### 2.4.1. Overview

Carbon has four crystalline (ordered) allotropes: diamond ($sp^3$), graphite ($sp^2$), carbene ($sp$) and fullerenes (distorted $sp^2$), from which only diamond and graphite are naturally found as minerals on Earth. However, carbon has many other amorphous allotropic structures and diverse structural forms. Most of the commercial carbons are engineered carbons that have different percentages of disordered microstructures in comparison with graphite. Basically, they have regions of hexagonal carbon layers not completely ordered in parallel. They are typically prepared by heat treatments under inert atmosphere, which enables them to have different degrees of graphitisation. Their properties depend on the carbon precursor, its dominant aggregation state during carbonisation, processing conditions and the structural and textural features of the products.

Carbon materials combine numerous chemical and physical properties making make them the most suitable materials for EDLCs (47). Among various forms of carbons, activated microporous carbons have become the materials of choice owing to their high SSA, around 2000 $m^2 g^{-1}$, which is required to maximize capacitance according to Equation 3. They also provide the high surface-to-volume ratio among other porous carbons, which is also favourable for volumetric performance. Other characteristics of microporous carbons that make them advantageous for EDLCs are their high conductivity, good corrosion resistance, high temperature stability, controlled pore structure, processability and compatibility with other materials, and, most importantly for industry, their relatively low cost. Commercial ACs are usually prepared by carbonization of carbon-rich organic precursors such as biomass or fossil fuels under inert atmosphere with subsequent creation of a pore network (activation, as detailed in the next subchapter) (48).

Templated microporous carbons are prepared as negative replicas of a hard template (the most interesting example is based on zeolite faujasite) whose pore walls are converted into well-ordered 3D micropore networks (49). The synthesis method includes polymerization (furfuryl alcohol) and/or chemical vapour deposition (CVD) processes inside the zeolite pores with the subsequent template removal to produce pores separated by graphene-like walls. This material is superior to most ACs due to its ultrahigh surface area and nearly straight pores, with high volumetric capacitance (80 F $m^{-3}$) and superior rate capability, but the high cost of the synthesis procedure renders its implementation in practical devices rather problematic (50).

Graphene and graphene oxide have undergone extensive research in the last years. Single layer graphene (Gr) is a 2D material composed by an atom thick hexagonal carbon lattice with delocalised π-electrons. Few layers graphene (FLG) contains up to ten layers and can be prepared by mechanical exfoliation, epitaxial growth onto SiC wafers, CVD on single layer metal surfaces, arc discharge of graphite and from metal intercalated multi-layers graphene (51). Multi-layer graphene (MLG) is a 2D material, either as a free-standing flake or substrate-bound coating, consisting of a small number (between 2 and about 10) of well-defined, countable, stacked graphene layers of extended lateral dimension. Although a single layer graphene has a high SSA of 2630 $m^2$ $g^{-1}$, it is difficult to make use of this surface area, since graphene layers tend to restack in powdered form due to strong van-der-Waals interaction. Restacking leads to a diminished SSA of graphene powders (up to a few hundred $m^2$ $g^{-1}$ only) and reduces the capacitance of such materials. Most graphene-like powders also have low density, which penalizes volumetric performance. However, graphene oxide can be used as a precursor for high SSA activated graphene that is able to maintain a high SSA (> 2000 $m^2$ $g^{-1}$) with porosity well accessible to electrolyte, resulting in high capacitance values (52; 53). Graphene can also be useful in microsupercapacitor devices (low-energy ultrahigh-speed supercapacitors intended for use in electronics). Vertically oriented plasma-grown graphene layers are suggested as a replacement to electrolytic capacitors since they are able to provide effective 120 Hz *ac* line filtering with higher energy (54).

Exohedral (positive-curvature) carbons are carbon nanotubes, nanohorns and nanoonions (55). Carbon nanoonions can be produced by vacuum anneling of nanodiamond powder at temperatures between 1200-2000 °C (56). Contrary to the ACs, their pore size does not depend on the annealing temperature. Exohedral carbons have properties similar to graphene with respect to their use in supercapacitors. These materials can only store counter ions on the outer surface which limits the SSA from storing competitive amounts of charge. However, they show improved rate performance due to the unhindered accessibility of their surface to electrolytes. This leads to interesting solutions for applications such as extending the temperature range of supercapacitor operation with ionic liquid electrolytes (ILs) since ILs fall short of rapid charge delivery in microporous carbons due to their high viscosity and limitations imposed by the tortuous pores of ACs (57).

Template mesoporous carbons are usually prepared by either soft- or hard-template procedures, and can be prepared with a variety of mesopore sizes and morphologies. They have limited SSA (usually up to 1000 $m^2.g^{-1}$) with associated limited capacitance values. With respect to supercapacitors, mesoporous carbons can also be beneficial in terms of improving rate capability and working with high-viscosity electrolytes such as ionic liquids. (58; 59)

### 2.4.2 Synthesis of activated carbons (ACs)

As mentioned earlier, ACs are the most utilised materials as electrodes for EDLCs. They are produced by physical (using steam or $CO_2$) or chemical activation (with KOH, NaOH, $H_3PO_4$, $ZnCl_2$,...) of carbonaceous precursors, such as coconut shells, pitch, coal, polymers, etc.

The texture of ACs presents an irregular network of pore channels, which is characterized by textural properties. Those properties of porous materials include SSA, pore volume, pore size distribution, average pore size, etc. They influence the electrochemical behaviour of supercapacitor electrodes. For example, their pore size distribution needs to be adapted to the ion size, so the pore size exceeds that

of the ions to avoid the so-called ion-sieving effect, which is caused by the limiting the accessibility of pores to ions (60). It has been demonstrated that when pores closely match the ion size the electrolyte accessibility is hindered also due to surface saturation causing limitations in the charge storage capability (61). Gate effects (bottleneck along pore channels) are also unwanted because some part of specific surface area can be inaccessible. ACs usually have some oxygenated surface groups, which, on the one hand, can increase the capacitance of supercapacitors by providing some contribution of pseudocapacitance (in aqueous electrolytes) (62). On the other hand, the presence of these resistive faradic reactions worsens the cycle life of these devices by promoting electrolyte decomposition due to highly reactive oxygen-rich sites (62).

The preparation of ACs includes two processes: carbonization and activation. In the carbonisation process carbon precursors are decomposed (pyrolysed) by getting rid of heteroatom-containing volatile compounds and forming macromolecular frameworks. At higher temperatures punctual graphitic units start to grow by condensation reactions to form microcrystallites that look like graphite. The size of graphene sheets ($L_a$), the stacking number of graphene sheets and the relative orientation of the crystallites depend on the nature of the precursor and determine the properties of the resultant carbon such as the texture and electrical conductivity.

Precursors, such as petroleum pitch, coal pitch, some polymers, which under heat treatment go through a fluid stage, a mesophase, can be structured into highly ordered graphite, so that they are referred to as graphitising carbons, or soft carbons. Whereas the ones that stay at a solid stage during pyrolysis, for example, derived from biomass, non-fusing coals and thermosetting polymers (PVC, PVDC), are non-graphitising carbons, or (hard carbons, since an ordered graphite structure cannot be achieved, even by the high-treatment processes. The release of volatiles from solid state creates a highly porous structure within these carbons.

Figure 7 shows the schematics of the structure of non-graphitising carbon proposed by Franklin, whose studies are fundamentals to understand these types of carbons (63). She concluded in 1950 by diffuse X-ray that the non-graphitic carbons had a 65% of graphite-like layers with a diameter of 1.6 nm, this value coming into agreement with the corresponding size of hexagonal structure of the carbon in graphite, while the remaining 35% were not organized, presenting defects of the planar structure. Furthermore, she observed that the 55% of the planar graphite-like structure had an interlayer spacing of 0.37 nm (64), this one differencing from graphite, 0.335 nm, due to the stacking of less number of layers than in graphite, due to the tension accumulated from the contracted non-ordered planar structure, while the remaining 45% of the layers did not have a mutual constant orientation. She attributed these defects to the formation of a strong cross-linked system at low temperatures that united the crystallites in a random orientation, forming a finely porous carbon structure (65). These types of carbons were obtained from precursors with low hydrogen or high oxygen content.

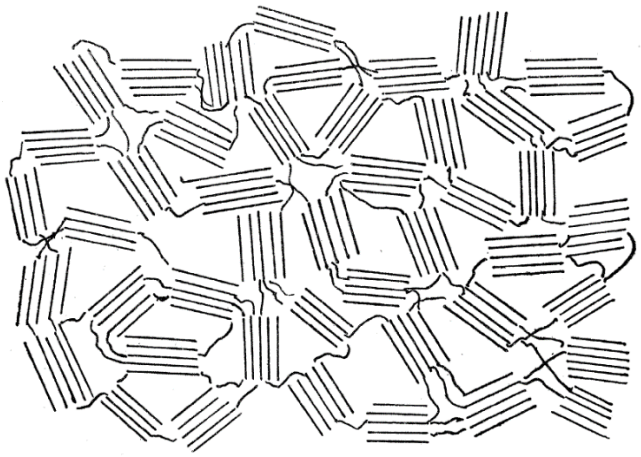

Figure 8 Schemicatic representation of the structure of non-graphitising carbon (65) ©

With regard to these strongly cross-linked systems, Harris suggested in 1997 by characterising non-graphitising carbons with high-resolution electron microscopy that they were composed by fullerene-like elements. Figure 9 shows his schematics for the structure of non-graphitising carbons. He proposed a model of hollow nanoparticles rather than a solid graphitic mass. Furthermore, his results showed the presence of pentagonal and other non-six-membered rings in the structure, which disables the graphitisation. Transmission electron microscopy (TEM) studies showed that non-graphitising carbons had curved fragments of ~1-1.5 nm, so they were transformed into fullerene-like nanoparticles, due to the high content of pentagons and a small content of heptagons in the original carbons. He characterised the micropore size to be ~0.5-1 nm.

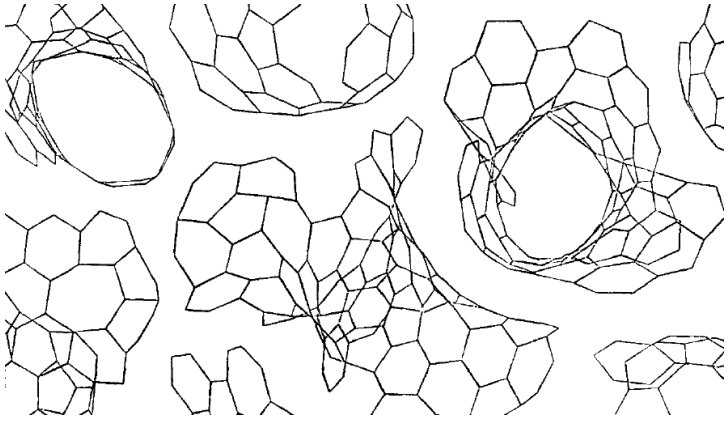

Figure 9 Schematic representation of the structure of non-graphitising carbons (66). ©

In such non-graphitizing carbons, pores are closed and not accessible to electrolyte. Therefore, additional treatment (activation) of pyrolized carbons is required to create porosity that can be exploited for charge storage by electrosorption. The process of activation increases the surface area and porosity of the carbons by opening the already existing pores and creating new ones. Temperature, time and activating agent can be varied in order to control the resulting porosity, pore size distribution and internal SSA.

Two types of activations are usually distinguished: physical and chemical activation. In the physical activation, temperatures between 700 and 1100 °C together with oxidising gases such as steam, $CO_2$, air, or mixtures of these gases are used. Scheme 1 summarizes the proposed mechanisms for the activation with steam, in which carbon atoms react with water molecules to give $H_2$ gas and CO or $CO_2$. The later chemical equation describes the activation mechanism with $CO_2$ gas, in which the carbon precursor reacts with $CO_2$ to produce CO.

$$C + H_2O \rightarrow H_2 + CO \quad \text{Equation 10}$$
$$C + 2H_2O \rightarrow 2H_2 + CO_2 \quad \text{Equation 11}$$
$$C + CO_2 \rightarrow 2CO \quad \text{Equation 12}$$

**Scheme 1.** Chemical reactions involved in the steam-activation process.

The amount of burn-off can be managed by the temperature and duration of activation. The higher the burn-off, the wider the pore size and lower the carbon strength, the density and the yield.

In the chemical activation, temperatures between 400 and 700 °C are used, and the carbon is preliminary mixed with an activating/dehydrating agent, such as, phosphoric acid, zinc, sodium or potassium chloride. The reaction mechanism proposed for hydroxide activation is summarized in the Scheme 2, where the MOH can react with the carbon to produce $M_2CO_3$, $M_2O$, $K_2CO_3$, $K_2O$ and hydrogen gas.

$$4MOH + C \rightarrow M_2CO_3 + M_2O + 2H_2 \quad \text{Equation 13}$$

(where M=K or Na)

**Scheme 2.** Chemical reactions involved in the KOH/NaOH-activation process.

A washing step with acids and water is usually required after activation to get rid of inorganic by-products of activation. With this type of activation higher SSA are usually achieved and the pores are wider than with physical activation.

Another type of activation process is the electrochemical activation, which takes place when a large positive potential is applied in an aqueous electrolytic solution, for instance 1 M $H_2SO_4$. The surface of a glassy carbon is reduced with this process creating, apart from porosity, functional groups that contribute to pseudocapacitance.

### 2.4.3 Olive pits as precursors for microporous carbons

Olive trees have existed since the twelfth millennium BC and witnessed the development of many civilisations (67). The wild olive tree, originated in Asia Minor, was spread from Siria to Greece where its planting was regulated in the 4$^{th}$ century BC. From the 6$^{th}$ century BC onwards, it was spread to Tripoli, Tunis, Sicily and the south of Italy. Then, the Romans expanded it to countries bordering the Mediterranean sea such as Marseilles, Gaul and Sardinia, and it arrived to Corsica after the fall of the Roman Empire. Olive growing was introduced in Spain by the Phoenicians. Olive trees occupied the Baetica valley after the third Punic War, and spread towards the central and the Iberian Peninsula, including Portugal. The Arabs also brought their varieties to the south of Spain and influenced so much on its cultivation that even the word for olive (aceituna) and oil (aceite) have Arabic roots. When America was found olive farming was spread to Mexico, Peru, California, Chile and Argentina. Now, it is farmed in southern Africa, Australia, Japan and China as well. Despite of the worldwide extension of the production of olive oil and the table olives nowadays, the 93% and 87% of it, correspondingly, is done in the European Union (68), of which Spain is the main olive producer without a doubt, as shown in Figure 10.

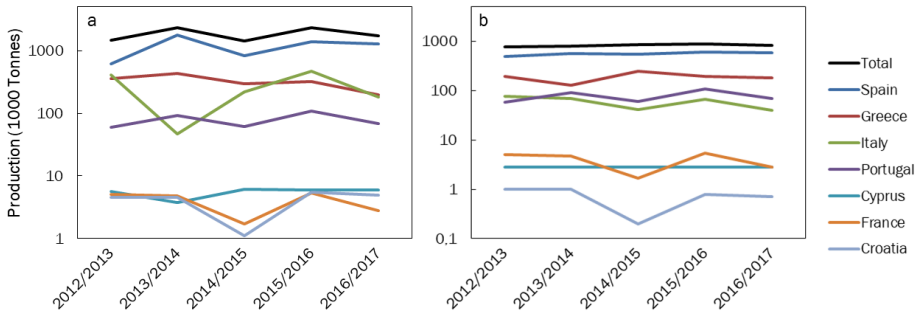


Figure 10 Evolution of the production of (a) olive oil and (b) table olives in the European Union.

On the one hand, the olive oil extraction process creates two main by products: the vegetation water, also called black water or vegetable water, and the olive husk which includes skins and stones (69). Depending on the production conditions, 50-100 kg of highly polluted water result from 100 kg of olives. The solid wastes are the alperujo, from the two phase extraction system, and the orujo, from the three phase system (70). On the other hand, the pitted olive industry creates the whole olive stone as a by product too.

Olive stone is a lignocellulosic material that, from the environmental and economic point of view, can be considered as a renewable energy source. It is also an important natural source of phenolic compounds (71). It has many uses, such as, for the production of energy through the combustion of the olive stones as biomass, for making ACs from olive stones as adsorbents, for the production of liquid and gas products as fuel, for the production of olive seed oil, for producing furfural, to prepare composites with polymers, to use it as an abrasive and in cosmetics for skin exfoliation (70).

In this sense, olive stones are an important source of carbonaceous precursors for producing ACs, not only from the industrial point of view, since it does not only make them really accessible and abundant in Spain, but also from the environmental point of view, because it helps to give a value to a waste that otherwise would not have a second life (72). The activation process is divided into two processes as described earlier. In particular for the case of lignocellulosic materials, the pyrolysis is one form of energy recovery process, in which char, oil and gas product are generated (73) By the pyrolysis, the resulting char develops some properties, such as, porosity, surface area, pore structure (micropore, mesopores and macropores) that their precursors did not have and the composition, elemental analysis and ash content is also changed, bringing high reactivity and the possibility to exploit them as adsorbents. This char can be further activated to produce activated carbons, useful for sorbents for air pollution and for water treatment. They are useful for removing organic compounds from air and water and they can be used as catalysts and catalyst supports too.

The particle size, temperature and heating rate influence the product of the pyrolysis. The produced ACs have high adsorption capacity, good mechanical strength, and low ash content. The following parameters have the most effect in order of significance: the temperature of pyrolysis, the heating rate, the nitrogen flow rate and the pyrolysis residence time. When the temperature is increased the yield of solid decreases and the yield of liquid and gases increases. Thus, higher temperature leads to better quality chars. The physical activation step requires a gas oxidising agent, such as, $CO_2$, steam, air or their mixtures. The longer the activation time, the greater the adsorption capacity of the resultant ACs is, thus, the surface area and the total pore volume increase when the activation duration is extended from 1 h to 2 h (74). In the chemical activation the two steps can also be carried out simultaneously, using dehydrating and oxidant agents, such as $ZnCl_2$, KOH, $H_3PO_4$ and $K_2CO_3$ (75). However, the two-step process is more effective, because it gives higher porosity with the highest specific surface areas (76).

### 2.4.4 Textural and surface area properties of ACs

ACs are nano-sized pore carbons which in essence can be described as randomly wrinkled graphene sheets (77). Figure 11 and Figure 12 show the annular dark-field-scanning transmission electron microscopy (ADF STEM) images and the segment of a simulated defective graphene sheets. The curvature of graphene-like layers making up porous carbons originates from the presence of nonhexagonal carbon rings, five- and seven-atom rings, which introduce topological defects to the otherwise planar structure. Thus, the spacing between the graphene planes is increased by ~10%. Thereby, the stacking of the layers is limited by local distortions and then the surface area and pore volume are increased. This suggests that defects on the graphene sheets, also by doping the edge sites, can enhance the porosity of the carbons. On the rest of the carbon structure graphene-like sheets tend to stack together, within graphitic domains. ACs have high rigidity, so the created porosity cannot be collapsed by applying pressure or other type of mechanical treatments during the electrode processing.

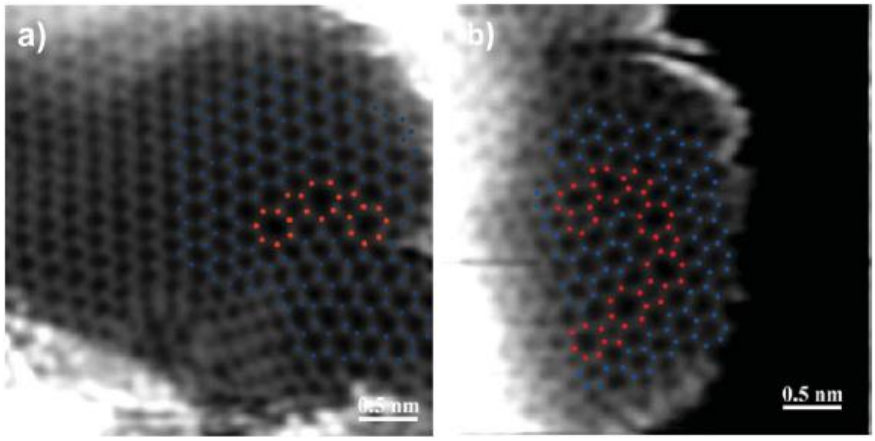


Figure 11. ADF STEM images of in plane carbon atoms with large areas of hexagonal lattice (blue) and a few five- and seven-atom ring defects (red) from ultramicroporous carbons (77).(C)

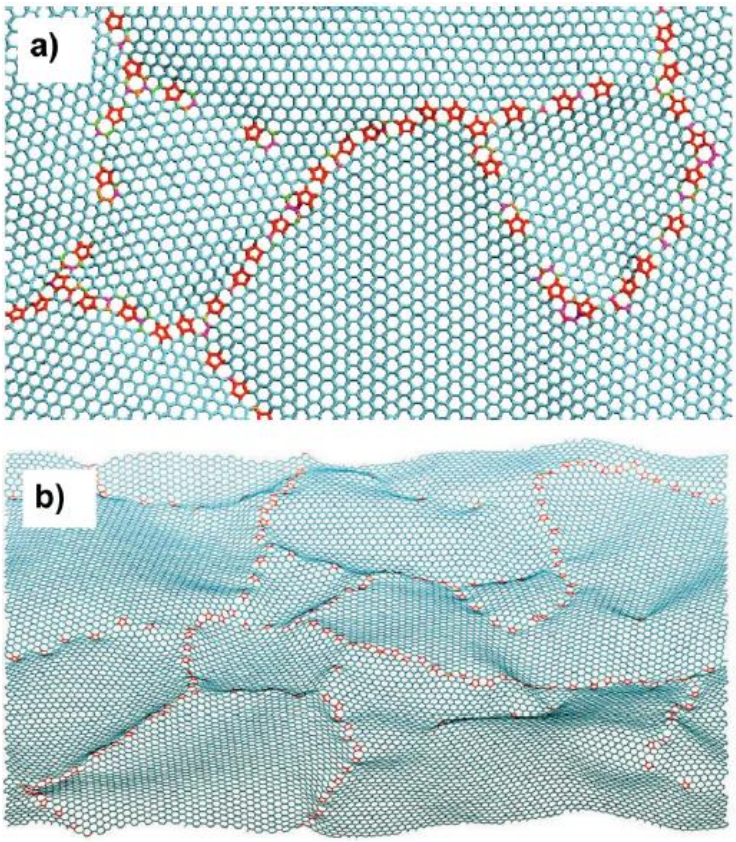


Figure 12 Segment of a simulated defective graphene sheet (blue), with five to seven dislocation structures (red), showing the height variations (77). ©

Nanoporous carbons have very large SSAs, between 500-3000 $m^2 g^{-1}$, due to the interconnection of internal pores. Depending on the pore size the IUPAC classifies them into micropores (diameters <2 nm), mesopores (between 2-50 nm) and macropores (>50 nm) (51). Micropores give a high surface area to volume ratio, in other words, they can increase the surface area of the material without sacrificing too much its density. Micropore sizes extend down to molecular dimensions and play an important role in the selectivity of adsorption-based processes, through restricted diffusion and molecular sieve effects, even to the point that they can be harshly characterized by conventional gas adsorption molecules.

Gas adsorption is a widely used technique for the characterization of porous solids. Generally, adsorption is the enrichment of molecules, atoms or ions in the vicinity of an interface, which in this case is the surface of the solid. The adsorbate is the material that is adsorbed, which is denominated as adsorptive when it is in the fluid phase. The physisorption occurs when an adsorbable gas (the adsorptive) is brought into contact with the surface of a solid (the adsorbent). Attractive dispersion forces and short range repulsive forces are the main intermolecular interactions involved, but specific molecular interaction, such as, polarisation, field-dipole and field gradient-quadropole can also occur due to particular geometrics and electronic properties of the adsorbent and adsorptive.

The adsorption isotherm is the relation between the amount adsorbed ($N_a$) and the equilibrium pressure of the gas at constant temperature. Usually, the relative pressure ($p/p^0$) is adopted at the adsorption temperature below the critical point, where p is the equilibrium pressure and $p_0$ is the saturation vapour pressure at the adsorption temperature.

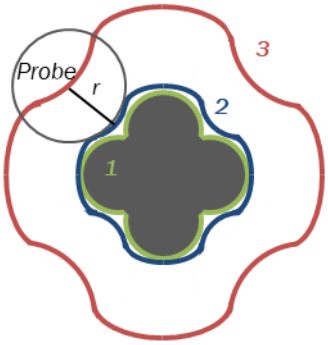


Figure 13. Schematic representation of several possible surfaces of an adsorbent. 1: van de Waals, 2: Connolly and 3: accessible, r-distance (51).

The surface of a solid can be considered and defined at different levels: Figure 13 shows the schematics of the possible adsorbed surfaces. The van der Waals surface is formed at the atomic scale, by the outer part of the surface atoms. The Connolly surface is the surface drawn by the bottom of a spherical probe molecule rolling over the van der Waals surface, the probe-accessible surface. This surface is assessed by physisorption and does not coincide with the van der Waals surface. The r-distance surface is at a certain distance, r, from the Connolly surface (51).

The surface can be subdivided into external, which is the surface outside the pores, and internal, which is the surface of the pore walls. The measured values of internal area and pore volume are dependent on the accessibility of the adsorptive molecules due to their size and shape.

Micropore filling is the primary physisorption process, which enables to distinguish between ultramicropores (<0.7 nm) and supermicropores (>0.7-2 nm). The physisortion in mesoporous adsorbents takes place into three steps: (i) the monolayer adsorption, in which all the adsorbed molecules are in contact with the surface of the adsorbent, (ii) the multilayer adsorption, in which not all the molecules are in direct contact with the surface, so there are more than one layer of adsorbed molecules in the adsorption space and (iii) the capillarity condensations, which reflects the vapour-liquid phase transition in the pore at a lower pressure than the saturation pressure $p^0$ of the bulk liquid.

The adsorption-desorption isotherms can be grouped into six main types, for which an updated classification has recently been proposed, in order to relate them more closely to particular pore structures (51).

Type I has a steep uptake at very low $p/p^0$, which draws a concave curve with respect to the axis, and the amount adsorbed approaches a limiting value resulting in micropore filling at low $p/p^0$. Type I(a) are given by microporous materials having mainly narrow micropores (of width < 1 nm) and type I(b) isotherms by materialsmaterial having a broader pore size distribution possibly including narrow mesopores (<~2.5 nm).

Type II isotherms are given by non-porous or macroporous absorbents, due to an unrestricted monolayer-multilayer adsorption up to high $p/p^0$. Point B usually corresponds to the completion of monolayer coverage and the thickness of the adsorbed multilayer generally increases without limit when $p/p^0=1$.

Type III isotherms appear also for nonporous or macroporous solids, but in theses ones there is not a B point, the interactions between adsorbent-adsorbate are weak and the amount adsorbed at $p/p^0$ remains finite.

Type IV isotherms are given by mesoporous adsorbents. First, monolayer-multilayer adsorption takes place, then, in-pore condensation, which is a phenomenon whereby a gas condenses to a liquid-like

phase in a pore at a pressure less than the saturation pressure of the bulk liquid, and finally a plateau of saturation with variable length. Type IV(a) isotherm, which shows hysteresis with the capillary condensation, occurs when the pores are wider than ~4 nm. Type IV(b) isotherms are given by smaller width mesopores and by conical and cylindrical mesopores that have a closed end.

Type V isotherm are observed for water adsorption on hydrophobic microporous and mesoporous adsorbents.

Type VI isotherm is representative of layer-by-layer adsorption on a highly uniform nonporous surface.

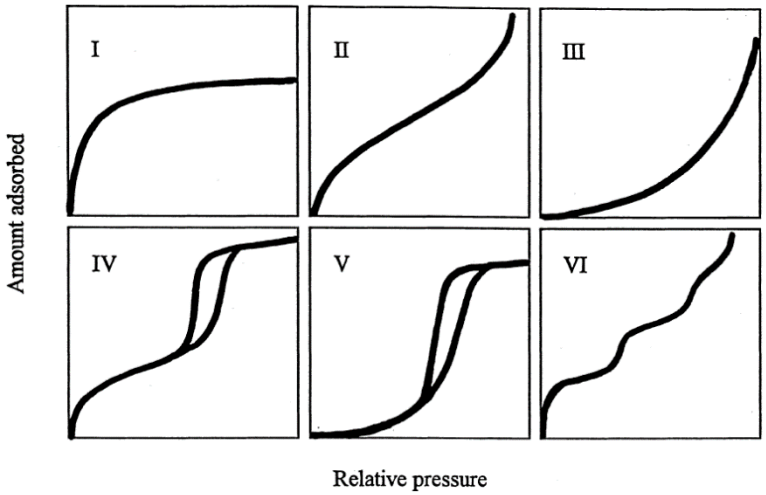


Figure 14. Classification of the types of isotherms (78) ©

Brunauer-Emmett-Teller (BET) is the most widely used method for determining the surface area of porous materials. Despite its adequacy for nonporous, macroporous or mesoporous solids with type II or IV isotherms, its application for microporous materials with type I isotherm must be very careful.

In the first stage, the physisorption isotherm has to be transform into the BET plot, by applying the BET equation in its linear form:

$$\frac{p/p^0}{n(1-p/p^0)} = \frac{1}{n_m C} + \frac{C-1}{n_m C}(p/p^0)$$ Equation 14

where $n$ is the specific amount adsorbed at the relative pressure $p/p_0$, nm is the specific monolayer capacity and $C$ is a parameter related to the energy of monolayer adsorption.

In the second stage, BET area has to be calculated from the monolayer capacity.

$$a_S(BET) = n_m L \sigma_m / m$$ Equation 15

where $a_S$ is the BET specific area, $L$ is the Avogadro constant, $\sigma_m$ is the molecular cross-sectional area and $m$ the mass.

Several semi empirical methods have been proposed for evaluating the pore size distribution of slit, cylindrical and spherical pores, by Horvath and Kawazoe (the HK method), Saito and Foley, and Cheng and Yang, respectively. These methods can be utilised to compare microporous materials despite their tendency to underestimate the pore size (51).

In order to provide a more reliable analysis of the pore size over the complete nanopore range, microscopic treatments applied to the molecular behaviour of confined fluids such as density functional theory and molecular simulations have been considered as superior methods. The fluid

solid interaction changes for different pore shapes (eg. slit and cylindrical, hybrid shapes), so many models have been developed for various materials (eg. carbons, silicas, zeolites)

Non-local-density functional theory (NLDFT) are extended in commercial software and allow calculating the kernel, which is a series of theoretical isotherms ($N(p/p_0, W)$) with pores of different widths of a given shape. The calculation of the pore size distribution function f(W) is based on a solution of the general adsorption isotherm (GAI) equation, which correlates the experimental adsorption isotherm $N(p/p_0)$ with the kernel of the theoretical adsorption or desorption isotherms $N(p/p_0,W)$. So the GAI equation:

$$N\left(\frac{p}{p^0}\right) = \int_{W_{min}}^{W_{max}} N\left(\frac{p}{p^0}, W\right) f(W) dW \qquad \text{Equation 16}$$

Meaningful and stable solutions can be found by using regularisation algorithms. NLDFT model has also some drawbacks from the fact that it assumes a smooth and homogeneous carbon surface. Most of the PSD analysis applications assume slit pores with energetically uniform surface walls of infinite extent. Therefore, two interrelated artefacts emerged: i) a minimum in the PSD plot at 1 nm and ii) a S-shaped deviation between the theoretical and the experimental isotherms near $10^{-4}$ $p/p_0$, which are linked with the layering transitions between monolayer, bilayer and so on. The 2D-NLDFT introduces the energetical heterogeneity or geometrical corrugation to the surface of pore walls in order to eliminate the artefacts of the standard model (79). The surface of pore wall is treated as randomly wrinkled graphene sheet containing non-hexagonal defect rings, in order to consider the spatial non-uniformity of the adsorbent surface. Whereas quenched solid density functional theory (QSDFT) treats carbon as an amorphous solid with variable density near the surface. It uses a surface roughness parameter in order to account for surface heterogeneity, which significantly improves the reliability of pore size analysis of nanoporous carbons (80). Althought they use different methods for accounting for the heterogeneity of the carbon, 2D-NLDFT and QSDFT methods give similar PSDs (81). The nanoporous system must be compatible with the chosen DFT/MC kernel to avoid a significant error in the derived pore size distribution.
Micropore volume evaluation can be analysed by Dubinin's pore volume filling theory too. According to Dubinin-Radushkevich (DR) equation, the plot of $log n$ vs $log^2(p/p_0)$ is linear if the micropore size has an uniform Gaussian distribution and thus, the micropore capacity can be obtained by extrapolating the ordinate. However, if the linear part is absent or restricted to a limited range of low relative pressures the DR method might not be reliable.

### 2.4.5 Electrical properties of ACs

Electrical properties of carbons depend on their structure, for instance, the electrical conductivity of ACs is directly related to the thermal treatment during the synthesis, the porous texture and the content of heteroatoms (82). Most carbon precursors are good insulators due to the high content of σ-bonds related to $sp^3$-carbon hybridisation. By using thermal treatments, the carbons start to lose acidic functionalities at 600-700 °C, to form $H_2O$ and $CO_2$, so the structural disorder is changed. Thereby, the conductivity is highly increased due to the transformation to $sp^2$ aromatic fragments because the π-bond electrons are delocalised. On the contrary, the formation of porous structure leads to a lower conductivity due to created insulating voids. Moreover, the formation of pores is linked to the cross-linked fragments, which do not fulfil the planarity required for π electrons to move freely. In general terms, functional groups also contribute to worsen the conductivity of the carbons, for example oxygenated groups at the edges are electron acceptors that localise the charge on their site, decreasing the electronic cloud over the carbon structure. However, the introduction of nitrogen atoms to the basal plane donates more π electrons, increasing the conductivity of the carbon.

Table 3 A comparison of various carbon electrode materials for supercapacitors (83) ©

| Carbon | Specific surface area ($m^2 g^{-1}$) | Density ($g cm^{-3}$) | Electrical conductivity ($S cm^{-1}$) |
|---|---|---|---|
| Fullerene | 1100-1400 | 1.72 | $10^{-8}$-$10^{-14}$ |
| CNTs | 120-500 | 0.6 | $10^{4}$-$10^{5}$ |
| Graphene | 2630 | >1 | $10^{6}$ |

| | | | |
|---|---|---|---|
| Graphite | 10 | 2.26 | $10^4$ |
| ACs | 1000-3500 | 0.4-0.7 | 0.1-1 |
| Templated porous carbon | 500-3000 | 0.5-1 | 0.3-10 |
| Funtionalised porous carbon | 300-2200 | 0.5-0.9 | >300 |
| Activated carbon fibers | 1000-3000 | 0.3-0.8 | 5-10 |
| Carbon aerogels | 400-1000 | 0.5-0.7 | 1-10 |

## 2.5 Charge storage and ion-adsorption in EDLCs

There are a four classified types of mechanisms to store energy in supercapacitors: electrical double-layer capacitance (interface capacitance between ions and an electrode's surface), solid-side capacitance (quantum or space charge capacitance in the subsurface solid layer of semiconductor electrodes), pseudocapacitance (fast and reversible redox process on surface or in the near-surface region of electrodes with no diffusion limitations), and additional diffusion-limited redox processes. In all cases, the ultimate goal is to have the capacity to intake ions. However, the knowledge of the ion storage and transport mechanisms is necessary in order to develop and improve the performance of the devices (46).

In the electrical double-layer capacitance, a plain homogeneous surface is electrically charged (positively or negatively, depending on the electrode) and counterions are accumulated onto the electrode-electrolyte interface to preserve local electroneutrality. The quantum capacitance is another capacitance in series with the double-layer capacitance, which arises in a low-density of states systems such as 2D semiconductors. Quantum capacitance is important for understanding supercapacitor limitations mainly because the main materials for supercapacitors are high-SSA porous carbons, which are composed of randomly distributed 2D semiconducting single and double defect-containing graphene layers (pore walls) that separate adjacent pores. Quantum capacitance is believed to be one of the main factors setting the upper capacitance limits in carbon materials as it appears to be the lower than double-layer capacitance (84). Heteroatoms, vacancies, edges, and other defects greatly impact the density of states at the Fermi level, and consequently, the quantum capacitance component (85). It is reported that the edge atoms-related capacitance of graphene is at least one order of magnitude higher than that of a basal graphene plane, which consequently points to the importance of the ratio of edge-to--plane carbon atoms for the capacitance value (86). However, defects such as dangling bonds are highly reactive towards supporting electrolyte solutions, and can promote electrolyte decomposition, which is an undesirable side effect that can decrease the lifespan of a supercapacitor device.

Defects, heteroatoms, and functional groups are also closely related to additional redox (Faradaic) charge storage that can add to the total charge storable by a supercapacitor device, especially as far as aqueous-based supercapacitors are concerned (87; 88). Importantly, some redox processes have an electric response nearly identical to that of non-Faradaic charge storage, that is, the state-of-charge is a continuous function potential, the so called pseudocapacitance. They also exhibit high charge/discharge rates approaching those of electrosorption-based non-Faradaic carbon electrodes, and are governed by capacitor-type kinetics. This kinetics is manifested by a proportionality between the current and the scan rate in voltammetry experiments or a nearly constant slope of charge/discharge voltage time (capacity) profiles under constant-current measurement conditions. The following equation applies for capacitive or pseudocapacitive current in 3-electrode cyclic voltammetry measurements:

$$i = C_a S_a \upsilon \qquad \text{Equation 17}$$

where $i$ is current (A), $C_a$ is the areal capacitance (F $m^{-2}$), $S_a$ is the surface area and $u$ is the scan rate (V $s^{-1}$).

By contrast, for a diffusion-limited process, typical of battery materials, the current is proportional to the square root of scan rate (the Cottrell equation):

$$i = k\sqrt{\upsilon} \qquad \text{Equation 18}$$

where *k* is the collection of constants for a given system (89). Pseudocapacitance can be classified as intrinsic and extrinsic, and the two types of pseudocapacitance are distinguished on the basis of nanosizing electroactive materials. Those materials showing capacitor-like electrical response only at nanosize are considered extrinsically pseudocapacitive whereas materials showing such response independently of nanosizing (ruthenium oxide, manganese oxide) are denoted as intrinsically pseudocapacitive. Examples of pseudocapacitive processes include underpotential deposition of metals, surface redox reactions ($RuO_2$ or $MnO_2$) or some rare ion intercalation processes (e.g., $Li^+$ intercalation in $Nb_2O_5$) that do not go along with a phase change.

### 2.5.1. Electrosorption from electrolyte solutions into nanoporous carbons and associated capacitance

Up to date there is no complete understanding regarding the capacitance in the subnanometer-sized pores. It is important to mention that double-layer capacitance depends basically on the charge separation (electronic charge on the solid and ion charge in the double-layer), dielectric permittivity and SSA. Understanding the effect of pore size requires exploring areal rather than gravimetric capacitance so as to exclude the extensive effect of SSA. Figure 15 shows the areal capacitance calculated by using BET SSA as the pore size is changed. In 2006 it was suggested that the areal capacitance increases exponentially in the small pores (90) (91) (92). Molecular dynamics simulations have also probed that the desolvation and the local charge stored on the electrode increase with the degree of confinement (93).

Later works by Stoeckli and Centeno (94) suggest that areal capacitance is constant in carbon pore of 0.7 to 15 nm and the effect of capacitance increase is due to the deficiencies of the BET method used elsewhere for calculating SSA (95; 96) (97). Figure 15 shows the comparison of the calculated areal capacitance by using BET SSA and a tetraethylammonium cation $(C_2H_5)_4N^+$ accessible average SSA. If BET SSA specific surface area is used for determining the porosity of microporous materials, SSA is overestimated for wide micropores and mesopores whereas it is underestimated for subnanometer pores. Hence, other methods such as Kaneko's comparison plot, immersion calorimetry, and DFT treatments of adsorption isotherms were proposed as more appropriate to give a more correct value of SSA, which ultimately leads to constant capacitance (98). It is important to know that first reports on increasing capacitance in subnanometer pores did not take into account electrolyte-inaccessible porosity as proposed later (99). The earlier studies from 2006 did not also consider the change in dielectric permittivity that can occurs due to desolvation/confinement of ions in nanopores. It was proposed that effective dielectric permittivity can also be diminished for lower pore size (100), which can mitigate the increase in capacitance in small pores, explaining in part the results by Stoeckli and Centeno. However, the increase of surface normalized capacitance using DFT SSA has still been shown for pores below 1 nm (101), even taking into account the size of the ions to account for the accessible SSA. Finally, it should be mentioned that recent works (102) also point that there exist inherent limitations in the DFT methods used in assessing porosity, and also the binder used in electrode preparation could obstruct the part of porosity whereas the isotherms are conventionally measured on powdered ACs. Furthermore, the use of the average pore size value can be misleading, because the same pore size value could be associated with different capacitive properties (103). So, the pore size distribution can play an important role on the areal capacitance of the supercapacitors. To conclude, the characterisation methods available today for evaluating the textural properties of microporous carbons still cannot provide completely unambiguous results which may produce different trends with respect to the dependence of capacitance on pore size.

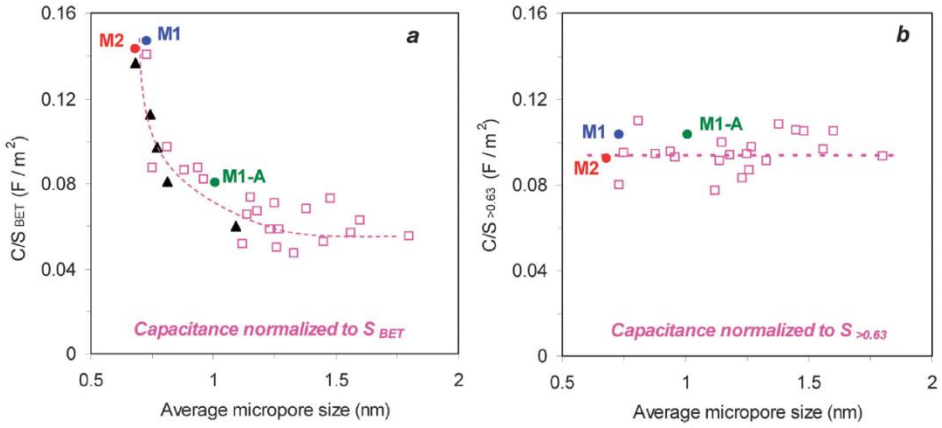


Figure 15. Areal capacitance calculated by (a) BET SSA and (b) accessible average SSA vs average pore size. Specific capacitance normalized by BET SSA for microporous carbons in $(C_2H_5)_4NBF_4$ electrolyte.

In addition, the structure and the surface groups of the activated carbons have a great influence on the electrochemical performance of the supercapacitors (104). For instance, the specific capacitance can be greatly impacted by the crystal orientation of the activated carbon. Thus, the edge orientation provides a higher electrical double layer capacitance and enhances the strong bonding of surface functional groups in comparison to that of the basal orientation, because the basal layer acts as a semiconductor, while the edge layer functions as an unsatisfied chemical bond. Therefore, the increase of areal capacitance as the pore size decreases could be also due to a higher contribution of the capacitance from the edge layer. Furthermore, the surface groups affect the wettability of the electrodes, contribute to pseudocapacitance and can be electrochemically reactive at certain potential. Therefore, the analysis of the performance of the positive and negative electrode is fundamental for carrying out the selection of the materials in an optimised supercapacitor cell.

### 2.5.3. In-situ studies on the charging mechanism by EQCM, NMR and SAXS

Supercapacitors are primarily power devices that need to operate at high charge/discharge rates. Therefore, there is a high interest in knowing the dynamics of the charging/discharging process onto the electrodes surface. Therefore, there is considerable ongoing effort in use electrochemical techniques in combination with other structural characterization methods such as solid-state nuclear magnetic resonance (NMR), small angle x-ray scattering (SAXS), or electrochemical quartz crystal microbalance (EQCM) in order to perform in-situ experiments that could help elucidating the mechanisms of ion accumulation on the surface. EQCM is a powerful technique to monitor the ionic fluxes in microporous carbons (105; 106), allowing one to distinguish peculiar charging mechanisms of activated carbon at different polarization degrees.

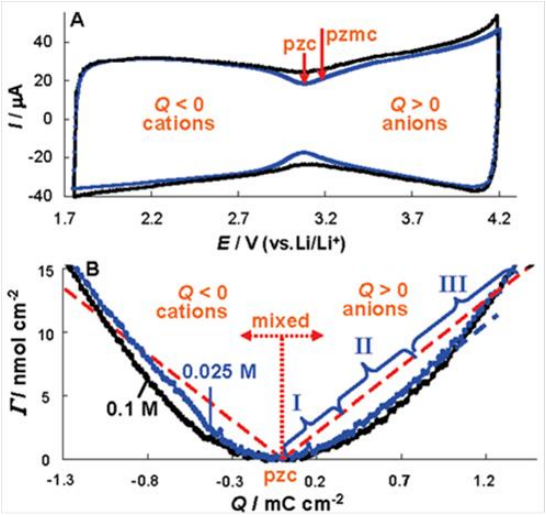

Figure 16 A) CVs of a carbon coated quartz electrode in 0.1 and 0.025 M (C2H5)4NBF4/PC solutions and the related treated EQCM responses (105).

EQCM studies onto YP-50F activated carbon in $Et_4NBF_4$ electrolyte have been able to track the charge storage mechanism at different potential range (107) as shown in Figure 16. At 0V, the electrode has an equal number of anions and cations. On the one hand, as the electrode is negatively charged, the cations are electrosorbed into the micropores to counterbalance the charge. On the other hand, as the electrode is positively charged, the anions are electrosorbed into the micropores as well as the cations expulsed. Thus, the mechanisms for positive and negative electrodes are slightly different. The asymmetry of the ion sizes could be the reason, since ions and solvent molecules should be reorganised. The packing inside the pores seems to be more efficient for the excess of cations (in the negative electrode), so more charge can be accommodated at negative potentials without having to expel the anions. Furthermore, cations tend to carry additional solvent molecules, so more space should be available inside the pores.

NMR studies have been able to detect ions ex-pore and in-pore (108) (107) (109) or even inside different porous environments (110) due to the difference in their resonances. These results show that the mechanism involved in the electrical double-layer formation in microporous carbon electrodes is much more complicated than the simplified model of the adsorption of a single counter ionic specie (107; 111). Ion exchange (swapping of co-ions for counter ions is often involved in the charging mechanisms, instead of a solely counter-ion adsorption (112). Many co-ions remain inside of the positive and negative electrodes pores during the charging process. For instance, in-situ NMR studies have revealed for YP50F commercial activated carbon in organic electrolyte that the charging mechanism can be divided into two steps (113). The first one, at low cell voltage (<0.75 V), is based on the short-scale rearrangements and the ejection of co-ions from the micropores. Thus, in the positive electrode, the amount of $BF_4^-$ anions remains constant, while in the negative electrode the amount of $BF_4^-$ decreases. During the second step, at high cell voltage (>0.75 V), both counterion adsorption and co-ion ejection occur, because the population of $BF_4^-$ anions suddenly increases in the positive electrode. When the concentration of the electrolyte is not sufficient (0.5 M), even all the $Et_4N^+$ cations can be expelled from the positive electrode in an intermediate point of the voltage so only electrosorpsion of $BF_4^-$ anions occurs. By using NMR, not only the changes of the electrolyte adsorption can be detected, but also the changes on the carbon electronic structure. So, the changes on the resonance frequency are linked to the addition or removal of electrons from the delocalised system, due to a shielding/deshielding effect. Furthermore, NMR in situ measurements have been used to observe the ion dynamics (114). So, the larger the size of the ions the more confined they are inside the nanopores, accordingly decreasing their diffusion coefficient. However, the in-pore ion diffusion can be increased by having extra pore volume between 1-3 nm. The ion-ion interactions during the charge mechanism greatly influence the diffusion coefficients in-pore. So, in the negative electrode where counterions are adsorbed during the charging the diffusion coefficient decreases, while in the positive electrode that counter-ion co-ion exchange takes place the diffusion coefficient does not vary as much. Ex situ NMR measurements using the same activated carbon YP50F and ionic liquid, $Pyr_{13}TFSI$, revealed that counterion adsorption as well as co-ion desorption take place during the charge storage. On the positive electrode anions enter the carbon micropores and some cations are ejected. On the negative electrode, primarily anions ejection happens an only some cations enter the micropores (115).

SAXS has been shown to be an useful technique to quantitatively describe the arrangement and transport of the ions as a function of the voltage (116). SAXS in-situ measurements for YP80F-based aqueous supercapacitors, using NaCl, KCl and CsCl aqueous electrolytes, have shown that the charging process does not significantly alter the total population of ions inside the pores, so ion swapping is observed under low polarisation voltages (117). When the voltage is increased though, counter-ions start to be preferred for the electrosorption. Furthermore, SAXS experiments have witnessed the movements of the ions towards the pore walls by monitoring the distance between ions and walls and also claimed a dense hydration shell of the small cations. Also by combining in-situ SAXS with electrochemical dilatometry it was shown that the dimensional changes that occur during the polarisation of the carbons are influenced by the amount of micropores, suggesting a possible pore swelling induced by electrosorption (118) Moreover, SAXS have shown that the tight attachment of the

aqueous solvation shell prevents ions from a complete desolvation in carbons with subnanometre pore size (119).

## 2.6 Electrolytes for electrochemical capacitors

The electrolyte is normally composed of a salt and a solvent and it is a fundamental component of electrochemical energy storage systems. The most conventional electrolytes for supercapacitors are aqueous- and organic-based. The electrolyte provides the electroneutrality to the electrode by forming the electrical double layer, compensating the charge that it is stored in it (120). Thus, the selection of the electrolyte plays a very important role on the energy and power density of the supercapacitor, since it directly affects the capacitance, the voltage window and the resistance of the devices.

Some properties of electrolytes can rule the electrochemical behaviour of EDLCs. The first one is the conductance, $\kappa$, which is the inverse of the resistance, $\rho$, of the solution, as shown in Equation 12.

$$\kappa = \frac{1}{\rho}$$ Equation 19

It depends on many parameters: the concentration of the cations and anions, the ionic mobility of the ions, the solubility of the salt in the solvent, the degree of dissociation of the dissolved salt into free ions, the viscosity of the solvent (temperature dependent) and the long range electrostatic interactions between ions (dielectric constant dependent). Minimising the resistance of the electrolyte and the electrode material is necessary for a reversible and fast charge/discharge process. The second one is the ion adsorption capacity, from the potential at zero charge to the maximum positive or negative potential in the positive and negative electrode correspondingly. The third one is the dielectric property of the solvent which also influences the capacitance (1).

Moreover, the electrochemical stable potential window of the electrolyte is directly linked with the operational voltage of the cell, which affects the energy and power density of the system and the life time and self-discharge are greatly influenced by the interactions between the interplay of ions, solvent and electrodes (120).

### 2.6.1. Aqueous electrolytes

Within aqueous electrolytes, potassium hydroxide (KOH) alkaline electrolyte, and sulfuric acid ($H_2SO_4$) acidic electrolyte are the most common ones. KOH has its maximum ionic conductivity, 0.6 S $cm^{-1}$, for 6M concentration and $H_2SO_4$ ~0.8 S $cm^{-1}$ for 1 M. Aqueous electrolytes can only operate at *ca.* 1V, under the thermodynamic stability voltage of water, which is 1.23 V. At 0 V *vs.* standard hydrogen electrode (SHE) hydrogen evolution occurs and at 1.23 V oxygen evolution. Because concentrated solutions are required to minimise the ESR, and acids tend to be more corrosive than hydroxides, KOH or NaOH solutions are normally preferred. The low operational voltage window is one of the main drawbacks of aqueous electrolytes, although some neutral aqueous electrolytes have demonstrated to be able to provide higher stable voltage windows, 1.6-2.2V (121; 122). This extension of the electrochemically stable potential window occurs due to the lower concentration of $H^+$ and $OH^-$ in neutral pH electrolytes, in comparison with the acidic and the alkaline electrolytes, which allows then to have a higher overpotential for hydrogen and oxygen evolution reactions (123). In general terms, aqueous electrolytes normally have high ionic concentrations and high conductivity, which enables them with low resistance and because the size of the ions is usually smaller than in the case of other type of electrolytes, they can access to a bigger part of the electrode surface, providing aqueous-based systems with higher values of capacitance. Other than that, the presence of water molecules can also contribute to the occurrence of faradaic reactions, especially with interactions between heteroatoms and their related functional groups, which are typically present in low content. This can add about 30% extra charge to double-layer charging (87; 88). Moreover, the double-layer capacitance in aqueous electrolytes is also high due to the higher dielectric constant of aqueous systems (124). KOH and $H_2SO_4$ have also been tested as possible electrolytes in hybrid capacitors, for instance a carbon/$PbO_2$ hybrid (125). However, they perform with a poor cyclibility due to the chemical instability of $PbO_2$ in

$H_2SO_4$. To overcome this issue an electrolyte composed of methanesulfonic acid and lead methanesulfonate was developed (126). In hybrid systems, neutral electrolytes such as KCl and $K_2SO_4$ can also perform more cycles with an extended operational voltage window (127; 128).

### 2.6.2. Organic electrolytes

Organic electrolytes are the most used ones in commercial devices, the most common one being tetraethylammonium tetrafluoroborate ($(C_2H_5)_4NBF_4$) generally dissolved in acetonitrile (AN), or in propylene carbonate (PC). AN is used because it has a large dielectric constant and, as a consequence, high conductivity. PC is used for a better safety, but the conductivity of the solutions is much lower, 15 mS $cm^{-1}$ vs 60 mS $cm^{-1}$. The operational voltage window of these solvents is much larger, ~2.7 V. Furthermore, the use of organic electrolytes allows the use of cheap current collectors, such as Al, due to the less corrosive nature of the salt. Working in organic-based electrolytes requires a high purity and dryness in all the components of the cell to avoid the decomposition of the functional groups and water traces before reaching the cell voltage. Moreover, on strong overcharge at the negative electrode, it can decompose (1). In comparison with aqueous electrolytes, organic-based ones provide a lower value of capacitance, because of larger ion sizes and lower dielectric constants, but this is compensated by the lager voltage window. Moreover, oxygenated functional groups provide an extra pseudocapacitance in aqueous media, while organic electrolytes lack of the protons required for such contribution (129). Therefore, it is very important to select an appropriate electrode material, with pores that can accommodate the bigger size ions, to maximise the interface between electrolyte and electrode (130). Organic electrolytes have also a lower conductivity, due to the lower solubility and they are less safe since they are more flammable, volatile and toxic. However, they are still the main commercial choice of electrolyte. Many hybrid capacitors have also been developed using organic electrolytes, for instance, triethylmethylammonium tetrafluoroborate $(C_2H_5)_3CH_3NBF_4$ in PC (131), $LiPF_6$ in ethylene carbonate and dimethyl carbonate (EC-DMC) (132), LiTFSI in AN (133), $LiPF_6$ in ethylene carbonate and ethyl methyl carbonate (EC-EMC) (134). Lithium-ion capacitors (LICs), in particular, use the same Li-containing electrolytes as in Lithium-ion batteries (LIBs), such as, $LiPF_6$ and $LiClO_4$ in mixtures of EC-DMC.

### 2.6.3. Ionic liquid (IL) electrolytes

ILs are also another type of electrolytes for supercapacitors. Essentially, they are organic salts which have lower melting points than room temperature, so they are present in liquid state (135). Their main advantages are the wide operational voltage window within a broad temperature range and their non-volatility (136). They can be classified into aprotic, protic and zwitterionic according to their composition. Table 4 shows the most commonly used IL cations and anions in electrochemical capacitors. However, because they tend to be quite viscous, their low conductivity is their main drawback, which limits the rate performance and their power density in supercapacitor applications. Imidazolium based ones have the highest conductivity, while pyrrolidium based ones have a broader voltage window (137).

**Table 4.** Most commonly used cations and anions of ILs for supercapacitors.

| Cations | Anions |
|---|---|
| Imidazolium | Tetrafluoronorate ($BF_4^-$) |
| Pyrrolidinium | Hexafluorophosphate ($PF_6^-$) |
| Ammonium | Bis(trifluoromethanesulfonyl)imide ($TFSI^-$) |
| Sulfonium | Bis((fluorosulfonyl)imide ($FSI^-$) |
| Phosphonium | Dicyanamide ($DCA^-$) |

Moreover, the specific capacitance has lower values in comparison with traditional electrolytes, due to the bigger size of ions in relationship with the carbon electrode porosity and the higher viscosity of the ILs. In ILs cations can aggregate like surfactants which reduces their mobility (138; 139). Therefore, the use of a eutectic mixture of ILs or using solvents can enhance the ion separation (140; 141). The former strategy not only enhances the ion mobility at room temperature, but it has also probed to work at low temperatures (-80 °C). Additionally, for practical applications, ILs still have quite a prohibitive

cost and require ultrastringent carbon drying process to exceed the practical voltage of solvent-based cell, which elevates the cost of supercapacitors.

## 2.7 Cell configurations

Cell configuration can be designed for optimising the energy density of the electrochemical capacitors, by maximising the capacitance of the electrodes and by increasing the operational voltage.
EDLC systems are generally considered to be symmetric, *i.e.* same material at both electrodes, although in commercial systems, very often, the mass of active material at each of the electrodes is different. In EDLC electrodes, one type of charge is located on a subsurface layer of a solid electrode material (usually microporous carbon) and the opposite charge belongs to the ions from a supporting electrolyte solution. Therefore, each electrode can be characterized by its own capacitance, which for the positive and the negative electrodes is:

$$C_+ = \frac{Q}{\Delta E_+} \qquad \text{Equation 20}$$

$$C_- = \frac{Q}{\Delta E_-} \qquad \text{Equation 21}$$

The two electrodes in an EDLC are considered to be in series connected, since each of them can represent an individual capacitor. The positive electrode suffers a change toward higher potentials during the charging process, while the negative is charged while its potential decreases. Thereby, the total capacitance of a two electrode cell can be expressed as:

$$C = \frac{C_+ C_-}{C_+ + C_-} \qquad \text{Equation 22}$$

where $C_+$ and $C_-$ are the capacitance of the positive and the negative electrodes, respectively.

In terms of mass, cell capacitance is:

$$C_{g,cell} = \frac{C_{g+} m_+ C_{g-} m_-}{(C_{g+} m_+ C_{g-} m_-)(m_+ + m_-)} \qquad \text{Equation 23}$$

where $C_{g+}$ and $C_{g-}$ are the gravimetric capacitance of the positive and the negative electrodes, respectively and $m_+$ and $m_-$ the masses of the positive and negative electrodes. Thus, in a symmetric cell where the two electrodes have the same mass,

$$C_{g,cell} = \frac{C_{g+} C_{g-}}{2(C_{g+} + C_{g-})} \qquad \text{Equation 24}$$

Thus, the total potential difference, which is the cell voltage, $\Delta V = \Delta E_+ + \Delta E_-$ is only known, and commonly it is assumed that $C_{g+}$ and $C_{g-}$ are the same. Thus:

$$C_{g,cell} = \frac{C_{ge}}{4} \qquad \text{Equation 25}$$

A reference or quasi reference electrode (QRE) electrode can be introduced into the cell in order to determine the exact values of $C_{g+}$ and $C_{g-}$ using the values of capacitance of each electrode separately through the potential span (difference) at each electrode, $\Delta E_+$ and $\Delta E_-$(Equation 26 and Equation 27). A reference electrode is not present in industrial cells.

In asymmetric cells $C_{g+}$ and $C_{g-}$ can be quite different, so the electrodes should be mass-balanced according to the same absolute amount of charge to use the maximum potential range allowed by electrolyte at each electrode, (electrochemical stability window ), $\Delta E_-$ and $\Delta E_+$.

$$C_{g,+} = \frac{Q}{m_+ \Delta E_+} \qquad \text{Equation 26}$$

$$C_{g,-} = \frac{Q}{m_- \Delta E_-} \qquad \text{Equation 27}$$

Asymmetric configurations can be designed by combining two non-Faradic electrodes with different capacitance values, capacitive and pseudocapacitive electrodes, capacitive/pseudocapacitive and battery-type electrodes, two composite electrodes involving both capacitive and battery type storage, and so on (5). The goal of building asymmetric cells is to reach higher energy than that of symmetric cells (142).

Asymmetric cells can be classified as internal series hybrids (ISHs) and internal parallel hybrids (IPHs) (143). An ISH contains one electrode, which is fully a battery-type electrode, having slower kinetics, higher capacity and a constant potential profile at constant current discharge. The other electrode is a rapid capacitive electrode with a lower capacity and a sloping potential profile typical of a supercapacitor under constant-current discharge. An example of ISH are lithium-ion capacitors (LICs) that are nowadays commercialized (144). LICs are a hybridisation of capacitors that was firstly carried out by pairing $Li_4Ti_5O_{12}$ (LTO) as negative electrode with activated carbon as positive electrode in $LiPF_6$ electrolyte (145). Later, an improved LIC came out by preparing nanocrystalised LTO with carbon nanofibers (CNF) for the negative electrode (146). Graphite was also introduced as an even lower-potential anode (147), thus the energy storage capacity was significantly improved, although graphite needed to be prelithiated. The prelithiation can be done by using an auxiliary metallic lithium electrode, but the leftovers of metallic lithium are potentially problematic due to thermal runaways (148). In general, these systems have demonstrated to have a higher cycle life in comparison with Li-ion batteries (LIBs) (149). Many other materials such as hard carbons (150), alloys (151) and metal organic frameworks (MOFs) (151; 152) have been already probed to work as negative electrodes for LICs.. Furthermore, the opposite hybridisation has also been proposed, in which the battery type electrode is used as positive electrode (e.g. $LiMn_2O_4$), while the AC is kept for the negative one, using several Li containing electrolytes (153). Similarly, sodium ion capacitors (NICs) have emerged in the last years as the Na-ion batteries (NIBs) have been investigated. NIBs present a greater stability window for sodium layered oxides than LIBs and sodium has a higher electrode potential than lithium (-2.71 V vs SHE and -3.02 V vs SHE, correspondingly (154). Furthermore, NIBs are meant to reduce the costs of batteries because sodium is the sixth most abundant element and it is not geographically limited and also because aluminium current collectors can be used which do not alloy with sodium. NICs have incorporated $V_2O_5$/carbon nanotube composites (155), $Na_2Ti_3O_7$ (NTO)/nanotubes (156), sodium predoped hard carbon (157) as negative electrode and AC as positive. Flexible NICs have also been reported which were composed of NTO nanosheet arrays/carbon textile as negative electrode and flexible reduced graphene oxide films as positive (158).

By contrast, an IPH uses battery and capacitive materials as part of each electrode. This configuration delivers the higher energy at low current because of the high-capacity battery materials, but also some energy at high current through rapid non-Faradic materials when battery materials fail to store/deliver charge (159). However, there are less examples of this configuration at the present moment.

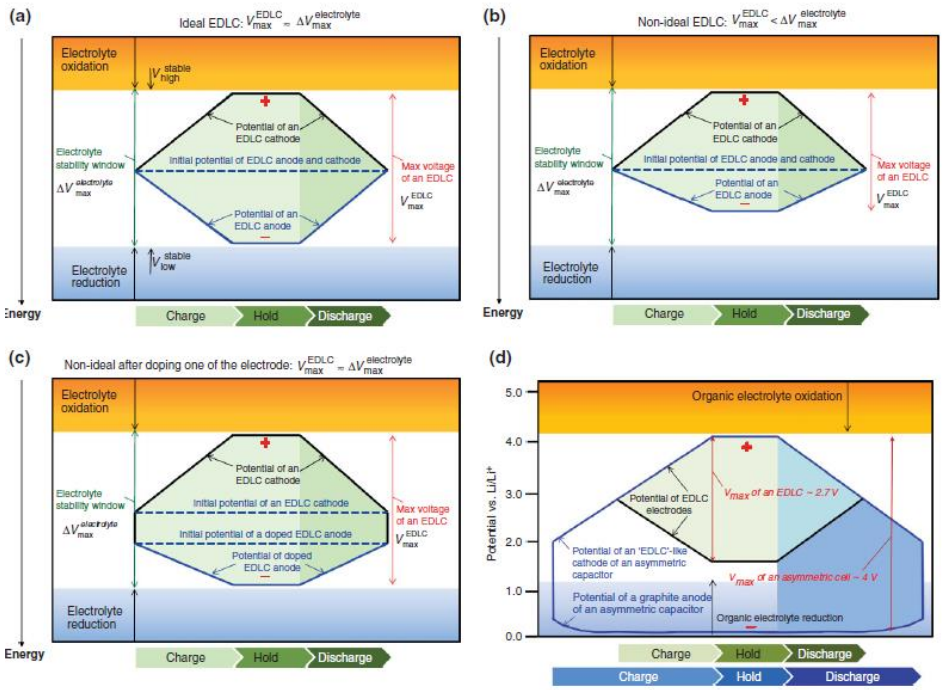


Figure 17 Schematic charge/discharge profiles of different cell configurations a) an ideal EDLC, b) a non-ideal EDLC, c) an EDLC with a doped electrode and d) a hybrid capacitor (160).

Furthermore, the voltage can be also optimised by utilising an increased operational voltage. Figure 17 shows the constant current charge discharge profiles of some configurations of electrochemical capacitors. The maximum operational voltage is limited by the stability potential window of each electrode, i.e. the potentials before electrolyte reduction and oxidation occurs. Functional groups and impurities in the electrodes can contribute to decrease the stable potential windows by a premature decomposition of the electrolyte. In an ideal symmetric EDLC, the potential window at which each electrode is charged/discharged is the same for both and located between the reduction and oxidation potentials of the negative and the positive electrodes, correspondingly. Thus, the maximum voltage can approach the maximum electrolyte stability window. In a non-ideal EDLC, one of the electrodes reaches the decomposition potential faster than the other (161). In this case, the maximum voltage would be lower that the electrolyte stability window. In order to fully utilise the electrolyte stability window two approaches can be followed. One is to dope one of the electrodes, so its potential is shifted and both electrode can be charged/discharged without reaching the electrolyte decomposition potentials and the other one is to mass balance the electrodes, so slopes of the potential change is adjusted between the degradation potentials (162; 163). Furthermore, in asymmetric capacitors different type of materials are used as positive and negative electrode, with most likely different capacitance and different stable potential limits. In most LICs and NICs, one of the electrodes is replaced by a battery-type electrode, which has a higher capacitance due to its faradaic ion storage mechanism. Therefore, they can increase the maximum voltage and energy of the electrochemical capacitors. Using battery type electrodes may shift the potential of that electrode to one of the electrolytes decomposition limits. Nevertheless, that decomposition of the electrolyte can form the so-called solid electrolyte interphase (SEI) layer, which allows the faradaic ion storage with a higher voltage. The SEI layer is a stable electrically isolative solid product which is uniformly coated onto the electrode surface. It makes the electrode impermeable to electrolyte solvent, preventing it from further electrolyte decomposition, but also disrupting the formation of the double layer and increasing the resistance for the ion transport.

## 2.8. Electrochemical evaluation of electrochemical capacitor performance

### 2.8.1. Cyclic voltammetry

Cyclic voltammetry (CV) is an electroanalytical technique that consists on sweeping the potential through a potential range at a constant scan rate while the current response is recorded. A cycle is formed when two consecutive sweeps are done, one in increasing and the other one in decreasing direction. This allows investigating the oxidation and reduction, respectively. Figure 18 shows the schematics of the voltammetry response for supercapacitors. In the case of ideal electrochemical double-layer capacitors (EDLCs) no redox reactions should be found, only electrical double-layer contribution. Therefore, the capacitance is constant and the cyclic voltammogram is formed by a straight line, which is extractedfrom the constant current response, as it can be ideally deduced from the basic :

$$C = \frac{\mathrm{Q}}{\Delta \mathrm{U}} = \int i \frac{dt}{\Delta U} = \frac{\mathrm{I}}{\upsilon} \qquad \text{Equation 28}$$

where $C$ is the capacitance, $\int I\,dt$ is the charge stored over $\Delta U$, a change of voltage, $I$ is the current and $\upsilon$ is the scan rate.

However, CVs are not the most accurate electrochemical techniques to determine capacitance, especially for real supercapacitors. CVs can present leak resistance, $R_f$, and series resistance, $R_s$, which cause distortions from the ideal squared shape. These deviations are magnified at high scan rates, which make it more difficult to read the value of capacitance.

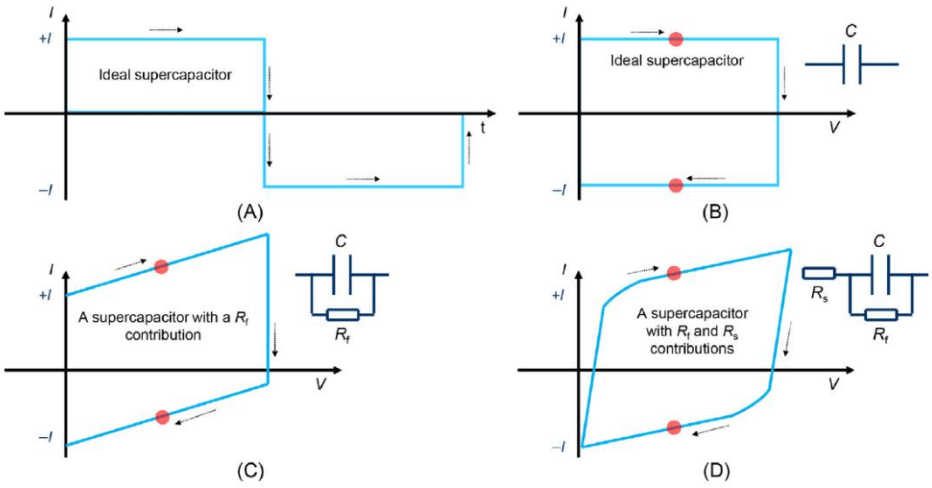


Figure 18 Voltammetry response of a two-electrode supercapacitor with constant capacitance. A) i-t plot, B) I-V plot, C) I-V plot of a supercapacitor with series resistance and D) i-V plot of a supercapacitor with series and leak resistance. (C)

### 2.8.2. Constant current charge/discharge

The galvanostatic charge/discharge (GA) is also an electrochemical technique very broadly used to characterise electrochemical capacitors. It consists in applying a constant current to an electrochemical cell within a voltage range and recording that voltage change. For ideal supercapacitors, the voltage increases linearly over time as the capacitance is constant and proportional to the slope. The capacitance value can be calculated using , as from CVs. One of the most widely used tests consists on cycling the supercapacitor at different current densities, in order to determine the capacitance and the resistance for each one, which enables to stablish the rate capability.

### 2.8.3. Electrochemical impedance spectroscopy

Electrochemical impedance spectroscopy (EIS) is another technique commonly used to characterise EDLCs. In EIS a low amplitude alternative voltage is applied to a certain potential, while a sinusoidal output current is measured. The sinusoidal signal is consecutively applied for different frequencies and different processes that occur in the cell can be identified. The impedance (*Z(ω)*) can be defined as a complex resistance of ac current and voltage and is expressed by:

$$Z(\omega) = \frac{\Delta V}{\Delta I} = |Z(\omega)|e^{-j\varphi} = Z' + jZ''$$ Equation 29

where *ω* is the pulsation, *ΔV* is the voltage, *ΔI* is the current, *φ* is the phase angle and *Z'* and *Z''* are the real part and the imaginary part of the impedance, respectively.

EIS is depicted most commonly by using the Nyquist plot, which illustrates the absolute imaginary impedance vs the real impedance. Figure 19 shows the Nyquist plots of capacitors. The ideal Nyquist plot of a capacitor is a linear vertical line which intercepts the x axis at the value of series resistance. When porous materials are used as electrode materials though, the plot is represented by a ~45° line at the high frequency region that is followed by a quasi-vertical line. The point where the 45° line crosses the x-axis corresponds to the series resistance and the point where the 45° line meets the quasivertical line is the ionic resistance inside the pores. Furthermore, a supercapacitor cell can have a semicircle at high frequency, which is representative of a resistance connected in parallel, $R_f$. *It* is assigned to the intergranular electronic resistance among particles, to the resistance between the electrode and the current collector and to the resistance of the passivating oxide layer of the current collectors. $R_f$ is a resistance that in commercial supercapacitors should be avoided by a well assembling of the cells. The Bode plot is another representation of the EIS, which shows the phase angle vs frequency.

Complex capacitance can be calculated by EIS data by

$$C(\omega) = C'(\omega) + jC''(\omega)$$ Equation 30

with,

$$C'(\omega) = \frac{Z''}{|Z|^2\omega}$$ Equation 31

$$C''(\omega) = \frac{Z'}{|Z|^2\omega}$$ Equation 32

where *C'(ω)* and *C''(ω)* are the real part and the imaginary part of capacitance *C(ω)*, correspondingly. The maximum *C''(ω)*, which also correspond to the inflection point of *C'(ω)*, provides the frequency, $f_0$, to calculate the time constant ($\tau_0$). The time constant is the dielectric relaxation time of the whole system.

$$\tau_0 = \frac{1}{f_0}$$ Equation 33

.

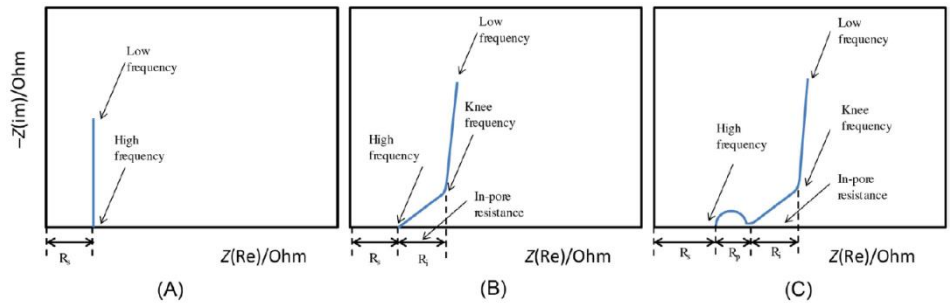


Figure 19 Nyquist plots of different systems(C)

### 2.8.4. Cycle life

The endurance test is another procedure to evaluate the performance of the supercapacitors. It consists in stablishing a dwell in the voltage at an elevated temperature (60 °C) and measuring the capacitance regularly by GA.  shows the schematic of endurance test procedure. The GA profile presents three parts either in the charge and the discharge. The first one is a voltage drop, which is referred as equivalent series resistance (ESR), the second one is a curve, which in combination with the first one is referred as the equivalent distributed resistance (EDR) and the third one is the linear part from which capacitance is calculated. The ESR is also called Ohmic drop and is caused by the resistivity inherent to the components, i.e. active material, electrolyte, separator, etc. The curvy part is associated to the charge redistribution process through the electrode, due to a difference in voltage across the porous network, similar to when the charge redistribution that happens when the cell is left to open circuit. ESR is not dependent on the current and EDR is, which is higher for the low current density.

As supercapacitors are expected to have a long cyclability several test can be run on them. The cycling ability tests consist also on consecutive and repeated GA charge/discharge cycles until the cell failure. The most extended one is the repeated galvanostatic charge-discharge test over a several thousands of cycles. However, they are not as useful as in batteries for electrochemical capacitors, because of their long cyclability, which make experiments not practical. Furthermore, EDLCs must be hold at the maximum voltage until the power delivery is required in many applications. Thus, another more interesting test is usually performed, the floating test, which consists in a dwell at the maximum voltage for a few hours (typically 2 h), followed by some cycles of constant current discharge charge. The end-of-life criteria are usually met when the resistance is increase to double and there is a 20-30% of capacitance loss.

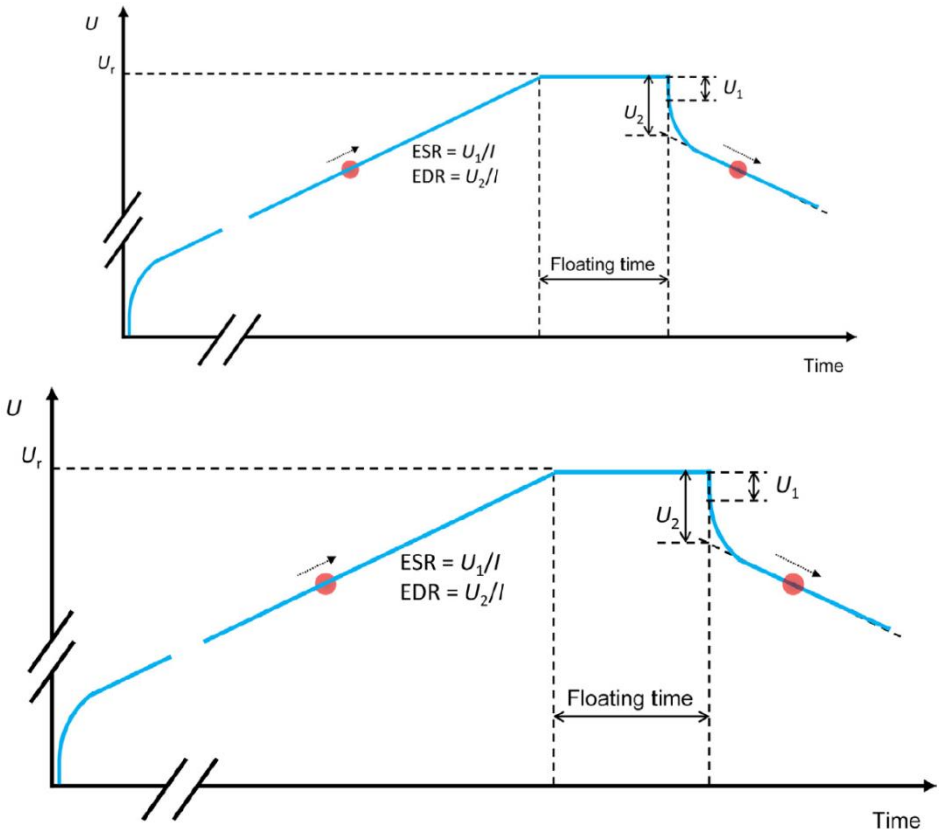


Figure 20 Endurance test. (C)

## 2.9 References


1. **Conway, B. E.** *Electrochemical Supercapacitors.* New York : Kluwer Academic, 1999.

2. **L. M. Rodriguez-Martinez, N. Omar, [ed.].** *Emerging Nanotechnologies in Rechargeable Energy Storage Systems.* s.l. : Elsevier, 2017.

3. *Review on supercapacitors: Technologies and materials.* **A. González, E. Goikole, J. A. Barrena, R. Mysyk.** 2016, Renewable and Sustainable Energy Reviews, Vol. 58, págs. 1189-1206.

4. *Trends and research challenges in supercapacitors.* **Berenguer, R.** 2015, Boletín del Grupo Español del Carbón, Vol. 37, págs. 9-13.

5. **F. Beguin, E. Frackowiak.** *Supercapacitors: Materials, Systems, and Applications.* Weinheim : Wiley-VCH, 2013.

6. https://ethw.org/Capacitors. [En línea]

7. https://hackaday.com/2016/07/12/history-of-the-capacitor-the-pioneering-years/. [En línea]

8. https://thingsthatilearnt.wordpress.com/2012/02/12/leydens-jar/. [En línea]

9. https://hackaday.com/2016/07/26/history-of-the-capacitor-the-modern-era/. [En línea]

10. *Progress of electrochemical capacitor electrode materials: A review.* **Y. Zhang, H. Feng, X. Wu, L. Wang, A. Zhang, T.i Xia, H. Dong, X. Li, L. Zhang.** 2009, International Journal of Hydrogen Energy, Vol. 34, págs. 4889-4899.

11. *Electrochemical Capacitors for Energy Management.* **J. R. Miller, P. Simon.** 5889, 2008, Science, Vol. 321, págs. 651-652.

12. *Electrochemical Capacitors: Challenges and Opportunities for Real-World Applications.* **J. R. Miller, A. F. Burke.** 1, s.l. : The Electrochemical Society Interface, 2008, Vol. 17, págs. 53-57.

13. *Materials for electrochemical capacitors.* **P. Simon, Y. Gogotsi.** 2008, Nature Materials, Vol. 7, págs. 845–854.

14. *Capacitive Energy Storage from −50 to 100 °C Using an Ionic Liquid Electrolyte.* **R. Lin, P. L. Taberna, S. Fantini, V. Presser, C. R. Perez, F. Malbosc, N. L. Ruspesinghe, K. B. K. Teo, Y. Gogotsi, P. Simon.** 19, 2011, J. Phys. Chem. Lett., Vol. 2, págs. 2396-2401.

15. *The effects of temperature on the performance of electrochemical double layer capacitors.* **S.I. Fletcher a, ∗, F.B. Sillars a, R. C. Carter, A. J. Cruden, M. Mirzaeian, N. E. Hudson, J. A. Parkinson, P. J. Hall.** 2010, Journal of Power Sources, Vol. 195, págs. 7484-7488.

16. *Critical review on lithium-ion batteries: are they safe? Sustainable?* **A. Mauger, C. M. Julien.** 2017, Ionics, Vol. 23, págs. 1933-1947.

17. *Valuing Reversible Energy Storage.* **Miller, J. R.** 2012, Science, Vol. 335, págs. 1312-1313.

18. *Engineering electrochemical capacitor applications.* **Miller, J. R.** s.l. : Journal of Power Sources, 2016, Vol. 326, págs. 726-735.

19. http://www.maxwell.com/images/documents/K2Series_DS_1015370_5_20141104.pdf. [En línea]

20. http://yunasko.com/en/products. [En línea]

21. http://www.chemi-con.co.jp/e/catalog/pdf/dl-e/dl-all-e1009f-2018.pdf. [En línea]

22. http://www.ioxus.com/files/6214/6981/0438/Ioxus_DataSheet_Titan_60mm_160418.pdf. [En línea]

23. http://www.jmenergy.co.jp/en/products_cell_can.html. [En línea]

24. http://www.wima.cn/EN/supercap_r_2.htm. [En línea]

25. https://www.skeletontech.com/hubfs/170525-1C-DataSheet-SCA.pdf?hsCtaTracking=9dad2c8b-c8b1-4a0e-acba-913103f71ac2%7C1b0ce536-e940-43b8-b00a-9d371a854c27. [En línea]

26. *Engineering electrochemical capacitor applications.* **R.Miller, J.** s.l. : Journal of Power Sources, 2016, Vol. 326, págs. 726-735.

27. http://www.maxwell.com/solutions/transportation/auto. [En línea]

28. http://www.maxwell.com/solutions/transportation/auto/power-assist-hybrid-electric-vehicles. [En línea]

29. http://www.maxwell.com/solutions/transportation/heavy-transportation. [En línea]

30. http://www.irizar.com/autobuses-y-autocares/autobuses/irizar-ie-tram/. [En línea]

31. http://www.maxwell.com/solutions/transportation/auto/start-stop-micro-hybrid. [En línea]

32. http://www.irizar.com/en/descargas/catalogos/irizar-i2e-catalogo/. [En línea]

33. http://www.maxwell.com/solutions/transportation/auto/regenerative-braking-energy-recovery. [En línea]

34. http://www.maxwell.com/solutions/industrial/forklifts-cranes. [En línea]

35. http://www.maxwell.com/solutions/industrial/forklifts-cranes. [En línea]

36. http://www.maxwell.com/solutions/industrial/forklifts-cranes. [En línea]

37. https://industrial.panasonic.com/cdbs/www-data/pdf/RDH0000/DMH0000C0L69.pdf. [En línea]

38. http://www.maxwell.com/solutions/power-grid/utility-grid. [En línea]

39. http://www.maxwell.com/solutions/power-grid/voltage-sag-mitigation-ups. [En línea]

40. *Carbons and Electrolytes for Advanced Supercapacitors.* **F. Beguin, V. Presser, A. Balducci, E. Frackowiak.** 14, s.l. : Adv. Mater., 2014, Vol. 26, págs. 2219–2251.

41. *Modern Theories of Carbon-Based Electrochemical Capacitors: A Short Review.* **V. Meunier, J. Huang, G. Feng, R. Qia, B. G. Sumpter.** 2010, Proceedings of the ASME 2010 International Mechanical Engineering Congress and Exposition, Vol. 11, págs. 21-30.

42. *Curvature effects in carbon nanomaterials: Exohedral versus endohedral supercapacitors.* **J. Huang, B. G. Sumpter, V. Meunier.** 8, 2010, Journal of Materials Research, Vol. 25, págs. 1525-1531.

43. *Where Do Batteries End and Supercapacitors Begin?* **P. Simon, Y. Gogotsi, B. Dunn.** 6176, 2014, Science, Vol. 343, págs. 1210-1211.

44. *To Be or Not To Be Pseudocapacitive?* **T. Brousse, D. Belanger, J. W. Long.** 5, 2015, Journal of The Electrochemical Society, Vol. 162, págs. A5185-A5189.

45. *How Do Pseudocapacitors Store Energy? Theoretical Analysis and Experimental Illustration.* **C. Costentin, T. R. Porter, J.-M. Savéant.** 2017, ACS Applied Materials & Interfaces, Vol. 9, págs. 8649-8658.

46. *Multidimensional materials and device architectures for future hybrid energy storage.* **M. R. Lukatskaya, B. Dunn, Y. Gogotsi.** 12647, 2016, Nature Communications, Vol. 7, págs. 1-13.

47. **Frackowiak, F. Beguin and E.** *Carbons for Electrochemical Energy Storage and Conversion Systems.* Boca Raton : CRC Press, 2009.

48. *Recent Advances in Design and Fabrication of Electrochemical Supercapacitors with High Energy Densities.* **J. Yan, Q. Wang, T. Wei, Z. Fan.** 1300816, 2014, Adv. Energy Mater., Vol. 4, págs. 1-43.

49. *The Large Electrochemical Capacitance of Microporous Doped Carbon Obtained by Using a Zeolite Template.* **C. O. Ania, V. Khomenko, E. Raymundo-Piñero, J. B. Parra, F. Béguin.** 11, s.l. : Adv. Funct. Mater., 2007, Vol. 17, págs. 1828–1836.

50. *Hierarchically Controlled Helical Graphite Films Prepared from Iodine-Doped Helical Polyacetylene Films Using Morphology-Retaining Carbonization.* **S. Matsushita, M. Kyotani, K. Akagi.** 44, s.l. : J. Am. Chem. Soc., 2011, Vol. 133, págs. 17977–17992.

51. *Physisorption of gases, with special reference to the evaluation of surface area and pore size distribution (IUPAC Technical Report).* **M. Thommes, K. Kaneko, A. V. Neimark, J. P. Olivier, F. Rodriguez-Reinoso, J. Rouquerol, K. S.W. Sing.** 9-10, s.l. : Pure Appl. Chem., 2015, Vol. 87, págs. 1051-1069.

52. *L. L. Zhang, X. Zhao, M. D. Stoller, Y. Zhu, H. Ji, S. Murali, Y. Wu, S. Perales, B. Clevenger, R. S. Ruoff.* **Supercapacitors, Highly Conductive and Porous Activated Reduced Graphene OxideFilms for High-Power.** 2012, Nano Letters, Vol. 12, págs. 1806-1812.

53. *Carbon-Based Supercapacitors Produced by Activation of Graphene.* **Y. Zhu, S.0 Murali, M. D. Stoller, K. J. Ganesh, W. Cai, P. J. Ferreira, A. Pirkle, R. M. Wallace, K. A. Cychosz, M. Thommes, D. Su, E. A. Stach, R. S. Ruoff.** 6037, 2011, Science, Vol. 332, págs. 1537-1541.

54. *Graphene Double-Layer Capacitor with ac Line-Filtering Performance.* **J. R. Miller, R. A. Outlaw, B. C. Holloway.** Science, Vol. 329, págs. 1637-1639.

55. *Curvature effects in carbon nanomaterials: Exohedral versus endohedral supercapacitors.* **J. Huang, B. G. Sumpter, V. Meunier, G. , Yushin, C. Portet, Y. Gogotsi.** 08, 2010, Journal of Materials Research, Vol. 25, págs. 1525-1531.

56. *Electrochemical performance of carbon onions, nanodiamonds, carbon black and multiwalled nanotubes in electrical double layer capacitors.* **C. Portet, G. Yushin, Y. Gogotsi.** 2007, Carbon, Vol. 45, págs. 2511-2518.

57. *Capacitive Energy Storage from -50 to 100ºC Using an Ionic Liquid Electrolyte.* **R. Lin, †, P.-L. Taberna, S. Fantini, V. Presser, C. R. Perez, F. Malbosc, N. L. Rupesinghe, K. B. K. Teo, Y. Gogotsi, P. Simon.** 2011, Journal of Physical Chemistry Letters, Vol. 2, págs. 2396-2401.

58. *Mesoporous Carbon Design for Ionic Liquid-Based, Double-Layer Supercapacitors.* **M. Lazzari, F. Soavi, M. Mastragostino.** 5, 2010, Fuel Cells, Vol. 10, págs. 840-847.

59. *High-surface area carbons from renewable sources with a bimodal micro-mesoporosity for high-performance ionic liquid-based supercapacitors.* **A. B. Fuertes, M. Sevilla.** s.l. : carbon, 2015, Vol. 94, págs. 41-52.

60. *Confinement of Symmetric Tetraalkylammonium Ions in Nanoporous Carbon Electrodes of Electric Double-Layer Capacitors.* **R. Mysyk, E. Raymundo-Piñero, J. Pernak, F. Béguin.** 30, 2009, Journal of Physical Chemistry C, Vol. 113, págs. 13443-13449.

61. *Role of Carbon Porosity and Ion Size in the Development of Ionic Liquid Based Supercapacitors.* **M. Lazzari, M. Mastragostino, A. G. Pandolfo, V. Ruiz, F. Soavi.** 1, s.l. : J. Electrochem. Soc., 2011, Vol. 158, págs. A22-A25.

62. *The influence of pore size and surface area of activated carbons on the performance of ionic liquid based supercapacitors.* **S. Pohlmann, B. Lobato, T. A. Centeno, A. Balducci.** 40, s.l. : Phys. Chem. Chem. Phys., 2013, Vol. 15, págs. 17287-17294.

63. *The interpretation of diffuse X-ray diagrams of carbon.* **Franklin, R. E.** s.l. : Acta Cryst., 1950, Vol. 3, págs. 107-121.

64. *The structure of graphitic carbons.* **Franklin, R. E.** s.l. : Acta Cryst., 1951, Vol. 4, págs. 253-261.

65. *Crystallite growth in graphitizing and non-graphitizing carbons.* **Franklin, R. E.** s.l. : Proc. R. Soc., 1951, Vol. 209, págs. 196-218.

66. *High-resolution electron microscopy studies of non-graphitizing carbons.* **P. J. F. Harris, S. C. Tsang.** 3, s.l. : Philosophical Magazine A, 1997, Vol. 76, págs. 667-677.

67. http://www.internationaloliveoil.org/web/aa-ingles/oliveWorld/olivo.html. [En línea]

68. http://www.internationaloliveoil.org/estaticos/view/131-world-olive-oil-figures. [En línea]

69. *By-products of plant food processing as a source of functional compounds — recent developments.* **A. Schieber, F.C. Stintzing, R. Carle.** 2001, Trends in Food Science & Technology, Vol. 12, págs. 401–413.

70. *Olive stone an attractive source of bioactive and valuable compounds.* **G. Rodriguez, A. Lama, R. Rodriguez, A. Jimenez, R. Guillen, J. Fernandez-Bolaños.** 2008, Bioresource Technology, Vol. 99, págs. 5261–5269.

71. *Current options for the valorization of food manufacturing waste: a review.* **N. Mirabella, V. Castellani, S. Sala.** 2014, Journal of Cleaner Production, Vol. 65, págs. 28-41.

72. *Activated carbons from lignocellulosic materials by chemical and/or physical activation: an overview.* **F. Rodriguez-Reinoso, M. Molina-Sabio.** 7, s.l. : Carbon, Vol. 30, págs. 1111-1118.

73. *Agricultural residues as precursors for activated carbon production—A review.* **O. Ioannidou, A. Zabaniotou.** 9, s.l. : Renewable and Sustainable Energy Reviews, 2007, Vol. 11, págs. 1966-2005.

74. *Control of pore development during CO2 and steam activation of olive stones.* **S. Román, J. F. González, C. M. González-García, F. Zamora.** 2008, Fuel Processing Technology, Vol. 89, págs. 715-720.

75. *Granular and monolithic activated carbons from KOH-activation of olive stones.* **R. Ubago-Perez, F. Carrasco-Marın, D. Fairen-Jimenez, C. Moreno-Castilla.** 2006, Microporous and Mesoporous Materials, Vol. 92, págs. 64–70.

76. *Activated carbon from olive kernels in a two-stage process: Industrial improvement.* **A. Zabaniotou, G. Stavropoulos, V. Skoulou.** 2008, Bioresource Technology, Vol. 99, págs. 320–326.

77. *Nanoporous Carbon: Topological Defects: Origin of Nanopores and Enhanced Adsorption Performance in Nanoporous Carbon.* **J. Guo, J. R. Morris, Y. Ihm, C. I. Contescu, N. C. Gallego, G. Duscher, S. J. Pennycook, M. F. Chisholm.** 21, s.l. : Small, 2012, Vol. 8, págs. 3283-3288.

78. *Classification of Gibbs adsorption isotherms.* **M.D. Donohue, G.L. Aranovich.** 1998, Advances in Colloid and Interface Science, Vols. 76-77, págs. 137-152.

79. *2D-NLDFT adsorption models for carbon slit-shaped pores with surface energetical heterogeneity and geometrical corrugation.* **J. Jagiello, J. P. Olivier.** 2013, Carbon, Vol. 55, págs. 70-80.

80. *Quenched solid density functional theory and pore size analysis of micro-mesoporous carbons.* **A. V. Neimark, Y. Lin, P. I. Ravikovitch, M. Thommes.** 7, 2009, Carbon, Vol. 47, págs. 1617-1628.

81. *Comparison of heterogeneous pore models QSDFT and 2D-NLDFT and computer programs ASiQwin and SAIEUS for calculation of pore size distribution.* **A. M. Puziy, O. I. Poddubnaya, B. Gawdzik, M. Sobiesiak.** 2016, Adsorption, Vol. 22, págs. 459-464.

82. *The role of the electric conductivity of carbons in the electrochemical capacitor performance.* **J. Sanchez-Gonzalez, F. Stoeckli, T. A. Centeno.** s.l. : Journal of Electroanalytical Chemistry, 2011, Vol. 657, págs. 176–180.

83. *Graphene-based materials as supercapacitor electrodes.* **L. L. Zhang, R. Zhou, X. S. Zhao.** 2010, Journal of Materials Chemistry, Vol. 20, págs. 5983-5992.

84. *Capacitance limits of high surface area activated carbons for double layer capacitors.* **O. Barbieri, M. Hahn, A. Herzog, R. Kotz.** 2005, Carbon, Vol. 43, págs. 1303-1310.

85. *Raman spectroscopy as a versatile tool for studying the properties of graphene.* **Basko, A. C. Ferrari and D. M.** s.l. : Nature Nanotechnology, 2013, Vol. 8, págs. 235–246.

86. *Studies of the activated carbons used in double-layer supercapacitors.* **Qu, D.** 2002, Journal of Power Sources, Vol. 109, págs. 403-411.

87. *Mesoporous nitrogen-rich carbons derived from protein for ultra-high capacity battery anodes and supercapacitors.* **Z. Li, Z. Xu, X. Tan, H. Wang, C. M. B. Holt, T. Stephenson, B. C. Olsen, D. Mitlin.** s.l. : Energy Environ. Sci., 2013, Vol. 6, págs. 871-878.

88. *Influence of graphene microstructures on electrochemical performance for supercapacitors.* **Y. Gong, D. Li, Q. Fu, C. Pan.** 5, s.l. : Progress in Natural Science: Materials International, 2015, Vol. 25, págs. 379-385.

89. *Electrochemical capacitors: mechanism, materials, systems, characterization and applications.* **Y. Wang, Y. Song, Y. Xia.** 2015, Chemical Sociecty Reviews, Vol. 45, págs. 5925-5950.

90. *Anomalous increase in carbon capacitance at pore sizes less than 1 nanometer.* **J. Chmiola, G. Yushin, Y. Gogotsi, C. Portet, P. Simon, P. L. Taberna.** 5794, s.l. : Science, 2006, Vol. 313, págs. 1760-1763.

91. *Relation between the Ion Size and Pore Size for an Electric Double-Layer Capacitor.* **C. Largeot, C. Portet, J. Chmiola, P. L. Taberna, Y. Gogotsi, P. Simon.** 9, s.l. : J. Am. Chem. Soc., 2008, Vol. 130, págs. 2730–2731.

92. *Relationship between the nanoporous texture of activated carbons and their capacitance properties in different electrolytes.* **E. Raymundo-Piñero, K. Kierzek, J. Machnikowski, F. Beguin.** 12, s.l. : Carbon, 2006, Vol. 44, págs. 2498-2507.

93. *Highly confined ions store charge more efficiently in supercapacitors.* **C. Merlet, C. Pean, B. Rotenberg, P. A. Madden, B. Daffos, P. L. Taberna, P. Simon, M. Salanne.** 2701, s.l. : Nature Communications, 2013, Vol. 4, págs. 1-6.

94. *The assessment of surface areas in porous carbons by two model-independent techniques, the DR equation and DFT.* **T.A. Centeno, F.Stoeckli.** 9, s.l. : Carbon, 2010, Vol. 48, págs. 2478-2486.

95. *Pore size distribution and capacitance in microporous carbons.* **F. Stoeckli, T. A. Centeno.** s.l. : Phys. Chem. Chem. Phys., 2012, Vol. 14, págs. 11589–11591.

96. *Capacitance in carbon pores of 0.7 to 15 nm: a regular pattern.* **T. A. Centeno, O. Sereda, F. Stoeckli.** s.l. : Phys. Chem. Chem. Phys., 2011, Vol. 13, págs. 12403-12406.

97. *Constant capacitance in nanopores of carbon monoliths.* **A. Garcia-Gomez, G. Moreno-Fernandez, B. Lobato, T. A. Centeno.** 24, s.l. : Phys. Chem. Chem. Phys., 2015, Vol. 17.

98. *Optimization of the characterization of porous carbons for supercapacitors.* **Centeno, F. Stoeckli and T. A.** 23, s.l. : J. Mater. Chem. A, 2013, Vol. 1, págs. 6865-6873.

99. *Saturation of subnanometer pores in an electric double-layer capacitor.* **R. Mysyk, E. Raymundo-Piñero, F.Beguin.** 3, s.l. : Electrochemistry Communications, 2009, Vol. 11, págs. 554-556.

100. *Superionic state in double-layer capacitors with nanoporous electrodes.* **S. Kondrat, A. Kornyshev.** 2, s.l. : J. Phys.: Condens. Matter, 2011, Vol. 23, pág. 022201.

101. *Increase in Capacitance by Subnanometer Pores in Carbon.* **N. Jackel, P. Simon, Y. Gogotsi, V. Presser.** 6, s.l. : ACS Energy Lett., 2016, Vol. 1, págs. 1262–1265.

102. *Elucidating the Importance of Pore Structure in Determining the Double-Layer Capacitance of Nanoporous Carbon Materials.* **J. E. Zuliani, C. Q. Jia, D. W. Kirk.** 38, s.l. : J. Phys. Chem. C, 2017, Vol. 121, pág. 20555−20566.

103. *Effect of pore size and its dispersity on the energy storage in nanoporous supercapacitors.* **S. Kondrat, C. R. Perez, V. Presser, Y. Gogotsi, A. A. Kornyshev.** 2012, Energy & Environmental Science, Vol. 5, págs. 6474-6479.

104. *Studies of the activated carbons used in double-layer supercapacitors.* **Qu, D.** 2002, Journal of Power Sources, Vol. 109, págs. 403–411.

105. *Electrochemical Quartz Crystal Microbalance (EQCM) Studies of Ions and Solvents Insertion into Highly Porous Activated Carbons.* **M. D. Levi, N. Levy, S. Sigalov, G. Salitra, D. Aurbach, J. Maier.** 38, s.l. : J. Am. Chem. Soc., 2010, Vol. 132, págs. 13220-13222.

106. *Application of a quartz-crystal microbalance to measure ionic fluxes in microporous carbons for energy storage.* **M. D. Levi, G. Salitra, N. Levy, D. Aurbach, J. Maier.** s.l. : Nature Materials, 2009, Vol. 8, págs. 872-875.

107. *In situ NMR and electrochemical quartz crystal microbalance techniques reveal the structure of the electrical double layer in supercapacitors.* **J. M. Griffin, A. C. Forse, W. Y. Tsai, P. L Taberna, P. Simon, C. P. Grey.** s.l. : Nature Materials, 2015, Vol. 14, págs. 812–819.

108. *Real-Time NMR Studies of Electrochemical Double-Layer Capacitors.* **H. Wang, T. K. J. Koster, N. M. Trease, J. Segalini, P. L. Taberna, P. Simon, Y. Gogotsi, C. P. Grey.** 48, s.l. : J. Am. Chem. Soc., 2011, Vol. 133, págs. 19270–19273.

109. *Ion counting in supercapacitor electrodes using NMR spectroscopy.* **J. M. Griffin, A. C. Forse, H. Wang, N. M. Trease, P. L. Taberna, P. Simon, C. P. Grey.** s.l. : Faraday Discuss., 2014, Vol. 176, págs. 49-68.

110. *Exploring electrolyte organization in supercapacitor electrodes with solid-state NMR.* **M. Deschamps, E. Gilbert, P. Azais, E. Raymundo-Piñero, M. R. Ammar, P. Simon, D. Massiot, F. Beguin.** s.l. : Nature Materials volume, 2013, Vol. 12, págs. 351–358.

111. *Solid-state NMR studies of supercapacitors.* **J. M. Griffin, A. C. Forse, C. P. Grey.** s.l. : Solid State Nuclear Magnetic Resonance, 2016, Vols. 74-75, págs. 16-35.

112. *New Perspectives on the Charging Mechanisms of Supercapacitors.* **A. C. Forse, C. Merlet, J. M. Griffin, C. P. Grey.** 18, s.l. : J. Am. Chem. Soc, 2016, Vol. 138, págs. 5731–5744.

113. *In Situ NMR Spectroscopy of Supercapacitors: Insight into the Charge Storage Mechanism.* **H. Wang, A. C. Forse, J. M. Griffin, N. M. Trease, L. Trognko, P. L. Taberna, P. Simon, C. P. Grey.** 50, s.l. : J. Am. Chem. Soc., 2013, Vol. 135, págs. 18968–18980.

114. *Direct observation of ion dynamics in supercapacitor electrodes using in situ diffusion NMR spectroscopy.* **A. C. Forse, J. M. Griffin, C. Merlet, J. Carretero-Gonzalez, A. R. O. Raji, N. M. Trease, C. P. Grey.** 16216, s.l. : Nature Energy, 2017, Vol. 2, págs. 1-7.

115. *NMR Study of Ion Dynamics and Charge Storage in Ionic Liquid Supercapacitors.* **A. C. Forse, J. M. Griffin, C. Merlet, P. M. Bayley, H. Wang, P. Simon, C. P. Grey.** 22, s.l. : J. Am. Chem. Soc., 2015, Vol. 137, págs. 7231–7242.

116. *A carbon nanopore model to quantify structure and kinetics of ion electrosorption with in situ small-angle X-ray scattering.* **C. Prehal, C. Koczwara, N. Jackel, H. Amenitsch, V. Presser, O. Paris.** 23, s.l. : Phys. Chem. Chem. Phys., 2017, Vol. 19, págs. 15549-15561.

117. *Tracking the structural arrangement of ions in carbon supercapacitor nanopores using in situ small-angle X-ray scattering.* **C. Prehal, D. Weingarth, E. Perre, R. T. Lechner, H. Amenitsch, O. Paris, V. Presser.** 6, s.l. : Energy Environ. Sci., 2015, Vol. 8, págs. 1725-1735.

118. *In Situ Measurement of Electrosorption-Induced Deformation Reveals the Importance of Micropores in Hierarchical Carbons.* **C. Koczwara, S. Rumswinkel, C. Prehal, N. Jackel, M. S. Elsasser, H. Amenitsch, V. Presser, N. Hüsing, O. Paris.** 28, s.l. : ACS Appl. Mater. Interfaces, 2017, Vol. 9, págs. 23319–23324.

119. *Quantification of ion confinement and desolvation in nanoporous carbon supercapacitors with modelling and in situ X-ray scattering.* **C. Prehal, C. Koczwara, N. Jackel, A. Schreiber, M. Burian, H. Amenitsch, M. A. Hartmann, V. Presser, O. Paris.** 16215, s.l. : Nature Energy, 2017, Vol. 2, págs. 1-8.

120. *A review of electrolyte materials and compositions for electrochemical supercapacitors.* **C. Zhong, Y. Deng, W. Hu, J. Qiao, L. Zhangd, J. Zhang.** 2015, Chemical Society Reviews, Vol. 44, págs. 7484-7539.

121. *Strategies to Improve the Performance of Carbon/Carbon Capacitors in Salt Aqueous Electrolytes.* **Q. Abbas, P. Ratajczak, P. Babuchowska, A. Le Comte, D. Belanger, T. Brousse, F. Beguin.** 5, 2015, Journal of the Electrochemical Society, Vol. 162, págs. A5148-A5157.

122. *Novel insight into neutral medium as electrolyte for high-voltage supercapacitors.* **K. Fic, G. Lota, M. Meller, E. Frackowiak.** s.l. : Energy Environ. Sci., 2012, Vol. 5, págs. 5842-5850.

123. *Exploring the large voltage range of carbon/carbon supercapacitors in aqueous lithium sulfate electrolyte.* **Q. Gao, L. Demarconnay, E. Raymundo-Piñero, F. Beguin.** s.l. : Energy Environ. Sci., 2012, Vol. 5, págs. 9611-9617.

124. *Carbon materials for supercapacitor application.* **Frackowiak, E.** 15, s.l. : Phys. Chem. Chem. Phys., 2007, Vol. 9, págs. 1774–1785.

125. *Peculiarities and requirements of asymmetric capacitor devices based on combination of capacitor and battery-type electrodes.* **W. G. Pell, B. E. Conway.** 2004, Journal of Power Sources, Vol. 136, págs. 334–345.

126. *Carbon/PbO2 asymmetric electrochemical capacitor based on methanesulfonic acid electrolyte.* **P. Perret, Z. Khani, T. Brousse, D. Bélanger, D. Guay.** 201, Electrochimica Acta, Vol. 56, págs. 8122-8128.

127. *Use of KCl Aqueous Electrolyte for 2 V Manganese OxideÕActivated Carbon Hybrid Capacitor.* **M. S. Hong, S. H. Lee and S. W. Kim.** 10, 2002, Electrochemical and Solid-State Letters, Vol. 5, págs. A227-A230.

128. *A Hybrid Activated Carbon-Manganese Dioxide Capacitor using a Mild Aqueous Electrolyte.* **T. Brousse, M. Toupin, D. Belanger.** 4, 2004, Journal of The Electrochemical Society, Vol. 151, págs. A614-A622.

129. *Amorphous Carbon Nanofibers and Their Activated Carbon Nanofibers as Supercapacitor Electrodes.* **V. Barranco, M. A. Lillo-Rodenas, A. Linares-Solano, A. Oya, F. Pico, J. Ibañez, F. Agullo-Rueda, J. M. Amarilla, J. M. Rojo.** 2010, Journal of Physical Chemistry C, Vol. 114, págs. 1002-10307.

130. *Nanowindow-Regulated Specific Capacitance of Supercapacitor Electrodes of Single-Wall Carbon Nanohorns.* **C.-M. Yang, Y.-J. Kim, M. Endo, H. Kanoh, M. Yudasaka, S. Iijima, K. Kaneko.** 2007, Journal of the American Chemical Society, Vol. 129, págs. 20-21.

131. *A 4 V-electrochemical capacitor using electrode and electrolyte.* **C. Zheng, M. Yoshio, L. Qi, H. Wang.** 2014, Journal of Power Sources, Vol. 260, págs. 19-26.

132. *Aligned Titania Nanotubes as an Intercalation Anode Material for Hybrid Electrochemical Energy Storage.* **D.-W. Wang, H.-T. Fang, F. Li, Z.-G. Chen, Q.-S. Zhong, G. Q. Lu, H.-M. Cheng.** s.l. : 18, 2008, Advanced Functional Materials, págs. 3787-3793.

133. *Exfoliated graphite nanoplatelets–V2O5 nanotube composite electrodes for.* **J. S. Bonso, A. Rahy, S. D. Perera, N. Nour, O. Seitz, Y. J. Chabal, K. J. Balkus Jr. J. P. Ferraris D. J. Yang.** 2012, Journal of Power Sources, Vol. 203, págs. 227-232.

134. *Electrochemical performance of hybrid supercapacitor fabricated using multi-structured activated carbon.* **M.-Y. Cho, M.-H. Kim, H.-K. Kim, K.-B. Kim, J. R. Yoon, K. C. Roh.** 2014, Electrochemistry Communications, Vol. 47, págs. 5-8.

135. *Ionic Liquids.* **R. D. Rogers, G. A. Voth.** 11, 2007, Accounts of Chemical Research, Vol. 40, págs. 1077-1078.

136. *ionic-liquid materials for the electrochemical challenges of the future.* **M. Armand, F. Endres, D. R. MacFarlane, H. Ohno, B. Scrosati.** 2009, Nature Materials, Vol. 8, págs. 621-629.

137. *Practical and theoretical limits for electrochemical double-layer capacitors.* **A. Lewandowski, M. Galinski.** 2007, Journal of Power Sources, Vol. 173, págs. 822-828.

138. *Inhibition of Self-Aggregation in Ionic Liquid Electrolytes for High-Energy Electrochemical Devices.* **M. Kunze, E. Paillard, S. Jeong, G. B. Appetecchi, M. Schonhoff, M. Winter, S. Passerini.** 2011, Journal of Physical Chemistry C, Vol. 115, págs. 19431-19436.

139. *New Insights to Self-Aggregation in Ionic Liquid Electrolytes for High-Energy Electrochemical Devices.* **M. Kunze, S. Jeong, E. Paillard, M. Schönhoff, M. Winter, S. Passerini.** 2, 2011, Advanced Energy Materials, Vol. 1, págs. 274-281.

140. *Outstanding performance of activated graphene based supercapacitors in ionic liquid electrolyte from -50 to 80ºC.* **W.-Y. Tsai, R. Lin, S. iMurali, L. L. Zhang, J. K.McDonough, R. S. Ruoff, P.-L.Taberna, Y. Gogotsi, P. Simon.** 2013, Nano Energy, Vol. 2, págs. 403-411.

141. *Capacitive Energy Storage from -50 to 100 ºC Using an Ionic Liquid Electrolyte.* **R. Lin, P.-L. Taberna, S. Fantini, V. Presser, C. R. Perez, F. Malbosc, N. L. Rupesinghe, K. B. K. Teo, Y. Gogotsi, P. Simon.** 2011, Journal of Physical Chemistry Letters, Vol. 2, págs. 396-2401.

142. *Peculiarities and requirements of asymmetric capacitor devices based on combination of capacitor and battery-type electrodes.* **W. G.Pell, B. E. Conway.** 2, 2004, Journal of Power Sources, Vol. 136, págs. 334-345.

143. *Hybridization of rechargeable batteries and electrochemical capacitors: Principles and limits.* **D. Cericola, R. Kötz.** 2012, Electrochimica Acta, Vol. 72, págs. 1-17.

144. http://www.jmenergy.co.jp/en/. [En línea]

145. *An Asymmetric Hybrid Nonaqueous Energy Storage Cell.* **G. G. Amatucci, F. Badway, A. Du Pasquier, T. Zheng.** 8, 2001, Journal of The Electrochemical Society, Vol. 148, págs. A930-A939.

146. *High-rate nano-crystalline Li4Ti5O12 attached on carbon nano-fibers for hybrid supercapacitors.* **K. Naoi, S. Ishimoto, Y. Isobe, S. Aoyagi.** 2010, Journal of Power Sources, Vol. 195, págs. 6250-6254.

147. *An Advanced Hybrid Electrochemical Capacitor That Uses a Wide Potential Range at the Positive Electrode.* **T. Aida, K. Yamada, M. Morita.** 12, 2006, Electrochemical and Solid-State Letters, Vol. 9, págs. A534-A536.

148. *Evaluation of lithium-ion capacitors assembled with pre-lithiated graphite anode and activated carbon cathode.* **S.R. Sivakkumar, A.G. Pandolfo.** 2012, Electrochimica Acta, Vol. 65, págs. 280-287.

149. *Characteristics and performance of 500 F asymmetric hybrid advanced supercapacitor prototypes.* **A. Du Pasquier, I. Plitz, J. Gural, S. Menocal, G. Amatucci.** 2003, Journal of Power Sources, Vol. 113, págs. 62-71.

150. *High performance lithium-ion hybrid capacitors with pre-lithiated hard carbon anodes and bifunctional cathode electrodes.* **X. Sun, X. Zhang, H. Zhang, N. Xu, K. Wang, Y. Ma.** 2014, Journal of Power Sources, Vol. 270, págs. 318-325.

151. *High Performance Titanium Antimonide TiSb2 Alloy for Na-Ion Batteries and Capacitors.* **M. Arnaiz, J. L. Gomez-Camer, J. Ajuria, F. Bonilla, B. Acebedo, M. Jauregi, E. Goikolea, M. Galceran, T. Rojo.** 22, 2018, Chemistry of Materials, Vol. 30, págs. 8155-8163.

152. *A self-assembled intercalated metal–organic framework electrode with outstanding area capacity for high volumetric energy asymmetric capacitors.* **N. Ogihara, Y. Ozawa, O. Hiruta.** 2016, Journal of Materials Chemistry A, Vol. 4, págs. 3398-3405.

153. *High-energy lithium-ion hybrid supercapacitors composed of hierarchical urchin-like WO3/C anodes and MOF-derived polyhedral hollow carbon cathodes.* **J. Xu, Y. Li, L. Wang, Q. Cai, Q. Li, B. Gao, X. Zhang, K. Huo, P. K. Chuc.** 2016, Nanoscale, Vol. 8, págs. 16761-16768.

154. *Aqueous energy-storage cells based on activated carbon and LiMn2O4 elecrodes.* **O. Hanna, S. Luski, T. Brousse, D. Aurbach.** 2017, Journal of Power Sources, Vol. 354, págs. 148-156.

155. *The re-emergence of sodium ion batteries: testing, processing, and manufacturability.* **S. Roberts, E. Kendrick.** 2018, Nanotechnology, Science and Applications, Vol. 11, págs. 23-33.

156. *High-Performance Sodium-Ion Pseudocapacitors Based on Hierarchically Porous Nanowire Composites.* **Z. Chen, V. Augustyn, X. Jia, Q. Xiao, B. Dunn, Y. Lu.** 5, 2012, ACS Nano, Vol. 6, págs. 4319-4327.

157. *Sodium Titanate Nanotubes as Negative Electrode Materials for Sodium-Ion Capacitors.* **J. Yin, L. Qi, H. Wang.** 2012, ACS Applied Materials and Interfaces, Vol. 4, págs. 2762-2768.

158. *Na-ion capacitor using sodium pre-doped hard carbon and activated carbon.* **K. Kuratani, M. Yao, H. Senoh, N. Takeichi, T. Sakai, T. Kiyobayashi.** 2012, Electrochimica Acta, Vol. 76, págs. 320-325.

159. *Flexible Sodium-Ion Pseudocapacitors Based on 3D Na2Ti3O7 Nanosheet Arrays/Carbon Textiles Anodes.* **S. Dong, L. Shen, H. Li, G. Pang, H. Dou, X.Zhang.** 21, 2016, Advanced Functional Materials, Vol. 26, págs. 3703-3710.

160. *Hybridization of electrochemical capacitors and rechargeable batteries: An experimental analysis of the different possible approaches utilizing activated carbon, Li4Ti5O12 and LiMn2O4.* **D. Cericola, P. Novák, A. Wokaun, R. Kötz.** 23, 2011, Journal of Power Sources, Vol. 196, págs. 10305-10313.

161. *Review of nanostructured carbon materials for electrochemical capacitor applications: advantages and limitations of activated carbon, carbide-derived carbon, zeolite-templated carbon, carbon aerogels, carbon nanotubes, onion-like carbon, and graphene.* **W. Gu, G. Yushin.** 5, 2014, Wiley Interdisciplinary Reviews: Energy and Environment, Vol. 3, págs. 424-473.

162. *A comparison of the aging of electrochemical double layer capacitors with acetonitrile and propylene carbonate-based electrolytes at elevated voltages.* **P. W. Ruch, D. Cericola, A. Foelske, R. Kötz, A. Wokaun.** 2010, Electrochimica Acta, Vol. 55, págs. 2352–2357.

163. *Effect of electrode mass ratio on aging of activated carbon based supercapacitors utilizing organic electrolytes.* **D. Cericola, R. Kötz, A. Wokaun.** 2011, Journal of Power Sources, Vol. 196, págs. 3114–3118.

164. *Mass-Balancing of Electrodes as a Strategy to Widen the Operating Voltage Window of Carbon/Carbon Supercapacitors in Neutral Aqueous Electrolytes.* **S. Vaquero, J. Palma, M. Anderson, R. Marcilla.** 2013, International Journal of Electrochemical Science, Vol. 8, págs. 10293-10307.

165. *Anomalous increase in carbon capacitance at pore sizes less than 1 nanometer.* **Chmiola, J, et al., et al.** 5794, 2006, Science, Vol. 313, pp. 1760-1763.

166. *One-pot hydrothermal synthesis of Nitrogen-doped graphene as high-performance anode materials for lithium ion batteries.* **Z. Xing, Z. Ju, Y. Zhao, J. Wan, Y. Zhu, Y. Qiang, Y. Qian.** 26145, s.l. : Scientific Reports, 2016, Vol. 6, págs. 1-10.

167. *Carbon properties and their role in supercapacitors.* **A. G. Pandolfo, A. F. Hollenkamp.** 1, 2006, Journal of Power Sources, Vol. 157, págs. 11-27.

168. *Where do batteries end and supercapacitors begin?* **Simon, Patrice, Gogotsi, Yury and Dunn, Bruce.** 6176, 2014, Science, Vol. 343, pp. 1210-1211.

169. **Béguin, François and Frackowiak, Elżbieta.** *Supercapacitors: Materials, Systems and Applications.* s.l. : Wiley-VCH Verlag GmbH & Co. KGaA, 2013.

170. *Peculiarities and requirements of asymmetric capacitor devices based on combination of capacitor and battery-type electrodes.* **Pell, Wendy G and Conway, Brian E.** 2004, Journal of Power Sources, Vol. 136, pp. 334-345.

171. *Hybridization of rechargeable batteries and electro-chemical capacitors: principles and limits.* **Cericola, D and Kötz, R.** 2012, Electrochimica Acta, Vol. 72, pp. 1-17.

172. *Hybridization of electrochemical capacitors and rechargeable batteries: An experimental analysis of the different possible approaches utilizing activated.* **Cericola, Dario y Kötz, Rüdiger.** 2011, Journal of Power Sources, Vol. 196, págs. 10305-10313.

173. **JM Energy Corporation.** [Online] [Cited: 23 05 2016.] http://www.jmenergy.co.jp/en/.

174. **F. Beguin, E. Frackowiak.** *Carbons for Electrochemical Energy Storage and Conversion Systems.* Boca Raton : CRC Press, 2009.

175. *High-surface area carbons from renewable sources with a bimodal micro-mesoporosity for high-performance ionic liquid-based supercapacitors.* **A. B. Fuertes, M. Sevilla.** s.l. : carbon, 2015, Vol. 94, págs. 41-52.

176. *Optimization of the characterization of porous carbons for supercapacitors.* **F. Stoeckli, T. A. Centeno.** 23, s.l. : Journal of the Materials Chemistry A, 2013, Vol. 1, págs. 6865-6873.

177. *NMR Study of Ion Dynamics and Charge Storage in Ionic Liquid Supercapacitors.* **A. C. Forse, J. M. Griffin, C. Merlet, P. M. Bayley, H. Wang, P. Simon, C. P. Grey.** 22, s.l. : J. Am. Chem. Soc., 2015, Vol. 137, págs. 7231–7242.

178. *Carbon properties and their role in supercapacitors.* **Hollenkamp, A. G. Pandolfo & A. F.** 1, s.l. : Journal of Power Sources, 2006, Vol. 157, págs. 11-27.

179. https://www.jsrmicro.be/sites/default/files/attachments/ultimo_lithium_ion_capacitor_brochure_0.pdf. [En línea]

180. *Critical review on lithium-ion batteries: are they safe? Sustainable?* **Julien, A. Mauger & C. M.** 2017, Ionics, Vol. 23, págs. 1933-1947.

181. *NMR Study of Ion Dynamics and Charge Storage in Ionic Liquid Supercapacitors.* **A. C. Forse, J. M. Griffin, C. Merlet, P. M. Bayley, H. Wang, P. Simon, C. P. Grey.** 22, 2015, Journal of American Chemical Sociecty, Vol. 137, págs. 7231–7242.

182. *Solid-state NMR studies of supercapacitors.* **J. M. Griffin, A. C. Forse, C. P. Grey.** 2016, Solid State Nuclear Magnetic Resonance, Vols. 74-75, págs. 16-35.

183. *Electrochemical Quartz Crystal Microbalance (EQCM) Studies of Ions and Solvents Insertion into Highly Porous Activated Carbons.* **M. D. Levi, N. Levy, S. Sigalov, G. Salitra, D. Aurbach, J. Maier.** 38, 2010, Journal of the American Chemical Society, Vol. 132, págs. 13220-13222.

184. *Tracking the structural arrangement of ions in carbon supercapacitor nanopores using in situ small-angle X-ray scattering.* **C. Prehal, D. Weingarth, E. Perre, R. T. Lechner, H. Amenitsch, O. Paris, V. Presser.** 6, 2015, Energy & Environmental Science, Vol. 8, págs. 1725-1735.

185. *In Situ Measurement of Electrosorption-Induced Deformation Reveals the Importance of Micropores in Hierarchical Carbons.* **C. Koczwara, S. Rumswinkel, C. Prehal, N. Jackel, M. S. Elsasser, H. Amenitsch, V. Presser, N. Hüsing, O. Paris.** 28, 2017, ACS Applied Materials & Interfaces, Vol. 9, págs. 23319–23324.

186. *Capacitance in carbon pores of 0.7 to 15 nm: a regular pattern.* **T. A. Centeno, O. Sereda, F. Stoeckli.** 2011, Physical Chemistry Chemical Physics, Vol. 13, págs. 12403-12406.

187. *Role of Carbon Porosity and Ion Size in the Development of Ionic Liquid Based Supercapacitors.* **M. Lazzari, M. Mastragostino, A. G. Pandolfo, V. Ruiz, F. Soavi.** 1, 2011, Journal of the Electrochemical Society, Vol. 158, págs. A22-A25.

188. *Carbon materials for supercapacitor application.* **Frackowiak, E.** 15, s.l. : Phys. Chem. Chem. Phys., 2007, Vol. 9, págs. 1774–1785.

# 3 OBJECTIVES

**The objective of this Doctoral Thesis is to fine-tune the porosity of microporous carbons derived from an abundant natural waste material - olive pits- and conduct a detailed study of the electrochemical response of these microporous carbon materials in different electrolytes, with the ultimate goal to build electrochemical capacitors with a performance comparable to or better than the state-of-the-art systems.** Olive pits are a cheap disposable by-product of olive oil industry, and their suitability as a precursor to prepare activated carbons was demonstrated in the 1990s, however, the use of these microporous carbons in electrochemical capacitors was not evaluated.

To get to this main objective several other partial objectives have been taken under consideration:

1. The development of a synthetic procedure through the pyrolysis and chemical activation of this lignocellulosic material (olive pits) to obtain carbons with nanopores suitable for the capacitive charge storage in aqueous alkali (KOH) and neutral salts based electrolytes, using supporting salts such as, sulfates, nitrates and chlorides), organic electrolytes such as (tetraethylammonium tetrafluoroborate, $(C_2H_5)_4N(BF_4)$, in acetonitrile, $CH_3CN$) and ionic liquids. The parameters to take under control have been the activation temperature and the relationship between the activating agent and the carbon. Thus, the resulting products aim to have a maximized specific surface area accessible to the ions from the electrolyte, a narrow pore size distribution adapted to ions of various sizes and a good conductivity.
2. The study of the capacitive electrosorption in the nanopores of each electrode, *i.e.* electrosorption of cations in the negative electrode and *vice versa*, by combining electroanalytical techniques with gas adsorption/desorption measurements. By determining: i) the solvation level, ii) the relationship between coions and counterions depending upon the polarization of the electrodes and iii) the pore size distribution of the carbons.
3. The study of the electrochemical performance of the supercapacitors built with the activated carbons derived from olive pits in various types of electrolytes in order to select the most promising active material/electrolyte combination in terms of capacitance value, rate capability and cyclability.
4. The maximisation of the energy and power, both in gravimetric and volumetric terms, of the energy storage devices by designing hybrid and asymmetric cell configurations.

# 4 RESULTS AND DISCUSSION

## 5.1 Effect of pore texture on performance of activated carbon supercapacitor electrodes derived from olive pits

Electrochimica Acta 160 (2015) 178–184

Contents lists available at ScienceDirect

Electrochimica Acta

journal homepage: www.elsevier.com/locate/electacta

# Effect of pore texture on performance of activated carbon supercapacitor electrodes derived from olive pits

Edurne Redondo, Javier Carretero-González, Eider Goikolea, Julie Ségalini, Roman Mysyk *

*CIC EnergiGUNE, Arabako Teknologi Parkea, Albert Einstein 48, 01510 Miñano, Spain*

ARTICLE INFO

*Article history:*
Received 2 December 2014
Received in revised form 27 January 2015
Accepted 1 February 2015
Available online 3 February 2015

*Keywords:*
Supercapacitors
microporosity
activated carbon
biomass

ABSTRACT

Activated carbon electrodes for electrochemical capacitors have been prepared by the chemical activation of a natural renewable and by-product material precursor – olive pits – from the olive oil production industry. The careful adjustment of the synthesis conditions has allowed synthesizing a series of microporous carbon electrodes with an optimized microporosity, enabling a gravimetric and volumetric capacitance in basic aqueous medium up to 260 F $g^{-1}$ and 140 F $cm^{-3}$, respectively, with good rate capability. A relation amongst capacitance, specific surface area, accessible average pore size and effective dielectric permittivity has been established, demonstrating that there is not just a single parameter decisively impacting the capacitance value. The collective analysis of experimental data suggests that solvation imposes an optimum pore size for each ion with regard to rate capability: moderate solvation contributes to enhancing capacitance in pores slightly exceeding solvated ion size while excessive solvation deteriorates the high-rate response of supercapacitor electrodes having pores much wider than ion size.



## 1. Introduction

Electrical double-layer capacitors (EDLCs), which are the most widespread type of supercapacitors, are one of the most promising electrochemical power sources, operating by the electrosorption of ions from an electrolyte onto high-surface area electrodes [1]. High capacitance values of a few hundred F per g of active material are attainable with EDLCs because of the high specific surface area (SSA) of electrode materials and the very small charge separation between the surface atoms from the electrode and the ions from the electrolyte (typically below 1 nm) [1]. Unlike batteries, EDLCs can be fully charged in a matter of seconds. They also compare favorably with batteries in discharge time (typically a few seconds) and, most importantly, they feature a much higher cycle life. However, the major drawback of supercapacitors is the lower energy density, in general about 5 Wh $kg^{-1}$ [2], although higher-energy systems have recently been offered by hybridizing battery-type and supercapacitor-type electrodes in a single cell (e.g., the Li-ion capacitor). A wide variety of carbon nanomaterials have been exploited as EDLC electrodes, in particular, template carbons [3], carbon nanoonions (e.g., [4]) and graphene (e.g., [5]), but microporous activated carbons (ACs) remain the material of choice owing to their moderate cost and large availability. Although ACs are traditionally produced from petroleum coke, pitch and coals, the scarcity of fossil fuels has recently stimulated an interest in electrode materials originated from inexpensive renewable precursors. Equally to their counterparts derived from fossil sources, they offer a number of attractive attributes such as high SSA, sufficient electrical conductivity, high capacitance values, acceptable cost and high cycle life, but, more advantageously, they can be derived from an abundant organic matter naturally reproducible within a relatively short period of time [6].

This work focuses on microporous carbon electrodes derived from crushed olive pits, which are agricultural olive mill waste byproducts extensively generated by the olive oil milling industry, with estimated production values at a level of 6.8 million tons/year in Europe only [7]. Olive pits have been the subject of thorough studies on the production of ACs by both physical and chemical activation (see, e.g., [7–12]), but do not appear to have been probed as precursors for microporous carbons designed to be used in EDLC electrodes. In this regard, tailoring olive pits-derived carbons for capacitive energy storage can be a good path to a better choice of

* Corresponding author. Fax: +34 94 529 71 08.
*E-mail address:* rmysyk@gmail.com (R. Mysyk).

http://dx.doi.org/10.1016/j.electacta.2015.02.006
0013-4686/

abundant and easily renewable precursors for carbon-based electrode materials.

Apart from the need for renewable sources of electrode materials, the performance requirements of the current and envisioned EDLC market should also be met. In this sense, high volumetric capacitance values are inevitably required [6] since the application areas of supercapacitors are centered on transportation, e.g., on hybrid electric vehicles (HEV) [2]. In this study, the optimization of chemical activation of carbons derived from olive pits has been conducted with the main goal of preparing electrode materials whose textural properties enable high volumetric capacitance values at high charge/discharge rate, *i.e.* on the timescale of supercapacitor applications (typical discharge in less than 10 s). The optimization of carbons derived from olive pits is described with a focus put on the use of carbons for supercapacitors working in basic aqueous electrolyte. We particularly show that minor alterations to textural properties lead to drastic changes in the capacitive response. Finally, we have explored the relation between the textural properties of carbon materials and the rate capability of the corresponding supercapacitor cells.

## 2. Experimental

### 2.1. Preparation of microporous carbons by alkali activation

The activation of carbons was conducted after carbonization of raw olive pits in a tubular furnace by heating under an Ar flow of 100 ml $min^{-1}$ at a ramp rate of 5 °C $min^{-1}$ to a predefined temperature and further holding the temperature for 2 h (the carbonization yield for olive pits is 25 ± 1% independently of the temperature between 600 °C and 800 °C). After carbonization, the resulting char was physically mixed with potassium hydroxide in variable mass ratios. Physical mixing was chosen as the contacting method because in most cases it has been proven to lead to better porosity development than impregnation [13]. The materials mixed with KOH were placed in an Inconel© boat and activated according to the procedures known in the literature by heating up to the maximum temperature under Ar flow (100 ml $min^{-1}$) inside a horizontal stainless steel tube within a tubular furnace [13]. The heating ramp rate was 5 °C $min^{-1}$ and the holding time at the maximum temperature was 2 h. The variable parameters were the KOH/carbon ratio (KOH/C ratio) and the maximum temperature. In all cases, preliminary carbonization and subsequent activation were both carried out at the same temperature. After activation, microporous carbons were washed off with a diluted solution of hydrochloric acid and water until neutral pH was reached and then dried at 120 °C under vacuum.

Table S1 details the activation yield as a function of the KOH/C ratio for the activations conducted at 700 °C (the optimum selected temperature as explained below).

### 2.2. Textural and X-ray photoelectron spectroscopy characterization

Nitrogen adsorption isotherms were measured at -195.8 °C using a Micromeritics ASAP 2020 instrument for relative pressure values ($P/P_0$) between $10^{-8}$ and 0.995 for samples preliminarily outgassed for 24 h at 200 °C. The SSA values and pore size distribution were calculated by applying the recently-developed 2D Non-Local Density Functional Theory (2D NLDFT) treatment to $N_2$ adsorption isotherms using the data reduction software SAEIUS [14]. The average pore size ($L_0$) was calculated as a weighted average from the DFT data according to the formula:

$$L_0 = \frac{\int_{V\min}^{V\max} LdV}{V_{\max} - V_{\min}} \quad (1)$$

where $V_{max}$ and $V_{min}$ are the total pore volume and the pore volume at the minimum pore size, correspondingly.

XPS C1s and O1s spectra were recorded using a PHOIBOS 150 analyzer (SPECS) and monochromated Mg Kα X ray source.

### 2.3. Electrode preparation and electrochemical measurements

Electrodes were prepared on the basis of the mixture of a carbon material (95 wt.%) and a polytetrafluorethylene (PTFE) binder (5 wt.%, from a 60 wt.% aqueous dispersion). The mixture was homogenized by adding a few milliliters of ethanol and then worked out until plasticity. The plastic composite was then rolled to a thickness of ~200 μm and dried under vacuum at 120 °C overnight. Disk-shaped electrodes of 11 mm in diameter were then cut out, weighed, and their thickness was measured again. Finally, two-electrode symmetric supercapacitor cells were assembled in a Nylon Swagelok® airtight system using two identical carbon electrodes, two titanium current collectors and a porous glass fiber (Whatman GFB) membrane separator. 6 M KOH was used as the electrolyte solution. An Hg/HgO reference electrode was introduced into two-electrode cells for discriminating the potential evolution of each of the two electrodes with the cutoff voltage being imposed between the positive and negative electrodes.

Cyclic voltammetry (CV), Galvanostatic (GA) charge-discharge cycling and electrochemical impedance spectroscopy (EIS) measurements were conducted using a multichannel VMP3 generator (Biologic, France). EIS measurements were conducted by applying a low sinusoidal amplitude alternating voltage of 10 mV at frequencies from 1 MHz to 10 mHz.

The average gravimetric capacitance per electrode was calculated from the data of the GA experiments according to the formula:

$$C = 2\frac{\int Idt}{\Delta V m_{am}} \quad (2)$$

where $C$ is the gravimetric capacitance per electrode (F $g^{-1}$), $Idt$ the differential charge (A s), $\Delta V$ the cell voltage (V), $m_{am}$ the mass of active material per electrode (g). The capacitance values are reported for the voltage range between 0 V and the maximum cell voltage, excluding the Ohmic drop.

The gravimetric capacitance per cell was calculated as

$$C_{\text{cell}} = C/4 \quad (3)$$

Additionally, the capacitance of the positive and negative electrodes was separately calculated from the potential variation at the corresponding electrode in the cases where a reference electrode was introduced in a 2-electrode cell. For instance, for the positive electrode

$$C_+ = \frac{\int Idt}{\Delta E_+ m_+} \quad (4)$$

where $C_+$ is the capacitance (F $g^{-1}$), $I$ the constant current (A), $\Delta t$ the discharge time (s), $\Delta E_+$ the potential evolution (V, excluding the Ohmic drop), $m_+$ the mass of the positive electrode (g). The corresponding values for the negative electrode are denoted as $C_-$, $\Delta E_-$, $m_-$.

The differential gravimetric capacitance per electrode of a two-electrode cell in the CV experiments was calculated according to the formula:

$$C = 2i/[(dV/dt)m_{am}] \quad (5)$$

where $C$ is the gravimetric capacitance per electrode ($F g^{-1}$), $i$ the current (A), $dV/dt$ the scan rate ($V s^{-1}$), $m_{am}$ the mass of active material per electrode (g).

The electrical conductivity was evaluated on pelletized electrodes using the van der Pauw four-probe method [15].

## 3. Results and discussion

### 3.1. Effect of synthesis temperature

Table 1 and Fig. S1 show the evolution of textural properties of the samples synthesized at a KOH/C ratio of 2.6, which are given here as an example, in the temperature range between 700 °C and 1000 °C. Essentially microporous carbons with a narrow pore size distribution (PSD) are prepared at 700 °C and 800 °C, featuring mostly pores in the subnanometer range with the corresponding change in the PSD and SSA (an increase of about 100 $m^2 g^{-1}$) being relatively minor (Fig. S1A and Table 1, respectively). However, further increasing the activation temperature up to 1000 °C significantly alters the PSD, leading to the emergence of larger micropores and narrow mesopores between 2 and 3 nm. The variations in the textural properties are reflected in the electrochemical performance: the gravimetric capacitance rises from 176 $F g^{-1}$ to 218 $F g^{-1}$ when increasing the activation temperature to 800 °C and undergoes a strong decay (~31 %) on further shifting the synthesis temperature to 1000 °C (see Table 1 and CVs in Fig. S1B). On one hand, this corresponds to an approximately 35% decrease in the SSA between 800 °C and 1000 °C, suggesting the SSA to be a major factor impacting capacitance. This is consistent with the gravimetric capacitance being approximately scaled with the SSA (up to a certain saturation limit) as reported elsewhere [16]. On the other hand, the increase in capacitance between 700 °C and 800 °C is more important (~25%) than the corresponding rise in the SSA (~ 5%), suggesting the SSA not to be the only factor determining capacitance. A more detailed analysis is therefore needed and can be provided on account of all the factors impacting the gravimetric capacitance, *i.e.* SSA, average pore size, ion size, and dielectric permittivity. Several formulae were developed to describe the capacitance of EDLCs in a more precise manner than using the parallel-plate capacitor model. As applied to our case, an electric wire-in-cylinder capacitor model was suggested for electrosorption into micropores [17]. More recently, a sandwich capacitance model was proposed to explain the experimentally observed behaviour of hydrated $K^+$ ions, assuming they are enclosed midway between pore walls in a slit-shaped micropore [18], which is a more reliable approximation to the pore shape in carbons.

$$C = S\varepsilon_0\varepsilon_r/(b-a_0) \quad (6)$$

where $S$ is the specific surface area, $\varepsilon_r$ – the effective dielectric permittivity, $\varepsilon_0$ – the electric constant, $b$- the pore half-width, $a_0$ – the ion radius. This formula can separately be applied to the gravimetric capacitance of negative ($C_-$) and positive ($C_+$) electrodes:

$$C_- = S_K\varepsilon_0\varepsilon_r/(b_K - a_{0K}) \quad \text{and} \quad C_+ = S_A\varepsilon_0\varepsilon_r/(b_A - a_{0A}) \quad (7)$$

where $S_K$ is the part of SSA accessible to cations, $b_K$ – the average pore half-width related to cation-accessible porosity, and $a_{0K}$ – the cation radius. $S_A$, $b_A$, $a_{0A}$ are the corresponding values for anions. $S_K$ and $S_A$ are calculated from the DFT data as the difference between the total surface area and the surface area built up by pores narrower than the size of the corresponding ion.

The average pore size accessible to cations ($L_{0K}$) and anions ($L_{0A}$) can be calculated separately as a weighted average from the DFT data, *e.g.* in the case of cations:

$$L_{0K} = 2b_K = \frac{\int_{V_K}^{V\max} L dV}{V_{\max} - V_K} \quad (8)$$

where $L_{0K}$ is the average pore size accessible to cations, $L$ the pore size, $V_K$ the pore volume at which the pore size corresponds to the cation size, and $V_{max}$ is the total pore volume from the cumulative DFT distribution. Univalent cations are known to be electrosorbed into carbon micropores in the hydrated state, with the size of hydrated $K^+$ ions being between 0.362 and 0.421 nm [19]. The size of hydrated $OH^-$ ions is taken as 0.63 nm as suggested in [20]. Therefore, the value of $V_K$ has been selected to correspond to the pore size of 0.421 nm whereas $V_A$ corresponds to the pore size of 0.63 nm.

The gravimetric capacitance per cell can be calculated as

$$C_{cell} = C_-C_+/(C_- + C_+)/2 \quad (9)$$

If the value of effective dielectric permittivity $\varepsilon_r$ is considered equal for the two electrodes, which can be taken as a first approximation, this equation translates into

$$C_{cell} = \varepsilon_r C_0 \quad (10)$$

where $C_0 = \varepsilon_0[S_K/(b_K-a_{0K})*S_A/(b_A-a_{0A})]/[S_K/(b_K-a_{0K}) + S_A/(b_A-a_{0A})]/2$ represents the gravimetric capacitance per cell in vacuum, *i.e.* if ions in micropores had the above size, but were completely solvent-free. The effective dielectric permittivity was calculated by dividing the experimental values of $C_{cell}$ by $C_0$. The results (Table 2) reveal that between 700 and 800 °C $\varepsilon_r$ is nearly constant

**Table 2**
Textural properties and capacitance of carbons synthesized at a KOH/C ratio of 2.6 between 700 °C and 1000 °C with respect to the accessibility of electrolyte ions.

| Temperature | 700 °C | 750 °C | 800 °C | 1000 °C |
|---|---|---|---|---|
| $SSA_K$, $m^2 g^{-1}$ | 1815 | 1707 | 1929 | 1321 |
| $SSA_A$, $m^2 g^{-1}$ | 758 | 694 | 943 | 685 |
| $L_{0K}$, nm | 0.7 | 0.71 | 0.80 | 1.39 |
| $L_{0A}$, nm | 0.84 | 0.86 | 0.96 | 1.77 |
| $C_0$, $F g^{-1}$ | 20.6 | 17.6 | 23.4 | 3.69 |
| $C_{cell}$, $F g^{-1}$ | 44 | 43 | 54.5 | 35 |
| $\varepsilon_r$ | 2.1 | 2.4 | 2.3 | 9.5 |

**Table 1**
Properties of carbons synthesized between 700 and 1000 °C using a KOH/C ratio of 2.6 and the related response of supercapacitor cells.

| Temperature | 700 °C | 800 °C | 1000 °C |
|---|---|---|---|
| SSA (DFT), $m^2 g^{-1}$ | 1815 | 1929 | 1344 |
| $L_0$, nm | 0.7 | 0.8 | 1.38 |
| Oxygent content, at % | 9 | 9 | 6 |
| Volumetric Capacitance, $F cm^{-3}$ | 121 | 124 | 75 |
| Gravimetric Capacitance, $F g^{-1}$ | 176 | 218 | 140 |
| Capacitance retention, $C/C_0$. C at 20 $A g^{-1}$ over $C_0$ at 0.1 $A g^{-1}$ | 0.72 | 0.84 | 0.72 |
| Electrical conductivity, $S m^{-1}$ | 2 | 10 | 41 |
| ESR measured, Ω | 0.168 | 0.19 | 0.095 |
| ESR fitted, Ω | 0.148 | 0.13 | 0.081 |

independently of the size of subnanometer pores, which demonstrates that the increase in capacitance is due to the effect of both accessible SSA and related average pore size. On the contrary, the drop in the gravimetric capacitance between 800 and 1000 °C is much lower than expected from the vacuum-based capacitance, pointing to the increase in $\varepsilon_r$ due to the higher solvation of both ions in wider micropores (shifting average pore size from 0.8 and 1.4 nm). This conclusion agrees well with the theoretical work [21], demonstrating that a pore width-dependent dielectric permittivity may mitigate the dependence of capacitance on pore size, which is exactly observed in our case.

Apart from a purely electrostatic charge storage, the total capacitance of nanoporous carbons in aqueous electrolytes is usually affected by surface functional groups, which can add a non-negligible pseudocapacitive contribution to the overall measured capacitance, as studied in detail elsewhere for the whole range of pH values [22]. The C1s XPS spectrum (Fig. S2) contains a high binding energy tail, which can be ascribed to C-O single bonds. The XPS data (Table 1) show that the amount of oxygen decreases from 9 to 6 at. % on increasing the synthesis temperature, which reflects the partial removal of oxygenated functional groups at higher synthesis temperature. A similar amount of oxygen (about 8%) in other alkali-activated carbons was determined in Ref. [23] where the associated pseudocapacitive contribution was evaluated to be 11%, which can also be considered as a fair estimation for our carbons. Thus, the rise of about 25 % in the gravimetric capacitance (Table 1, samples of 700 °C and 800 °C) could be partially attributed to pseudocapacitance as already observed for other carbon materials in KOH electrolyte [20,23]. However, the evaluated contribution of pseudocapacitance is limited and does not significantly impact the overall capacitive response. Thus, it seems more reasonable to state that the features of porous networks and associated changes in the solvation of each ion are more likely to be at the origin of the significant alterations in the gravimetric capacitance. Additionally, the XPS spectra show the presence of carbon and oxygen only, which indicates that carbon surface is free of impurities.

Electrical conductivity is another parameter significantly affecting the rate capability, which depends strongly on the synthesis temperature [24]. Table 1 shows an about 20-time increase in the electrical conductivity when the synthesis temperature is raised from 700 °C to 1000 °C. This is related to the lower oxygen content and more order induced to the carbon structure. In our case, the improvements in electrical conductivity with synthesis temperature are not directly linked to the capacitance retention at increasing current density (Table 1). For this reason, impedance spectroscopy was used in an attempt to distinguish different contributions in the electrochemical response, in particular the conductivity of the material and the effect of pore size distribution. The intrinsic conductivity of the electrode materials is included in the equivalent series resistance (ESR, the high-frequency limit) whereas the inhomogeneous porosity is a main source of non-ideal ac response in the medium- and low-frequency regions. Pore size distribution can be particularly taken into consideration with an equivalent circuit (Fig. S3A) put forward to model the shape of the Nyquist plot of real porous electrodes [25]. It comprises 2 constant phase elements (CPE), with the first (CPE1) describing the deviation in slope from 45° in a Nyquist plot at intermediate frequencies while the second (CPE2) accounts for the non-ideality of the low-frequency vertical line characteristic of an ideal capacitor. The fitting results are provided in Fig S3B and Table 1, particularly showing that the fitted ESR values are quite close to the ones obtained from the experimental Nyquist plots. Importantly, there is a link between the ESR and the conductivity of the electrode materials, with more conductive electrode materials reasonably providing lower ESR values.

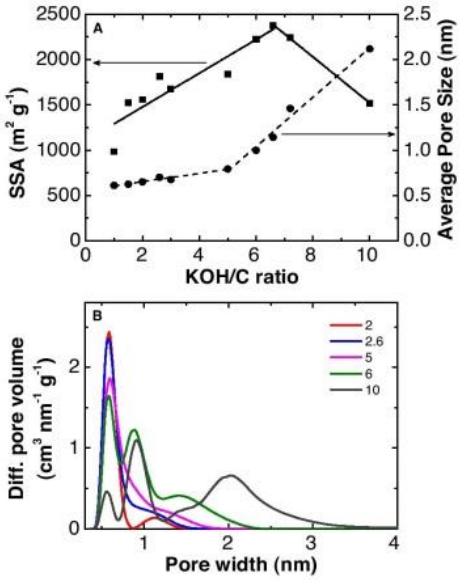


**Fig. 1.** Textural properties of activated carbons prepared at different KOH/C ratios. A. Specific surface area and average pore size. B. Pore size distribution.

On the practical side, the balance between volumetric capacitance and synthesis temperature suggests that 700 °C is the optimum temperature for carbon activation, and therefore, the alkali-to-carbon ratio was further optimized with the temperature set at 700 °C.

### 3.2. Effect of the alkali-to-carbon ratio

Fig. 1 shows the evolution of textural properties vs KOH/C ratio. As a general trend, the average pore size experiences almost linear growth with the KOH/C ratio, similarly to the data obtained for anthracites [13], but in our case the main porosity is represented by subnanometer pores until a KOH/C ratio of 5:1. However, for a higher KOH load, the linear trend changes slope, reflecting a stronger change in the average pore size with the KOH/C ratio. The DFT SSA also rises up to 2400 $m^2$ $g^{-1}$ for the KOH/C ratio of 6.6, but displays more deviation from linearity. The SSA drops for a higher KOH load, apparently as a result of excessive carbon burn–off, resulting in coalescing pore walls. The 2D NLDFT pore size distribution (Fig. 1B) reflects the trend observed in the average pore size, showing a progressive widening of porosity with a higher amount of large micropores for the samples prepared with more alkali. Notably, the gradual changes in the PSD are very minor, indicating a high controllability of the pore-widening procedure by adjusting the amount of alkali (as established elsewhere for

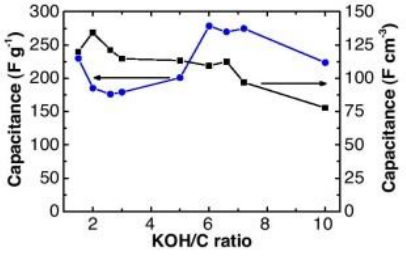


**Fig. 2.** Evolution of capacitance for carbons prepared at different KOH/C ratios.

other precursors [13] in a different range of pore size). The cyclic voltammograms in Fig. S4 confirm the typical capacitive behaviour of microporous carbons whereas Fig. 2 shows that gravimetric capacitance fluctuates with the maximum value corresponding to a KOH/C ratio of 6.6. At the same time, the maximum of volumetric capacitance ($135\,F\,cm^{-3}$) is observed at a KOH/C ratio of 2:1, decreasing for higher KOH loads. The dependence of the volumetric capacitance on the KOH/C ratio has an important practical implication: the high volumetric capacitance values correspond to a moderate KOH consumption (2:1) and low burn-off of the materials, making it easier to treat the wastewater and decrease the overall cost of the activation process.

Similarly to the case of the capacitance dependence on temperature, a closer look at the interplay between surface area, average pore size and ion solvation can clarify the fluctuating dependence of the gravimetric capacitance on the KOH/C ratio. As the dataset on alkali/carbon ratio is more complete than that on temperature, the capacitance of each individual electrode of a two-electrode cell was separately measured using a reference electrode. The experimental capacitance was further compared with the calculated capacitance in vacuum per electrode, e.g., for the positive electrode

$$C_+ = \varepsilon_{r+} C_{0+}, \tag{11}$$

$$\text{where } C_{0+} = \varepsilon_0 [S_A/(b_A - a_{0A})] \tag{12}$$

and $\varepsilon_{r+}$ is the effective dielectric permittivity in the pores of the positive electrode. Textural parameters are given in Table.S2. Fig. 3A shows that there is no clear relation between $C_+$ and $C_{0+}$, and $C_-$ and $C_{0-}$. This suggests that the dielectric permittivity is not constant and is strongly linked to the average pore size, in agreement with the previous finding for the series of carbons prepared at different temperatures. Fig. 3B shows that there exists a nearly linear correlation between the effective dielectric permittivity and the average pore size, apparently reflecting the fact that wider pores allow for more water molecules to surround ions. Inversely, the values of $\varepsilon_{r+}$ and $\varepsilon_{r-}$ are also consistent with the assumption of gradual ion desolvation when average pore size decreases [26]. Notably, the dielectric permittivity changes more significantly in the case of cation electrosorption ($\varepsilon_{r-}$). This suggests that solvation of $K^+$ ions is higher than that of $OH^-$ ions, undergoing more substantial transformation as the pore size increases. The absolute values also fall in the range suggested for the solvents surrounding ions in micropores [18,20].

As the next step in the evaluation of the suitability of olive-pits-derived carbons, the rate capability of cells built using carbons synthesized at 700 °C was probed. In this regard, it makes sense to relate not only the capacitance, but also the rate performance of supercapacitors to the textural properties of carbon materials. As supercapacitors are primarily focused on power delivery, the capacitance fading should be minimized as the current density increases. Fig. 4 shows that the capacitance retention improves in a broad range of current densities (up to $40\,A\,g^{-1}$) with increasing the KOH/C ratio, *i.e.* for the higher average pore size. Evidently, pores wider than solvated ion size allow less hindered ion transport at high rate, and the KOH/C ratio between 2.6 and 6 can be considered as the optimum in terms of capacitance and capacitance retention. More precisely, the corresponding accessible average pore size values for samples 2.6 and 6 (see Table S2) are about 25 % higher than the size of solvated ions (0.421 nm for $K^+$ and 0.63 nm for $OH^-$), thus arguing that pores about 25% wider than the size of solvated electrolyte ions provide the most effective high-rate operation in EDLCs.

In agreement with the literature, higher low-rate specific capacitance can be ensured by pores whose width is closer to the size of ions (*e.g.*, compare the volumetric capacitance of samples 2 and 6 and accessible average pore size, Fig. 2 and Table S2), which is in line with the literature reports that the capacitance increases due to partial ion desolvation, as particularly evidenced for organic electrolyte [27]. However, in this case the capacitance is less maintained at high current, *i.e.* where the discharge time corresponds to the practical requirements for supercapacitor applications (Fig. 4). The inset of Fig. 4 presents the capacitance dependence on the discharge time, which can be helpful in assessing the practical applicability of developed carbons in basic aqueous electrolytes. Notably, for practical applications important capacitance values are kept up in the time domain of real supercapacitor operation (discharge time $<10$ s).

Importantly, the capacitance retention drops if the accessible pore size significantly surpasses the size of solvated ions (compare materials 6 and 10, Fig. 4 and Table S2). Thus, there exists an optimum pore size value, *i.e.* important capacitance values at low discharge time are delivered by the carbons whose pores are moderately wider than solvated ion size.

A more detailed look into the existence of optimum pore size with regard to capacitance retention can be taken by assessing the

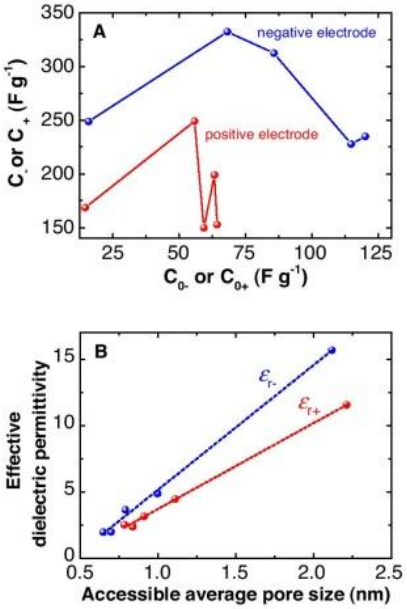


**Fig. 3.** Influence of solvation on capacitance of separate electrodes. A. Capacitance of each electrode vs its corresponding capacitance in vacuum. B. Dielectric permittivity vs accessible average pore size.

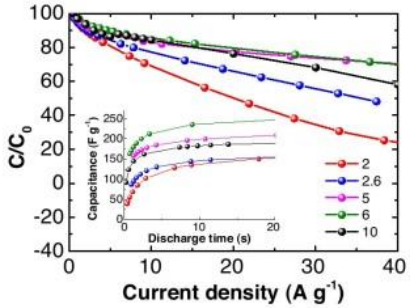


**Fig. 4.** Rate capability of supercapacitors based on microporous carbons from olive pits. Numbers refer to the KOH/C ratio. The inset shows the gravimetric capacitance vs discharge time.

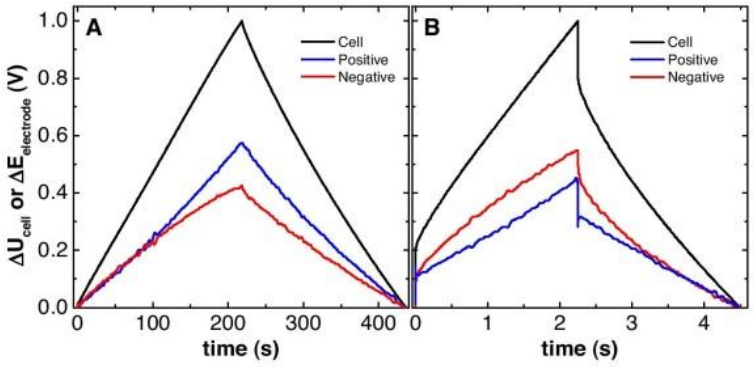


**Fig. 5.** Galvanostatic charge/discharge profile for individual electrodes of the cell built with carbon 6 at different current densities. A. 0.5 A $g^{-1}$. B. 30 A $g^{-1}$.

electrochemical response of individual electrodes. On the basis of the equivalence of charges stored in the positive and negative electrodes of a two-electrode cell, the relationship between the capacitance values of the negative and positive electrodes can be set as:

$$\frac{C_-}{C_+} = \frac{\Delta E_+ \cdot m_+}{\Delta E_- \cdot m_-} \quad (13)$$

Fig. 5 shows the GA charge/discharge profiles of the cell built with the carbon synthesized with a KOH/C ratio of 6. As can be easily noticed, the potential evolution of the negative electrode is lower at a low current density (0.5 A $g^{-1}$), which points to the higher capacitance of the negative electrode. However, the trend is reversed at a higher rate according to equation (13). Fig. 6 shows the evolution of the $C_-/C_+$ relationship with the current density for selected carbon samples differing in the average pore size. Again, it can be clearly seen that $C_-/C_+$ exceeds unity at low current density, but falls for high current densities (below unity for sample 10 at 10 A $g^{-1}$), demonstrating that electrosorption of $OH^-$ ions is favoured over that of $K^+$ ions at a high current density. This effect can be reasonably explained on the basis of the differences in solvation as inferred by the data on dielectric permittivity: the higher solvation of $K^+$ ions may reduce their mobility more than that of $OH^-$ ions, which results in more hindrance to the high-rate transport of potassium ions as compared to hydroxyl ions. Thus, the rate response of gravimetric capacitance appears to depend on the relation amongst ion size, SSA, average pore size and solvation: smaller ions can access a higher portion of SSA, increasing the capacitance, but the pore size related to accessible surface of the electrode should not be disproportionately large so as to prevent excessive solvation, which slows down ion transport. Additionally,

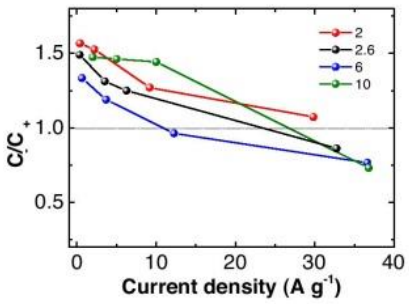


**Fig. 6.** Capacitance ratio of the negative and positive electrodes vs. current density.

a minor pseudocapacitive contribution, possibly appearing at the negative electrode only, can also deteriorate the rate capability, which is usually inferior for pseudocapative systemes due to the higher resistivity inherent in Faradaic charge transfer processes compared to electrosorption [2]. In practical terms, the negative electrode has been identified as the source of capacitance loss in the studied series of microporous carbons at high current density values.

## 4. Conclusions

We have shown that an efficient supercapacitor electrode material can be prepared by the chemical activation of carbon derived from an abundant renewable material - olive pits. Volumetric capacitance values of about 140 F $cm^{-3}$ can be reached at a relatively low KOH/C ratio (less than 3) with good capacitance retention at extremely high current load (up to 40 A $g^{-1}$) and low discharge time (about 1 s). Capacitive rate performance is seemingly controlled by pore-width-dependent ion solvation: moderate solvation contributes to enhancing capacitance while excessive solvation in large micropores worsens capacitance retention at the high-rate.

## Acknowledgments

The work was supported by the Basque Government under the Etortek Energigune'12 Program. The kind donation of crushed olive pit samples from AESA (Agropecuaria Ecológica Sierra de Alcaraz, Albacete, Spain) is gratefully acknowledged. The authors also thank Dr. Oleksandr Bondarchuk from CIC EnergiGUNE for taking XPS spectra and Dr. Iñaki Orue from the University of The Basque Country for his support and guidance during the measurement of electrical conductivity.

## Appendix A. Supplementary data

Supplementary data associated with this article can be found, in the online version, at http://dx.doi.org/10.1016/j.electacta.2015.02.006.

## References

[1] F. Béguin, E. Frackowiak, Carbons for Electrochemical Energy Storage and Conversion Systems (Advanced Materials and Technologies), CRC Press, Boca Raton, 2010.
[2] P. Simon, Y. Gogotsi, Nanostructured activated carbons from natural precursors for electrical double layer capacitors, Nat. Mater. 7 (11) (2008) 845–854.
[3] H. Itoi, H. Nishihara, T. Kogure, T. Kyotani, Three-Dimensionally Arrayed and Mutually Connected 1. 2-nm Nanopores for High-Performance Electric Double Layer Capacitor, JACS 133 (5) (2011) 1165–1167.

[4] J.K. McDonough, A.I. Frolov, V. Presser, J. Niu, C.H. Miller, T. Ubieto, M.V. Federov, Y. Gogotsi, Influence of the structure of carbon onions on their electrochemical performance in supercapacitor electrodes, Carbon 50 (9) (2012) 3298–3309.
[5] Y. Zhu, S. Murali, M.D. Stoller, K.J. Ganesh, W. Cai, P.J. Ferreira, A. Pirkle, R.M. Wallace, K.A. Cychosz, M. Thommes, D. Su, E.A. Stach, R.S. Ruoff, Carbon-based supercapacitors produced by activation of graphene, Science 332 (6037) (2011) 1537–1541.
[6] L. Wei, G. Yushin, Nanostructured activated carbons from natural precursors for electrical double layer capacitors, Nano Energy 1 (4) (2012) 552–565.
[7] S. Román, J.F. González, C.M. González-García, F. Zamora, Control of pore development during $CO_2$ and steam activation of olive stones, Fuel Processing Technology 89 (8) (2008) 715–720.
[8] F. Rodriguez-Reinoso, M. Molina-Sabio, Activated carbons from lignocellulosic materials by chemical and/or physical activation: an overview, Carbon 30 (7) (1992) 1111–1118.
[9] M.T. González, M. Molina-Sabio, F. Rodríguez-Reinoso, Steam activation of olive stone chars, development of porosity, Carbon 32 (8) (1994) 1407–1413.
[10] F. Rodríguez-Reinoso, M. Molina-Sabio, M.T. Gonzalez, The use of steam and CO2 as activating agents in the preparation of activated carbons, Carbon 33 (1) (1995) 15–23.
[11] C. Moreno-Castilla, F. Carrasco-Marın, M.V. López-Ramón, M.A. Alvarez-Merino, Chemical and physical activation of olive-mill waste water to produce activated carbons, Carbon 39 (9) (2001) 1415–1420.
[12] M. Molina-Sabio, M.T. Gonzalez, F. Rodriguez-Reinoso, A. Sepúlveda-Escribano, Effect of steam and carbon dioxide activation in the micropore size distribution of activated carbon, Carbon 34 (4) (1996) 505–509.
[13] M.A. Lillo-Ródenas, D. Lozano-Castelló, D. Cazorla-Amorós, A. Linares-Solano, Preparation of activated carbons from Spanish anthracite: II. Activation by NaOH, Carbon 39 (5) (2001) 751–759.
[14] J. Jagiello, J. Oliver, 2D-NLDFT adsorption models for carbon slit-shaped pores with surface energetical heterogeneity and geometrical corrugation, Carbon 55 (2013) 70–80.
[15] J. van der Pauw, A method of measuring specific resistivity and Hall effect of discs of arbitrary shape, Philips Research Reports 13 (1958) 1–9.
[16] O. Barbieri, M. Hahn, A. Herzog, R. Kötz, Capacitance limits of high surface area activated carbons for double layer capacitors, Carbon 43 (6) (2005) 1303–1310.
[17] J. Huang, B.G. Sumpter, V. Meunier, A Universal Model for Nanoporous Carbon Supercapacitors Applicable to Diverse Pore Regimes, Carbon Materials, and Electrolytes, Chem. Eur. J. 14 (22) (2008) 6614–6626.
[18] G. Feng, R. Qiao, J. Huang, B.G. Sumpter, V. Meunier, Ion Distribution in Electrified Micropores and its role in the anomalous Enhancement of Capacitance, ACS Nano 4 (4) (2010) 2382–2390.
[19] L. Eliad, G. Salitra, A. Soffer, D. Aurbach, Ion Sieving Effects in the Electrical Double Layer of Porous Carbon Electrodes: Estimating Effective Ion Size in Electrolytic Solutions, J. Phys. Chem. B 105 (29) (2001) 6880–6887.
[20] A. Garcia-Gomez, V. Barranco, G. Moreno-Fernandez, J. Ibañez, T.A. Centeno, J.M. Rojo, Correlation between Capacitance and Porosity in Microporous Carbon Monoliths, J. Phys. Chem. C 118 (10) (2014) 5134–5141.
[21] S. Kondrat, A. Kornyshev, F. Stoeckli, T.A. Centeno, The effect of dielectric permittivity on the capacitance of nanoporous electrodes, Electrochem. Comm. 34 (2013) 348–350.
[22] H. Andreas, B.E. Conway, Examination of the double-layer capacitance of an high specific-area C-cloth electrode as titrated from acidic to alkaline pHs, Electrochim. Acta 51 (28) (2006) 6510–6520.
[23] V. Ruiz, C. Blanco, E. Raymundo-Piñero, V. Khomenko, F. Béguin, R. Santamaría, Effects of thermal treatment of activated carbon on the electrochemical behaviour in supercapacitors, Electrochim. Acta 52 (15) (2007) 4969–4973.
[24] J. Sánchez-González, F. Stoeckli, T.A. Centeno, The role of the electric conductivity of carbons in the electrochemical capacitor performance, J. Electroanal.Chem 657 (2011) 176–180.
[25] H.-K. Song, H.-Y. Hwang, K.-H. Lee, Le H. Dao, The effect of pore size distribution on the frequency dispersion of porous electrodes, Electrochimica Acta 45 (2000) 2241–2257.
[26] T. Centeno, F. Stoeckli, Surface-related capacitance of microporous carbons in aqueous and organic electrolytes, Electrochim. Acta 56 (21) (2011) 7334–7339.
[27] J. Chmiola, C. Largeot, P.L. Taberna, P. Simon, Y. Gogotsi, Desolvation of Ions in Subnanometer Pores and Its Effect on Capacitance and Double-Layer Theory, Angew. Chem. Int. Ed. 47 (18) (2008) 8020–8024.

**SUPPLEMENTARY MATERIAL**

# Effect of pore texture on performance of activated carbon supercapacitor electrodes derived from olive pits

Edurne Redondo[a], Javier Carretero-González[a], Eider Goikolea[a], Julie Ségalini[a], Roman Mysyk[a]*

[a]CIC energiGUNE, Parque Tecnológico de Álava, Albert Einstein 48, 0150 Miñano, Spain

*Corresponding author. Tel.: +34 94 529 71 08. E-mail address: rmysyk@cicenergigune.com.

**Table S1.** Yield of activation at 700 °C vs. KOH/carbon ratio.

| KOH/carbon ratio | 1.5 | 2 | 2.6 | 3 | 5 | 6 | 6.6 | 7.2 | 10 |
|---|---|---|---|---|---|---|---|---|---|
| Activation yield, % | 95 | 84 | 75 | 70 | 70 | 65 | 65 | 53 | 38 |

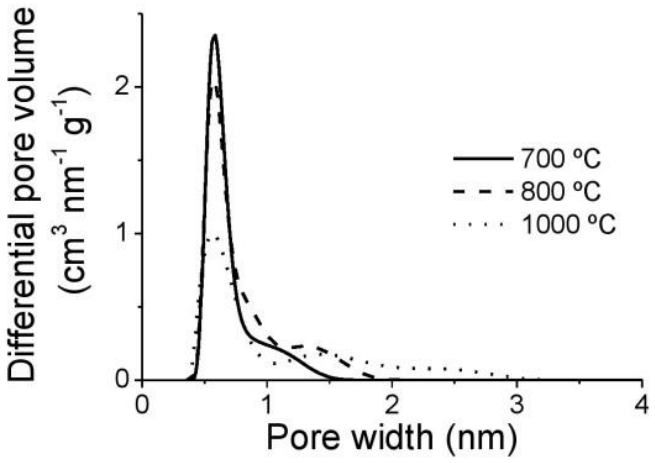


(a)

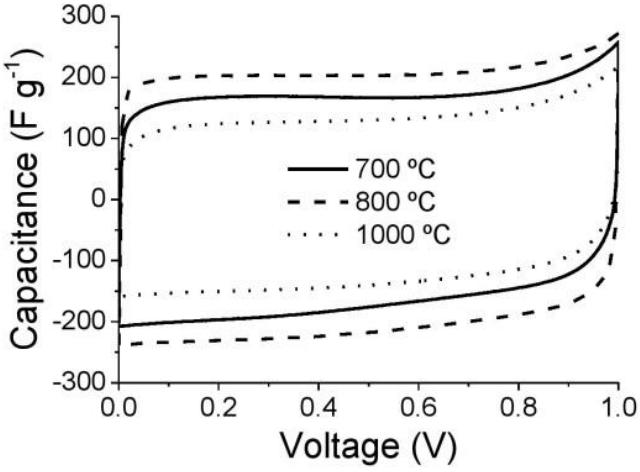


(b)

Figure S1. Textural properties and electrochemical response of activated carbons produced at different activation temperatures. a) Pore size distribution; b) Cyclic voltammograms of symmetric supercapacitors cells built with 6M KOH electrolyte.

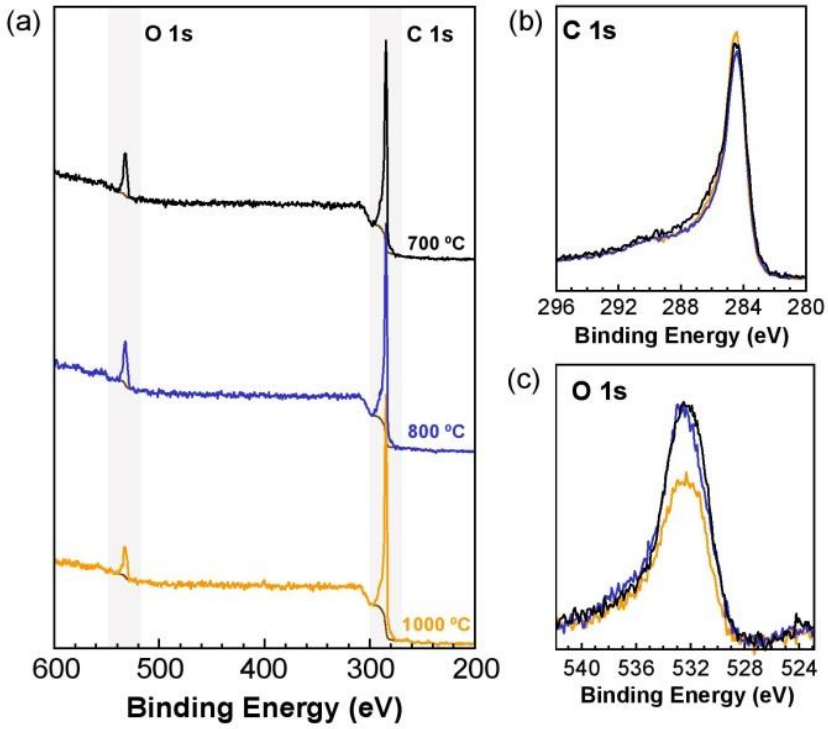


Figure S2. XPS analysis. Survey (a), C1s (b) and O1s (c) spectra for carbons prepared using a KOH/C ratio of 2.6 at different temperatures.

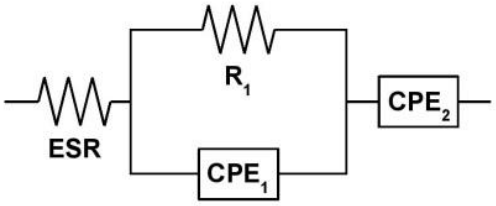


(a)

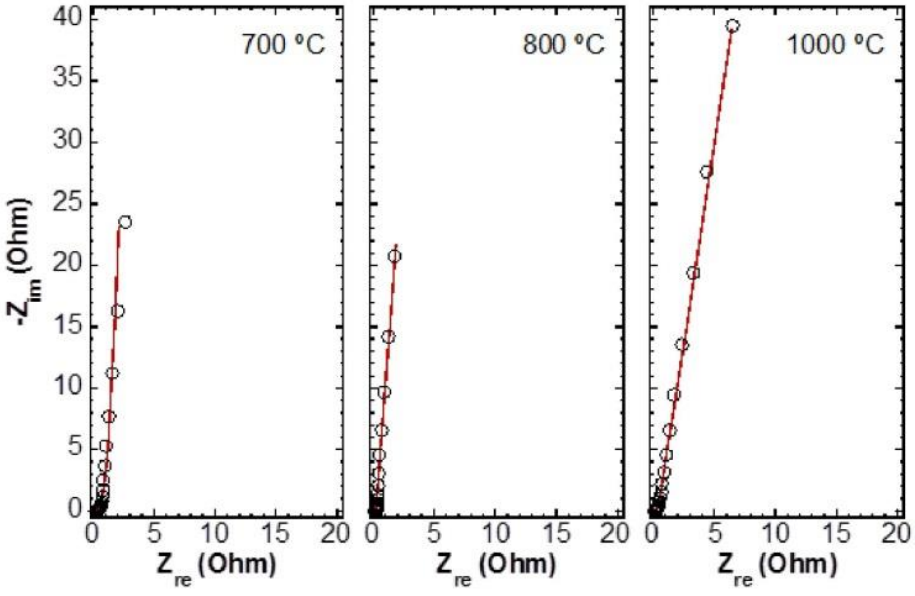


(b)

Figure S3.Impedance spectroscopy. a) The equivalent circuit selected for fitting experimental data; b) Comparison between experimental and fitted Nyquist plots.

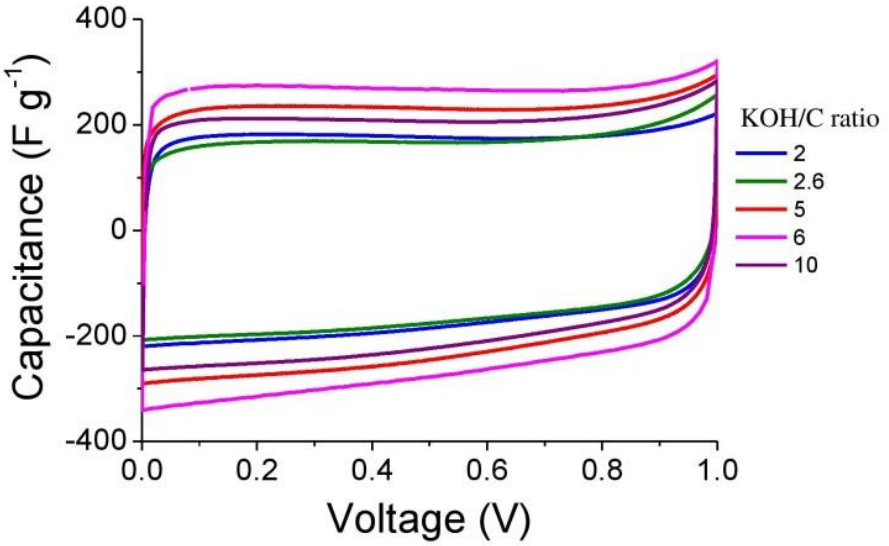


Figure S4. Cyclic voltammograms of symmetric supercapacitors cells (scan rate 5 mV $s^{-1}$) built with 6M KOH electrolyte for the materials synthesized at different KOH/C ratios.

**Table S2**. Textural properties and capacitance of selected carbons synthesized at different KOH/carbon ratios with respect to the accessibility of electrolyte ions.

| ***KOH/carbon ratio*** | ***2*** | ***2.6*** | ***5*** | ***6*** | ***10*** |
|---|---|---|---|---|---|
| $SSA_K$, $m^2\ g^{-1}$ | *1558* | *1815* | *1798* | *2224* | *1519* |
| $L_{0K}$, *nm* | *0.65* | *0.7* | *0.79* | *1.00* | *2.11* |
| $C_{0-}$, $F\ g^{-1}$ | *120* | *115* | *86* | *68* | *16* |
| $C_-$, $F\ g^{-1}$ | *235* | *228* | *312* | *332* | *248* |
| $\varepsilon_{r-}$ | *1.96* | *1.98* | *3.64* | *4.87* | *15.68* |
| $SSA_A$, $m^2\ g^{-1}$ | *518* | *758* | *1005* | *1517* | *1302* |
| $L_{0A}$, *nm* | *0.79* | *0.84* | *0.91* | *1.11* | *2.21* |
| $C_{0+}$, $F\ g^{-1}$ | *59* | *64* | *63* | *58* | *14* |
| $C_+$, $F\ g^{-1}$ | *150* | *153* | *199* | *249* | *169* |
| $\varepsilon_{r+}$ | *2.52* | *2.38* | *3.14* | *4.46* | *11.56* |

## 5.2 Relation between textural properties and capacitive rate response of microporous carbon electrodes in acetonitrile-based supercapacitors under opposite polarization

Electrochimica Acta 293 (2019) 496–503

Contents lists available at ScienceDirect

Electrochimica Acta

journal homepage: www.elsevier.com/locate/electacta

# Relation between texture and high-rate capacitance of oppositely charged microporous carbons from biomass waste in acetonitrile-based supercapacitors

Edurne Redondo [1], Julie Ségalini, Javier Carretero-González [2], Eider Goikolea*, Roman Mysyk**

*CICenergiGUNE, Arabako Teknologi Parkea, calle Albert Einstein 48, 0150, Miñano, Spain*

ARTICLE INFO

*Article history:*
Received 30 July 2018
Received in revised form
27 September 2018
Accepted 6 October 2018
Available online 10 October 2018

*Keywords:*
Supercapacitors
Microporous carbons
Organic electrolyte
Rate capability
Biomass

ABSTRACT

A biomass-derived activated carbon with a systematic control over the pore size distribution is used to decode the effect of pore size distribution on charge dynamics in organic acetonitrile-based supercapacitors. Distinct trends in the high-current capacitance of the positive and negative electrodes are revealed by isolating the ion-specific accessible pore width and specific surface area from the total values calculated on the basis of low-temperature nitrogen adsorption/desorption isotherms. A size match between ions and pores for each separate electrode is established to maximize gravimetric capacitance under high current load. Most importantly, the high-current gravimetric capacitance demonstrates the existence of an optimum micropore width depending on polarization as well as no need for wide micropores or mesopores for ensuring rapid capacitive response.



## 1. Introduction

Electrical double-layer capacitors (EDLCs) are electrochemical power sources working through non-Faradaic electrostatic attraction of ions from an electrolyte to an electrode's surface [1]. EDLCs compare favorably with other electrochemical energy storage technologies in multiple respects, particularly offering almost infinite cycle life as well as high discharge and especially charge rates. Nowadays they are used as both independent and complementary power sources [2], but their main drawback is the low energy density, typically about 5 Wh $kg^{-1}$ for packaged devices [2]. The maximum energy density of a supercapacitor cell can be calculated in either gravimetric or volumetric terms

$$E = 0.5CU^2/3.6$$

where E is the energy density defined gravimetrically (Wh $kg^{-1}$) or volumetrically (Wh $L^{-1}$), C - the capacitance per cell mass or volume (F $g^{-1}$ or F $cm^{-3}$), U – the cell voltage (V).

The gravimetric energy density depends on gravimetric capacitance being governed by areal capacitance (typical values about up to 5–10 μF $cm^{-2}$ [3]) and specific surface area (SSA), which is typically about 1000–2000 $m^2$ $g^{-1}$ for activated microporous carbons (ACs), industrial EDLC materials. As a result, characteristic values of non-Faradaic gravimetric capacitance are commonly comprised between 100 and 200 F $g^{-1}$ depending on the specific AC and the electrolyte. ACs have been traditionally produced from fossil fuels and derived products, but the poorly renewable character of such precursors has intensified the alternative use of abundant biomass waste [4]. Commercialized EDLC materials from renewable waste are often ACs from coconut shell [5].

The optimization of EDLCs is particularly hindered by a non-sufficient understanding of electrosorption in micropores. The size, shape, length and tortuosity of pores as well as surface chemistry and defects all influence capacitive performance, but their relative contributions have yet to be fully clarified. Much

* Corresponding author. Present address: Inorganic Chemistry Department, University of the Basque Country, P.O. Box 644, 48080, Bilbao, Spain.
** Corresponding author. CIC energiGUNE, Arabako Teknologi Parkea, calle Albert Einstein 48, 01510, Miñano, Spain.
*E-mail addresses:* eider.goikolea@ehu.eus (E. Goikolea), rmysyk@cicenergigune.com (R. Mysyk).
[1] Present address: National Graphene Institute, University of Manchester, Oxford Road, Manchester M13 9PL, UK.
[2] Present address: Institute of Polymer Science and Technology, ICTP-CSIC, Juan de la Cierva 3, 28006, Madrid, Spain.

https://doi.org/10.1016/j.electacta.2018.10.031
0013-4686/

theoretical and experimental effort has also been pursued on the dynamics of charge storage in ACs, particularly including *in-situ* and *ex-situ* studies [6–12]. However, even most common textural parameters such as specific surface area (SSA) and pore size (width) are not easy to establish with high certainty since various treatments of adsorption data can be applied, which leads to controversial views on how textural properties influence areal capacitance [13–15]. From the practical perspective, not only is capacitance important, but rather its retention under high current load. This is further complicated by opposite polarization making the capacitance retention of the same AC in a symmetric cell different due to the build-up of dissimilar oppositely charged ions. The relation between high-rate capacitance under oppositely directed polarization and textural parameters is therefore essential but is less explicitly studied. In this work, we aim primarily at relating the high-rate capacitance of organic-based supercapacitor cells and their separate constituent electrodes with the textural properties of carbons. We use activated carbons from agricultural olive mill waste (previously also studied in aqueous alkali electrolyte [16]). They also present a particular interest for understanding non-Faradaic capacitance in micropores since they stand out of other microporous carbons owing to their unusually good capacitive response recently evidenced in room-temperature ionic liquid electrolyte, yet for unknown reasons [17]. To decode the maximum performance reachable under high-current conditions for real-world EDLCs, this work is based on industrial organic electrolyte. Accessible SSA and accessible pore size were isolated for the positive and negative electrodes using carbons with systematically tailored pore size distributions.

## 2. Experimental

### 2.1. Preparation of microporous carbons

The activation of carbons was conducted as described elsewhere [16]. Briefly, solid KOH was physically mixed with the char in a varied ratio and placed in an Inconel© boat inside a horizontal stainless steel tube within a tubular furnace. Activation was conducted by heat-treatment under an Ar flow of 100 mL $min^{-1}$ with a heating ramp rate of 5 °C $min^{-1}$and the dwell time of 2 h at 700 °C. The samples were washed off with a diluted solution of hydrochloric acid and water until neutral pH and then dried at 120 °C under vacuum until constant mass.

### 2.2. Textural characterization of carbons

Nitrogen adsorption/desorption isotherms were acquired at −195.8 °C using Micromeritics ASAP 2020 for relative pressure ($P/P_0$) between $10^{-8}$ and 0.995 for samples preliminarily outgassed for 8 h at 200 °C. The SSA values and pore size distribution were derived from the 2D Non-Local Density Functional Theory (2D NLDFT) treatment of $N_2$ adsorption isotherms using software SAEIUS [18]. The average pore size nitrogen-accessible ($L_0$) was evaluated as a weighted average from the DFT data:

$$L_0 = \frac{\int_{V\min}^{V\max} L dV}{V_{\max} - V_{\min}} \quad (1)$$

where $V_{max}$ and $V_{min}$ are the total pore volume and the pore volume at the minimum pore size, correspondingly, L the pore size corresponding to the running total of volume V. For comparison purposes, SSA was also calculated by the BET method (Table S1).

### 2.3. Electrode preparation and electrochemical measurements

Electrodes were prepared by homogenizing and plasticizing a mixture of carbon (95 wt %) and polytetrafluorethylene (PTFE) used as a binder (5 wt %, from a 60 wt % aqueous dispersion). The plastic mass was then rolled to a ~150 μm thick film dried under vacuum at 120 °C overnight. Disk-shaped electrodes of 11 mm in diameter were cut out and their thickness was measured again. The electrode mass loading was ~7 mg $cm^{-2}$. Two-electrode symmetric supercapacitor cells were assembled in a Nylon Swagelok® airtight system using two identical carbon electrodes, two titanium current collectors (from Caldereria Juncal, Vitoria-Gasteiz, Spain), and a porous Celgard® 2500 membrane separator (from Celgard) in a glove-box under argon atmosphere with less than 1 ppm of $O_2$ and $H_2O$. A standard organic electrolyte, 1.5 M tetraethylammonium tetrafluoroborate in anhydrous acetonitrile ($TEA^+$ $BF_4^-$/ACN) was used. An Ag wire based quasireference electrode was introduced into two-electrode cells for separately tracking the potential evolution of each electrode whereas the cell voltage was controlled. The symmetric cells were cycled under constant-current charge/discharge (1 A $g^{-1}$) for at least 20 cycles between 0 and 2.7 V to stabilize the reading of discharge time (*i.e.* capacitance). At least 3 parallel cells were run for each carbon. The deviation of capacitance values is ≤ 10% in parallel measurements. Capacitance values were averaged out from 3 parallel measurements.

Cyclic voltammetry (CV) and constant-current (galvanostatic, GA) charge-discharge cycling were conducted using a multichannel VMP3 potentiostat/galvanostat (Biologic, France). Capacitance was calculated for the cell and each separate electrode as detailed previously in Ref. [16] (also see Eqs. (S1)–(S4)).

The electrical conductivity (Table S1) was evaluated with the van der Pauw four-probe method [19] using the exact same pelletized PTFE-bound electrodes employed for the assembly of supercapacitor cells.

## 3. Results and discussion

### 3.1. Textural properties related to accessibility of pores by ions of organic electrolyte

An adequate assessment of the effective SSA is of utmost importance for the correct determination of areal capacitance [20–22]. More importantly, the SSA accessible to each type of electrolyte ions is relevant to electrosorption rather than the total SSA measured with $N_2$ or Ar gases. We calculated the accessible SSA from the cumulative 2D NLDFT SSA, only counting the pores wider than the ion size. The adopted ion size is 0.68 nm for $TEA^+$ and 0.48 nm for $BF_4^-$ according the partial desolvation of ions in the narrowest electrolyte-accessible micropores [23]. The accessible surface area in each electrode can be estimated as

$$S_C = S - S_{0.68} \quad \text{and} \quad S_A = S - S_{0.48}\,, \quad (2)$$

where $S_C$ and $S_A$ is the SSA accessible to cations and anions, correspondingly; *SSA* is the total specific surface area accessible to nitrogen ($m^2$ $g^{-1}$), $S_{0.68}$ *and* $S_{0.48}$ is the surface area of pores narrower than the counterion size (0.68 and 0.48 nm for the negative and positive electrodes, correspondingly).

Fig. 1A shows that $S_C$ is 3–5 times lower than SSA for the KOH/C ratio below 5. This comparison demonstrates clearly that trustworthy SSA estimations are vital to rigorously address the dependence of capacitance on SSA with some specific ions such as $TEA^+$.

In the same way, we also consider the average pore size (APS) accessible to specific ions. This is a more realistic value than nitrogen-accessible APS (calculated, for example, using the

Dubinin-Radushkevich equation [24]). The average pore size accessible to cations ($L_{0C}$) and anions ($L_{0A}$) was calculated as a weighted average from the DFT data:

$$L_{0C} = 2b_C = \frac{\int_{V_{0.68}}^{V\max} LdV}{V_{\max} - V_{0.68}} \quad L_{0A} = 2b_A = \frac{\int_{V0.48}^{V\max} LdV}{V_{\max} - V_{0.48}} \tag{3}$$

where $V_{0.68}$ *and* $V_{0.48}$ are the pore volume built up by pores narrower than the size of partially desolvated cation and anions, correspondingly, $b_C$ and $b_A$ - the average half-pore width pertaining to $TEA^+$- and $BF_4^-$-accessible porosity.

Fig. 1B shows clearly a substantial deviation in the sub-nanometer size region between the cation-accessible APS and that measured from the total pore size range.

For applying those data to the characterization of supercapacitors, it is important to address the uncertainties in adsorption data. $N_2$ adsorbate can have diffusion-limited access to ultramicroporosity in carbon materials at 77 K [25], and combined $CO_2$/$N_2$ adsorptions study is usually recommended [26,27]. However, Fig. S1 demonstrates only minor differences between the cumulative SSA curves derived using either $N_2$ only or $CO_2$/$N_2$ combined treatment for carbons with narrow ultramicroporosity. This indicates that $CO_2$ analysis cannot be considered critical for the characterization of the particular series of carbons under study. Another uncertainty pertains to the pore size distribution that can be altered with the chosen DFT model, e.g., NLDFT and QSDFT, and the adopted pore shape [28]. However, the deviations in cumulative SSA do not usually exceed 10% [28], which is within a fairly acceptable error range, also comparable to the error in capacitance. Finally, the assessment of porosity can also be altered by the binder [22,29,30], but its effect is minor in our study as evidenced from the comparison between the powdered AC and the PTFE-bound electrodes (Fig. S2). Thus, the textural properties calculated on the basis of $N_2$ adsorption/desorption isotherms of powdered activated carbons can be deemed correct and reliable for further analysis.

### 3.2. Dependence of capacitive response on textural properties of carbons

The voltammogramms of two-electrode supercapacitor cells (Fig. 2 A) demonstrate clearly a decreasing capacitance at about the high voltage limit for $L_{0C} \leq 1$ nm (red line), which is detrimental to supercapacitor operation and can be alternatively explained as either the "ion-sieving" or "surface saturation" effects [31–33]. By contrast, cyclic voltammogramms regain the rectangular shape of a typical supercapacitor for $L_{0C} \geq 1$ nm (Fig. 2A). The discrepancies between $L_{0C}$ and $L_0$ (Fig. 1B) show clearly that the capacitive response of carbons can be associated with a systematically lower $L_0$ than the effective ion-accessible APS value ($L_{0C}$), leading to a

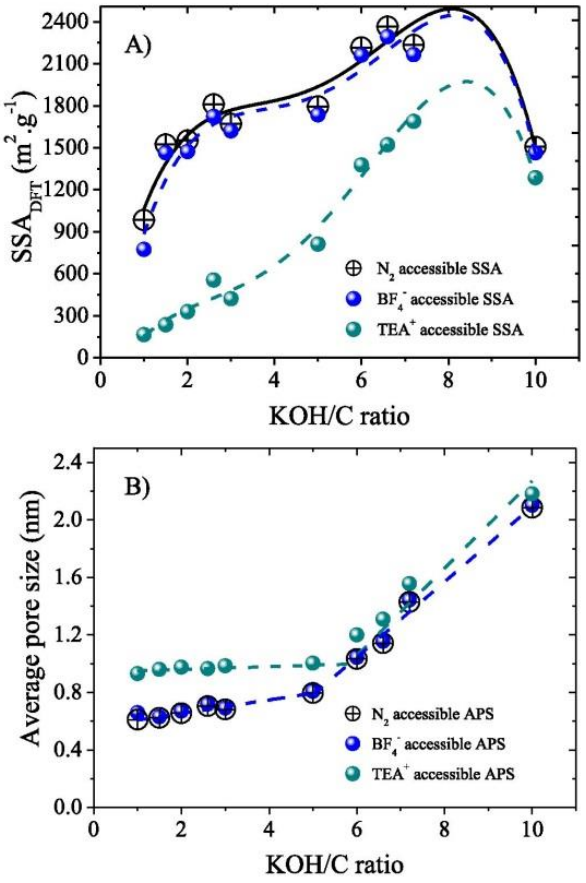


**Fig. 1.** SSA and APS of activated carbons prepared at different KOH/C ratios with respect to $N_2$, $TEA^+$ and $BF_4^-$ species. A) Accessible specific surface vs KOH/C ratio; B) Accessible pore size vs KOH/C ratio. The lines are plotted to guide the eye only.

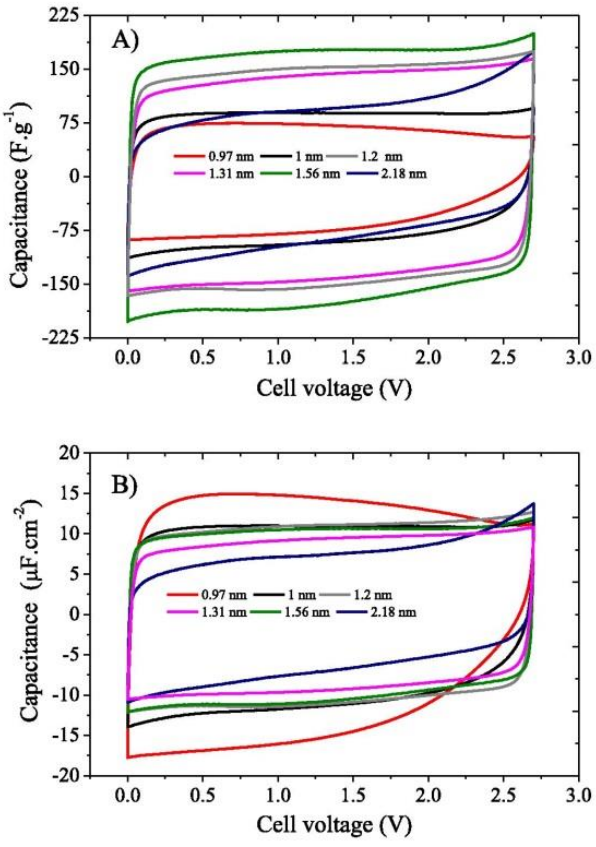


**Fig. 2.** Cyclic voltammograms for carbons with porosity differently accessible to $TEA^+$-ions: A) Gravimetric capacitance; B) Surface capacitance per $TEA^+$-accessible specific surface area. Scan rate = 5 mV s$^{-1}$. The numbers refer to $L_{0C}$.

misinterpretation of electrochemical data. It can also be remarked that the capacitance decay appears for $L_{0C}$ higher than the size of partially desolvated $TEA^+$ ions (0.68 nm) [13], which may be an indication that the removal of the close solvation shell is hindered on the timescale of voltammetry experiments.

Fig. 2B presents capacitance normalized by $S_C$ to establish the effect of pore size by removing the contribution of SSA and compare the results with other works [15,22,30]. Fig. 2B demonstrates clearly that cyclic voltammogramms almost overlap at a capacitance of *ca.* 10 μF cm$^{-2}$ for $L_{0C} > 1$ nm, with somewhat smaller values for the sample with APS above 2 nm. Notably, the capacitance of 10 μF cm$^{-2}$ is close to values for microporous carbons [15,30,34], exohedral carbons [35], and graphene [36]. The slight decrease in capacitance for about 2 nm-wide pores is also in agreement with recent theoretical predictions [37], suggesting the lower capacitance for the narrowest mesopores.

The initial capacitance exceeds 10 μF cm$^{-2}$ for carbons exhibiting a decrease in the capacitive current as observed elsewhere [32,33], and was associated with a virtually full coverage of TEA-accessible surface with cations. However, the values in Fig. 2B are based on the average capacitance per electrode of a two-electrode system, which assumes the same capacitance of the positive and negative electrodes. In fact, the gravimetric capacitance of the electrodes can be quite dissimilar because the pore size distribution can differently restrict access to differently sized ions.

Therefore, a more precise information on capacitance is needed for separate electrodes, which can be extracted using a quasi-reference electrode in a full symmetric cell. The areal capacitance of each electrode, $C_{exp-}/S_C$ and $C_{exp+}/S_A$, can be directly calculated by dividing the experimental gravimetric capacitance of the corresponding electrode by the values derived according to Eq. (2).

Fig. 3A presents the dependence of areal capacitance on the effective distance between the charges, which can be defined as:

$$d_{\text{eff}} = b - a_0, \tag{4}$$

where $d_{eff}$ – the effective distance between electronic and ionic charges, $b$-the accessible pore half-width ($b = b_C$ for the negative electrode and $b_A$ for the positive electrode), $a_0$ – the corresponding ion radius.

Fig. 3A shows that the capacitance of the positive electrode is nearly constant and equals ~5 μF cm$^{-2}$ at a current density of 1 A g$^{-1}$ (chosen as an example), independently of the average accessible pore size. By contrast, the value for the negative electrode is greatly enhanced for the smallest $d_{eff}$ (therefore, the smallest APS). In this case, the calculated capacitance value is given for the straight portion of the galvanostatic discharge curve, excluding its distortion due to hindered ion transport in the vicinity of the lowest potential of the negative electrode.

The capacitance of a non-Faradaic carbon electrode as a sum of components [38], which can be rewritten for comparison with our experimental data as:

$$\frac{S_a}{C_{\text{exp}}} 10^2 = \frac{1}{C_q} + \frac{1}{C_H} + \frac{1}{C_{dl}}, \tag{5}$$

where $S_a$ – accessible SSA depending on the ion size, m$^2$ g$^{-1}$, *i.e.* $S_C$ or $S_A$; $C_{exp}$ is the experimentally measured capacitance, F g$^{-1}$; $10^2$ is the factor for unit conversion to μF cm$^{-2}$, $C_q$ – solid-side capacitance component in semiconductor electrodes (it is a quantum capacitance (graphene) [39] or space-charge capacitance (graphite [40])), μF cm$^{-2}$; $C_H$ – the gravimetric capacitance of the compact double layer, μF cm$^{-2}$; $C_{dl}$ – the capacitance of the diffuse ionic layer, μF cm$^{-2}$.

The value of $C_q$ for ACs can be estimated knowing that biomass-derived ACs are usually made up of isotropic, three-dimensional networks of wrinkled one-atom-thick graphene sheets [41]. Therefore, the quantum capacitance values for graphene can be taken as a guideline. The differential $C_q$ is considered the limiting contribution to the double-layer capacitance of single-layer graphene [39,40]. It also exhibits a strong almost linear dependence on the potential with a rate varying between about 23 and 30 μF cm$^{-2}$V$^{-1}$ with a minimum at the potential of zero charge (PZC). Moreover, the capacitance of edge carbon atoms in graphite is much higher than the one of a basal plane, varying between 70 and 100 μF cm$^{-2}$ [42,43]. Furthermore, a 4 orders of magnitude higher specific capacitance was reported for graphene edges [44]. Knowing that the ratio of edge to basal C atoms in ACs can be between 10 and 20% [45] and considering only one graphene layer with a minimum capacitance of 5 μF cm$^{-2}$, the minimum estimated quantum capacitance in ACs would range between 11.5 and 14.5 μF cm$^{-2}$. To be consistent with the literature, our experimental data and Eq. (5), the minimum realistic estimate of $C_q$ should be at least slightly higher than the highest value between $C_{exp-}/S_C$ and $C_{exp+}/S_A$ in the series of measured carbons. Thus, $C_q$

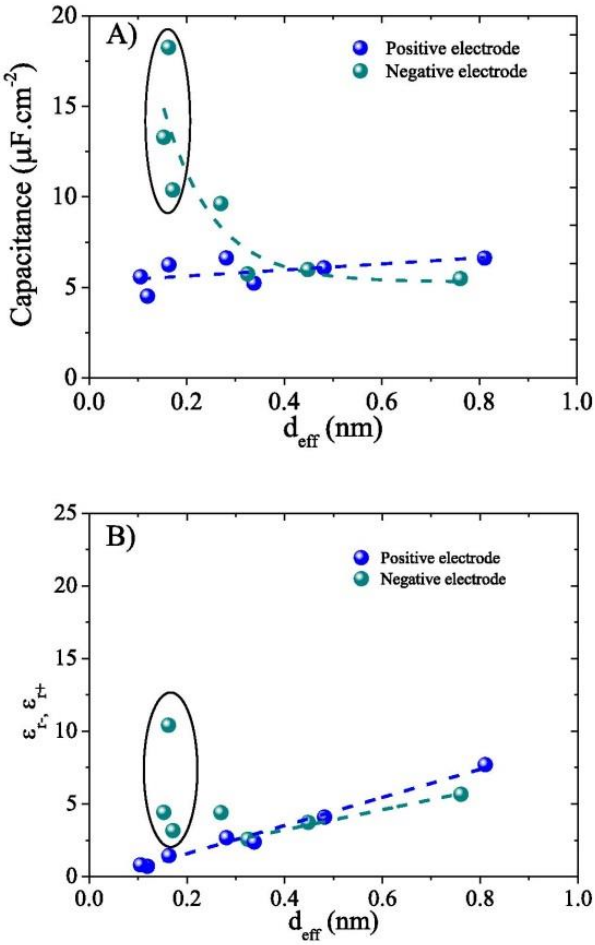


**Fig. 3.** Capacitance per ion accessible surface area (A, recalculated from gravimetric capacitance at 1 A g$^{-1}$) and relative dielectric permittivity (B) as a function of effective charge separation. $\varepsilon_{r-}$, $\varepsilon_{r+}$ calculated assuming $C_q = 25$ μF cm$^{-2}$. The dashed lines are plotted to guide the eye only. The ellipses highlight those materials exhibiting restricted electrosorption into the negative electrode.

~20–30 μF cm$^{-2}$ can be taken as an educated guess. Finally, $C_q$ can be considered to be roughly the same among our carbons having similar SSA (about 2000 m$^2$ g$^{-1}$), *i.e.* the pore wall thickness and the average number of graphene layers have little disparity from one carbon to another [46]. Another contribution in Eq. (5), $C_{dl}$, is very high in concentrated electrolytes (>100 μF cm$^{-2}$) and can be neglected as a non-limiting contribution.

Although relatively constant for plane surface, the capacitance of a compact layer inside pores can be influenced by ion confinement and was suggested to be described by one of the corresponding models [47]. The sandwich capacitance model appears to be the most realistic, assuming that ions are located in the middle between the pore walls of a slit-shaped micropore [48].

$$C_H = \varepsilon_0 \varepsilon_r \Big/ d_{eff} = \varepsilon_0 \varepsilon_r / (b - a_0) \tag{6}$$

where $\varepsilon_r$ – the effective dielectric permittivity, $\varepsilon_0$ – the electric constant.

Therefore, the following formulae can be applied to the compact layer capacitance of each separate electrode:

$$C_{H-} = \varepsilon_0 \varepsilon_{r-} \Big/ \left(b_c^+ - a_{0C}^+\right) \text{ and } C_{H+} = \varepsilon_0 \varepsilon_{r+} \Big/ \left(b_{\bar{A}}^- - a_{0A}^-\right) \tag{7}$$

$\varepsilon_{r-}$ and $\varepsilon_{r+}$ is the dielectric permittivity of electrolyte inside pores of the negative and positive electrodes, $a_{0C}^+$ is the $TEA^+$ ion radius, 0.34 nm and $a_{0A}^-$ the $BF_4^-$ ion radius, 0.24 nm [13].

Thus, the only unknown quantity in Eq. (7) is dielectric permittivity, which can be related to ion solvation and can be obtained for separate electrodes for each carbon employed on the basis of Eqs. (5)–(7):

$$\varepsilon_{r-} = \left[C_{exp-} \cdot C_q \cdot (b_C - a_{0C})\right] / \left[(S_C \cdot C_q - C_{exp-}) \cdot \varepsilon_0\right] \tag{8}$$

$$\varepsilon_{r+} = \left[C_{exp+} \cdot C_q \cdot (b_A - a_{0A})\right] / \left[(S_A \cdot C_q - C_{exp+}) \cdot \varepsilon_0\right] \tag{9}$$

Fig. 3B shows that $\varepsilon_{r+}$ changes linearly with $L_{0A}$ for the positive electrode, which leads to a constant value of $C_{H+}$, also resulting in a constant measured value of $C_{exp+}$. By contrast, $\varepsilon_{r-}$ exhibits more dispersion, but still a relatively linear relationship between $\varepsilon_{r-}$ and $b_C$ is evidenced for the carbons displaying no restrictions for ion transport with regard to pore size. Thus, it becomes clear that the areal capacitance of both positive and negative electrodes is nearly constant whenever unhindered electrosorption can proceed, again in agreement with recent literature [15,30]. However, $\varepsilon_{r-}$ demonstrates dispersion rather than clear decay for the smallest $L_{0\ A}$ values, which can be supposed to arise due to the extreme confinement of acetonitrile molecules between the ethyl groups of $TEA^+$ ions. This hypothesis can be indirectly supported by the increase in $\varepsilon$ of polar solvents under confinement [49], but necessarily requires further experimental evidence using 1.5 M $TEA^+$ $BF_4^-$/ACN. The higher $\varepsilon$ of nanoconfined acetonitrile may lead to somewhat abnormal capacitance since the decrease in charge separation is not anymore cancelled out by the corresponding decrease in $\varepsilon_r$, unlike for unrestricted electrosorption in wider pores. One possible implication is the almost complete filling of electrode surface with cations within the electrolyte stability window ([32,33]). To conclude, $\varepsilon_r$ decreases with decreasing pore size as long as pore size restrictions do not exist but appears to somewhat stabilize under extreme confinement where pore size limitations are noticeable for the negative electrode. This can result in a higher areal capacitance that can charge up a negative supercapacitor electrode before reaching the electrolyte breakdown potential. Although this phenomenon was evidenced experimentally [32,33] and suggested

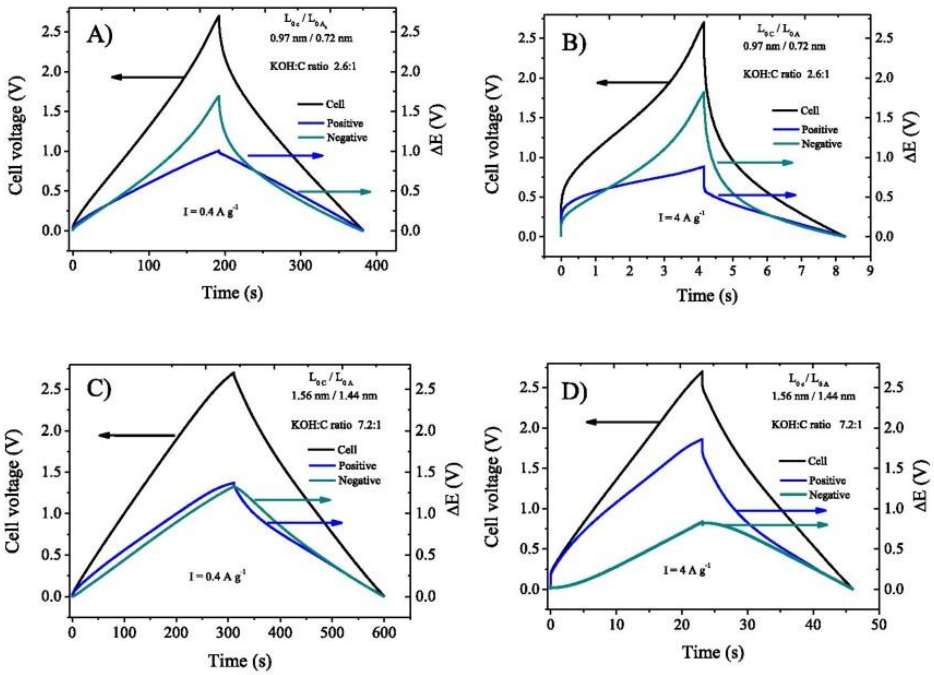


**Fig. 4.** Galvanostatic charge/discharge profiles of symmetric supercapacitor cells for carbons with different porosity: (A) KOH/C ratio 2.6, I = 0.4 A g$^{-1}$; (B) KOH/C ratio 2.6, I = 4 A g$^{-1}$; (C) KOH/C ratio 7.2, I = 0.4 A g$^{-1}$; (D) KOH/C ratio 7.2, I = 4 A g$^{-1}$.

theoretically [50], it can adversely affect supercapacitor performance as the full voltage window cannot be profited from for charge storage.

On the practical side, the maximum gravimetric capacitance is relatively high, approaching 140–150 F $g^{-1}$. The volumetric capacitance is slightly over 60 F $cm^{-3}$ (Fig. S3), comparable to the best values of ACs used in industry [5].

### 3.3. Rate capability of separate electrodes as function of textural properties of carbons

Fig. 4 shows constant current charge/discharge curves at 0.4 and 4 A $g^{-1}$ of symmetric capacitor cells and separate electrodes for carbons 2.6 and 7.2 KOH/C ratio used here as examples. These carbons are chosen to exemplify the extreme difference in electrochemical response between ion-confining and freely ion-accessible pores. Pore size restrictions (carbon 2.6) heavily accelerate capacitance fading at high rates as seen from the comparison of the charge/discharge profiles of the negative electrode at the lower and higher current density (Fig. 4A and B). By contrast, carbon 7.2 demonstrates almost equal capacitance values at the lowest current density, displaying a regular capacitive pattern. Remarkably, the charge/discharge behavior at 4 A $g^{-1}$ for carbon 7.2 is different: the negative electrode has a higher slope and operates in a smaller potential window, *i.e.* its capacitance is clearly higher than that of the positive electrode. Fig. 5A depicts a summary of these dissimilarities, highlighting that the $C_-/C_+$ capacitance ratio increases gradually as the porosity becomes wider over the whole series of carbons, with the negative electrode displaying the higher gravimetric capacitance for most of the ACs.

Fig. 5B and C show the rate capability of symmetric supercapacitor cells, demonstrating that there exists an optimum pore size (at a KOH/C ratio of 6), which provides the maximum average capacitance value per electrode, which corresponds to $L_{0C}$ and $L_{0A}$ 1.2 nm and 1.04 nm, correspondingly. Notably, these values approach the size of solvated ions [37]. At the same time, Fig. 5A shows that the $C_-/C_+$ does not significantly deviate from unity over the whole range of current densities for the same KOH/C ratio of 6. The higher APS values (the KOH/C ratio over 6) for both electrodes lead to the lower capacitance retention of symmetric cells, which also corresponds to $C_-/C_+ > 1$.

The value of $C_-/C_+ > 1$ for most of the cells that can be selected for practical use (those showing no sieving effect) has another important implication beyond the scope of our work: it demonstrates that the degradation of acetonitrile-based supercapacitors under high current load should mostly occur at positive electrodes, in line with the degradation studies available for acetonitrile-based cells [51,52].

Electrical conductivity is another parameter that impacts rate capability. Table S1 shows that the electrical conductivity values of electrodes fluctuate and are not drastically different. No evident link can be established between the rate capability of supercapacitors and the electrical conductivity of carbons since the highest capacitance retention (sample 6) is not associated with the highest value of electrical conductivity.

Our result seems to be counter-intuitive: quicker charge accumulation in the negative electrode seems to be provided by the transport of larger $TEA^+$ ions, which can rather be expected to have lower mobility inside the pores than $BF_4^-$ ions. However, recent NMR work on the same $TEA^+$ $BF_4^-$ electrolyte and standard biomass-derived YP-50 carbon suggests that under negative polarization the preferred mechanism of charge build-up in microporous carbons is cation electrosorption whereas positive polarization involves not only anion adsorption but also ion exchange [53]. It can therefore be hypothesized that ion exchange in the positive electrode is slower than the build-up of $TEA^+$ ions in the negative electrode. Another NMR study [54] concludes that $TEA^+$ ions have more affinity toward graphene-like pore walls in ACs than $BF_4^-$ ions, which can be the reason for the higher capacitive

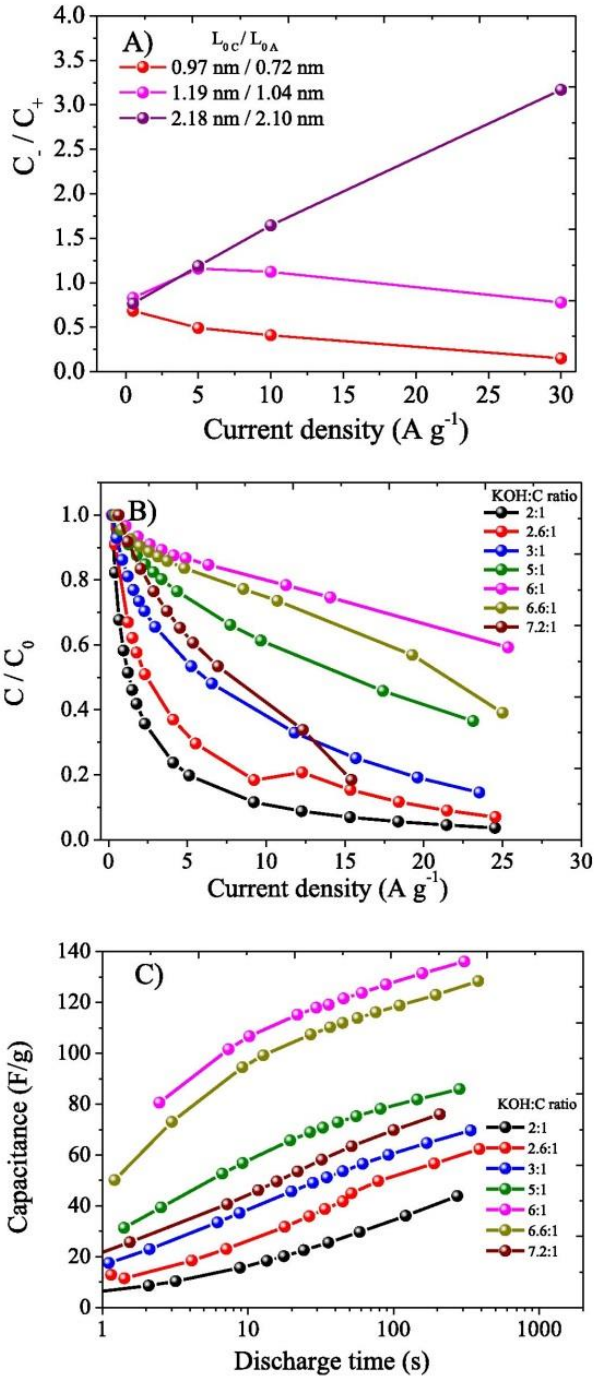


**Fig. 5.** Rate capability of selected separate electrodes and symmetric supercapacitor cells: (A) Capacitance ratio of the negative and positive electrodes vs current density; (B) Capacitance of symmetric cells vs current density; (C) Capacitance of symmetric cells vs discharge time.

response of the negative electrode. This can also be indirectly supported with the results on water-based electrolytes with the lower desolvation energy and the higher interaction energy between the hydrophobic carbon surface and hydrophobic alkyl chains of the cation [55]. From the practical perspective, the data in Fig. 5C illustrate undoubtedly once again that a proper selection of carbons for each separate electrode is a key factor for maximizing the rate response of supercapacitors since the experimentally observed trend for the rate capability of supercapacitors goes through a maximum. It will be further pertinent to study how the state of carbon surface (topological defects and functional groups) impacts the rate performance of separate electrodes with other parameters such as porosity and electrical conductivity being kept as close as possible. The series of activated carbons studied here can be considered as a good reference as it contains no heteroatoms and impurities and is made up of carbon and oxygen only (a typical maximum oxygen content of 10 at % on the basis of XPS data [16]).

## 4. Conclusions

This work gives a detailed account of the electrochemical response of a series of biomass-derived carbons with a high degree of control over average ion-accessible pore size and a high variation in ion-accessible specific surface area. The results infer that the low-rate areal capacitance of the negative electrode can be somewhat enhanced under extreme confinement but can also bring about poor rate capability and a lower usable cell voltage.

In practical terms, we have established a dependence between the conditions of chemical activation and the performance of supercapacitors to offer another alternative material being comparable to coconut shell-derived microporous carbons most often used in supercapacitor industry. The maximum gravimetric capacitance of about 150 $F\,g^{-1}$ and a volumetric capacitance of 65 $F\,cm^{-3}$ have been reached in industrial organic electrolyte.

The most important conclusion relates to high-rate capacitance: a link between the porosity of oppositely charged electrodes and their rate capability has been established, with the capacitance of the negative electrode exceeding that of the positive electrode as the accessible pores become progressively wider. The maximum capacitance retention is demonstrated when the capacitance values of both electrodes is approximately equal over the wide range of current densities. This corresponds to the average ion-accessible pore width of 1.2 nm ($TEA^+$ ions) and 1.04 nm ($BF_4^-$ ions) for the negative and positive electrodes, respectively. Our analysis can be used as a guideline for the rational choice of microporous carbons for separate electrodes to build optimum symmetric/asymmetric EDLC cells.

On the fundamental side, even though the correlation between high-rate capacitance and porosity is evident, other properties associated with carbon origin and fabrication methods (functional surface chemistry, edge atoms and heteroatoms, structural defects of graphene-like pore walls, etc.) may also be critically important but are still difficult to decrypt due to their irregularity as well as the shortcomings of instrumental techniques to probe local ion transport.

## Acknowledgments

The work was supported by the Basque Government under the Etortek Energigune'12 (Project Reference IE12-335) and Elkartek 2015 (Project CICE2015, Reference KK-2015/0000100) Program. The donation of olive mill waste from Agropecuaria Ecológica Sierra de Alcaraz (Albacete, Spain) is gratefully acknowledged. The authors also thank Dr. Iñaki Orue (University of The Basque Country) for help in measuring the electrical conductivity of carbon electrodes.

## Appendix A. Supplementary data

Supplementary data to this article can be found online at https://doi.org/10.1016/j.electacta.2018.10.031.

## References

[1] F. Béguin, E. Frackowiak, Supercapacitors: Materials, Systems, and Applications, Wiley-VCH Verlag GmbH & Co. KGaA, 2013, p. 2013.
[2] P. Simon, Yu. Gogotsi, Materials for electrochemical capacitors, Nat. Mater. 1 (2008) 845–854.
[3] B.E. Conway, Electrochemical Supercapacitors. Scientific Fundamentals and Technological Applications, Kluwer Academics/Plenum Publishers, New York, 1999, p. 1999.
[4] L. Wei, G. Yushin, Nanostructured activated carbons from natural precursors for electrical double layer capacitors, Nano Energy 1 (2012) 552–565.
[5] http://www.kuraray-c.co.jp/en/products/function.html. (Accessed 10 October 2018).
[6] M.D. Levi, S. Sigalov, D. Aurbach, L. Daikhin, In situ electrochemical quartz crystal admittance methodology for tracking compositional and mechanical changes in porous carbon electrodes, J. Phys. Chem. C 117 (2013) 14876–14889.
[7] J.M. Griffin, A.C. Forse, W. Yu Tsai, P.-L. Taberna, P. Simon, C.P. Grey, *In-situ* NMR and electrochemical quartz crystal microbalance techniques reveal the structure of the electrical double layer in supercapacitors, Nat. Mater. 14 (2015) 812–819.
[8] S. Boukhalfa, D. Gordon, L. He, Yu. Melnichenko, N. Nitta, A. Magasinski, G. Yushin, In situ small angle neutron scattering revealing ion sorption in microporous carbon electrical double layer capacitors, ACS Nano 8 (2014) 2495–2503.
[9] C. Prehal, D. Weingarth, E. Perre, R.T. Lechner, H. Amenitsch, O. Paris, V. Presser, Tracking the structural arrangement of ions in carbon supercapacitor nanopores using in situ small-angle X-ray scattering, Energy Environ. Sci. 8 (2015) 1725–1735.
[10] C. Prehal, C. Koczwara, N. Jäckel, A. Schreiber, M. Burian, H. Amenitsch, M.A. Hartman, V. Presser, O. Paris, Quantification of ion confinement and desolvation in nanoporous carbon supercapacitor modelling and in situ X-ray scattering, Nat. Energy 2 (2017) 1–8.
[11] R. Futamura, T. Iayama, Y. Takasaki, Y. Gogotsi, M.J. Biggs, M. Salanne, J. Segalini, P. Simon, K. Kaneko, Partial breaking of the Coulombic ordering of ionic liquids confined in carbon nanopores, Nat. Mater. 16 (2017) 1225–1232.
[12] B. Wang, A.J. Fielding, R.A. Dryfe, In situ electrochemical electron paramagnetic resonance spectroscopy as a tool to probe electrical double layer capacitance, Chem. Commun. 54 (2018) 3827–3830.
[13] J. Chmiola, G. Yushin, Y. Gogotsi, C. Portet, P. Simon, P.L. Taberna, Anomalous increase in carbon capacitance at pore sizes less than 1 nanometer, Science 313 (2006) 1760–1763.
[14] E. Raymundo-Piñero, K. Kierzek, J. Machnikowski, F. Béguin, Relationship between the nanoporous texture of activated carbons and their capacitance properties in different electrolytes, Carbon 44 (2006) 2498–2507.
[15] T.A. Centeno, O. Sereda, F. Stoeckli, Capacitance in carbon pores of 0.7 to 15 nm: a regular pattern, Phys. Chem. Chem. Phys. 27 (2011) 12403–12406.
[16] E. Redondo, J. Carretero-González, E. Goikolea, J. Ségalini, R. Mysyk, Effect of pore texture on performance of activated carbon supercapacitor electrodes derived from olive pits, Electrochim. Acta 160 (2015) 178–184.
[17] E. Redondo, W.-Y. Tsai, B. Daffos, P.-L. Taberna, P. Simon, E. Goikolea, R. Mysyk, Outstanding room-temperature capacitance of biomass-derived microporous carbons in ionic liquid electrolyte, Electrochem. Commun. 79 (2017) 5–8.
[18] J. Jagiello, J. Oliver, 2D-NLDFT adsorption models for carbon slit-shaped pores with surface energetical heterogeneity and geometrical corrugation, Carbon 55 (2013) 70–80.
[19] L.J. van der Pauw, A method of measuring specific resistivity and Hall effect of discs of arbitrary shape, Philips Res. Rep. 13 (1958) 1–9.
[20] T.A. Centeno, F. Stoeckli, The assessment of surface areas in porous carbons by two model-independent techniques, the DR equation and DFT, Carbon 48 (2010) 2478–2486.
[21] F. Stoeckli, T.A. Centeno, Optimization of the characterization of porous carbons for supercapacitors, J. Mater. Chem. A 1 (2013) 6865–6873.
[22] A. Garcia-Gomez, V. Barranco, G. Moreno-Fernandez, J. Ibañez, T.A. Centeno, J.M. Rojo, Correlation between capacitance and porosity in microporous carbon monoliths, J. Phys. Chem. C 118 (2014) 5134–5141.
[23] J. Chmiola, C. Largeot, P.L. Taberna, P. Simon, Y. Gogotsi, Desolvation of ions in subnanometer pores and its effect on capacitance and double-layer theory, Angew. Chem. Int. Ed. 47 (2008) 8020–8024.
[24] F. Stoeckli, L. Ballerini, Evolution of microporosity during activation of carbon, Fuel 70 (1991) 557–559.
[25] D. Lozano-Castelló, D. Cazorla-Amorós, A. Linares-Solano, Usefulness of CO2 adsorption at 273 K for the characterization of porous carbons, Carbon 42 (2004) 1233–1242.
[26] X. Wu, W. Xing, J. Florek, J. Zhou, G. Wang, S. Zhuo, Q. Xue, Z. Yan, F. Kleitz, On

the origin of the high capacitance of carbon derived from seaweed with an apparently low surface area, J. Mater. Chem. A 2 (2014) 18998–19004.
[27] N. Jäckel, M. Rodner, A. Schreiber, J. Jeongwook, M. Zeiger, M. Aslan, D. Weingarth, V. Presser, J. Power Sources 326 (2016) 660–671.
[28] J.N. Caguiat, D.W. Kirk, C.Q. Jia, Uncertainties in characterization of nanoporous carbons using density functional theory-based gas physisorption, Carbon 72 (2014) 47–56.
[29] Q. Abbas, D. Pajak, E. Frąckowiak, F. Béguin, Effect of binder on the performance of carbon/carbon symmetric capacitors in salt aqueous electrolyte, Electrochim. Acta 140 (2014) 132–138.
[30] A. García-Gómez, G. Moreno-Fernández, B. Lobato, T.A. Centeno, Constant capacitance in nanopores of carbon monoliths, Phys. Chem. Chem. Phys. 17 (2015) 15687–15690.
[31] L. Eliad, G. Salitra, A. Soffer, D. Aurbach, Ion sieving effects in the electrical double layer of porous carbon electrodes: estimating effective ion size in electrolytic solutions, J. Phys. Chem. B 105 (2001) 6880–6887, 29.
[32] R. Mysyk, E. Raymundo-Piñero, F. Béguin, Saturation of subnanometer pores in an electric double-layer capacitor, Electrochem. Commun. 11 (2009) 554–556.
[33] R. Mysyk, E. Raymundo-Piñero, J. Pernak, F. Béguin, Confinement of symmetric tetraalkylammonium ions in nanoporous carbon electrodes of electric double-layer capacitors, J. Phys. Chem. C 113 (2009) 13443–13449.
[34] T. Centeno, F. Stoeckli, Surface-related capacitance of microporous carbons in aqueous and organic electrolytes, Electrochim. Acta 56 (2011) 7334–7339.
[35] J. Huang, B.G. Sumpter, V. Meunier, G. Yushin, C. Portet, Y. Gogotsi, Curvature effects in carbon nanomaterials: exohedral versus endohedral supercapacitors, J. Mater. Res. 25 (2010) 1525–1531.
[36] R. Kötz, M.M. Hantel, D. Weingarth, A. Foelske-Schmitz. Graphene as electrode material for supercapacitors? In: Annual Report 2012-Electrochemistry Laboratory, Paul Scherrer Institut, 5232 Villigen PSI, Switzerland https://doi.org/10.3929/ethz-a-007047464.
[37] W. Hsieh, T.A. Horng, H. Huang, H. Teng, Facile simulation of carbon with wide pore size distribution for electric double-layer capacitance based on Helmholtz models, J. Mater. Chem. A 3 (2015) 16535–16543, 2015.
[38] D. Qu, Studies of the activated carbons used in double-layer supercapacitors, J. Power Sources 109 (2002) 403–411.
[39] J. Xia, F. Chen, J. Li, N. Tao, Measurement of the quantum capacitance of graphene, Nat. Nanotechnol. 4 (2009) 505–509.
[40] H. Gerischer, R. McIntyre, D. Scherson, W. Storck, Density of the electronic states of graphite: derivation from differential capacitance measurements, J. Phys. Chem. 91 (1987) 1930–1935.
[41] J. Guo, J.R. Morris, Y. Ihm, C.I. Contescu, N.C. Gallego, G. Duscher, S.J. Pennycook, M.F. Chisholm, Topological defects: origin of nanopores and enhanced adsorption performance in nanoporous carbon, Small 8 (2012) 3283–3288.
[42] M.D. Stoller, C.W. Magnuson, Ya. Zhu, Sh. Murali, Ji-W. Suk, R. Piner, R.S. Ruoff, Interfacial capacitance of single layer graphene, Energy Environ. Sci. 4 (2011) 4685–4689.
[43] J.-P. Randin, E. Yeager, Differential capacitance study on the edge orientation of pyrolytic graphite and glassy carbon electrodes, J. Electroanal. Chem. Interfacial Electrochem. 58 (1975) 313–322.
[44] W. Yuan, Yu Zhou, Y. Li, Ch. Li, H. Peng, J. Zhang, Zh. Liu, L. Dai, G. Shi, The edge- and basal-plane-specific electrochemistry of a single-layer graphene sheet, Sci. Rep. 3 (2013) 2248.
[45] L. Radovic, Surface Chemistry of activated carbon materials: state of the art and implications for adsorption, in: James A. . Schirarz, Cristian I. . Contescu (Eds.), Surfaces of Nanoparticles and Porous Materials, CRC Press, 1999.
[46] O. Barbieri, M. Hahn, A. Herzog, R. Kötz, Capacitance limits of high surface area activated carbons for double layer capacitors, Carbon 43 (2005) 1303–1310.
[47] J. Huang, B.G. Sumpter, V. Meunier, A universal model for nanoporous carbon supercapacitors applicable to diverse pore regimes, carbon materials, and electrolytes, Chem. Eur. J. 14 (2008) 6614–6626.
[48] G. Feng, R. Qiao, J. Huang, B.G. Sumpter, V. Meunier, Ion distribution in electrified micropores and its role in the anomalous enhancement of capacitance, ACS Nano 4 (2010) 2382–2390.
[49] V. Ballenegger, J.P. Hansen, Dielectric permittivity profiles of confined polar fluids, J. Chem. Phys. 122 (2005) 114711.
[50] S. Kondrat, C.R. Pérez, V. Presser, Y. Gogotsi, A.A. Kornyshev, Effect of pore size and its dispersity on the energy storage in nanoporous supercapacitors, Energy Environ. Sci. 5 (2012) 6474–6479.
[51] P.W. Ruch, D. Cericola, A. Foelske, R. Kötz, A. Wokaun, A comparison of the aging of electrochemical double layer capacitors with acetonitrile and propylene carbonate-based electrolytes at elevated voltages, Electrochim. Acta 55 (2010) 2352–2357.
[52] P.W. Ruch, D. Cericola, A. Foelske-Schmitz, R. Kötz, A. Wokaun, Aging of electrochemical double layer capacitors with acetonitrile-based electrolyte at elevated voltages, Electrochim. Acta 55 (2010) 4412–4420.
[53] J.M. Griffin, A.C. Forse, H. Wang, N.M. Trease, P.-L. Taberna, P. Simon, C.P. Grey, Ion counting in supercapacitor electrodes using NMR spectroscopy, Faraday Discuss 176 (2014) 49–68.
[54] M. Deschamps, E. Gilbert, P. Azais, E. Raymundo-Piñero, M.R. Ammar, P. Simon, D. Massiot, F. Béguin, Exploring electrolyte organization in supercapacitor electrodes with solid-state NMR, Nat. Mater. 12 (2013) 351–358.
[55] T. Hrobárik, L. Vrbka, P. Jungwirth, Selected biologically relevant ions at the air/water interface: a comparative molecular dynamics study, Biophys. Chem. 124 (2006) 238–242.

## Electronic Supplementary Information

# Relation between texture and high-rate capacitance of oppositely charged microporous carbons from biomass waste in acetonitrile-based supercapacitors

Edurne Redondo[a], Julie Ségalini[a], Javier Carretero-González[a†], Eider Goikolea*[‡a], Roman Mysyk**[a]

[a]CICenergiGUNE, Arabako Teknologi Parkea, calle Albert Einstein 48, 0150 Miñano, Spain

[†]Present Address: Institute of Polymer Science and Technology, ICTP-CSIC, Juan de la Cierva 3, 28006, Madrid, Spain

[‡]Present Address: Inorganic Chemistry Department, University of the Basque Country, P.O. Box 644, 48080, Bilbao, Spain

**Corresponding Authors**

*Eider Goikolea. Inorganic Chemistry Department, University of the Basque Country, P.O. Box 644, 48080, Leioa, Spain. E-mail: eider.goikolea@ehu.eus

**Roman Mysyk. CIC energiGUNE, Parque Tecnológico, c/Albert Einstein 48, 01510 Miñano, Alava, Spain. Fax: +34 945 297 108. E-mail: rmysyk@cicenergigune.com

The average gravimetric capacitance ($C$, F $g^{-1}$) was calculated per electrode from the data of the GA experiments according to the formula:

$$C = 2\frac{\int_0^t Idt}{\Delta V m_{am}} \quad \text{(S1)}$$

where $Idt$ is the differential charge (A s), $\Delta V$ the cell voltage (V), $m_{am}$ the mass of active material per electrode (g). The capacitance values are reported for the voltage range between 0 V and the maximum cell voltage, excluding the resistive part of the discharge (equivalent series and distributed resistance). Additionally, the capacitance of the positive and negative electrodes was separately calculated from the potential variation at the corresponding electrode.

$$C_+ = \frac{\int_0^t Idt}{\Delta E_+ m_+} \text{ and } C_- = \frac{\int_0^t Idt}{\Delta E_- m_-} \quad \text{(S2)}$$

where $C_+$, $C_-$ are the capacitance of the positive and negative electrodes, correspondingly (F $g^{-1}$), $\Delta E_+$, $\Delta E_-$ - the potential evolution (V, excluding the resistive part of the discharge curve) at the corresponding electrode, $m_+$, $m_+$ - the mass of the corresponding electrode (g).

The average differential gravimetric capacitance per electrode of a two-electrode cell in the CV experiments was calculated according to the formula:

$$C = 2i/[(dV/dt)\, m_{am}] \quad \text{(S3)}$$

where $C$ is the gravimetric capacitance per electrode (F $g^{-1}$), $i$ the current (A), $dV/dt$ the scan rate (V $s^{-1}$), $m_{am}$ the mass of active material per electrode (g).

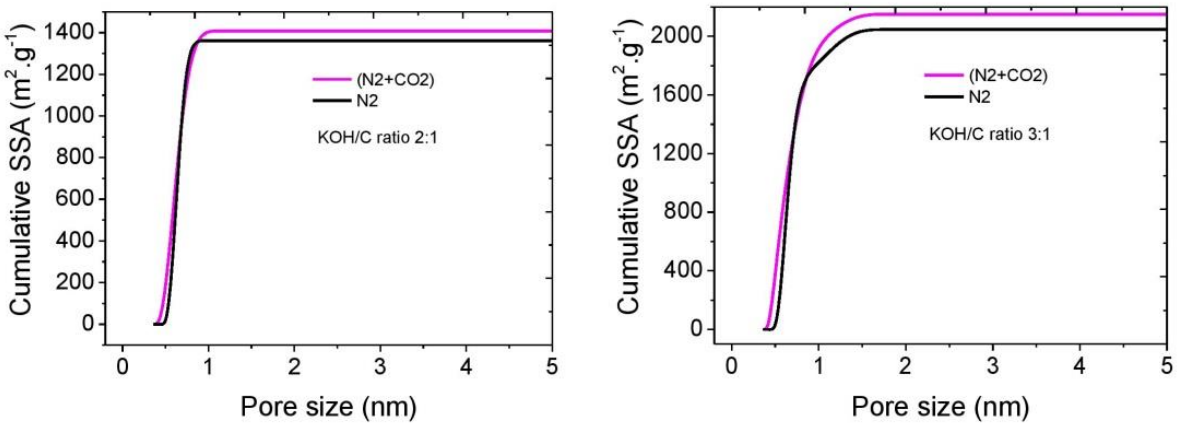


Figure S1. Cumulative pore size distributions calculated using the 2D-NLDFT method on the basis of either $N_2$ adsorption/desorption isotherms or $N_2/CO_2$ adsorption/desorption isotherms. Examples are given for carbons containing a high share of ultramicropores where $CO_2$ adsorption measurements are believed to provide better accuracy in comparison non-equilibrium diffusion-hindered $N_2$ adsorption. The comparison of PSDs shows that the $CO_2$ measurements bring about a minor improvement in the PSD over the corresponding data for $N_2$ adsorption alone. This conclusion supports the suitability of $N_2$-based cumulative PSD curves for calculating electrolyte-accessible SSA within acceptable error.

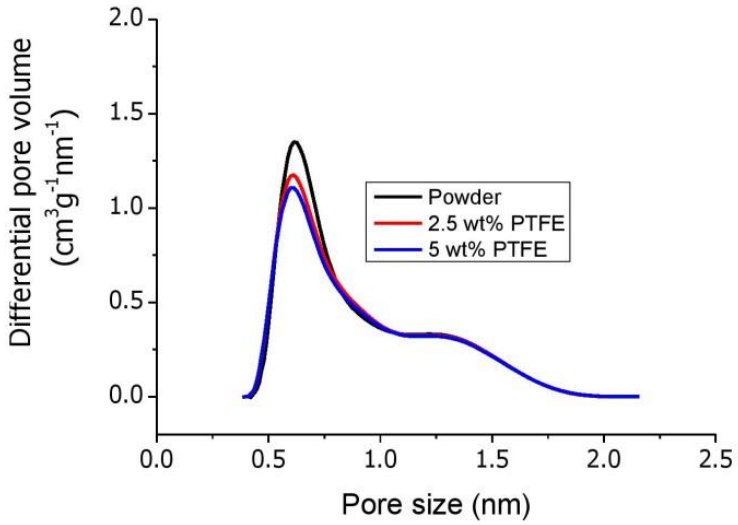


Figure S2. Pore size distribution of powdered activated carbon and electrodes with different amounts of PTFE binder (carbon 6).

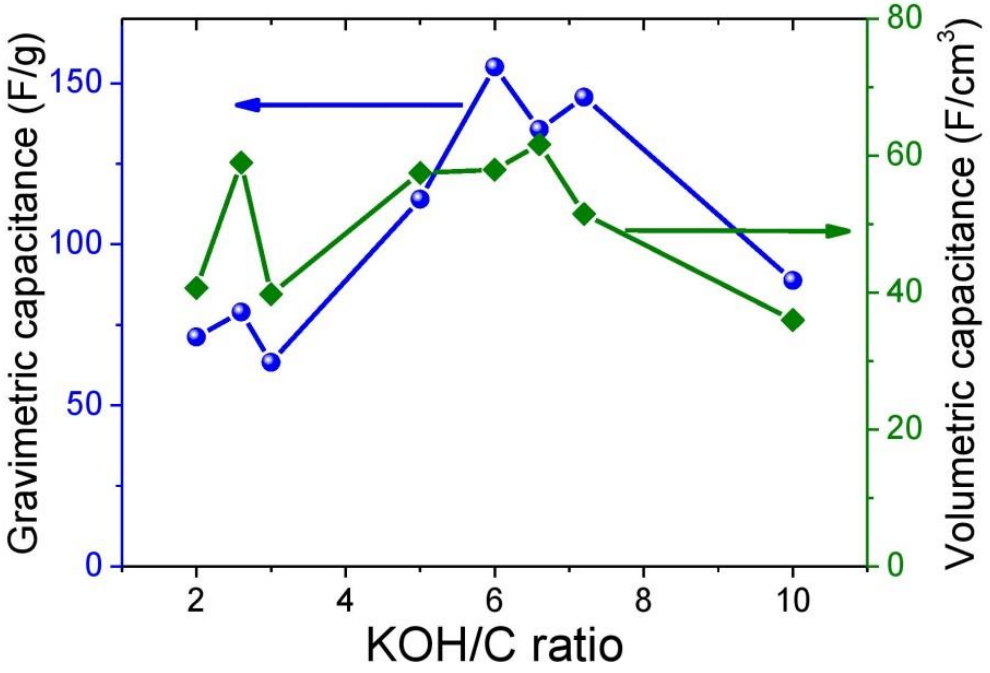


Figure S3. Maximum gravimetric and volumetric average electrode capacitance in symmetric supercapacitor cells.

**Table S1.** Specific surface area calculated by BET and 2D-NLDFT methods.

| KOH/C ratio, g/g | SSA (BET), $m^2/g$ | SSA (2D-NLDFT), $m^2/g$ | $SSA_{micro}$ (2D-NLDFT)*, $m^2/g$ |
|---|---|---|---|
| 2 | 1232 | 1552 | 1552 |
| 2.6 | 1539 | 1809 | 1809 |
| 3 | 1386 | 1670 | 1670 |
| 5 | 1704 | 1795 | 1795 |
| 6 | 2414 | 2216 | 2193 |
| 6.6 | 2700 | 2364 | 2291 |
| 7.2 | 2868 | 2234 | 2084 |
| 10 | 2091 | 1506 | 1209 |

* $SSA_{micro}$ -specific surface area of micropores derived from cumulative SSA by 2D-NLDFT.

**Table S2.** Electrical conductivity of supercapacitor electrodes.

| KOH/carbon ratio | 2.6 | 3 | 5 | 6 | 6.6 | 10 |
|---|---|---|---|---|---|---|
| Electrical conductivity, $S.m^{-1}$ | 2.1 | 6.8 | 3.1 | 11.3 | 30.4 | 15.5 |

## 5.3 The decisive role of electrolyte concentration in the performance of aqueous chloride-based carbon/carbon supercapacitors with extended voltage window

Electrochimica Acta 221 (2016) 177–183

Contents lists available at ScienceDirect

Electrochimica Acta

journal homepage: www.elsevier.com/locate/electacta

# The decisive role of electrolyte concentration in the performance of aqueous chloride-based carbon/carbon supercapacitors with extended voltage window

Edurne Redondo, Eider Goikolea*, Roman Mysyk

*CICenergiGUNE, Arabako Teknologi Parkea, Albert Einstein 48, 0150 Miñano, Spain*

ARTICLE INFO

*Article history:*
Received 4 August 2016
Received in revised form 28 September 2016
Accepted 21 October 2016
Available online 22 October 2016

*Keywords:*
Supercapacitors
microporosity
activated carbon
neutral aqueous electrolytes
chlorides

ABSTRACT

In the present study aqueous alkali metal chloride electrolytes are investigated as potential candidates for carbon/carbon supercapacitors. High-current capacitance retention is greatly enhanced by using the electrolyte concentrations at the maximum electrical conductivity, *i.e.* 6 M LiCl, 5 M NaCl and 2 M KCl, in supercapacitor cells working at 1.6 V. The resistance of the symmetric cells is also significantly diminished by using the optimum electrolyte concentrations, with remarkable improvements not only in the equivalent series resistance, but also in the distributed resistance. Both high-rate capacitance and lower resistance are beneficial to increase the energy of supercapacitors working at high discharge rates. The small size of electrosorbed dehydrated chloride ions allows the use of less expensive carbons with narrower micropores instead of strongly activated carbons with larger micropores required for bulkier anions.



## 1. Introduction

Electrochemical capacitors or supercapacitors have found their niche as a promising solution for fast charging and regenerative energy acquisition. In most of the applications they are used to complement batteries but, owing to their excellent low temperature performance, calendar and cycle life, fast charge-discharge and reliability [1], they can even replace them in those applications where size and weight are not of primary concern. One of the key parameters hindering the more extensive use of supercapacitors is indeed their low energy density; in the best cases about an order of magnitude lower than batteries [2]. Two main approaches can be followed to increase the energy density of supercapacitors; one involves the usage of active materials of higher capacitance and the other one the enlargement of the cell voltage by using novel electrolytes and asymmetric/hybrid cells [3]. Although several transition metal oxides and polymers have exhibited capacitance values that exceed by far those obtained with carbonaceous materials (up to 1000 F $g^{-1}$ *vs.* 250 F $g^{-1}$), the latter ones continue to be the materials of choice as they provide the best trade-off between performance and cost. Linked to environmental consciousness, the exploitation of sustainable and renewable systems for the preparation of electrode materials is nowadays a priority, and thus, activated carbons (ACs) derived from biomass feed-stock or natural wastes are acquiring increased importance in the field of supercapacitors [4].

The use of aqueous over organic electrolytes has the advantage of providing lower equivalent series resistance (ESR), higher ionic conductivity, and higher capacitance. Safety is another important parameter that is strengthened when working with water instead of organic solvents such as acetonitrile or propylene carbonate [5]. For instance, acetonitrile can cause cyanide poisoning and has a flash point of only 6 °C [6] (Flammability of Chemical Substances, 2003-2004). Nevertheless, the energy stored in a supercapacitor is proportional to the square of the cell voltage as expressed in Eq. (1),

$$E = \frac{1}{2}CV^2 \quad (1)$$

where $C$ is the capacitance and $V$ the cell voltage. Thus, most of the commercially available supercapacitors work in organic-based electrolytes due to the limited voltage window of alkali- and acid-based aqueous systems, typically below 1 V (thermodynamic stability window of water is 1.23 V) while organic systems can easily reach 2.5–2.7 V [7,8].

Very recently several studies have shown that electrodes made of AC can work in aqueous sulphate salts in a voltage window of about 1.9 V without significant capacitance fading [9–11]. A local

* Corresponding author.
*E-mail address:* egoikolea@cicenergigune.com (E. Goikolea).

http://dx.doi.org/10.1016/j.electacta.2016.10.141
0013-4686/

increase in the concentration of $OH^-$ ions in the porosity of the negative carbon electrode due to water reduction and concomitant weak chemisorption of atomic hydrogen seems to be the reason for the extended voltage window [11], shifting the potential of molecular hydrogen evolution at the negative electrode to lower values (according to the Nernst equation) [12]. All these results have opened up the possibility of using inexpensive and less hazardous electrolytes without drastically sacrificing the energy density of the device. On the electrode side, the compatibility between the size of ions and pores should be sought at least to maximize volumetric capacitance. Additionally, some studies claim that areal capacitance can be enhanced if the pore size and ion size are matched [13–15]. However, for an efficient power response, the ion size should be slightly smaller than the carbon pore size [16]. Monovalent anions such as $Cl^-$ are electrosorbed in the nonhydrated state whereas sulphate ions are adsorbed in the hydrated state with a size exceeding 0.733 nm [9]. In this sense, if smaller ions such as $Cl^-$ (a diameter slightly larger than 0.362 nm [13]) could also be successfully used in an extended-voltage cell instead of a much bulkier sulphate anion, a larger variety of ultramicroporous carbon electrodes with moderate specific surface area (SSA) could be employed. Importantly, such carbons can be expected to be somewhat denser (because of their moderate pore volume) and less expensive (milder activation conditions). However, the main problem caused by the presence of chlorides is pitting corrosion occurring on several metals, which reduces the choice of well-suited current collectors. To conclude, the affordability and variety of compatible carbons make chlorides an alternative to other neutral salts, provided inexpensive chloride-resistant current collectors are used.

This work concentrates on the enhancement of chloride-based aqueous symmetric supercapacitors through the optimization of electrolyte concentration using two microporous carbons with significantly different pore size distributions.

## 2. Experimental

### 2.1. Preparation of microporous carbons by alkali activation

The activation of carbons was conducted after carbonization of raw olive pits as described elsewhere [17]. Briefly, the raw material was heated under an Ar flow of 100 ml $min^{-1}$ at a ramp rate of 5 °C $min^{-1}$ in a tubular furnace to a predefined temperature and further holding the temperature for 2 h at 700 °C (the carbonization yield for olive pits is 25 ± 1%). After carbonization, the resulting char was physically mixed with potassium hydroxide, KOH, in a mass ratio of 1 to 6 and 1 to 2. The materials mixed with KOH were placed in an Inconel© boat and activated by heating up to 700 °C under Ar flow (100 ml $min^{-1}$) inside a horizontal stainless steel tube within a tubular furnace. The heating ramp rate was 5 °C $min^{-1}$ and the holding time at 700 °C was 2 h. After activation, the resulting microporous carbons, hereafter referred to as AC16 and AC12 (see Table S1), were washed off with a diluted solution of hydrochloric acid and water until neutral pH was reached and then dried at 120 °C under vacuum. The activation yield was 65 % and 75 %, correspondingly.

### 2.2. Textural and X-ray photoelectron spectroscopy characterization

Nitrogen adsorption isotherms were measured at −195.8 °C using a Micromeritics ASAP 2020 instrument for relative pressure ($P/P_0$) between $10^{-8}$ and 0.995 for samples preliminarily outgassed for 24 h at 200 °C. The SSA values and pore size distribution were calculated by applying the recently-developed 2D Non Local Density Functional Theory (2D NLDFT) treatment to $N_2$ adsorption isotherms using the data reduction software SAEIUS [18]. The average pore size ($L_0$) was calculated as a weighted average from the DFT data according to the formula:

$$L_0 = \frac{\int_{V\min}^{V\max} L dV}{V_{\max} - V_{\min}} \quad (2)$$

where $V_{max}$ and $V_{min}$ are the total pore volume and the pore volume at the minimum pore size, correspondingly, and $L$ the pore size corresponding to the total pore volume $V$ accumulated by the pores with size $\leq L$.

XPS C1 s and O1 s spectra were recorded using PHOIBOS 150 analyser (SPECS, Germany) and monochromated Mg $K_\alpha$ X ray source.

### 2.3. Electrode preparation and electrochemical measurements

Electrodes were prepared by mixing AC (95 wt. %) and polytetrafluorethylene (PTFE) binder (5 wt. %, from a 60 wt. % aqueous dispersion, Sigma-Aldrich) with a few millilitres of ethanol until plasticity was achieved. The plastic composite was then rolled to a thickness of ~200 μm and dried under vacuum at 120 °C overnight. Electrodes of 11 mm in diameter were then cut, weighed, and their thickness was measured again. Finally, two-electrode symmetric supercapacitor cells were assembled in a Nylon Swagelok® airtight system, using two titanium current collectors, a porous glass fibre (Whatman GFB) membrane separator and Li, Na and K chloride solutions of various concentrations as supporting electrolytes. A saturated calomel electrode (SCE) was used to monitor the potential evolution of each electrode in some of the symmetric two-electrode cells.

Cyclic voltammetry (CV), galvanostatic (GA) charge-discharge cycling and electrochemical impedance spectroscopy (EIS) measurements were conducted using a multichannel VMP3 generator (Biologic, France). EIS measurements were carried out by applying a low sinusoidal amplitude alternating voltage of 10 mV at frequencies from 1 MHz to 10 mHz using the same instrument.

The average gravimetric capacitance per electrode of a two-electrode symmetric cell was calculated from the data of the GA experiments according to the formula:

$$C = 2\frac{\int Idt}{\Delta V m_{am}} \quad (3)$$

where $C$ is the gravimetric capacitance per electrode (F $g^{-1}$), $Idt$ the differential charge (A s), $\Delta V$ the cell voltage (V), $m_{am}$ the mass of active material per electrode (g). The capacitance values are reported for the voltage range between 0 V and the maximum cell voltage, excluding the voltage drop from equivalent series and distributed resistance.

The differential gravimetric capacitance per electrode of a two-electrode cell in the CV experiments was calculated according to the formula:

$$C = \frac{2i}{\left(\frac{dV}{dt}\right) m_{am}} \quad (4)$$

where $C$ is the gravimetric capacitance per electrode (F $g^{-1}$), $i$ the instant current (A), $dV/dt$ the scan rate (V $s^{-1}$), $m_{am}$ the mass of active material per electrode (g).

Three-electrode CV measurements were conducted in Swagelok cells by scanning an activated carbon (AC12 or AC16) pellet as the working electrode *vs.* a saturated calomel electrode in 6 M LiCl, 5 M NaCl, and 2 M KCl electrolytes using an oversized Norit DLC Super 30 activated carbon as the counter electrode.

The floating test procedure applied to the cells was described previously by Kötz et al. [19]. Briefly, a maximum voltage was applied to the cells and during this voltage holding period, 5 GA charge/discharge cycles at a constant current of 1 A $g^{-1}$ were

performed every 2 h between 0 and the maximum usable voltage so as to determine the specific capacitance.

The electrical conductivity was evaluated on pelletized electrodes using the van der Pauw four-probe method [20], measuring 2 and 30 $S.m^{-1}$ for carbons AC12 and AC16, correspondingly.

## 3. Results and discussion

### 3.1. Textural characterization of carbons

Fig. 1 depicts the pore size distribution of carbons AC12 and AC16, demonstrating that the first is almost exclusively made up of subnanometer pores whereas the second exhibits a broad micropore size distribution with almost no mesoporosity. The values of $L_0$ for AC12 and AC16 are 0.65 nm and 1.15 nm, correspondingly, suggesting that there should be no restrictions for either alkali cations or chloride anions (an electrosorbed size of 0.362-0.421 nm [13]) although the accessibility of sulphate ions would be limited for AC12 carbon (0.58-0.733 nm [9]). Remarkably, the $L_0$ value of the moderately activated carbon AC12 exceeds the size of sulphate ions only marginally, implying that the comparison of supercapacitors based on chloride and sulphate-based electrolytes can reveal differences in performance connected with the effect of pore size.

More precisely, the 2D NLDFT data allow calculating the average effective pore size accessible to any specific ion [17], which can be defined as:

$$L_{0e} = \frac{\int_{V_e}^{V\max} LdV}{V_{\max} - V_e} \quad (5)$$

where $L_{0e}$ is the effective average accessible pore size; $V_{max}$ is the total pore volume; and $V_e$ is the volume pertaining to pores smaller than ion diameter.

Knowing the diameter of the electrosorbed ions (as discussed above), it is easy to see from Fig. 1 that $L_{0e}$ coincides with $L_0$ for alkali and chloride ions (no pores below the ion sizes are probed by $N_2$) whereas $L_{0e}$ and $L_0$ for sulphate ions are calculated to be slightly different, 0.79 nm *vs.* 0.65 nm for AC12 and 1.24 nm *vs* 1.15 nm for AC16, correspondingly. Textural properties of both carbons are summarized in Table S1.

### 3.2. Electrochemical characterization

In order to investigate the best alternatives to aqueous neutral sulphate electrolytes and to remove possible restrictions of the electrolyte ions accessing the pores, a screening of various salts was undertaken using AC16 carbon with a relatively broad pore size distribution. Two-electrode symmetric cells were prepared and CVs were recorded in the safe voltage range of 0 to 1.0 V. Based on previous results where a better ion-mobility of $Li^+$ was evidenced over that of $Na^+$ and $K^+$ [9], in all cases $Li^+$ was selected as the common cation. Fig. 2 shows the CVs recorded using 1 M lithium sulphate, nitrate and chloride at 5 mV $s^{-1}$. All the CVs in Fig. 2 approach the typical rectangular shape of supercapacitors. Moreover, the results show that regardless of the nature of the anion, the electrochemical performance of all cells is very similar, with the capacitance values ranging from 87 F $g^{-1}$ for 1 M $Li_2SO_4$ to 111 F $g^{-1}$ for 1 M LiCl. The slightly higher values for LiCl and $LiNO_3$ can be ascribed to the smaller size of monovalent $NO_3^-$ and $Cl^-$ ions (0.36 nm) in an electrosorbed nonhydrated state as compared to hydrated bivalent $SO_4^{2-}$ ions (> 0.58 nm) [13]. Therefore, it can be speculated that this allows monovalent nonhydrated ions to access a larger portion of SSA, encompassing a higher volume of narrower pores, giving rise to a higher gravimetric capacitance. In what follows we chose to optimize chloride electrolytes because the preliminary evaluation had shown high capacitance decay for nitrate based electrolytes if the cell voltage is set to above 1 V (Fig. S1).

In order to optimize the cell performance, especially at high current densities, we studied the effect of electrolyte concentration. It is well known that 6 M KOH and 1 M $H_2SO_4$ have the highest conductivity values among the commonly employed aqueous electrolytes, 625 and 425 mS $cm^{-1}$, respectively, at 25 °C [21,22]. In the case of neutral chloride electrolytes, the maximum electrical conductivities are obtained when the concentrations are 6 M LiCl (170 mS $cm^{-1}$), 5 M NaCl (220 mS $cm^{-1}$) and 2 M KCl (205 mS $cm^{-1}$) (Fig. S2) [21]. Fig. 3 shows the CVs obtained at 5 mV $s^{-1}$ using 1 M and the above mentioned concentrations (at 1 V). In all cases, increasing the concentration is beneficial for the cell performance, leading to almost perfectly rectangular-shaped CVs with a nearly negligible resistive contribution. Additionally, the capacitance values are identical for all systems, viz. ~150 F $g^{-1}$, and the CV curves can be perfectly superimposed one on top of the other for the concentrations providing the maximum electrolyte conductivity. Thus, as distinct from sulphate-based supercapacitors where the maximum electrolyte conductivity did not provide the highest capacitance and the lowest resistance [9], the optimum cell response follows the maximum electrolyte conductivity in the case of chlorides.

Electrochemical impedance spectroscopy is another technique that can help in assessing the differences derived from the use of different electrolytic solutions. All the cells in Fig. 4 exhibit the typical supercapacitor impedance behaviour, characterized by a near-vertical low-frequency line changing into a steep medium-frequency line intersecting the real axis with a ~45° angle. The

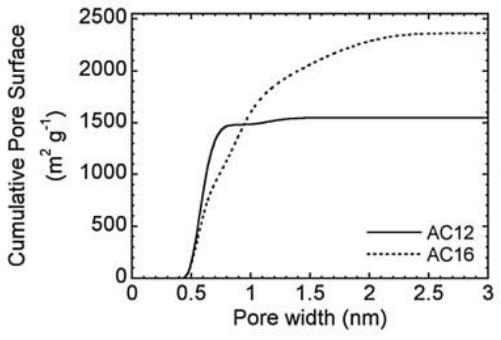


**Fig. 1.** Pore size distribution of carbons AC12 and AC16.

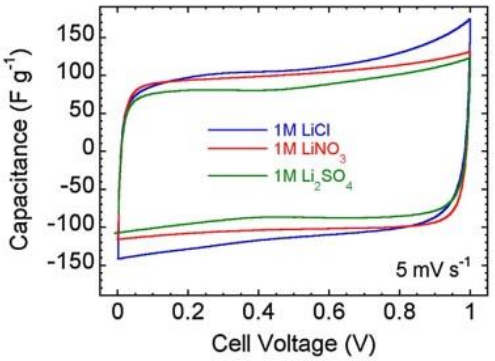


**Fig. 2.** Cyclic voltammogramms of symmetric supercapacitors using carbon AC16 and various inorganic lithium salts.

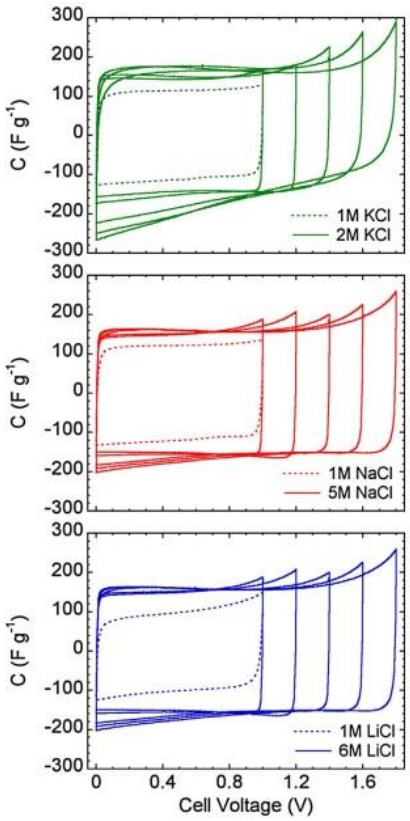


**Fig. 3.** CVs of symmetric supercapacitor cells (at 5 mV $s^{-1}$) using carbon AC16 in 1 M chloride solutions and 2 M KCl, 5 M NaCl and 6 M LiCl electrolytes, respectively.

intersection point (the high frequency limit) is the equivalent series resistance (ESR) which is commonly attributed to the electronic resistance of electrodes and the ionic resistance of bulk electrolyte [8]. Although in all cases the values are below ~0.50 Ω $cm^2$, there is a clear improvement from increasing the electrolyte concentration, reaching ESR values as low as ~0.20 Ω $cm^2$ in all the systems. As the electrochemical cells are prepared using the same cell components and following the same cell assembly procedure, the improvement in the ESR is assumed to be due to the higher electrolyte conductivity. Note also that the conductivities of all the electrolytes are very similar, and thus, not much divergence in the values can be expected. Moreover, for the highest electrolyte concentrations, the medium-frequency steep line, which is characteristic of ion transport in the porosity [23,24] is shifted towards lower resistance values. Noteworthy, the electrolyte resistance inside the pores is in line with the trend in the electrolyte conductivities for bulk electrolyte, which can be anticipated but is not an obvious result. As the only difference between the cells is the electrolyte concentration, it can be speculated that the lower in-pore resistance is due to the higher population of ions in the pore network, which shortens transport pathways under electrode polarization.

As is the case for their sulphate counterparts, the pH of aqueous alkali metal chloride solutions is also close to neutral, *i.e.*, the operational voltage window of the cells using these electrolytes can also be extended beyond the typical ~1.0 V of aqueous cells. Fig. 3 depicts a CV recorded for the 3 electrolytes at 5 mV $s^{-1}$ from 1.0 V up to 1.8 V. For the cells prepared using LiCl and NaCl the shape of the CVs remains rectangular despite the increase in the cell voltage. However, the cell working in 2 M KCl exhibits a much more distorted rectangular shape, which is mostly due to water reduction (as detailed below). In fact, in the latter case the absolute value of both anodic and cathodic currents increases significantly when the cell is cycled above 1.6 V.

The lower electrolyte stability is also reflected in the rate capability (Fig. 5). The recorded capacitance at low current densities is higher in those cells using NaCl and KCl, mainly due to the faradic contribution derived from the partial electrolyte decomposition, which is not a reversible charge storage mechanism. Nevertheless, the capacitance retention is higher in the cells operating in LiCl upon increasing the current density, *i.e.* 63, 47 and 32% at 30 A $g^{-1}$ for Li, Na and K metal chloride salts respectively.

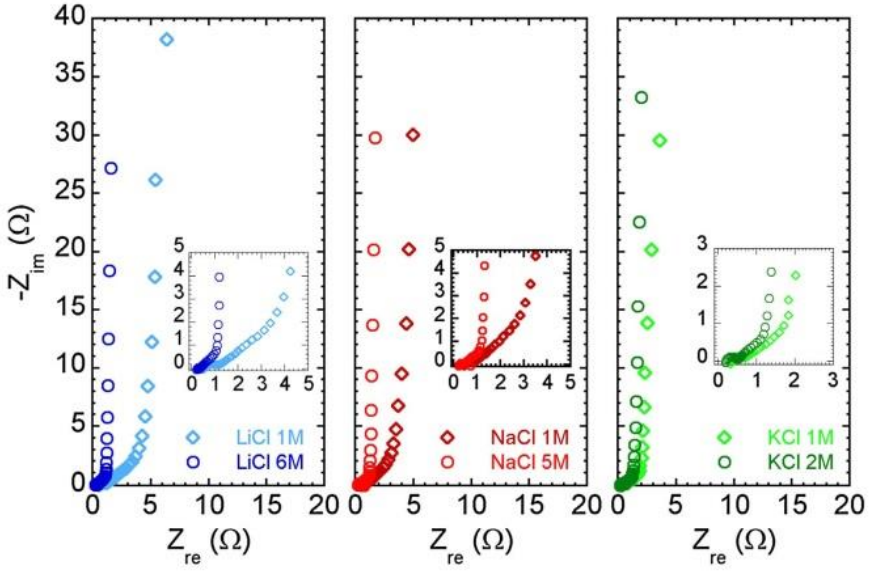


**Fig. 4.** Comparison of Nyquist plots for chloride-based symmetric supercapacitor cells using 1 M solutions and solutions providing maximum electrical conductivity.

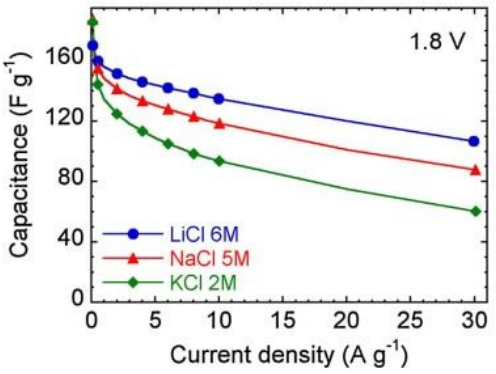


**Fig. 5.** Capacitance as a function of the current density for a cell voltage of 1.8 V.

In order to check the stability of the different cells at 1.8 V, floating tests were carried out. Given a certain upper cut-off voltage value, the total time required to provide for reliable stability estimation is significantly shortened in floating tests, typically taking few hundred hours over a few thousand hours spent in conventional cycling typical of battery testing. The floating tests show a clear difference among the three different systems. KCl-based cell presents a capacitance decrease of more than 50% at 1.8 V after the floating time slightly exceeding 4 h. In the case of NaCl, the capacitance decreases to 60% after a 100 h test at the same operation voltage whereas the capacitance retention is higher than 60% under the same conditions when using LiCl electrolyte (Fig. 6a). In any case, if the end-of-life criterion is set as a capacitance loss of 20% of the initial value [19], none of the symmetric systems would meet this condition if the maximum voltage is pushed up to 1.8 V.

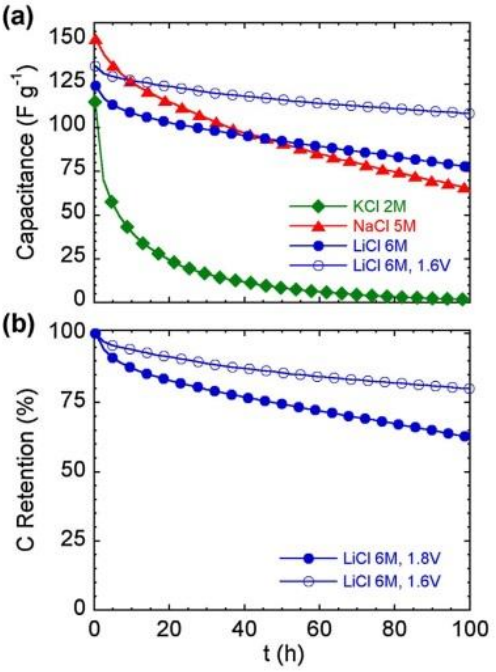


**Fig. 6.** Capacitance as a function of floating time: a) for chloride salts at the maximum cell voltage of 1.8 V and b) lithium chloride salts at the maximum cell voltage of 1.6 V and 1.8 V.

On the contrary, when the upper cut-off voltage is decreased to 1.6 V, the cell working in 6 M LiCl exhibits a much more stable profile, retaining 80 % of the initial capacitance after holding the maximum voltage for 100 h (Fig. 6b). Thus, although the rate capability measurements suggest a voltage of 1.8 V as the optimum value, floating experiments clearly show that this upper voltage limit is too demanding. Therefore, for alkali metal chloride salts, *viz.* 6 M LiCl, 1.6 V should be considered as the optimum voltage for symmetric cells [25], which is still 0.6–0.8 V higher than the typical 0.8–1.0 V used when operating in either 6 M KOH or 1 M $H_2SO_4$. Although the specific capacitance of carbon AC16 in 6 M LiCl is about 45% lower than in basic or acidic media, according to Eq. (1) the specific energy of the system will still be up to 40% higher in neutral medium using chloride salts.

The reasons for the varied stability of symmetric supercapacitors based on different chloride salts can be looked into in the behaviour of the separate electrodes in two-electrode symmetric cells, as presented in Fig. 7 for cut-off voltages of 1.6 and 1.8 V. Both negative and positive electrodes work outside the thermodynamic stability window of water defined by the Nernst equation for all symmetric cells charged up to 1.8 V. However, three-electrode measurements clearly demonstrate that the practical stability range at negative potential values goes well beyond the corresponding thermodynamic stability limit. As mentioned in the introduction, this is due to the excess of $OH^-$ ions in the porosity of the negative electrode at pH values ~7 [11,26]. By comparing the potential ranges of each electrode with the stability range defined by three-electrode measurements, one can evidence that negative electrodes operate at a potential lower than the practical potential of molecular hydrogen evolution. Noteworthy, the positive electrodes of the cells using LiCl and KCl surpass the positive potential stability limit to a lower extent

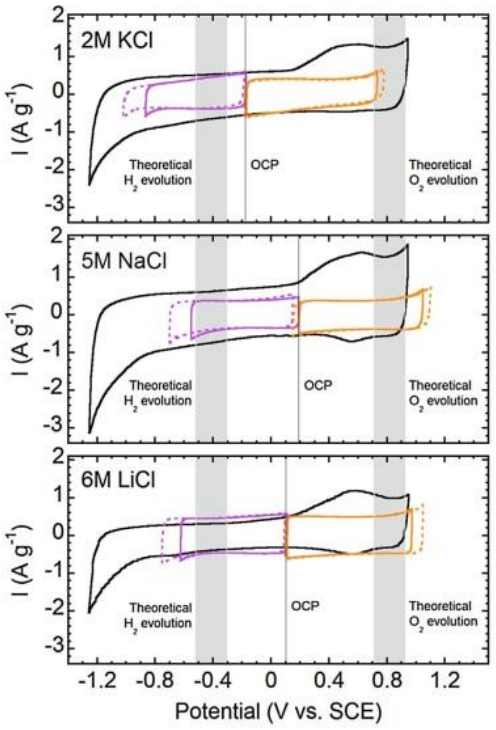


**Fig. 7.** Cyclic voltammograms in three- (black line) and two-electrode (positive electrode in orange and negative electrode in purple) cell configurations at 5 mV $s^{-1}$ in 2 M KCl, 5 M NaCl and 6 M LiCl.

(virtually not exceeding the oxygen evolution potential for the cells operating up to 1.6 V) whereas the potential of the positive electrode of the NaCl-based cell is significantly above the oxygen evolution potential, which explains its worse cell performance under floating (Fig. 6a). The limitation of symmetric cells set by the positive electrode coincides with the results obtained for neutral sulphate electrolytes [26]. Fig. 7 also shows that the open circuit potential (OCP) of the cell using 2 M KCl is shifted towards more negative values compared to LiCl and NaCl-based cells. This leads to the negative electrode of the symmetric cell being close to the stability limit established from three-electrode measurements. Thus, the most probable origin of the extremely poor floating response of the 2 M KCl-based cell is dihydrogen evolution in the negative electrode. To sum up, the comparison between the CVs of three- and two-electrode cells clearly shows that a symmetric configuration is not the optimum option for neutral chloride electrolytes. Taking into account the potential of oxygen evolution and the practical potential of irreversible molecular hydrogen evolution, an asymmetric cell operating stably in a voltage window of 1.8 V can be foreseen. Further improvements can also be expected from a purposeful oxidation of carbon surface to raise the practical stability limit at the positive electrode [11].

The advantage of using an electrolytic salt with low-sized ions is further highlighted using a moderately-activated AC with most of the pores in the ultramicropore range (<0.7–0.8 nm). The advantages of such carbons can be, in some cases, their higher density (*i.e.*, higher volumetric energy) and lower cost (they are produced under milder activation conditions). For this purpose, an activated carbon prepared with a low KOH consumption in the synthesis, AC12, was selected as the active material (Table S1). For comparison with chlorides, 1 M $Li_2SO_4$ was chosen as the electrolyte since this concentration was shown to provide the optimum supercapacitor performance [9]. On cycling up to 1.6 V at low scan rates in both LiCl and $Li_2SO_4$, *i.e.* at 5 mV $s^{-1}$, the shape of the CVs is close to the expected rectangular profile of capacitive systems and the capacitance is similar (Fig. 8a), ~150 F $g^{-1}$. This is further corroborated by GA charge/discharge cycles at low current densities (Fig. 8b) (see also charge/discharge profiles in Fig. S3). However, the increase in the current density up to 30 A $g^{-1}$ leads to a more pronounced capacitance decay in the cell working in $Li_2SO_4$, observing just 15% of capacitance retention for the sulphate-based cell whereas the retention of the cell working in the chloride salt is 27%. For comparative purposes the rate capability of the cell operating in 6 M LiCl is also shown, *i. e.* ~66% of capacitance retention. Again, the drastic change in capacitance retention underlines the decisive role of electrolyte concentration in ensuring efficient high-rate capacitive response.

The overall capacitance decay of the latter system is comparable to that observed when working up to 1.8 V in carbon AC16 (Fig. 5). The capacitance loss at 1.8 V for AC16 carbon with more open porosity is related to a detrimental Faradaic contribution (electrolyte decomposition in the positive electrode) whereas the capacitance loss observed for AC12 carbon at a cell voltage of 1.6 V is rather associated with the size match between the ions and the pores, impeding high-rate ion transport in the pores of AC12 to a higher extent than for AC16.

In other words, taking into account that the average pore size of AC12 is only slightly larger than the size of hydrated $SO_4^{2-}$ (0.79 nm *vs* 0.733 nm), applying medium-to-high current density values would lead to the transport of sulphate ions being much more hindered than that of smaller $Cl^-$ anions. Thus, these results reveal LiCl as a good alternative electrolyte choice if one aims at not being limited by the AC used as the active material in terms of pore size distribution. Despite the quite different electrical conductivities of AC12 and AC16 carbons, 2 and 30 S $m^{-1}$ correspondingly, the capacitance retention in 6 M LiCl is very similar in both cases,

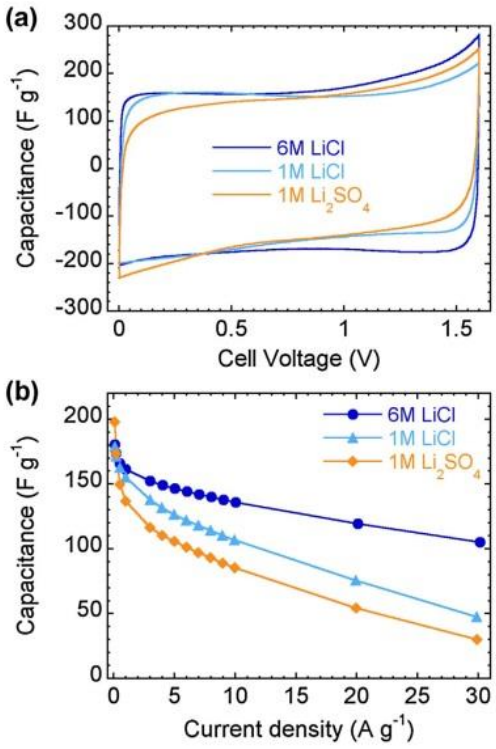


**Fig. 8.** (a) CVs of symmetric supercapacitor cells using AC12 carbon in LiCl and $Li_2SO_4$ electrolytes at 5 mV $s^{-1}$ in a cell voltage of 1.6 V. (b) Capacitance as a function of current density for cell voltage of 1.8 V.

which also evidences that high-rate capacitance can be related to the concentration-dependent electrical conductivity of the electrolyte and not to that of the electrode material as long as carbon pores are sufficiently wide not to impede ion transport.

## 4. Conclusion

We have demonstrated a drastic effect of chloride salts' concentration on the performance of the corresponding symmetric supercapacitor cells: the highest capacitance retention and the lowest cell resistance are enabled by the electrolyte concentration providing the maximum electrical conductivity of the related solutions. The EIS study has clearly evidenced that bulk electrolyte conductivity not only impacts ESR, but it also significantly reduces the resistance related to the ion transport inside the pores. Knowing that chlorides can be coupled with more affordable ultramicroporous carbons due to their smaller size, we have demonstrated that using chlorides with such ultramicroporous carbons can provide better rate response in aqueous extended-voltage supercapacitors. In a broader context, our work emphasizes that optimizing electrolytes can bring about substantial improvements in the performance of supercapacitors even using traditional electrode materials such as activated microporous carbons.

## Acknowledgments

The work was supported by the Basque Government under the Etortek Energigune'12 and Elkartek 2015 Programs. The authors acknowledge Norit for providing activated carbon.

## Appendix A. Supplementary data

Supplementary data associated with this article can be found, in the online version, at http://dx.doi.org/10.1016/j.electacta.2016.10.141.

## References


[1] P. Simon, Y. Gogotsi, Nanostructured activated carbons from natural precursors for electrical double layer capacitors, Nat Mater. 7 (11) (2008) 845–854.
[2] F. Béguin, E. Frackowiak, Supercapacitors: Materials, Systems, and Applications, Wiley-VCH Verlag GmbH & Co KGaA, 2013.
[3] F. Béguin, V. Presser, A. Balducci, E. Frackowiak, Carbons and electrolytes for advanced supercapacitors, Adv. Mater. 26 (14) (2014) 2219–2251.
[4] L. Wei, G. Yushin, Nanostructured activated carbons from natural precursors for electrical double layer capacitors, Nano Energy 1 (4) (2012) 552–565.
[5] C. Zhong, Y. Deng, W. Hu, J. Qiao, L. Zhang, J. Zhang, A review of electrolyte materials and compositions for electrochemical supercapacitors, Chem. Soc. Rev 44 (2015) 7484–7539.
[6] http://www.sigmaaldrich.com/catalog/product/sial/271004 (last access 28/09/2016).
[7] A. Burke, Ultracapacitors: why, how, and where is the technology, J.Power Sources 91 (1) (2000) 37–50.
[8] R. Kötz, M. Carlen, Principles and applications of electrochemical capacitors, Electrochim. Acta 45 (15–16) (2000) 2483–2498.
[9] K. Fic, G. Lota, M. Meller, E. Frackowiak, Novel insight into neutral medium as electrolyte for high-voltage supercapacitors, Energy Environ Sci. 5 (2) (2012) 5842–5850.
[10] L. Demarconnay, E. Raymundo-Piñero, F. Béguin, A symmetric carbon/carbon supercapacitor operating at 1.6 V by using a neutral aqueous solution, Electrochem. Comm. 12 (10) (2010) 1275–1278.
[11] Q. Gao, L. Demarconnay, E. Raymundo-Piñero, F. Béguin, Exploring the large voltage range of carbon/carbon supercapacitors in aqueous lithium sulfate electrolyte, Energy Environ Sci. 5 (11) (2012) 9611–9617.
[12] S.-E. Chun, J. Whitacre, Investigating the role of electrolyte acidity on hydrogen uptake in mesoporous activated carbons, J. Power Sources 242 (2013) 137–140.
[13] L. Eliad, G. Salitra, A. Soffer, D. Aurbach, Ion sieving effects in the electrical double layer of porous carbon electrodes: Estimating effective ion size in electrolytic solutions, J. Phys. Chem. B 105 (29) (2001) 6880–6887.
[14] J. Chmiola, G. Yushin, Y. Gogotsi, C. Portet, P. Simon, P.L. Taberna, Anomalous increase in carbon capacitance at pore sizes less than 1 nanometer, Science 313 (5794) (2006) 1760–1763.
[15] E. Raymundo-Piñero, K. Kierzek, J. Machnikowski, F. Béguin, Relationship between the nanoporous texture of activated carbons and their capacitance properties in different electrolytes, Carbon 44 (12) (2006) 2498–2507.
[16] H. Tamai, M. Kouzu, M. Morita, H. Yasuda, Highly mesoporous carbon electrodes for electric double-layer capacitors, Electrochem. Solid State Lett. 6 (10) (2003) A214–A217.
[17] E. Redondo, J. Carretero-González, E. Goikolea, J. Ségalini, R. Mysyk, Effect of pore texture on performance of activated carbon supercapacitor electrodes derived from olive pits, Electrochim. Acta 160 (2015) 178–184.
[18] J. Jagiello, J. Oliver, 2D-NLDFT adsorption models for carbon slit-shaped pores with surface energetical heterogeneity and geometrical corrugation, Carbon 55 (2013) 70–80.
[19] D. Weingarth, A. Foelske-Schmitz, R. Kötz, Cycle versus voltage hold—Which is the better stability test for electrochemical double layer capacitors? J. Power Sources 225 (2013) 84–88.
[20] L.J. van der Pauw, A method of measuring specific resistivity and Hall Effect of discs of arbitrary shape, Philips Research Reports 13 (1958) 1–9.
[21] R. Gilliam, J. Graydon, D. Kirk, S. Thorpe, A review of specific conductivities of potassium hydroxide solutions for various concentrations and temperatures, Int. J. Hydrogen Energy 32 (3) (2007) 359–364.
[22] International Critical Tables, Vol. VI, pp. 230-258; McGraw Hill, 1929.
[23] R. de Levie, Porous Electrodes in Electrolyte Solutions, I Capacitance effects, Electrochim. Acta 8 (10) (1963) 751–780.
[24] R. de Levie, On Porous Electrodes in Electrolyte Solutions -IV, Electrochim. Acta 9 (9) (1964) 1231–1245.
[25] M.P. Bichat, E. Raymundo-Piñero, F. Béguin, High voltage supercapacitor built with seeweed carbons in neutral aqueous electrolyte, Carbon 48 (2010) 4351–4361.
[26] Q. Abbas, P. Ratajczak, P. Babuchowska, A. Le Comte, D. Bélanger, T. Brousse, F. Béguin, Strategies to improve the performance of carbon/carbon capacitors in salt aqueous electrolytes, J. Electrochem. Soc. 162 (5) (2015) A5148–A5157.

**SUPPLEMENTARY INFORMATION**

# Investigating the role of electrolyte concentration on the performance of aqueous chloride-based supercapacitors with extended voltage window

Edurne Redondo[a], Eider Goikolea[a*], Roman Mysyk[a]

[a]CICenergiGUNE, Arabako Teknologi Parkea, Albert Einstein 48, 0150 Miñano, Spain

[*]Corresponding author Tel.: +34 94 529 71 08

E-mail address: egoikolea@cicenergigune.com

Table S1. Textural properties of microporous carbons with respect to the accessibility of ions to pore surface.

| **Carbon** | ***AC12*** | ***AC16*** |
|---|---|---|
| ***BET SSA, $m^2 g^{-1}$*** | *1826* | *2429* |
| ***DFT SSA, $m^2 g^{-1}$*** | *1551* | *2364* |
| ***Micropore volume, $cm^3.g^{-1}$*** | *0.48* | *1.03* |
| ***Mesopore volume, $cm^3.g^{-1}$*** | *0* | *0.08* |
| ***Accessible DFT SSA ($Cl^-$), $m^2 g^{-1}$*** | *1551* | *2364* |
| ***Accessible DFT SSA ($SO_4^{2-}$), $m^2 g^{-1}$*** | *821* | *1828* |
| ***Accessible DFT SSA, ($M^+$), $m^2 g^{-1}$**** | *1551* | *2364* |
| ***Average pore size, nm*** | *0.65* | *1.15* |
| ***Accessible average pore size ($Cl^-$)**** | *0.65* | *1.15* |
| ***Accessible average pore ($SO_4^{2-}$)**** | *0.79* | *1.24* |
| ***Accessible average pore size ($M^+$)**** | *0.66* | *1.15* |

*The lower limit to accessible porosity is set according to Ref [13]. Dehydrated $Cl^-$ 0.362-0.42 nm, hydrated alkali metals ($M^+$) 0.362-0.42 nm, hydrated $SO_4^{2-}$ - 0.58 nm. For the ions whose size is comprised within a size range, the upper limit was taken in the calculations of average accessible pore size as a threshold value (the lowest accessible pore size).

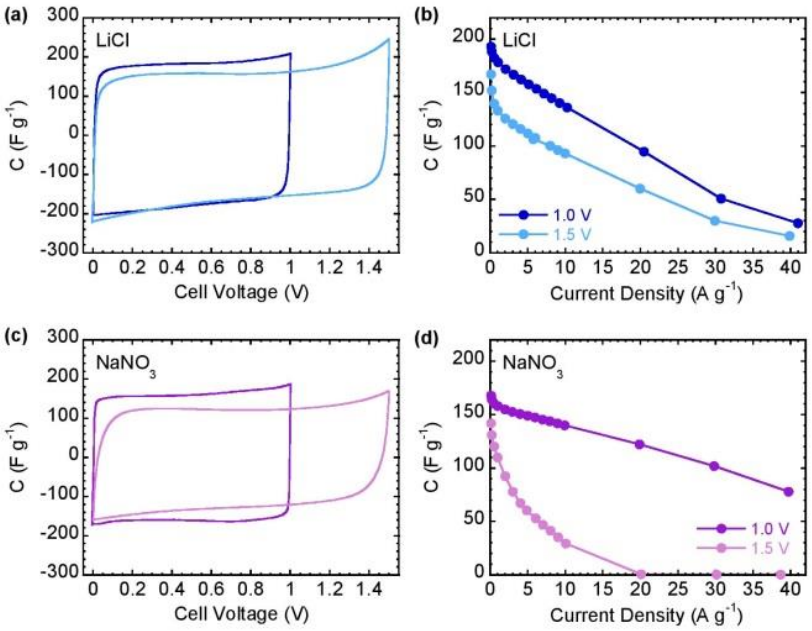


Fig. S1. Comparative electrochemical response of the cells using lithium chloride and sodium nitrate aqueous solutions as electrolytes. (a) and (c) CVs measured at 5 mV $s^{-1}$ at a cell voltage of 1.0 V and 1.5 V. (b) and (d) Rate capability in terms of specific capacitance for the cells cycled up to 1.0 V and 1.5 V.

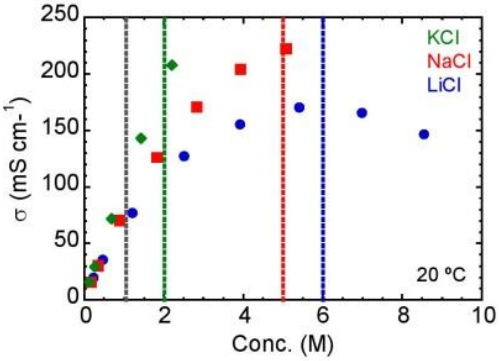


Fig. S2. Electrical conductivity of electrolyte solutions as a function of concentration (from Ref 22).

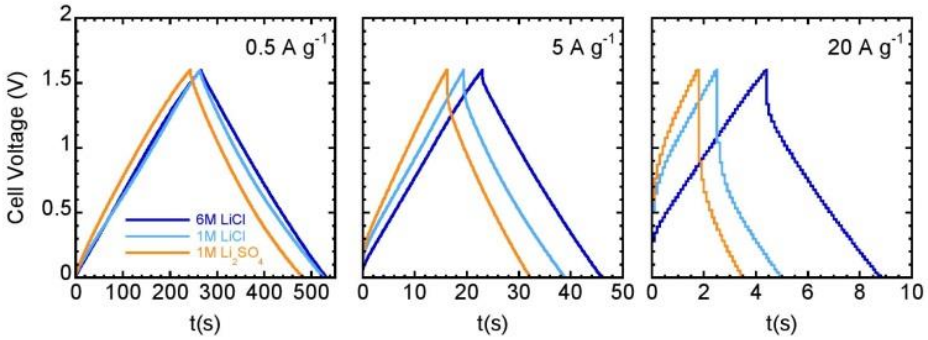


Fig. S3. Galvanostatic charge/discharge profiles of supercapacitor cells using AC12 carbon and working in 6M and 1M LiCl and 1M $Li_2SO_4$ at various current densities.

## 5.4 Outstanding room-temperature capacitance of biomass-derived microporous carbons in ionic liquid electrolyte

Electrochemistry Communications 79 (2017) 5–8

Contents lists available at ScienceDirect

Electrochemistry Communications

journal homepage: www.elsevier.com/locate/elecom

# Outstanding room-temperature capacitance of biomass-derived microporous carbons in ionic liquid electrolyte

Edurne Redondo[a], Wan-Yu Tsai[b,c], Barbara Daffos[b,c], Pierre-Louis Taberna[b,c], Patrice Simon[b,c,*], Eider Goikolea[a], Roman Mysyk[a,**]

[a] CIC Energigune, Arabako Teknologi Parkea, Albert Einstein 48, 01510 Miñano, Spain
[b] Université Paul Sabatier Toulouse III, Institut Carnot CIRIMAT, UMR CNRS 5085, 118 route de Narbonne, 31062 Toulouse, France
[c] Réseau sur le Stockage Electrochimique de l'Energie (RS2E), FR CNRS 3459, France

ARTICLE INFO

*Keywords:*
Supercapacitors
Activated carbon
Micropores
Ionic liquids

ABSTRACT

A remarkable capacitance of 180 $F \cdot g^{-1}$ (at 5 $mV \cdot s^{-1}$) in solvent-free room-temperature ionic liquid electrolyte, 1-ethyl-3-methylimidazolium bis(trifluoromethylsulfonyl)imide, was achieved in symmetric supercapacitors using microporous carbons with a specific surface area of ca. 2000 $m^2 \cdot g^{-1}$ calculated from gas sorption by the 2D-NLDFT method. The efficient capacitive charge storage was ascribed to textural properties: unlike most activated carbons, high specific surface area was made accessible to the bulky ions of the ionic liquid electrolyte thanks to micropores (1–2 nm) enabled by fine-tuning chemical activation. From the industrial perspective, a high volumetric capacitance of ca. 80 $F \cdot cm^{-3}$ was reached in neat ionic liquid due to the absence of mesopores. The use of microporous carbons from biomass waste represents an important advantage for large-scale production of high energy density supercapacitors.

## 1. Introduction

Electrical double layer capacitors (EDLCs) store charge by electrostatic interaction between electrolyte ions and electrode surface charges [1]. Room temperature ionic liquids (RTILs) [2] have been proposed as electrolytes for advanced and safe EDLCs for their wide stable electrochemical window, wide operational temperature range and non-volatility. However, RTILs exhibit high viscosity and low ionic conductivity at room temperature; hence, electrolyte ions have hindered access into the narrow micropores of commercial activated carbons (ACs). Thus, RTIL-based supercapacitors often show low capacitance and high resistance compared to those using conventional electrolytes, based on organic solvents (acetonitrile or propylene carbonate) [3,4,5,6]. In this regard, two different approaches have been pursued to circumvent the drawbacks of RTILs and make them efficient in supercapacitors: i) dissolving RTILs in small amounts of organic solvents to increase ionic conductivity [7], and ii) employing electrode materials with fully electrolyte-accessible (open) surface, such as exohedral carbons [8] or mesoporous carbons [9]. The first approach is achieved detrimentally to the maximum cell voltage. The second cannot provide high capacitance (due to the low specific surface area (SSA) of such materials), and also requires complex synthetic procedures and/or expensive synthetic precursors. Recent investigations demonstrated improvements in gravimetric capacitance by combining RTILs containing 1-ethyl-3-methylimidazolium ($EMI^+$) ion and micro/mesoporous carbons with high pore volume (~2 $cm^3 \cdot g^{-1}$) [10,11]. However, high mesopore volume is detrimental to the density of materials. Thus, volumetric capacitance, the most industry-demanded metric, can be adversely affected with such carbons.

In this work, a series of ACs derived from low-cost green precursors (olive pits) was synthesized [12] and tested as electrode materials in neat 1-ethyl-3-methylimidazolium bis(trifluoromethanesulfonyl)imide (EMI-TFSI) at room temperature. These carbons contain only micropores that can be easily fine-tuned through synthesis parameters. The results showed high gravimetric and volumetric capacitance using such mesopore-free materials and EMI-TFSI within 3 V, thus offering interesting opportunities for industrial development since ACs come from cheap and abundant natural precursors.

## 2. Experimental

ACs were prepared by chemical KOH activation of olive pits, as reported elsewhere [12,13]. Briefly, the precursor was carbonized in a tubular furnace under an Ar flow of 100 $mL \cdot min^{-1}$ by heating at

* Correspondence to: P. Simon, Université Paul Sabatier Toulouse III, Institut Carnot CIRIMAT, UMR CNRS 5085, 118 route de Narbonne, 31062 Toulouse, France.
** Corresponding to: R. Mysyk, CIC Energigune, Arabako Teknologi Parkea, Albert Einstein 48, 01510 Miñano, Spain
*E-mail addresses:* simon@chimie.ups-tlse.fr (P. Simon), rmysyk@cicenergigune.com (R. Mysyk).

http://dx.doi.org/10.1016/j.elecom.2017.04.004
Received 22 February 2017; Received in revised form 20 March 2017; Accepted 5 April 2017
Available online 06 April 2017

5 °C·min$^{-1}$ and dwelling for 2 h at 700 °C. The samples of carbon char were mixed with different amounts of KOH and heated up under the same conditions described in the first step. Last, the ACs were washed off with diluted HCl and water until neutral pH, and dried at 120 °C under vacuum overnight.

$N_2$ adsorption was conducted using an ASAP2460 instrument (Micromeritics). The samples were outgassed under vacuum at 250 °C for 24 h before analysis. $N_2$ isotherms were measured at 77 K for relative pressures ($P/P_0$) between $10^{-7}$ and 0.995. The SSA and pore size distribution (PSD) were calculated using the SAIEUS software with 2D-NLDFT [14]. The differential pore volume (dV/dlgL) was calculated as:

$$dV/d\lg L = dV/dL \, L \ln 10 \quad (1)$$

Average pore size was calculated as the weighted average from PSD, according to Eqs. (2) or (3):

$$L_0 = \int_{V_{min}}^{V_{tot}} L dV / (V_{tot} - V_{min}) \quad (2)$$

$$L_i = \int_{V_{is}}^{V_{tot}} L dV / (V_{tot} - V_{is}) \quad (3)$$

where $L_0$ and $L_i$ correspond to the average pore size and the average ion-inaccessible pore size, L the pore size, $V_{is}$ the ion-inaccessible pore volume, and $V_{tot}$ the total pore volume from the cumulative DFT distribution [12].

The electrodes were made by mixing 95 wt% of ACs with 5 wt% of polytetrafluoroethylene (PTFE) binder from a 60 wt% aqueous dispersion. The mixture was stirred in ethanol to form a dough further rolled to a thickness of ~170 μm and dried under vacuum at 120 °C overnight. Disk electrodes of 11 mm diameter were cut out with the electrode mass between 7 and 8 mg·cm$^{-2}$. Two-electrode symmetric supercapacitors were assembled in Swagelok® cells using two identical activated carbon electrodes, a borosilicate glass fiber separator (Whatman GF/B) and EMI-TFSI, 99.9% (Solvionic) as electrolyte. Cell assembly was conducted in a glove box under Ar atmosphere with < 1 ppm of water and oxygen.

Electrochemical measurements were done at room temperature, 20 °C, using a multichannel potentiostat/galvanostat VMP3 (Biologic): cyclic voltammetry (CV) at a scan rate of 5 mV·s$^{-1}$, galvanostatic cycling (GC) at 0.1–30 A·g$^{-1}$·of active material per electrode and electrochemical impedance spectroscopy (EIS) from 1 MHz to 10 mHz.

Gravimetric and volumetric electrode capacitance (C) was calculated using Eqs. (4) and (5), respectively:

$$C = 2 \cdot \int Idt / (U \cdot m) \quad (4)$$

$$C = 2 \cdot \int Idt / (U \cdot \pi \cdot r^2 \cdot h) \quad (5)$$

where I is the current, t the discharge time, U the voltage, m the active material mass per electrode, r the radius and h the electrode thickness.

Series resistance was evaluated from the intercept of the real axis at high frequency of the Nyquist plot, and in-pore ionic resistance from the intercept of quasi-vertical line at low frequency with the real axis after excluding the series resistance [15].

## 3. Results and discussion

Textural properties are shown in Fig. 1 and Table 1. Since the maximum capacitance of carbide-derived porous carbons was found at pore size of ~0.72 nm using neat EMI-TFSI [16], pores narrower than 0.70 nm are considered poorly accessible to electrolyte ions due to the ion-sieving effect. Ion-accessible pore volume and surface area calculated using this cut-off (> 0.70 nm), $d_{50}$ and $d_{90}$ are listed in Table 1. $d_{50}$ and $d_{90}$ are the pore widths corresponding to 50 and 90% of the

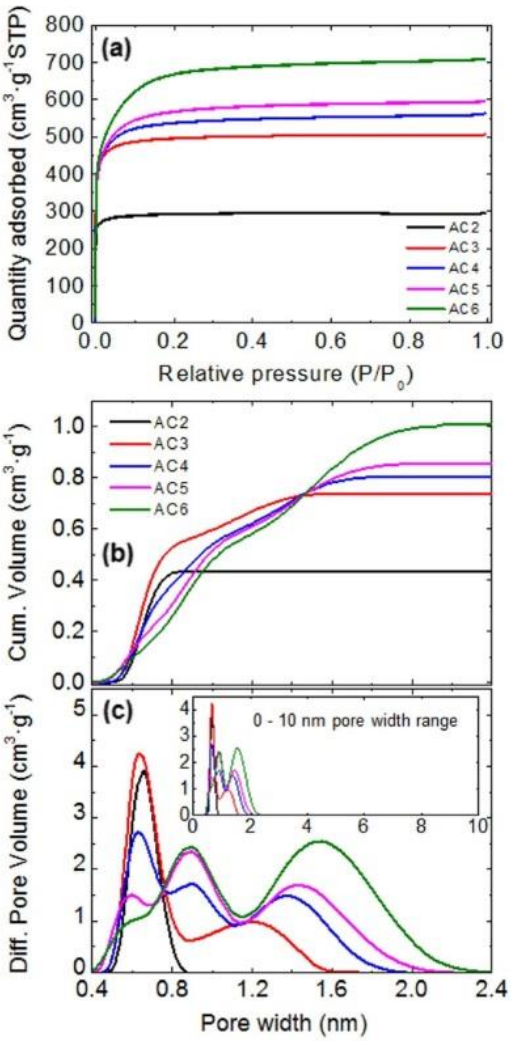


**Fig. 1.** (a) $N_2$ adsorption/desorption isotherms (b) cumulative (c) differential pore volume (dV/dlgL) vs pore size calculated by the 2D-NLDFT model.

total pore volume and their use was recently suggested for assessing PSD [17]. All the ACs have pores in the micropore range (< 2 nm) and, as reported elsewhere [18], PSD is widened with the higher KOH/carbon ratio. Thus, AC2 exhibits the smallest $L_0$ and $d_{50}$ among the studied ACs. Although AC3–AC6 have similar SSA, an increasing $L_0$ is observed from AC3 to AC6. Moreover, the difference between $d_{90}$ and $d_{50}$ increases correspondingly, meaning higher pore size dispersity with more KOH.

Fig. 2a and b show the CVs of symmetric cells for AC2-AC6 at 5 mV·s$^{-1}$ in EMI-TFSI. Most of the samples exhibit rectangular CVs typical of supercapacitors. Most importantly, high specific capacitance of 179 F·g$^{-1}$, 163 F·g$^{-1}$ and 171 F·g$^{-1}$ was measured for AC4, AC5 and AC6, respectively. To our knowledge, such high capacitance values have never been reported for purely microporous carbons in neat RTILs. By contrast, AC2 shows very low gravimetric capacitance since $d_{90}$ is below 0.75 nm, thus poorly accessible to cations and anions, in agreement with the accessible SSA of only 292 m$^2$g$^{-1}$ (Table 1). Compared with AC2, AC3 shows decent gravimetric capacitance with huge distortion at high polarisation, meaning that, even with higher SSA, not all the pores are easily accessible to the electrolyte. The increase in $d_{50}$ beyond 0.70 nm and the associated $L_i$, such as that

**Table 1**
Textural properties of the ACs.

| Sample Name | KOH-carbon Ratio | DFT-SSA ($m^2 \cdot g^{-1}$) | Volume ($cm^3 \cdot g^{-1}$) | $L_0$ (nm) | $d_{50}$ (nm) | $d_{90}$ (nm) | DFT-SSA (> 0.70 nm) ($m^2 \cdot g^{-1}$) | Volume (> 0.70 nm) ($cm^3 \cdot g^{-1}$) | $L_i$ (> 0.70 nm) (nm) |
|---|---|---|---|---|---|---|---|---|---|
| AC2 | 2 | 1362 | 0.439 | 0.66 | 0.65 | 0.75 | 292 | 0.107 | 0.74 |
| AC3 | 3 | 2048 | 0.738 | 0.78 | 0.68 | 1.19 | 713 | 0.328 | 0.97 |
| AC4 | 4 | 1965 | 0.807 | 0.98 | 0.83 | 1.45 | 1031 | 0.523 | 1.14 |
| AC5 | 5 | 1986 | 0.858 | 1.01 | 0.91 | 1.55 | 1223 | 0.642 | 1.15 |
| AC6 | 6 | 2084 | 1.010 | 1.18 | 1.04 | 1.73 | 1486 | 0.844 | 1.30 |

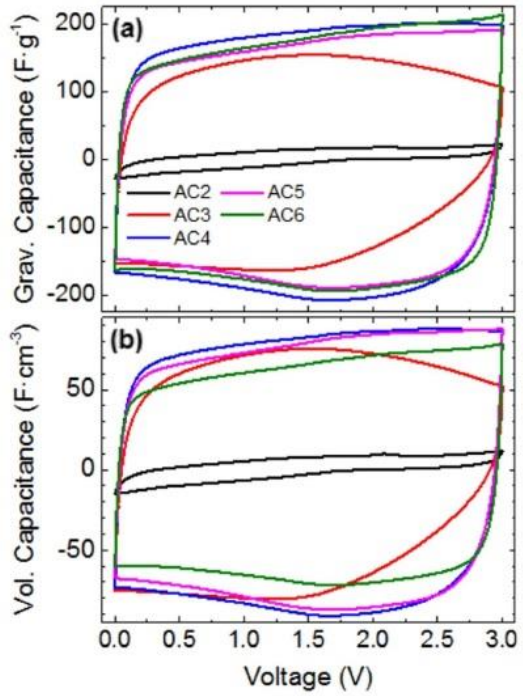


**Fig. 2.** Cyclic voltammograms of ACs from olive pits at a scan rate of 5 $mV \cdot s^{-1}$ in neat EMI-TFSI at room temperature [20 °C] (a) gravimetric and (b) volumetric capacitance.

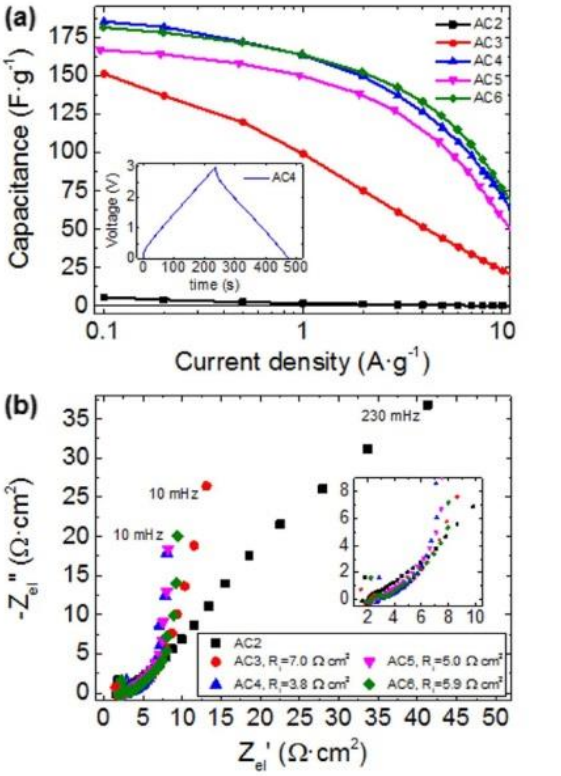


**Fig. 3.** (a) Capacitance of ACs in neat EMI-TFSI as a function of current density (inset - galvanostatic charge-discharge profile at 1 $A \cdot g^{-1}$); (b) Nyquist plot Ohm·$cm^2$ per electrode (inset - high frequency range).

achieved for AC4, enable a nice typical capacitive signature within 3 V. Thus, AC4 has a PSD wide enough to provide good access for $EMI^+$ and $TFSI^-$ ions to a large part of microporous surface, also achieving high gravimetric capacitance. Further increasing $L_i$ shows no improvement in capacitance (from AC4 to AC6). The higher capacitance of AC4 vs AC5 can arise due to stronger ion confinement due to narrower PSD as suggested theoretically [19] and experimentally measured [16,17,22].

More interestingly, Fig. 2b shows that a high volumetric capacitance of 80, 75 and 63 $F \cdot cm^{-3}$ was achieved for AC4, AC5 and AC6, respectively. Such high values in RTILs are unusual for biomass-derived microporous carbons with irregular porosity and are comparable or even higher than in solvent-based electrolytes [20]. Since the volumetric capacitance is a key parameter from industrial prospective regarding device miniaturization, these results are highly promising for the energy density of devices. Obviously, high volumetric capacitance was achieved thanks to the moderate pore volume in strictly microporous carbons, which distinguishes them from carbons with ultrahigh-pore volume (~2 $cm^3 \cdot g^{-1}$) that also provide high gravimetric capacitance, but have significant mesoporosity, which is detrimental to volumetric performance [9]. A recent study [21] also reports high gravimetric capacitance in neat IL electrolyte for a carbon with ~20% higher pore volume than that of AC4, detrimentally to the volumetric capacitance (not calculated).

Rate capability is an important metric in supercapacitor performance, which depends on the complex interplay between textural and electrical properties of porous carbons and in-pore ion transport [22,23]. Fig. 3 shows that capacitance retention is poor for AC2 and AC3, due to the poorly accessible porous structure. It increases for AC4–AC6 showing similar capacitance retention of ~65% at 5 $A \cdot g^{-1}$ and ~40% at 10 $A \cdot g^{-1}$. The similar capacitance retention for AC4 to AC6 evidences that AC4 provides a well-suited PSD to ensure not only high capacitance, but also sufficiently fast ion transport in micropores. No harsher activation conditions are required other than a KOH-carbon ratio of 4 at 700 °C. The observed capacitance loss can be linked to the limited ionic conductivity (8.4 $mS \cdot cm^{-1}$) and high viscosity (28.0 mPa·s) of EMI-TFSI [6]. For the conventional EDLC salt, $TEABF_4$, conductivity reaches up to 60 $mS \cdot cm^{-1}$ in acetonitrile [24] and 20 $mS \cdot cm^{-1}$ in propylene carbonate [25].

Nyquist plots (Fig. 3b) show typical capacitive impedance response with a quasi-vertical line at the low frequency (except for AC2), and a ~ 45° slope line in the medium frequency due to the porous electrode RC distribution [26,27]. Fig. 3b demonstrates a rather low series resistance, varying between 2.0 and 2.8 $\Omega \cdot cm^2$ for AC4-AC6 electrodes, whereas the in-pore ionic resistance fluctuates within 3.8–7.0 $\Omega \cdot cm^2$.

The last confirms that the porosity of AC4 is well adapted to provide efficient ion transport with EMI-TFSI, and further pore enlargement is not needed for high power demand.

Both low series and in-pore resistance are comparable with the literature data for another ionic liquid with the same cation ($EMI^+ BF_4^-$) [9]. In that case, carbons with a significant mesopore volume favoured more rapid in-pore ion transport, detrimentally to volumetric capacitance. By contrast, our results are obtained with the ACs of a $d_{90}$ below 2 nm, thereby suggesting that mesoporosity is not always required to ensure fast propagation of RTIL ions inside pores. Overall, impedance data also evidence efficient high-rate operation with RTILs and the studied microporous carbons.

## 4. Conclusions

In summary, microporous carbons from olive pits deliver a high capacitance of 180 $F \cdot g^{-1}$ and a low resistance of 4 $\Omega \cdot cm^2$ at room temperature in neat EMI-TFSI ionic liquid. This work reveals efficient capacitive response with RTILs and strictly microporous carbons, which also enables a high volumetric capacitance of 80 $F \cdot cm^{-3}$. Furthermore, carbons were prepared from biomass waste via a regular chemical activation procedure, which excludes complicated high-cost synthetic routes and synthetic precursors, and is therefore easily scalable.

Although the electrochemical behaviour showed good agreement with the ion-accessible area, it is still difficult to know the best carbon microstructure (PSD, relationship between ion-accessible SSA and volume …) due to the lack of techniques to probe carbon geometric topology, and in-situ ion transport. Apart from the accessibility of pores to ions, other parameters, including surface chemistry and defects [28], need to be thoroughly investigated to provide detailed insight into the outstanding performance of microporous carbons in RTILs.

## Acknowledgments

This work was funded by the Basque Government under the Etortek Energigune '12 (Project Reference IE12-335) and Elkartek 2015 (Project CICE2015, Reference KK-2015/0000100) Programs. W.-Y. T. was supported by the European Research Council (ERC, Advanced Grant, ERC-2011-AdG, Project 291543—IONACES).

## References

[1] P. Simon, Y. Gogotsi, Materials for electrochemical capacitors, Nat. Mater. 7 (2008) 845–854.
[2] H. Ohno, Electrochemical Aspects of Ionic Liquids, 2nd edition, Wiley, 2011.
[3] A. Matic, B. Scrosati, Ionic liquids for energy applications, MRS Bull. 38 (2013) 533–537.
[4] D.R. Mac-Farlane, N. Tachikawa, M. Forsyth, J.M. Pringle, Patrick C. Howlett, G.D. Elliot, J.H. David, M. Watanabe, P. Simon, C.A. Angell, Energy applications of ionic liquids, Energy Environ. Sci. 7 (2014) 232–250.
[5] R. Mysyk, V. Ruiz, E. Raymundo-Piñero, R. Santamaria, F. Béguin, Capacitance evolution of electrochemical capacitors with tailored nanoporous electrodes in pure and dissolved ionic liquids, Fuel Cells 10 (2010) 834–839.
[6] N. Handa, T. Sugimoto, M. Yamagata, M. Kuta, M. Kono, M. Ishikawa, A neat ionic liquid electrolyte based on FSI anion for electric double layer capacitor, J. Power Sources 185 (2008) 1585–1588.
[7] A. Brandt, C. Ramirez-Castro, M. Anouti, A. Balducci, An investigation about the use of mixtures of sulfonium-based ionic liquids and propylene carbonate as electrolytes for supercapacitors, J. Mater. Chem. A 1 (2013) 12669–12678.
[8] R. Lin, P.L. Taberna, S. Fantini, V. Presser, C.R. Pérez, F. Malbosc, N.L. Rupesinghe, K.B.K. Teo, Y. Gogotsi, P. Simon, Capacitive energy storage from − 50 to 100 °C using an ionic liquid electrolyte, J. Phys. Chem. Lett. 2 (2011) 2396–2401.
[9] L. Wei, M. Sevilla, A.B. Fuertes, R. Mokaya, G. Yushin, Polypyrrole-derived activated carbons for high-performance electrical double-layer capacitors with ionic liquid electrolyte, Adv. Funct. Mater. 22 (2012) 827–834.
[10] X. Wang, H. Zhou, E. Sheridan, J.C. Walmsley, D. Ren, D. Chen, Geometrically confined favourable ion packing for high gravimetric capacitance in carbon–ionic liquid supercapacitors, Energy Environ. Sci. 9 (2016) 232–239.
[11] M. Lazzari, F. Soavi, M. Mastragostino, Mesoporous carbon design for ionic liquid-based, double-layer supercapacitors, Fuel Cells 10 (2010) 840–847.
[12] E. Redondo, J. Carretero-Gonzalez, E. Goikolea, J. Segalini, R. Mysyk, Effect of pore texture on performance of activated carbon supercapacitor electrodes derived from olive pits, Electrochim. Acta 160 (2015) 178–184.
[13] M. Molina-Sabio, F. Rodriguez-Reinoso, Colloids Surf. A Physicochem. Eng. Asp. 241 (2004) 15–25.
[14] J. Jagiello, J. Oliver, 2D-NLDFT adsorption models for carbon slit-shaped pores with surface energetical heterogeneity and geometrical corrugation, Carbon 55 (2013) 70–80.
[15] P.L. Taberna, P. Simon, J.F. Fauvarque, Electrochemical characteristics and impedance spectroscopy studies of carbon-carbon supercapacitors, J. Electrochem. Soc. 150 (2003) A292–A300.
[16] C. Largeot, C. Portet, J. Chmiola, P.L. Taberna, Y. Gogotsi, P. Simon, Relation between the ion size and pore size for an electric double-layer capacitor, J. Am. Chem. Soc. 130 (2008) 2730–2731.
[17] N. Jäckel, P. Simon, Y. Gogotsi, V. Presser, Increase in capacitance by subnanometer pores in carbon, ACS Energy Lett. 1 (6) (2016) 1262–1265.
[18] A. Ahmadpour, D.D. Do, The preparation of active carbons from coal by chemical and physical activation, Carbon 34 (4) (1996) 471–479.
[19] C. Merlet, C. Pean, B. Rotenberg, P.A. Madden, B. Daffos, P.L. Taberna, P. Simon, M. Salanne, Highly confined ions store charge more efficiently in supercapacitors, Nat. Commun. 4 (2013) 1–6.
[20] L. Wei, G. Yushin, Nanostructured activated carbons from natural precursors for electrical double layer capacitors, Nano Energy 1 (2012) 552–565.
[21] S. Leyva-Garcia, D. Lozano-Castello, E. Morallon, T. Vogl, C. Schutter, S. Passerini, A. Balducci, D. Cazorla-Amoros, Electrochemical performance of a superporous activated carbon in ionic liquid-based electrolytes, J. Power Sources 336 (2016) 419–426.
[22] J. Chmiola, G. Yushin, Y. Gogotsi, P. Simon, P.L. Taberna, Anomalous increase in carbon capacitance at pore sizes less than 1 nanometer, Science 313 (5794) (2006) 1760–1763.
[23] H. Tamai, M. Kouzu, M. Morita, H. Yasuda, Highly mesoporous carbon electrodes for electric double-layer capacitors, Electrochem. Solid-State Lett. 6 (10) (2003) A214–A217.
[24] T. Devaraian, S. Higashiya, C. Dangler, M. Rane-Fondacaro, J. Snyder, P. Haldar, Novel ionic liquid electrolyte for electrochemical double layer capacitors, Electrochem. Commun. 11 (3) (2009) 680–683.
[25] M. Ue, Chemical capacitors and quaternary ammonium salts, Electrochemistry 75 (8) (2007) 565–572.
[26] M. Hahn, M. Baertschi, O. Barbieri, J.-C. Sauter, R. Kötz, R. Gallay, Interfacial capacitance and electronic conductance of activated carbon double-layer electrodes, Electrochem. Solid-State Lett. 7 (2004) A33–A36.
[27] C. Portet, P.L. Taberna, P. Simon, C. Laberty-Robert, Modification of Al current collector surface by sol–gel deposit for carbon–carbon supercapacitor applications, Electrochim. Acta 49 (2004) 905–912.
[28] G. Moussa, C.M. Ghimbeu, P.L. Taberna, P. Simon, C. Vix-Guterl, Relationship between the carbon nano-onions (CNOs) surface chemistry/defects and their capacitance in aqueous and organic electrolytes, Carbon 105 (2016) 628–637.

## 5.5 Lithium and sodium ion capacitors with high energy and power densities based on carbons from recycled olive pits

Journal of Power Sources 359 (2017) 17–26

Contents lists available at ScienceDirect

Journal of Power Sources

journal homepage: www.elsevier.com/locate/jpowsour

# Lithium and sodium ion capacitors with high energy and power densities based on carbons from recycled olive pits

Jon Ajuria [a, *], Edurne Redondo [a], Maria Arnaiz [a], Roman Mysyk [a], Teófilo Rojo [a, b], Eider Goikolea [a, **]

[a] CIC Energigune, Albert Einstein 48, Alava Technology Park, 01510, Miñano, Vitoria-Gasteiz, Spain
[b] Inorganic Chemistry Department, University of the Basque Country UPV/EHU, P.O. Box 644, 48080, Bilbao, Spain

## HIGHLIGHTS

- Synthesis of Hard Carbon and Activated Carbon from recycled olive-pit bio-waste.
- Fabrication of Lithium Ion Capacitor exceeding 100 Wh $Kg^{-1}_{AM}$ and 10 KW $Kg^{-1}_{AM}$.
- Lithium Ion Capacitor with 90% capacity retention after 10000 cycles.
- Fabrication of Sodium Ion Capacitor exceeding 100 Wh $Kg^{-1}_{AM}$ and 7 kW $kg^{-1}$
- Sodium Ion Capacitor with 70% capacity retention after 5000 cycles.

## GRAPHICAL ABSTRACT

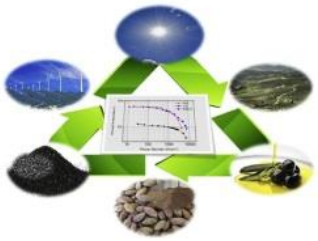

## ARTICLE INFO

*Article history:*
Received 31 January 2017
Received in revised form
25 April 2017
Accepted 30 April 2017
Available online 18 May 2017

*Keywords:*
Hard carbon
Activated carbon
Supercapacitor
EDLC
Lithium ion capacitor
Sodium ion capacitor

## ABSTRACT

In this work, we are presenting both lithium and sodium ion capacitors (LIC and NIC) entirely based on electrodes designed from recycled olive pit bio-waste derived carbon materials. On the one hand, olive pits were pyrolized to obtain a low specific surface area semigraphitic hard carbon to be used as the ion intercalation (battery-type) negative electrode. On the other hand, the same hard carbon was chemically activated with KOH to obtain a high specific surface area activated carbon that was further used as the ion-adsorption (capacitor-type) positive electrode. Both electrodes were custom-made to be assembled in a hybrid cell to either build a LIC or NIC in the corresponding Li- and Na-based electrolytes. For comparison purposes, a symmetric EDLC supercapacitor cell using the same activated carbon in 1.5 M $Et_4NBF_4$/acetonitrile electrolyte was also built. Both LIC and NIC systems demonstrate remarkable energy and power density enhancement over its EDLC counterpart while showing good cycle life. This breakthrough offers the possibility to easily fabricate versatile hybrid ion capacitors, covering a wide variety of applications where different requirements are demanded.



## 1. Introduction

In 1987 The World Commission on Environment and Development (WCED) defined the term sustainable development as the development that meets the needs of the present without compromising the ability of future generations to meet their own

* Corresponding author.
** Corresponding author.
*E-mail addresses:* jajuria@cicenergigune.com (J. Ajuria), egoikolea@cicenergigune.com (E. Goikolea).

http://dx.doi.org/10.1016/j.jpowsour.2017.04.107
0378-7753/

needs [1]. Since then, the increasing demand of energy consumption has boosted the consumption of fossil fuels, responsible of 65% of worldwide greenhouse emissions gases, which nowadays are accepted by wide scientific consensus to be the main accelerating factor of global warming. Accordingly, almost 30 years later, the latest report on climate change from the Intergovernmental Panel on Climate Change (IPCC), released in 2014, predicts that climate change will cause shortages of food and water and increased risk of flooding that will affect billions of people, particularly those living in poverty [2]. Thus, the next big challenge for society is to set alternative energy sources as vehicle for sustainable development. In this context, renewable energy that is infinite in its supply will help in environmental protection and long term sustainability. Nevertheless, renewables are intermittent and electrical energy storage systems (EESs) will be essential for the development of a low carbon energy system. EESs can supply more flexibility and balancing to the grid, providing a back-up to intermittent renewable energy [3]. In addition, the development of more efficient and cost-effective EESs will speed up the growth of electric vehicles (EVs) that promises to curb worldwide greenhouse gas emissions if powered from renewable sources.

Nowadays secondary batteries and supercapacitors are the two main technologies used to store electrochemical energy. Among secondary batteries, Li-ion batteries (LIBs) are the most popular for portable electronics and are growing in popularity for EV and aerospace applications [4]. LIBs store charge by means of electrochemical reactions taking place in the bulk of electrode materials. On one side, this faradaic mechanism enables batteries to have high energy density and low self-discharge. On the other side, it limits power capabilities and cycle life and charge and discharge times are in the range of several minutes to hours. With regard to supercapacitors, they store charge by means of physical adsorption of ions at the interface of the electrolyte and the surface of the electrode materials. This non-faradaic mechanism enables high power density, fast charge-discharge times within few seconds (<10 s) and long cycle life. On the contrary, it limits charge storage capacity, output voltage and energy density. It stands to reason that supercapacitors and batteries ideally complement each other to deliver high energy densities while affording peak power and offering longer cycle life [5–7]. In this context, the idea of merging a battery type and a supercapacitor type electrode in a single device emerged with the aim of bringing together high energy and high power densities combined with long cycle life.

In 2001 Amatucci et al. were amongst the first who brought the above-mentioned idea to life, assembling and characterizing a new generation energy storage system named Lithium Ion Capacitor (LIC) [8]. The combination of a negative battery-type lithium titanate (LTO) electrode and a positive capacitor type activated carbon (AC) resulted in a packaged energy of ca. 20 Wh $kg^{-1}$ which is about 4–5 times that of a standard Electric Double Layer Capacitor (EDLC). Since the redox potential of LTO is 1.5 V vs $Li/Li^+$, the operating voltage of the system was limited to 1.5–3.0 V. This system was intensively studied in the following years, in terms of electrode material [9], electrolyte [10] and cycle life [11] but it was not until 2010 that Naoi et al. made a real breakthrough in the field developing a high rate performing nano-structured composite of LTO with carbon nanofibers (LTO/CNF) prepared by simple sol–gel method under ultra-centrifugal force (65,000 N). Named by the authors as the "nanohybrid supercapacitor" (NHC), the system leads to 2–3 times higher volumetric energy densities with respect to EDLCs with 90% of capacity retention after 15000 cycles [12,13]. Currently the NHC is under co-development with Nippon Chemi-Con Corp. for mass production to place it in the market [14]. Recently, as a further step, Ogihara et al. have developed a novel hybrid capacitor system consisting of an intercalation metal–organic framework electrode which exhibits a flat plateau near 0.8 V vs. $Li/Li^+$ and an energy density 5–6 times higher than that of typical EDLCs maintaining a comparable power density [15].

In parallel, research has also been focused on the replacement of LTO by means of partially disordered graphitic carbons that present lower redox potential values, typically 1.5–0.01 V vs $Li/Li^+$, allowing for a wider cell voltage and ultimately higher energy density. In 2006 Aida et al. reached an outstanding volumetric energy density of 80 Wh $L^{-1}$ over the 1.0–4.3 V operating voltage window using a Li dopable non-graphitizable carbon as the anode and an AC as the cathode [16]. Despite the exceptional energy density value, this approach presents a series of shortcomings, such as the cycle life limitation or the inherent risk of intercalating lithium into graphite close to lithium plating voltage values. Some years later, in 2012, Sivakkumar et al. provided important insight into the degradation mechanisms of this sort of LIC, identifying the instability of the pre-lithiated graphite anode during the cycling as the root cause for the severe cell capacity fade. The observed positive potential drift of the pre-lithiated graphite was linked to the self-discharge of the graphite electrode, most probably due to poor solid electrolyte interphase (SEI) film formation, and the importance of a proper pre-lithiation process as one solution to circumvent this drawback was highlighted [17]. To date, the scientific studies related to new carbonaceous materials such as mesocarbon microbeads [18], hard carbons [19,20] or soft carbons [21] to be used as anodes have been scarce. Although pre-lithiation and the inherent risk of dendrite formation on graphitic anodes seemed to be major drawbacks, the technology has achieved tremendous progress under the secrecy of industrial policies and has gone up to commercialization [22,23].

A persistently major criterion to make hybrid supercapacitors a more viable energy solution is the overall cost of the system. With this regard there are two major constraints inherent to LICs: the cost of electrode materials and the usage of lithium. On the one side, it is well known that electrode materials are one of the major contributors to the cost of the supercapacitors [24]. Accordingly inexpensive electrode materials from renewable sources have recently received increased attention as a strategy to reduce the cost of the pristine materials [25]. On the other side, lithium is regarded as a non-abundant material and its occurrence is geographically limited to a few countries worldwide. Price is expected to skyrocket with the advent of the EV, which together with the promise of low-cost materials to replace lithium might hinder large scale production of EESs based on lithium-ion technology. In contrast to lithium, sodium resources are unlimited worldwide, moreover it is one of the most abundant elements on Earth. Hence, Na-ion battery (NIB) chemistries are currently under development as a less expensive and accessible alternative to LIBs [26,27]. Although much effort has been ongoing around sodium within the battery field, regarding hybrid supercapacitors there are very few works published to date. Indeed, it was not until 2012 that Yin et al. launched the first NIC based on titanate nanotubes that provided half the energy density of their LIC counterparts [28]. Also in 2012 Kuratani et al. fabricated the first NIC based on hard carbon (HC) and AC that performed similar to its lithium equivalent [29]. After a period without any apparent progress, in 2015 Ding et al. surprisingly surpassed performance of LICs both in terms of energy/power densities and cycle life using a system working with carbons entirely derived from peanut shells [30].

In this framework, we have selected recycled olive pit as the precursor material to prepare carbonaceous materials to be used in both electrodes of the hybrid supercapacitor. Yearly, around 1 million ton of olive pit waste is generated worldwide, of which a third originates in the Spanish olive oil industry [31]. Therefore, we are not only using a low-cost precursor but we are also recycling local bio-waste towards a more sustainable use of natural resources

and the development of a more eco-friendly olive oil industry model (Fig. 1). Moreover, this set of low-cost electrode materials has been tailored to be valid for both lithium- and sodium-ion technologies, switching from one technology to the other by only shifting the electrolyte. This fact is not trivial since the size difference between the two ions, an ionic radius of 116 pm for $Na^+$ versus 90 pm for $Li^+$, implies very often LIB and NIB technologies not to be interchangeable. The most significant benefit of this versatility is that it enables the fabrication of high energy and high power density LICs or NICs, with their own particular assets, suitable to cover a wide variety of different applications. For instance, grid stability to improve the management of distribution networks where high energy density combined with fast response and high cyclability is required, is suitable to be covered by a LIC. Any off-grid storage application where high energy densities together with low-cost are essential, but a few thousands of cycles are sufficient to cover performance during several years, is suitable to be covered by NICs [5].

## 2. Experimental

### 2.1. Material synthesis

To prepare the HC raw olive pits were crushed and loaded in a tubular furnace for the pyrolysis process by heating under an Ar flow of 100 ml $min^{-1}$ at a ramp rate of 5 °C $min^{-1}$ to a predefined temperature of 800 °C and further holding it for 2 h (the carbonization yield for olive pits was ~25%).

To prepare the AC, the HC obtained from the pyrolysis of raw olive pits at 700 °C was physically mixed with potassium hydroxide, KOH, in a 1/6 mass ratio. The materials mixed with KOH were placed in an Inconel© boat and activated according to the procedures known in the literature by heating up to the maximum temperature under an Ar flow (100 ml $min^{-1}$) inside a horizontal stainless steel tube within a tubular furnace. The heating ramp rate was 5 °C $min^{-1}$ and the holding time at 700 °C was 2 h. After activation, the microporous AC was washed off with a diluted solution of hydrochloric acid and water until neutral pH was reached and then dried at 120 °C under vacuum (the activation yield was ~75%). The optimum selected temperature both for pyrolysis and activation are based on a previous study reported elsewhere [32].

**Fig. 1.** Sustainable use of natural resources: the olive pit case. The Sun provides the energy to grow the olives, which are used for culinary purposes, generating tons of biowaste that once recycled and converted into carbons are used to store the energy coming from the sun.

### 2.2. Material characterization

$N_2$ adsorption isotherms were measured at −195.8 °C using a Micromeritics ASAP 2020 instrument for relative pressure values ($P/P_0$) between $10^{-8}$ and 0.995 for samples preliminarily outgassed for 24 h at 200 °C. The Specific Surface Area (SSA) values and pore size distribution were calculated by applying the recently-developed 2D Non-Local Density Functional Theory (2D NLDFT) treatment to $N_2$ adsorption/desorption isotherms using the data reduction software SAEIUS [33]. The average pore size was calculated as a weighted average from the DFT data.

X-ray diffraction (XRD) patterns were recorded for powdered samples in a Bruker D8 X-ray diffractometer; data was collected at 40 kV and 30 mA using CuKα radiation over a 2θ range within 15–80°. Raman spectra were recorded with a Renishaw spectrometer (Nanonics multiview 2000) operating at an excitation wavelength of 532 nm. The spectra were acquired after 10 s of exposition time of the laser beam to the sample. Scanning electron microscopy (SEM) images were acquired with a field emission Quanta 200 FEG microscope from FEI. X-ray photoelectron spectroscopy (XPS) measurements were carried out in a UHV spectrometer chamber with base pressure below $10^{-10}$ mbar. The chamber features a hemispherical analyzer PHOIBOS 150 with a 2D-DLD detector (SPECS) and monochromatic X-ray source FOCUS 500 (SPECS) with two anodes: Al Ka (hn ¼ 1486.74 eV) and Ag La (hn ¼ 2984.3 eV).

### 2.3. Electrode assembly and electrochemical characterization

The electrode slurry for the anode was prepared by a mixture of the HC, Super C C65 (Imerys Graphite & Carbon), and polyvinylidene fluoride (PVdF) as the binder in the mass ratio of 90:5:5 in N-methyl-2-pyrrolidone (NMP) followed by vigorous stirring for 1 h. For the cathode, the slurry was prepared by a mixture of the AC and PVdF as the binder in the mass ratio of 95:5 in NMP followed also by vigorous stirring for 1 h. The HC slurry was deposited onto a copper current collector sheet whereas the AC slurry was laminated onto an aluminum current collector sheet. Laminates were immediately transferred into a vacuum oven and dried at 80 °C under constant vacuum for 12 h before 0.95 $cm^2$ circular individual electrodes were cut out. All electrodes weighed between 2 and 2.5 mg $cm^{-2}$ with a thickness about 40–60 μm and 80–100 μm for the HC and AC respectively. Before cell assembly all electrodes were dried at 120 °C overnight in a vacuum oven. Prior to the assembly of full hybrid cells, HC-based electrodes were characterized in half cells using either metallic Li or Na, correspondingly, both as the counter and reference electrode in 2032 type coin cells. AC electrodes were also preliminarily tested in a three-electrode Swagelok® airtight system using the AC as the working electrode, commercial YP-80F (Kuraray, Japan) as the counter electrode and lithium or sodium metals as the reference electrode. The mass of the counter electrode was a few times higher than that of the working electrode to ensure its higher surface area and the narrow potential range for preventing electrolyte degradation. This set-up allows one to minimize the resistance of the cell and extract the real rate capability of the AC electrodes [34]. The capacity of AC electrodes was calculated between 1.5 and 4.2 V vs $Li/Li^+$ or $Na/Na^+$, correspondingly. Finally, hybrid supercapacitor cells were assembled in a three-electrode Swagelok® system using stainless steel current collectors and a porous glass fiber (Whatman GFB) membrane separator. In-house prepared 1 M $NaPF_6$ in 1:1 (EC:PC) and 1 M $LiPF_6$ in 1:1 (EC:DMC)) were used as electrolytes in NIC and LIC cells, respectively. Cyclic voltammetry (CV), Galvanostatic (GA)

charge-discharge cycling and electrochemical impedance spectroscopy (EIS) measurements were conducted using a multichannel VMP3 generator (Biologic, France) applying a low sinusoidal amplitude alternating voltage of 10 mV over zero current potential (OCP) at frequencies from 1 MHz to 10 mHz.

## 3. Results and discussion

### 3.1. Physicochemical characterization of carbons

The olive pit is a waste residue coming from the olive industry whose elemental analysis shows a strong lignocellulosic character composed by 25% of α-cellulose, 35% of hemicellulose and 40% of lignin with a 50.8% of carbon content, a relatively high oxygen content of 42.7%, 7.1% of hydrogen, 0.48% of nitrogen and 0.04% of sulfur although the exact composition might slightly vary depending on the olive variety [35]. Microstructural analysis of a dried olive stone (Fig. S1a) reveals the typical lignocellulosic structure combining both cellulosic and spherical lignin moieties. Pyrolysis of lignocellulosic materials liberates most of the non-carbon elements, mainly hydrogen, oxygen and nitrogen in the form of gases and tars, leaving behind a rigid carbon skeleton (Fig. 2a) formed by non-graphitic stacked graphene layers known as HC [36]. Those graphene layers can even be inferred at low magnifications by SEM, where transparent graphene sheets appear in the particle boundaries (Fig. S1b). TEM micrographs (Figs. 2b and S1c) show areas of partial graphitization, confirming some graphitic features of the HC. Variations in the textural properties introduced by the further chemical activation of the HC are reflected on the microscale where the surface of the AC presents randomly distributed cracks with respect to the HC (Fig. 2c). In addition, Fig. 2d reveals that KOH activation satisfactorily induced micropores within the graphene layers, essential for ion adsorption, which is further confirmed by the porosity analysis of the AC by means of $N_2$ adsorption isotherms (Fig. S2).

The XRD pattern of the HC is shown in Fig. 3a. The broad diffraction peaks at ~24° and ~43° corresponding to (002) and (100) reflexions are characteristic of a low degree graphitization. The structure of the HC was further investigated by Raman spectroscopy. As shown in Fig. 3b, the HC exhibits a G-band at ~1580 $cm^{-1}$ (in-plane C-C vibrations) and a D-band at ~1340 $cm^{-1}$ (a breathing mode only active when there is disorder in the structure). The ratio between $I_D$ and $I_G$ bands ($I_D/I_G = 2.75$), similar to the one reported by Portet et al., confirms the disordered morphology and low graphitization degree of the HC [37]. The XPS survey reveals the presence of surface oxygen heteroatoms (Fig. 3c). The amount of oxygen is as high as 10% which is within the typical oxygen content range found in HCs, which results from the oxidation of the surface during the synthesis and storage. However, due to the extremely low SSA of the HC (~5 $m^2 g^{-1}$), no influence on the electrochemical performance is expected [38]. With regard to the AC, it was previously designed and reported [32]. Briefly, with the described synthetic procedure a carbon with a DFT SSA of 2225 $m^2 g^{-1}$ with a broad pore size distribution (calculated by 2D NLDFT theory) limited to the micropore range was achieved (see Fig. 3d for the pore size distribution and Fig. S2 for the raw isotherm).

### 3.2. Electrochemical characterization of carbons

Both HC and AC were characterized by means of CV and GA charge/discharges. Fig. 4 shows the electrochemical characterization of the HC. Fig. 4a and b show the 1st and the 10th CVs taken at 1 $mV^{-1}$ between 0.002 and 2 V vs $Na/Na^+$ and $Li/Li^+$ respectively. In both cases voltammograms look similar although some differences can be inferred from the shape of the CV curves. Both voltammograms show a reversible broad oxidation/reduction peak below 1 V, which indicates that most of the capacity is stored below this voltage. A further narrow reduction peak below 0.25 V is also

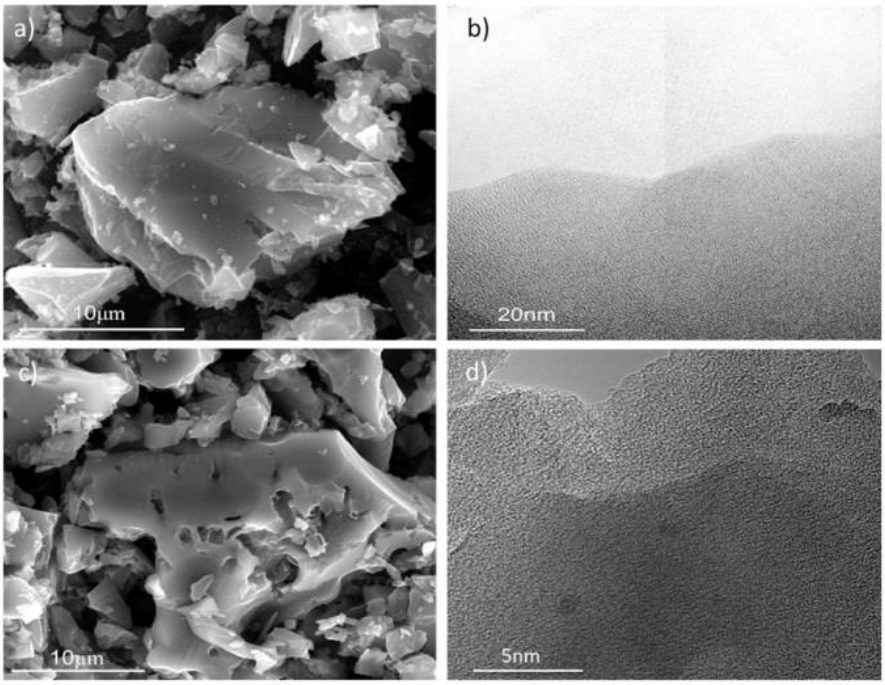


**Fig. 2.** a) and c) are SEM micrographs of the HC and the AC, respectively. b) and d) are TEM micrographs of the HC and the AC, respectively.

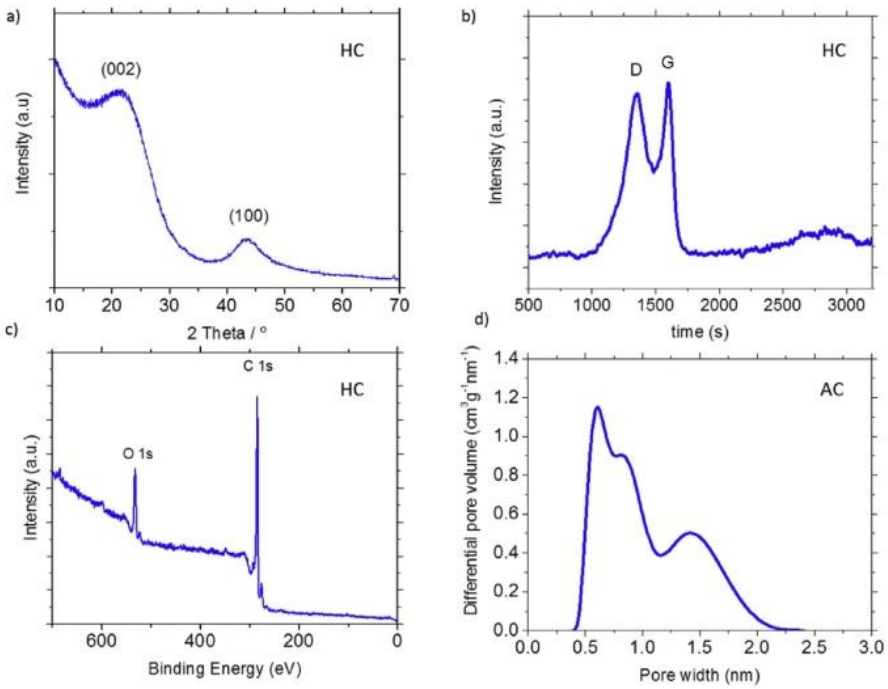


**Fig. 3.** a) XRD pattern of the HC. b) Raman spectra of the HC. c) XPS survey of the HC. d) Pore size distribution of the AC calculated from the $N_2$ adsorption isotherm by applying the 2D-NLDFT model.

observed, in good agreement with the plateau observed in Fig. 4c and d. In the case of $Na/Na^+$, CV curves show higher reduction-oxidation voltage hysteresis that might imply a lower degree of reversibility for the sodium insertion electrode with respect to that of lithium due to the larger ionic radius of Na ion (about 25% larger than Li ion), which makes insertion-extraction more hindered [39]. GA charge-discharge profiles are shown in Fig. 4c and d. The first discharge step delivers a total specific capacity of 360 mAh $g^{-1}$ in the Na-based electrolyte while it is only slightly higher in the Li-based one, 375 mAh $g^{-1}$. Although the solvent mixture has been optimized to each technology, and thus the comparison is not perfectly rigorous, in both cases SEI formation due to carbonate solvent decomposition starts at about ~1.0–0.8 V and the reductive decomposition of organic electrolytes continues down to ~0.25 V, where ion insertion into nanopores starts. However, significant differences arise in the second and posterior discharges steps. The second cycle stabilizes at 243 mAh $g^{-1}$ in Na-based electrolyte while it is considerably higher in Li-based electrolyte, set at 290 mAh $g^{-1}$. Analyzing the sloping region of the second discharge cycle -from 1 V to 0.2 V-, where ions are intercalated into the interlayer between graphene sheets following the "house of cards" model [40], both technologies present similar capacities. For instance, at 0.5 V vs $Na/Na^+$ and vs $Li/Li^+$ the HC shows 54 mAh $g^{-1}$ and 61 mAh $g^{-1}$ correspondingly, and the values remain still similar at 0.25 V with a capacity of 93 mAh $g^{-1}$ and 109 mAh $g^{-1}$, respectively. Therefore, we can conclude that the reversible ion insertion mechanisms at the high-voltage charge storage region into the HC are comparable. Differences arise at the low-voltage region where ions are reversibly inserted into pores in the HC via analogous processes in both metal ion cases. In this region, the Li ion based system presents a much higher capacity value than the Na ion counterpart (180 mAh $g^{-1}$ vs 147 mAh $g^{-1}$), most probably due to the higher volume of Na ions that might find partially restricted access to the pores. Fig. 4e compares the rate capability of both technologies. At low and moderate rates, they present virtually similar capacities being always the Li ion based system in the forefront of both technologies. However, at high rates (i.e. 5C and 10C), noteworthy differences arise, where Na ion based cell shows a remarkable drop in capacity while Li ion system presents much better capacity retention. This fact can be ascribed to a higher charge transfer resistance of $Na^+$ with respect to $Li^+$ as EIS measurements reveal in Fig. 4f, suggesting a hindered diffusion of $Na^+$ throughout the electrode [41].

Fig. 5 shows the electrochemical characterization of the AC in a potential window of 1.5–4.2 V vs $Na/Na^+$ and $Li/Li^+$. CVs from Fig. 5a exhibit profiles indicative of a capacitive charge storage mechanism combined with a gradual increase of capacitive current at potentials remote from the point of zero current in agreement with the corresponding rise in the space charge component of capacitance [42]. The AC presents an open circuit potential (OCP) of 2.9 V and 3.3 V vs $Na/Na^+$ and $Li/Li^+$, respectively. Upon positive polarization -above the OCP-, where reversible ion electrosorption into micropores takes place onto the carbon surface, the charge storage mechanism is purely capacitive. However, under negative polarization –below the OCP-, the capacitive rectangular shape is distorted, which indicates a limited accessibility of cations into pores, with a more pronounced feature for the Li-based electrolyte due to the bigger solvated size of $Li^+$ with respect to that of $Na^+$ (the so-called "ion-sieving effect") [43]. Nevertheless we find out –and show below in Figs. 7c and 8b- that hydrid cells do not allow the capacitive electrodes reaching the ion sieving potential since the potential swing of the negative battery-type HC electrode keeps the AC electrode above those potentials, avoiding cation-sieving to become a limiting factor for the hybrid device performance at high rates. Fig. 5b shows the capacity evolution vs the current density. Although in supercapacitor technology charge storage capability is

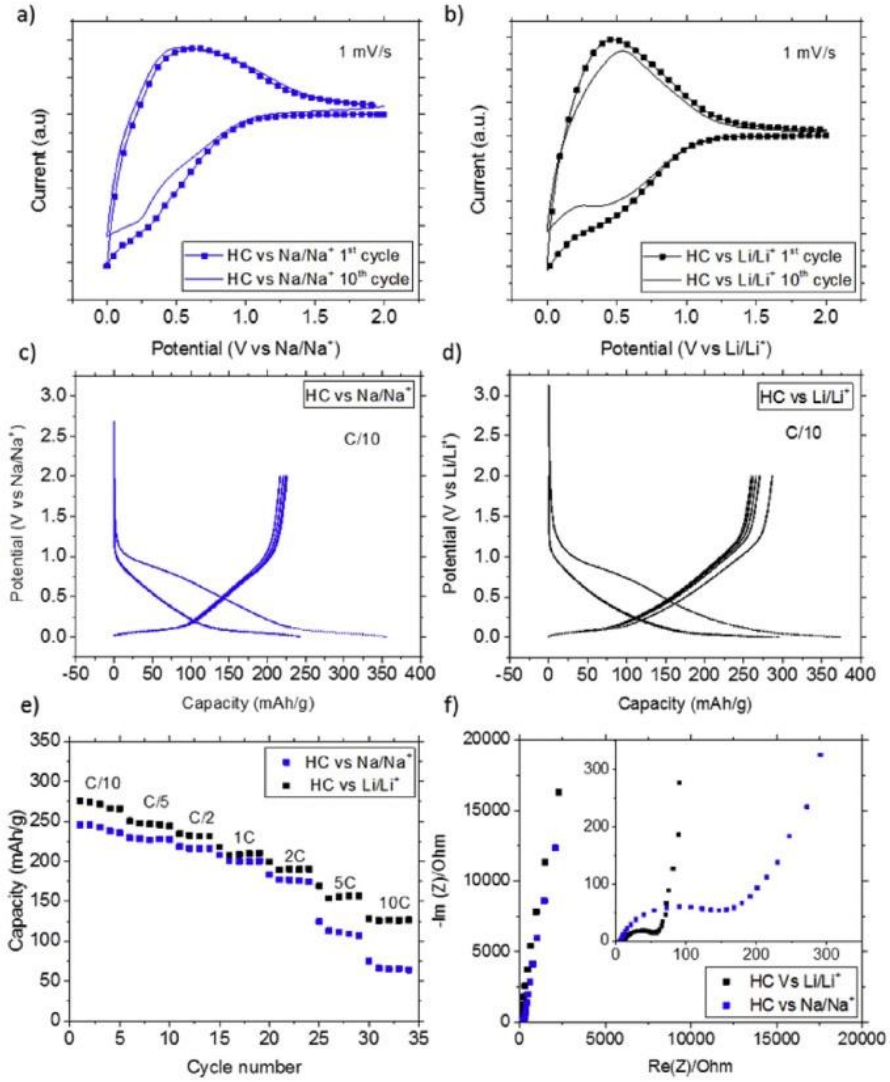


**Fig. 4.** Electrochemical characterization of HC in half cell configuration tested between 0.002 and 2 V vs $Na/Na^+$ and $Li/Li^+$: a) CV vs $Na/Na^+$ b) CV vs $Li/Li^+$ c) GA charge-discharge vs $Na/Na^+$ d) GA charge-discharge vs $Li/Li^+$ e) rate capability f) EIS.

described in terms of capacitance, for the sake of clarity, capacity will be used for comparison with the anode and the overall full hybrid system. Opposite to what is observed for the HC, increasing the cycling rate of the AC makes no difference between both technologies. Figs. 5c and S3 show GA charge-discharge profiles of the AC in Na- and Li-based electrolytes at low, medium and high rates (i.e. 0.1 A $g^{-1}$, 1 A $g^{-1}$ and 5 A $g^{-1}$). The IR drop increment is very similar for the Na-based electrolyte with respect to the Li-based while the current density increases from 0.1 A $g^{-1}$ to 5 A $g^{-1}$. This trend is also confirmed by the EIS data expressed in the Nyquist Plot in Fig. 5d, which shows no difference between both systems neither in the de Levie porous electrode segment at medium frequencies, nor in the almost vertical capacitive line at the lowest frequencies. This is a clear evidence for the optimum and well balanced design achieved for this series of ACs guaranteeing their best performance in both technologies.

### 3.3. Fabrication and characterization of EDLC

For comparison purposes, a symmetric EDLC supercapacitor cell using the same olive pit derived AC in a standard organic electrolyte for EDLC, 1.5 M $Et_4NBF_4$/ACN, was also built. Fig. 6a show the CV curves of the EDLC system in terms of both gravimetric and volumetric capacitance. A rectangular, almost perfect box-like shape profile can be observed, indicative of purely capacitive behaviour, with an estimated capacitance of ~120 F $g^{-1}$ and 50 F $cm^{-3}$. GA charge-discharge profiles shown in Fig. 6b are symmetric and exhibit a low voltage drop suggesting very low total resistance of the system. The specific capacitance values are calculated at different current densities, ranging from 0.1 A $g^{-1}$ to 40 A $g^{-1}$. At a current density of 0.1 A $g^{-1}$ the measured capacitance is 115 F $g^{-1}$ and 52 F $cm^{-3}$, in good agreement with values obtained from the CV technique. At higher current densities capacitance fades out due to pore surface being underused at rapid charge/discharge,

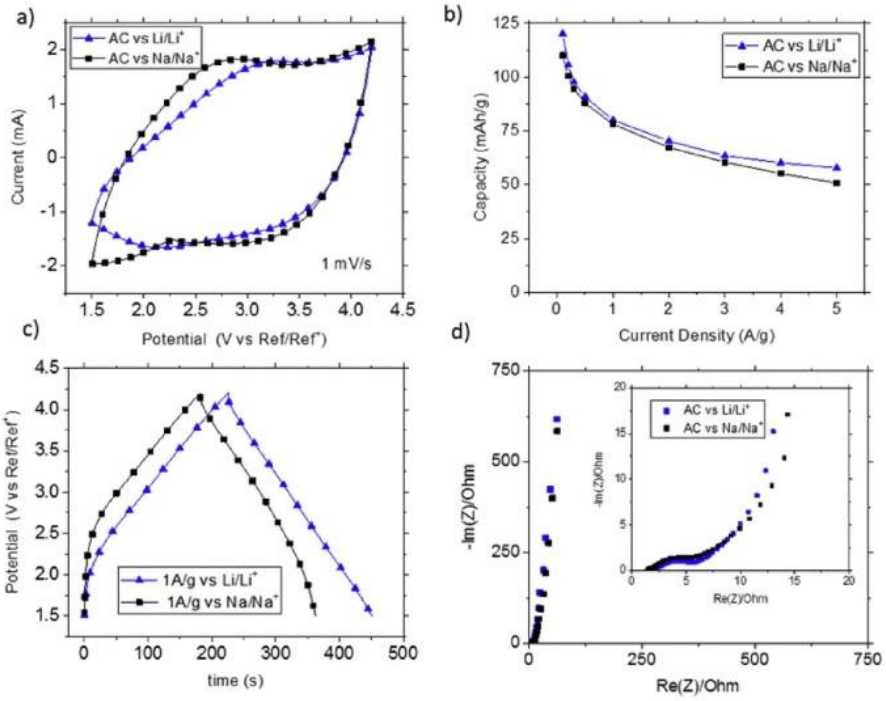


**Fig. 5.** Electrochemical characterization of the AC tested in a three-electrode Swagelok® airtight system between 1.5 and 4.2 V vs $Na/Na^+$ and $Li/Li^+$: a) CV b) Capacity vs current density c) GA charge/discharge profiles for cells with Li- and Na-based electrolytes at 1 A $g^{-1}$ e) Nyquist Plot.

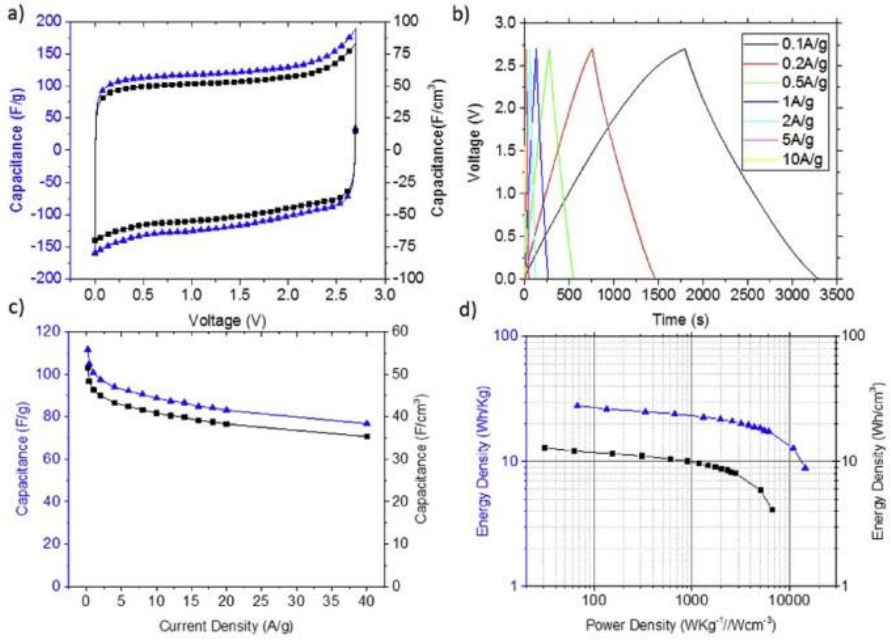


**Fig. 6.** Electrochemical characterization of an EDLC fabricated with two symmetric olive pit based AC electrodes in 1.5 M $Et_4NBF_4$/(ACN) tested between 0 and 2.7 V: a) CV b) GA charge-discharge profiles at different current densities c) capacitance vs current density d) Ragone Plots with respect to total active material. Gravimetric and volumetric values are represented by squares and triangles respectively.

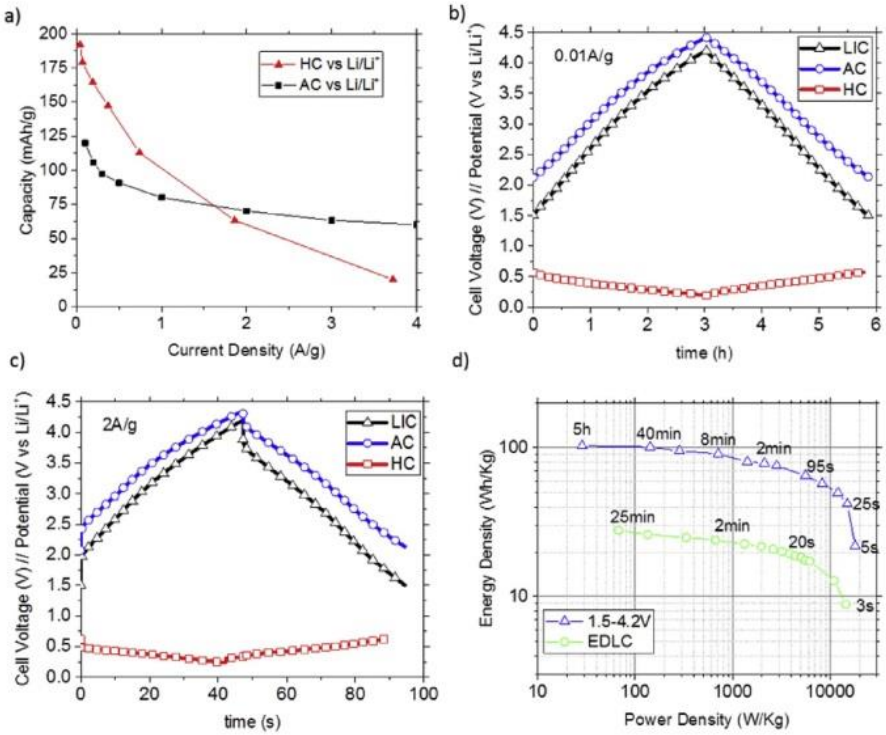


**Fig. 7.** a) Capacity of HC vs AC at different applied current densities b) GA charge-discharge at applied 0.01 A $g^{-1}$ current density of a LIC fabricated with olive pit based HC as anode and AC as cathode in 1 M $LiFP_6$ EC:DMC tested between 1.5 and 4.2 V c) GA charge-discharge at applied 2 A $g^{-1}$ current density and d) Gravimetric Ragone Plot respect to total active material comparing EDLC and LIC performance tested at operating cell voltage between 1.5 and 4.2 V.

although still about 70% of the initial capacitance (83 F $g^{-1}$ and 36 F $cm^{-3}$) is retained at 20 A $g^{-1}$, which slightly decreases to 67% (77 F $g^{-1}$ and 35 F $cm^{-3}$) at 40 A $g^{-1}$. Values for energy and power densities were calculated on the basis of the active material only. Maximum energy density values of 28 Wh $kg^{-1}$ and 13 Wh $cm^{-3}$ at power densities of 67 Wh $kg^{-1}$ and 30 Wh $cm^{-3}$ within a discharge time of 25 min are achieved. Regarding maximum power density values, at a discharge time of 3 s 15 Wh $kg^{-1}$ and 7 Wh $cm^{-3}$ are obtained at 10 Wh $kg^{-1}$ and 4 Wh $cm^{-3}$.

### 3.4. Fabrication and characterization of LIC

In order to build a LIC, olive pit derived carbons were assembled —HC as the anode and AC as the cathode- in a T-shaped Swagelok® cell using 1 M $LiFP_6$ in EC:DMC as electrolyte. In order to profit from the maximum cell capacity output the mass of the electrodes was balanced to maximize cell performance. In Fig. 7a capacities of both HC and AC at different applied current density values are shown. Since the profiles of both materials diverge, three clearly differentiated zones can be observed: i) at low-medium discharge rates below 2 A $g^{-1}$ the HC electrode shows higher capacity than the AC, ii) around 2 A $g^{-1}$ the capacities of both materials tend to be equal and iii) at high discharge rates AC electrode's capacity clearly overcomes that of the HC. Since it is impossible to define a proper mass balance for the whole applied current density range, a 1 to 1 mass balance was selected aiming at the design of an optimal system for an application that requires charge/discharge times of ~0.5–1 min (i.e. a current density of ~2 A $g^{-1}$). Both electrodes were preconditioned in order to maximize the output voltage. Thus, the HC electrode was cycled five times between 0.002 and 2 V vs $Li/Li^+$ at C/10 rate in order to form a SEI and supply sufficient lithium to compensate for the first cycle irreversibility. Then, a cut-off potential of 0.2 V vs $Li/Li^+$ was set in order to avoid any lithium plating. AC was charged to a cut-off potential of 4.2 V vs $Li/Li^+$. In Fig. 7b and c the galvanostatic charge/discharge profiles of each electrode together with the full hybrid cell performance are shown at low and high current densities. The hybrid cell charge-discharge profile is absolutely symmetric in both cases, typical of supercapacitors, indicating that the AC determines the overall cell response profile at any charge-discharge rate. The cathode swings from 2.1 to 4.4 V while the anode fluctuates only between 0.2 and 0.6 V at an applied 0.01 A $g^{-1}$ current density ($t_{discharge}$ ~ 3 h). This avoids safety issues due to lithium plating and ensures long cyclability since the state-of-charge of the HC electrode changes minimally. A 200-fold increase in the applied current density, from 0.01 A $g^{-1}$ to 2 A $g^{-1}$, reduces the discharge time from ~3 h to 40 s. At the highest current density the HC electrode swings within a larger operating potential window, from 0.2 V to 0.8 V, which concomitantly reduces the potential window of the AC electrode from 2.3 to 4.3 V. Overall, the whole hybrid cell still performs as a perfect supercapacitor. Regarding energy and power densities, Figs. 7d and S3 show Ragone Plots for the LIC both in gravimetric and volumetric terms. At a discharge time of about 40 min, therefore within the battery working regime, the cell delivers about 100 Wh kg $_{AM}^{-1}$ at a power density of 150 W kg $_{AM}^{-1}$ in gravimetric terms, which is more than three times the energy density that its EDLC counterpart can deliver at the same power density. At the same discharge time but in volumetric terms, the LIC delivers almost 60 Wh $cm_{AM}^{-3}$ at a power density of 50 W $cm_{AM}^{-3}$, which is 5 times larger than that delivered by the EDLC (12 Wh $cm_{AM}^{-3}$ and

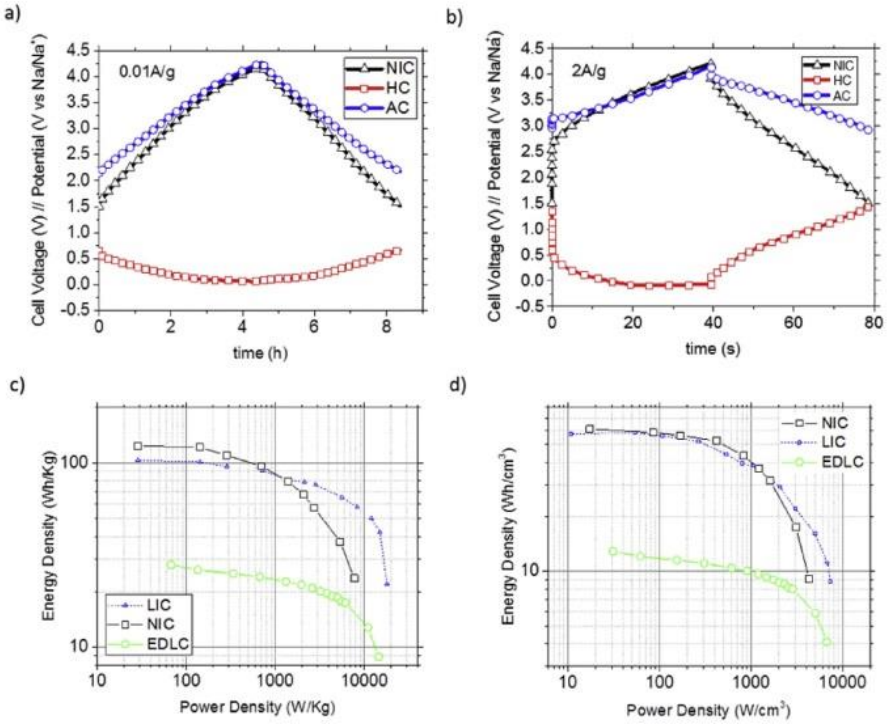


**Fig. 8.** Electrochemical characterization of a NIC fabricated with olive pit based HC as anode and AC as cathode in 1 M $NaFP_6$ EC:PC tested between 1.5 and 4.2 V: a) GA charge-discharge at a current density of 0.01 A $g^{-1}$ b) GA charge-discharge at a current density of 2 A $g^{-1}$ c) and d) Gravimetric and volumetric Ragone Plot respect to total active material comparing NIC vs EDLC and LIC technologies.

50 W cm $_{AM}^{-3}$). At a discharge time of 2 min, the LIC outperforms the EDLC both in terms of energy and power by a factor of 3 in gravimetric terms and a factor of 4 in volumetric terms. Energy density is still doubled in both cases when discharge time is further reduced to a few seconds. Despite the remarkable energy and power density improvement, stability is one of the hallmarks of EDLCs, and LICs should be close to EDLC durability rather than the battery cycling life in order to present a serious candidacy as a new alternative energy storage system. For that reason, a cyclability test, shown in Fig. S5, was run at 2 A $g^{-1}$ and after 10000 cycles the capacity retention was as high as 94%.

### 3.5. Fabrication and characterization of NIC

Similarly to the LIC and only switching the electrolyte from 1 M $LiPF_6$ EC:DMC to 1 M $NaPF_6$ EC:PC a NIC system was fabricated. Both electrodes were also preconditioned: HC was cycled five times between 0.002 and 2 V vs $Na/Na^+$ at C/10 rate and a posterior cut-off potential of 0.2 V vs $Na/Na^+$ was set while the AC was charged to a cut-off potential of 4.2 V vs $Na/Na^+$. In Fig. 8a and b both positive and negative electrodes together with the full hybrid cell performances are shown at low and high current densities. Different to the LIC system at low rates, in this case the negative HC electrode swings from 0.1 V to 0.7 V at a current density of 0.1 A $g^{-1}$, which is almost the double of its LIC counterpart. Consequently, the AC operating potential window is reduced to the range between 2.2 and 4.3 V. More importantly, significant differences arise at high current densities. The charge/discharge profile losses its symmetrical shape and is now governed by the HC behavior, showing high polarization while charging and a tilted potential profile within the discharge region. The slope of the discharge profile of the full NIC cell is more important compared with that of the positive capacitive AC electrode, indicating that the HC electrode limits the deliverable capacity. The HC is used to its maximum extent with a voltage swing of 1.5 V, which concomitantly limits the AC swing to 1.2 V -i. e. from 3 to 4.2 V- and consequently limits the overall capacity of the hybrid cell. EIS shows a much higher semicircle -both in charge and discharge state- for NIC with respect to LIC (Fig. S6) suggesting that slow Na-ion kinetics together with a limited access into pores (the low-voltage plateau) of the HC seem to be the major factors that limit the cell performance at high rates. As observed in the Ragone Plot (Fig. 8c and d), this also causes a more pronounced energy-to-power decay within the high power region. Still the NIC system outperforms the EDLC in energy density throughout the whole power density range, with a 4-fold and a 5-fold energy density gain at low power densities in both gravimetric and volumetric terms, respectively. This remarkable improvement in energy density is not that high in the maximum power energy density region, restricted by the limited $Na^+$ diffusion kinetics. The same cyclability test performed at 2 A $g^{-1}$ (shown in Fig. S7) reveals 90% retention after 1000 cycles which constantly diminishes, retaining 70% of its capacity after 5000 cycles and showing 40% capacity retention after 10000 cycles.

## 4. Conclusions

In summary, we have shown the possibility to fabricate both LICs and NICs, a new generation of hybrid EESs showing high energy density, high power density and good cyclability based on a low-cost recycled bio-waste. To the best of our knowledge, it is the

first time that carbonaceous materials coming from the same precursor have been specifically tailored enabling them to be used in both metal ion capacitor technologies. All fabricated hybrid LIC and NIC devices overcome their EDLC counterpart in terms of energy density throughout the whole power density range, exceeding the highly challenging energy density barrier of 100 Wh kg $_{\overline{AM}}^{-1}$. Furthermore, both technologies equal the EDLC system in terms of power density (>10 kW kg $_{\overline{AM}}^{-1}$), showing the ability to be charged and discharged within a few seconds. LICs show a cycle life similar to EDLCs, thus holding promise for traditional EDLC applications based on multiple charge/discharge pulses. The NIC is effectively limited to 5000 cycles, which allows suggesting this type of capacitors, *e.g.*, for electricity storage from the utility grid where storage systems are usually designed to withstand about 5000 cycles over 10 years [44] and which can be challenging for low-cost batteries. In this scenario, a NIC based on a low-cost material with high volume-based performance can be especially of choice when the volume of the storage system is limited. Overall, the wide variety of hybrid energy storage devices, all fabricated on the basis of the same precursor material, opens new avenues for covering a large assortment of technological applications with different requirements.

## Acknowledgments

The work was financially supported by the Basque Country Government under the Elkartek 15 program (Project CICE2015, Reference KK-2015/0000100). The authors also want to thank Dr. Wei Zhang, Dr. Francisco Bonilla, Dr. Alex Bondarchuk, Dr. Yan Zhang and Maria Jauregi for TEM imaging, XPS survey, Raman spectroscopy, X-ray data acquisition and posterior data analysis and interpretation.

## Appendix A. Supplementary data

Supplementary data related to this article can be found at http://dx.doi.org/10.1016/j.jpowsour.2017.04.107.

## References

[1] World commission on environment and development, Our Common Future, Oxford University Press, London, 1987.
[2] Intergovernmental Panel on Climate Change, 25.04.2017. http://www.ipcc.ch/.
[3] P. Denholm, E. Ela, B. Kirby, M. Milligan, The role of energy storage with renewable electricity generation, Technical Report. NREL/TP-6A2–47187, 2010.
[4] R. Liu, L. Zhang, X. Sun, H. Liu, J. Zhang, Electrochemical technologies for energy storage and conversion, Wiley, Germany, 2012.
[5] J. Miller, Engineering electrochemical capacitor applications, J. Power Sources 326 (2016) 726–735.
[6] M.R. Lukatskaya, B. Dunn, Y. Gogotsi, Multidimensional materials and device architectures for future hybrid energy storage, Nat. Commun. 7 (2016) 12647.
[7] P. Simon, Y. Gogotsi, Br Dunn, Where do batteries end and supercapacitors begin? Science 343 (2014) 1210–1211.
[8] G.G. Amatucci, F. Badway, A. Pasquier, T. Zheng, An asymmetric hybrid nonaqueous energy storage cell, J. Electrochem. Soc. 148 (2001) 930–939.
[9] L. Cheng, X. Li, H. Liu, H. Xiong, P. Zhang, Y. Xia, Carbon-coated $Li_4Ti_5O_{12}$ as a high rate electrode material for Li-Ion intercalation, J. Electrochem. Soc. 154 (2007) 692–697.
[10] K. Zaghib, P. Charest, A. Guerfi, M. Dontigny, K. Kinoshita, HQ asymmetric super capacitor: graphite-Li4Ti5O12/ionic liquid/carbon, ECS Trans. 3 (2007) 89–93.
[11] A. Pasquier, I. Plitz, J. Gural, F. Badway, G.G. Amatucci, Power-ion battery: bridging the gap between Li-ion and supercapacitor chemistries, J. Power Sources 136 (2004) 160–170.
[12] K. Naoi, S. Ishimoto, Y. Isobe, S. Aoyagi, High-rate nano-crystalline $Li_4Ti_5O_{12}$ attached on carbon nano-fibers for hybrid supercapacitors, J. Power Sources 195 (2010) 6250–6254.
[13] K. Naoi, S. Ishimoto, J. Miyamotoa, W. Naoi, Second generation 'nanohybrid supercapacitor': evolution of capacitive energy storage devices, Energy Environ. Sci. 5 (2012) 9363–9373.
[14] K. Naoi, in: International Conference on Advanced Capacitors, May 2016. Japan.
[15] N. Ogihara, Y. Ozawa, O. Hiruta, A self-assembled intercalated metal–organic framework electrode with outstanding area capacity for high volumetric energy asymmetric capacitors, J. Mater. Chem. A 4 (2016) 3398–3405.
[16] T. Aida, K. Yamada, M Morita, An advanced hybrid electrochemical capacitor that uses a wide potential range at the positive electrode, Electrochem. Solid-State Lett. 9 (2006) 534–536.
[17] S.R. Sivakkumar, A.G. Pandolfo, Evaluation of lithium-ion capacitors assembled with pre-lithiated graphite anode and activated carbon cathode, Electrochim. Acta 65 (2012) 280–287.
[18] L.N. Ping, J.M. Zheng, Z.Q. Shi, C.Y. Wang, Electrochemical performance of lithium ion capacitors using $Li^+$-Intercalated mesocarbon microbeads as the negative electrode, Acta Physico-Chimica Sin. 280 (2012) 1733–1738.
[19] W.J. Cao, J.P. Zheng, Li-ion capacitors with carbon cathode and hard carbon/stabilized lithium metal powder anode electrodes, J. Power Sources 213 (2012) 180–185.
[20] J. Ni, Y. Huang, L. Gao, A high-performance hard carbon for Li-ion batteries and supercapacitors application, J. Power Sources 223 (2013) 306–311.
[21] M. Schroeder, M. Winter, S. Passerini, A. Balducci, On the cycling stability of lithium-ion capacitors containing soft carbon as anodic material, J. Power Sources 238 (2013) 388–394.
[22] http://www.t-yuden.com/news/Pid=166_detail.html (25.04.2017).
[23] http://www.jmenergy.co.jp/en/(25.04.2017).
[24] A. González, E. Goikolea, J.A. Barrena, R. Mysyk, Review on supercapacitors: technologies and materials, Renew. Sustain. Energy Rev. 58 (2016) 1189–1206.
[25] F.A. López, F. Puertas, F.J. Alguacil, A. Guerrero, in: 1st Spanish National Conference on Advances in Materials Recycling and Eco–energy Madrid, November 2009.
[26] V. Palomares, P. Serras, I. Villaluenga, K.B. Hueso, J. Carretero-González, T. Rojo, Na-ion batteries, recent advances and present challenges to become low cost energy storage systems, Energy Environ. Sci. 5 (2012) 5884–5901.
[27] N. Yabuuchi, K. Kubota, M. Dahbi, S. Komaba, Research development on sodium-ion batteries, Chem. Rev. 114 (2014) 11636–11682.
[28] J. Yin, L. Qi, H. Wang, Sodium titanate nanotubes as negative electrode materials for sodium-ion capacitors, Appl. Mater. Interfaces 4 (2012) 2762–2768.
[29] K. Kuratani, M. Yao, H. Senoh, N. Takeichi, T. Sakai, T. Kiyobayashi, Na-ion capacitor using sodium pre-doped hard carbon and activated carbon, Electrochim. Acta 76 (2012) 320.
[30] J. Ding, H. Wang, Z. Li, K. Cui, D. Karpuzov, X. Tan, A. Kohandehghan, D. Mitlin, Peanut shell hybrid sodium ion capacitor with extreme energy - power rivals lithium ion capacitors, Energy Environ. Sci. 8 (2015) 941–955.
[31] http://faostat3.fao.org/browse/Q/QD/E (25.04.2017).
[32] E. Redondo, J. Carretero-González, E. Goikolea, J. Ségalini, R. Mysyk, Effect of pore texture on performance of activated carbon supercapacitor electrodes derived from olive pits, Electrochim. Acta 160 (2015) 178–184.
[33] J. Jagiello, J.P. Olivier, 2D-NLDFT adsorption models for carbon slit-shaped pores with surface energetical heterogeneity and geometrical corrugation, Carbon 55 (2013) 70–80.
[34] J. Come, V. Augustyn, J.W. Kimc, P. Rozier, P.L. Taberna, P. Gogotsi, Jeffrey W. Long, B. Dunn, P. Simon, Electrochemical kinetics of nanostructured $Nb_2O_5$ electrodes, J. Electrochem. Soc. 161 (2014) 718–725.
[35] S. Alami, PhD thesis, Universidad de Granada, 2010.
[36] F. Rodríguez-Reinoso, M. Molina-Sabio, Activated carbons from lignocellulosic materials by chemical and/or physical activation: an overview, Carbon 30 (1992) 1111–1118.
[37] C. Portet, G. Yushin, Y. Gogotsi, Electrochemical performance of carbon onions, nanodiamonds, carbon black and multiwalled nanotubes in electrical double layer capacitors, Carbon 45 (2007) 2511–2518.
[38] E.M. Lotfabad, J. Ding, K. Cui, A. Kohandehghan, W.P. Kalisvaart, M. Hazelton, D. Mitlin, High-density sodium and lithium ion battery anodes from banana peels, ACS Nano 8 (2014) 7115–7129.
[39] C. Wang, Y. Xu, Y. Fang, M. Zhou, L. Liang, S. Singh, H. Zhao, A. Schober, Y. Lei, Extended π-conjugated system for fast-charge and -discharge sodium-ion batteries, J. Am. Chem. Soc. 137 (2015) 3124–3130.
[40] D.A. Stevens, J.R. Dahn, The mechanisms of lithium and sodium insertion in carbon materials, J. Electrochem. Soc. 148 (2001) 803–811.
[41] S. Komaba, W. Murata, T. Ishikawa, N. Yabuuchi, T. Ozeki, T. Nakayama, A. Ogata, K. Gotoh, K. Fujiwara, Electrochemical Na insertion, solid electrolyte, interphase for hard-carbon electrodes and application to Na-ion batteries, Adv. Funct. Mater. 21 (2011) 3859–3867.
[42] M. Hahn, M. Baertschi, O. Barbieri, J.-C. Sauter, R. Kötz, R. Gallay, Interfacial capacitance and electronic conductance of activated carbon double-layer electrodes, Electrochem. Solid-State Lett. 7 (2004) 33–36.
[43] L. Eliad, G. Salitra, A. Soffer, D. Aurbach, Ion sieving effects in the electrical double layer of porous carbon electrodes: estimating effective ion size in electrolytic solutions, J. Phys. Chem. B 29 (2001) 6880–6887.
[44] J.E. Miller, A.F. Burke, Electrochemical capacitors: challenges and opportunities for real-world applications, Electrochem. Soc. Interface 17 (2008) 53–57.

**SUPLEMENTARY INFORMATION**

# Lithium and Sodium Ion Capacitors with High Energy and Power Densities based on Carbons from Recycled Olive Pits

Jon Ajuria[1,*], Edurne Redondo[1], Maria Arnaiz[1], Roman Mysyk[1], Teófilo Rojo[1,2] and Eider Goikolea[1,*]
[1]CIC Energigune, Albert Einstein 48, Alava Technology Park, 01510 Miñano, Vitoria-Gasteiz, Spain
[2]Inorganic Chemistry Department, University of the Basque Country UPV/EHU, P.O. Box 644, 48080, Bilbao, Spain.
[*]E-mail: jajuria@cicenergigune.com

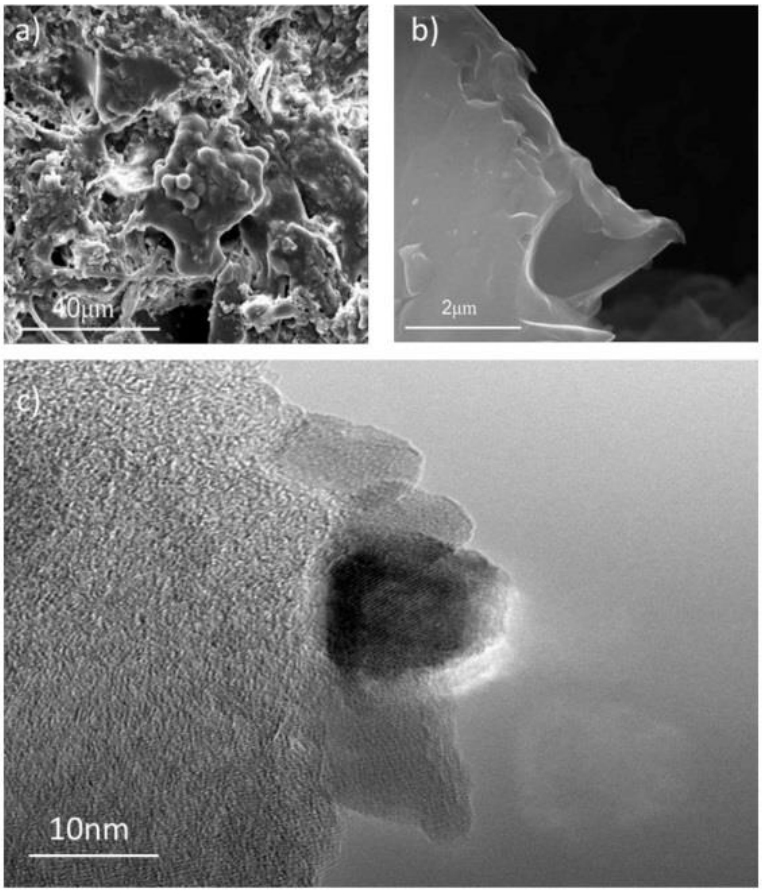


**Figure S1:** a) SEM micrograph of an Olive Pit b) SEM micrograph of the HC where graphene layers can be observed in the edges. c) TEM micrograph showing the pseudo-graphitic nature of the HC, with a highly ordered moiety within a mostly amorphous environment.

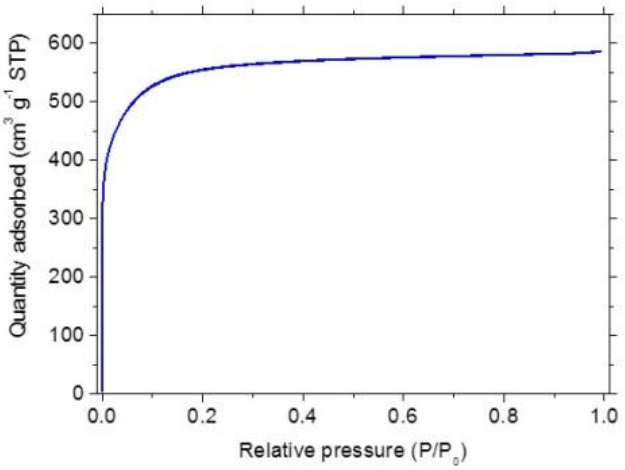


**Figure S2:** $N_2$ adsorption isotherm for AC

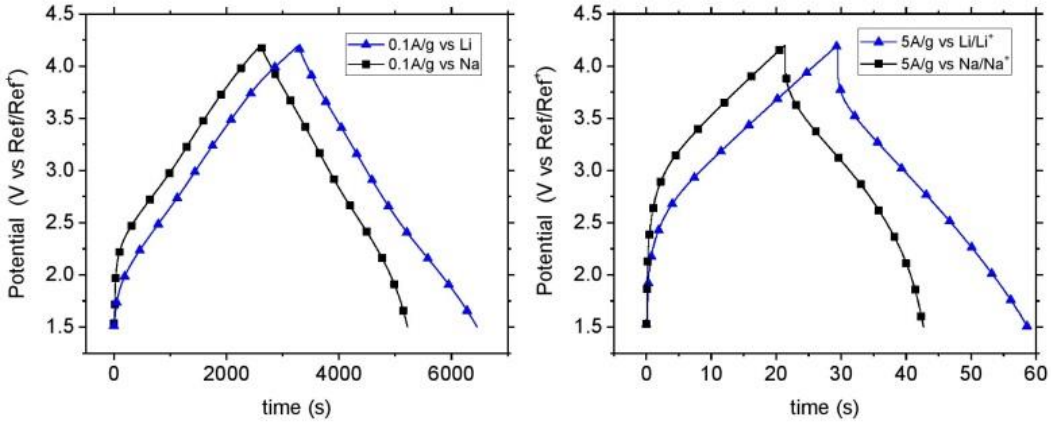


**Figure S3:** Charge-discharge profiles of AC in three-electrode configuration tested between 1.5 - 4.2 V vs $Na/Na^+$ and $Li/Li^+$ at applied 0.1 A $g^{-1}$ and 5 A $g^{-1}$ current densities.

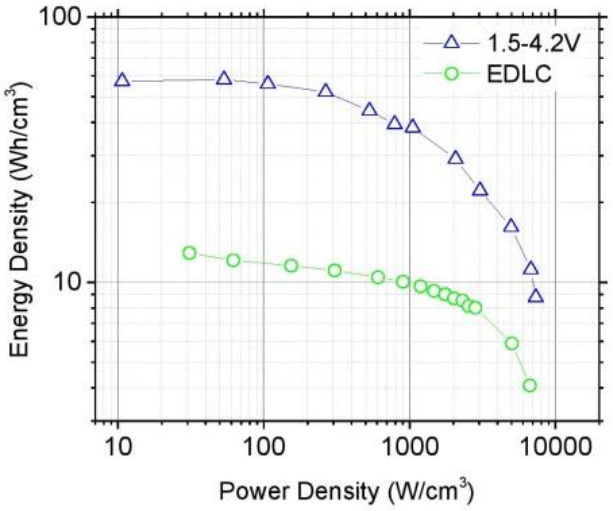


**Figure S4:** Volumetric Ragone Plot with respect to total active material comparing EDLC and LIC performance tested at 1.5 – 4.2 V operating cell voltage window.

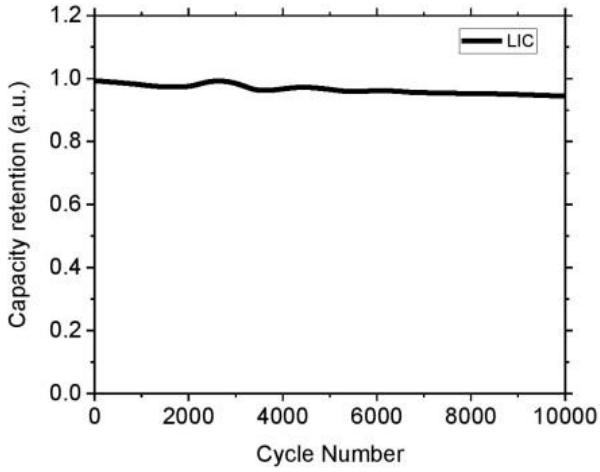


**Figure S5:** Stability test run for LICs within the 1.5 - 4.2 V voltage window at applied 2 A $g^{-1}$ current density.

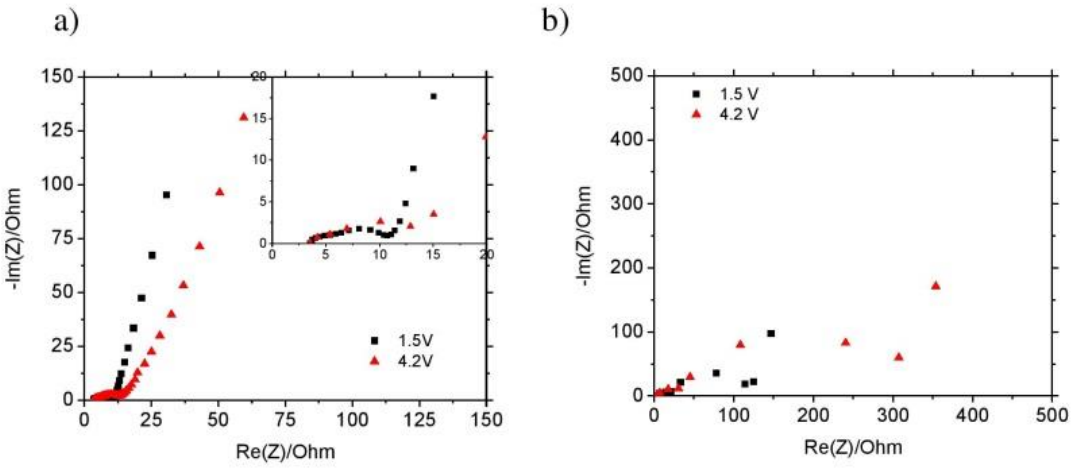


**Figure S6:** a) Impedance spectroscopy of LIC at 1.5 V and 4.2 V b) Impedance spectroscopy of NIC at 1.5 V and 4.2V

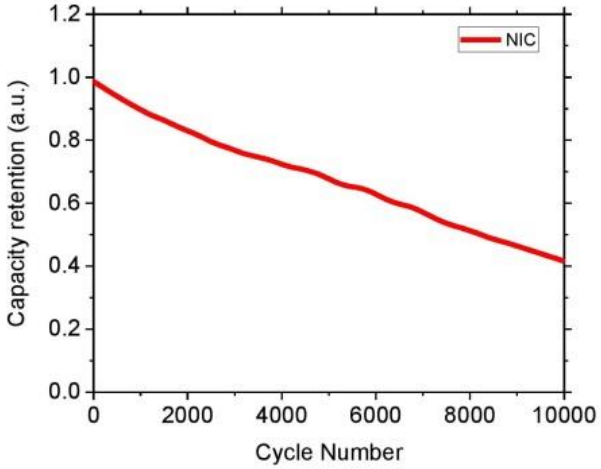


**Figure S7 :** Stability test run for NIC at applied 2 A $g^{-1}$ current density.

# 5 SUMMARY

Electrochemical capacitors are one of the most promising electrochemical energy storage systems due to their high power density and their long cyclability. The use of supercapacitors in the means of transport is very interesting, since these systems can be charged and discharged in the time interval characteristic of braking and acceleration of vehicles. In hybrid vehicles, they absorb the power demand peaks, prolonging the useful life of the batteries and in the field of urban public transport (bus, tram and metro) its use for the elimination of the catenary of the wagons stands out, which can save 20% of the electricity through the recovery of braking energy.

In the simplest of configurations, a supercapacitor is formed by two carbon electrodes of high specific surface immersed in an electrolytic solution and separated by an electrically insulating membrane, but good ionic conductor. The success in the implementation of these systems will be closely linked to the ability to produce renewable materials of low cost and high performance for its manufacture. Another challenge facing this technology is the improvement of its energy density, which is again closely linked to the development of new materials or the improvement of the methods of preparation of existing materials. The structure and the surface functional groups of the carbon electrodes have a great influence on the specific capacitance. Thus, activated carbons with high SSA, high conductivity and adapted pore size are required for supercapacitors are expected to dominate the market of electrochemical capacitors. In this sense, a possible way to avoid economic and environmental costs is, on the one hand, the use of natural precursors, and on the other hand, the optimization of the chemical activation method via alkaline agents, which is precisely what is done in the present thesis.

Olive pits are by-products of the olive oil industry that become a waste for the manufacturers. Their chemical composition makes them good candidates as precursors for the preparation of microporous carbons. In this Doctoral Thesis, they have been used to produce a series of activated carbons (ACs) with different porosity and hard carbons (HCs). Then, these ACs and HC have been utilised as active material for electrochemical capacitors. Thus, the influence of different porous features has been analysed in relationship to the electrochemical behaviour of supercapacitors in order to deepen in the understanding on the role of pore size in the dielectrical permittivity and capacitance of these systems and to optimize the textural properties for a maximised electrochemical performance.

Olive pits used in this study are composed of a 50.8% of carbon, 42.7% oxygen, 7.1% of hydrogen, 0.48% of nitrogen and 0.04% of sulphur content.

Activated carbons (ACs) were prepared by a two-step activation process. The first step was the carbonisation of the raw material, which yielded a carbonaceous product (non-graphitizable carbon or HC) and released most of the other elements, mainly, hydrogen, oxygen and nitrogen, by forming gases and tars. In this process, the yield of HC was *ca.* 25 %. Although the HC has some graphitic domains, some rigid cross-links prevent it from graphitising at high temperatures. This HC was also used as a battery-type electrode in hybrid supercapacitor cells.

The second step was a chemical activation with KOH, for which the previously obtained char was mixed physically with different ratios of KOH. The mixture of char and KOH was submitted to the temperature treatment. In all the cases, the carbonisation and activation temperatures were the same. The yield of ACs decreased as the KOH/HC ratio increased. In the activation process, randomly distributed cracks were formed and micropores were introduced within the graphene- layers.

Firstly, the effect of the synthesis temperature was analysed by comparing the textural properties of the samples activated with a KOH/HC ratio of 2.6 at temperatures between 700 and 1000°C. On the one hand, a narrow pore size distribution was achieved at 700 to 800 °C, with an average pore size below 1 nm and a difference in the specific surface area (SSA) of ~100 $m^2 g^{-1}$. On the other hand, when the temperature was increased to 1000 °C, the pore size distribution was significantly enlarged, with an average pore size larger than 1 nm.

As expected, the gravimetric capacitance changed according to the different textural properties of the ACs. In aqueous 6 M KOH electrolyte, the capacitance increased from 176 to 218 F $g^{-1}$ by increasing the temperature of the activation process to 800 °C and then decayed to 150 F $g^{-1}$ when the temperature was 1000 °C. The decrease in capacitance on increasing the activation temperature from 800 to 1000 ºC is directly linked to the fact that the SSA decreased. However, the increase in capacitance when shifting the activation temperature from 700 °C to 800 °C does not follow the increase in SSA.

Secondly, the effect of the amount of KOH per HC used in the synthesis was analysed on the variation of SSA and average pore size ($L_0$). The SSA increases almost linearly to a maximum value of 2400 $m^2$ $g^{-1}$ for a KOH/HC ratio of 6.6, then decreasing for higher KOH/HC ratios due to an excessive carbon burn-off wiping out some of the pore walls. Simultaneously, the $L_0$ increased with a linear trend as the KOH/HC ratio was increased, staying under 1 nm until a KOH/HC ratio of 6. For higher KOH/HC ratios, the slope increased more rapidly. The pore size distribution (PSD) showed that, in fact, the amount of activating agent progressively widens the pore size towards 2 nm. The gradual change in the pore size enables using the KOH/HC ratio as a parameter to tailor textural parameters (SSA and PSD).

When this series of ACs was tested as active material for symmetric EDLCs in aqueous 6 M KOH electrolyte, cyclic voltammograms showed that the value of gravimetric capacitance increased up to 260 F $g^{-1}$ for the KOH/HC of 6.6, in correlation with the increase in the SSA. In contrast, volumetric capacitance reached its highest value of 135 F $cm^{-3}$ for a KOH/HC ratio of 2, when the AC had less pore volume, thus being denser. From the practical point of view, the fact that the volumetric capacitance, the industrially most-demanded parameter, had a high value at a low burn-off is an advantage, because that would require less activating agent for the activation and, presumably, less water in the washing step, thereby reducing the overall cost of the process.

The specific capacitance is not solely affected by the SSA of the ACs, as there is a fluctuating dependence of gravimetric capacitance on synthesis temperature and on the KOH/HC ratio. This means that other capacitance-determining factors, such as the dielectric permittivity and the distance between charges should also be taken into account. Hence, the capacitance and the dielectric permittivity in pores of each electrode were correlated in the aqueous electrolyte by using the sandwich capacitance model, which encloses the ions in between the pore walls of slit-shaped micropores using an adaptation of Equation 2:

$$C = \frac{S\varepsilon_0\varepsilon_r}{b - a_0} \qquad \text{Equation 34}$$

where S is the specific area, $\varepsilon_0$ the electric constant in vacuum, $\varepsilon_r$ the effective dielectric permittivity, $b$ the pore half width and $a_0$ the ion radius. The formula can be applied individually to the capacitance of the positive and the negative electrodes:

$$C_+ = \frac{S_{OH^-}\varepsilon_0\varepsilon_r}{b_{OH^-} - a_{0OH^-}} \qquad \text{Equation 35}$$

$$C_- = \frac{S_{K^+}\varepsilon_0\varepsilon_r}{b_{K^+} - a_{0K^+}} \qquad \text{Equation 36}$$

where $S_{K+}$ and $S_{OH-}$ are the specific area accessible to $K^+$ and $OH^-$ ions, $\varepsilon_r$ the effective dielectric permittivity, $b_{K+}$ and $b_{OH-}$ the average pore half width accessible to each ion and $a_{0K+}$ and $a_{0OH-}$ the ion radius of the $K^+$ and $OH^-$ ions. $S_{K+}$ and $S_{OH-}$ were calculated from DFT data by subtracting the SSA that belongs to pore sizes below the size of each ion, to the total SSA.

The average pore width accessible to each ion can be calculated by:

$$L_{0K^+} = 2b_{K^+} = \frac{\int_{V_{K^+}}^{V_{max}} LdV}{V_{max} - V_{K^+}}$$ Equation 37

$$L_{0OH^-} = 2b_{OH^-} = \frac{\int_{V_{OH^-}}^{V_{max}} LdV}{V_{max} - V_{OH^-}}$$ Equation 38

where $L_{0K+}$ and $L_{00H-}$ is the average pore size accessible to each ion, $L$ the pore size, $V_{K+}$ and $V_{0H-}$ the volume corresponding to the ions size and $V_{max}$ the total pore volume. The size of $K^+$ was considered to be 0.42 nm as it was established in the literature to be hydrated and the size of hydrated $OH^-$ is 0.63 nm.

Thus, on the one hand, the theoretical capacitance per electrode ($C_0$) was calculated by using the data from gas adsorption measurements and the value of dielectric permittivity in vacuum, as a function of the relative dielectric permittivity for each of the ions. While, on the other hand, the experimental capacitance of each electrode (C) inside a two-electrode symmetrical cell was separately measured by introducing a reference electrode. Then, the calculated and the experimental capacitance were compared.

$$C_+ = \varepsilon_+ C_{0+}$$ Equation 39

$$C_- = \varepsilon_- C_{0-}$$ Equation 40

$$C_{0+} = \frac{\varepsilon_0 S_{OH^-}}{b_{OH^-} - a_{0OH^-}}$$ Equation 41

$$C_{0-} = \frac{\varepsilon_0 S_{K^+}}{b_{K^+} - a_{0K^+}}$$ Equation 42

where $\varepsilon_+$ and $\varepsilon_-$ are the effective dielectric permittivity in pores of the positive and negative electrode correspondingly.

When the calculated capacitance was represented against the experimental capacitance for the positive and the negative electrode, no correlation between points for different microporous carbons was found, implying that the effective dielectric permittivity is not a constant value. However, when the effective permittivity value was plotted *vs.* the $L_0$, there was a linear correlation. That suggested that widening the pores allows more solvating water molecules. Furthermore, a more significant change in permittivity was observed for the increasing pore size of the negative electrode, suggesting that the $K^+$ ions have a larger solvation sheath than $OH^-$ ions.

As part of the evaluation of the ACs from olive pits as suitable active materials for supercapacitors, the rate capability was analysed and related to the porous features. Since these devices are meant to have high power, the capacitance loss should be avoided at high current densities. The capacitance retention of the cells increased as the KOH/HC ratio employed for the preparation of the ACs was increased up to a ratio of 6, *i.e.* up to the ACs with highest SSA and an $L_0$ of ~1 nm. Moreover, as the $L_0$ of the ACs was increased the retention was improved, in such a way that unblocking the electrosorption of the solvated ions enhances the ion transport at high rates. The capacitance dependence on the discharge time showed that the highest capacitance values at low discharge time were obtained by carbons with slightly wider pores than the size of solvated ions. On the contrary, when the pore size was significantly wider than the ion size, the capacitance dropped.

The AC obtained using a KOH/HC ratio of 6 was used as an example to show that each electrode undergo a different potential range. At low current density, the negative electrode used a lower potential window at low current density, which implied that the capacitance of that electrode was higher in comparison with the positive. Contrarily, when the current density was high, this behaviour

was switched and the positive electrode became the highest in capacitance. Taking this into account, the relationship of the capacitance of the positive and the negative electrode was used to have a closer insight of the effect of the pore size on the rate capability. Thus, using the concept of the equivalence of charges stored the relationship of capacitances between the electrodes can be calculated:

$$\frac{C_-}{C_+} = \frac{\Delta E_+ m_+}{\Delta E_- m_-} \qquad \text{Equation 43}$$

In our case, the capacitance of the positive and the negative electrode and their relationship changed as the current density was increased. At low current density, the negative electrode showed the highest capacitance of both, for all the porous features, and at high current density, the positive became the highest in capacitance. Therefore, the electrosorption of $OH^-$ ions was favoured over the $K^+$ at high current density. The higher dielectric permittivity on the solution-side of the negative electrode let us put forward the hypothesis that the lower capacitance of the negative electrode may be associated with the larger solvation sheath, eventually leading to the more reduced mobility of $K^+$ ions.

In conclusion, the rate capability was linked to the ion size, the SSA, the average pore size and the solvation. On the one hand, smaller ions could access a higher portion of SSA, providing higher gravimetric capacitance. Also, a disproportionately wide pore size allowed a higher solvation of the ions, which resulted in the decrease in the rate of ion transport at high current density. Additionally, a minor pseudocapacitive contribution at the negative electrode such as nascent hydrogen chemisorption, can also deteriorate the capacitance retention at high current density due to the higher resistivity of the Faradaic charge transfer process. In any case, the negative electrode was identified as the source of capacitance loss at high current density for this series of ACs.

Similar investigations were conducted to relate the porous features of these ACs with their electrochemical performance when they were used as active materials in in organic 1.5M $(C_2H_5)_4NBF_4$ in acetonitrile electrolyte based supercapacitors. The SSA and $L_0$ accessible to each of the ions for the carbons activated different KOH/HC ratios was assessed by taking into account the pores with wider size than the ion size from the DFT calculations of the $N_2$ gas adsorption experiments. The size taken for $(C_2H_5)_4N^+$ was 0.68 nm and for $BF_4^-$ 0.48 nm, so they are partially desolvated. Thus, accessible surface area is:

$$S_C = SSA - S_{0.68} \qquad \text{Equation 44}$$
$$S_A = SSA - S_{0.48} \qquad \text{Equation 45}$$

where *SSA* is the total specific surface area accessible to $N_2$ gas, $S_{0.68}$ and $S_{0.48}$ are the surface area of pores narrower than the size of cations and anions.

The surface area accessible to $BF_4^-$ was found to be very closely similar to the values of the total SSA. However, the accessible surface area to $(C_2H_5)_4N^+$ was 3 to 5 times lower depending on the AC sample. Evidently, the SSA determined by $N_2$ gas adsorption cannot be taken as the accessible surface area for the electrolyte, especially when the size of the ions is bigger than the size of the probe molecule. Similarly, the accessible pore size was calculated taking into account the pores bigger than the size of each ion:

$$L_{0C} = 2b_C = \frac{\int_{V_{0.68}}^{V_{max}} LdV}{V_{max} - V_{0.68}}$$ Equation 46

$$L_{0A^-} = 2b_{A^-} = \frac{\int_{V_{0.48}}^{V_{max}} LdV}{V_{max} - V_{0.48}}$$ Equation 47

where $V_{0.68}$ and $V_{0.48}$ were the pore volume from pores narrower than the size of the cation and anion, $b_C$ and $b_-$ were the average half pore width accessible to $(C_2H_5)_4N^+$ and $BF_4^-$.

Similarly to the considerations for the SSA, when the accessible porosity was taken into account to calculate the average pore size, the pore size accessible to the $BF_4^-$ did not differ much from the one calculated from $N_2$ gas adsorption, whereas the pore size accessible to $(C_2H_5)_4N^+$ varied much more (~0.35 nm).

On one hand, for ACs with average pore size smaller than 1 nm the cyclic voltammograms showed a capacitance decrease at the high voltage limit alternatively explained in the literature as the ion-sieving effect or the surface saturation. Thus, the narrowest pores in the subnanometer range appear to be unfavourable for capacitive charge storage in the negative electrode. On the other hand, for ACs with average pore size bigger than 1 nm, the typical rectangular shape of supercapacitors was recovered. Since the average pore size and the cation accessible pore size were different, using the former to describe the electrochemical performance could lead to misinterpretation of capacitance dependence on pore size. The capacitance decay happened for accessible pore size bigger than the partially desolvated $(C_2H_5)_4N^+$ (0.68 nm), indicating that the removal of the solvation shell was hindered on the timescale of the voltammetry measurements.

The areal capacitance normalised by the accessible surface area to $(C_2H_5)_4N^+$ showed that the capacitance overlapped at ~10 μF $cm^{-2}$ at a scan rate of 5 $mV.s^{-1}$ when the average accessible pore size was bigger than 1 nm. In the case of ACs that showed decaying capacitive current at the high voltage limit, the areal capacitance exceeded 10 μF $cm^{-2}$. However, this effect was observed by relying on the average capacitance per electrode in two-electrode cells, which assumes the same capacitance for the positive and the negative electrodes. However, there could be a significant difference in capacitance depending on the carbon/ion compatibility, for instance, due to pore size restrictions. Therefore, it was necessary to analyse this effect by measuring the capacitance of the positive and negative electrodes separately by using a reference electrode. Thus, the areal capacitance of each electrode was calculated by dividing the experimental gravimetric capacitance of each electrode by the values of accessible surface area to the corresponding counterion, namely, $C_{exp-}/S_C$ and $C_{exp+}/S_A$. The capacitance of the positive electrode was almost constant, ~5 μF $cm^{-2}$, independently of the accessible pore size. On the contrary, the capacitance of the negative electrode was greatly increased at the smallest accessible pore sizes, using the capacitance value extracted from the linear part of the galvanostatic discharge profile.

In the case of the positive electrode, the $\varepsilon_{r+}$ changed linearly as the pore size was increased, which came to be in agreement with the observation regarding the capacitance of the positive electrode. In the case of the negative electrode, the $\varepsilon_{r-}$ also changed linearly for the pore sizes that did not show restrictions for ion transport regarding the pore size. However, for the pore sizes which showed restricted ion storage near the charging limit, the $\varepsilon_{r+}$ stood out of the linear tendency due to a supposedly extreme confinement of acetonitrile molecules solvating $(C_2H_5)_4N^+$ ions. This abnormal increase of capacitance may be caused by the decrease in charge separation which was not counterbalanced by the corresponding decrease in $\varepsilon_r$ before reaching the electrolyte breakdown potential. However, this adversely affected the supercapacitor performance since the full voltage window could not be utilised for charge storage. From the practical perspective, the maximum gravimetric capacitance reached was 140-150 F $g^{-1}$ and volumetric 60 F $g^{-1}$, comparable values to those of found in the industry using the best commercial biomass-derived carbons (coconut shell derived ACs).

Galvanostatic charge/discharge profiles for both cells and separate electrodes varied depending on the porous features of the ACs. Pore size restrictions provoked capacitance fading on approaching the lowest potential for the negative electrode at both low and high current densities, with a more pronounced effect for the higher current. By contrast, unrestricted pore access showed equal capacitance values for both electrodes at low current density, In this case the capacitance fading belonged mostly to the positive electrode, which also underwent a larger potential window, close to the electrolyte decomposition limit.

Thus, for ACs with different pore sizes the relationship between the capacitance of positive and the negative electrode changed over the current density. For restricted pore sizes the capacitance of the positive electrode became higher than that of the negative electrode at high current density; for unrestricted electrosorption both capacitances were similar and for the extensively wider pores the capacitance of the negative electrode became higher at high current density. So, $C_-/C_+$ gradually increased as the pore size became wider and the current density higher.

Based on the rate capability, there was an optimum pore size that gave the maximum capacitance retention over current density The symmetric EDLC giving such performance was built using and AC with an accessible pore size of 1.2 and 1.04 nm to $(C_2H_5)_4N^+$ and $BF_4^-$, respectively. Interestingly, this approaches the size of the solvated ions, which means that the optimum rate response is likely to be ensured when accessible pores are similar in size to solvated ions. For this activated carbon, the $C_-/C_+$ value over the current density did not deviate from the unity, also meaning that the equal potential window of the negative and the positive electrode, which also guarantees the maximum durability of the cell since none of the electrodes works outside its respective corrosion potential at high current. By contrast, with ACs that have wider pore sizes, the rate capability was lower at the same time that the $C_-/C_+$ value increased, so, the working potential window of the positive electrode is larger, closer to the corrosion potential on the positive side.

The electrical conductivity of these ACs fluctuated and was not significantly different between them. Thus, no meaningful correlation could be stablished between the electrical conductivity and the rate capability.

An AC with a relatively broad pore size accessibility was selected to study various aqueous salt electrolytes at neutral pH by varying cations, anions and electrolyte concentration. First, the effect of the anion was investigated. Accordingly, 1 M lithium chloride, nitrate and sulfate solutions were tested within a 1 V of stable voltage window. The slightly higher capacitance of LiCl in comparison with $Li_2SO_4$ could be ascribed to the smaller size of $Cl^-$ anions (0.36 nm, established in the literature to be adsorbed in the non-hydrated state) than the $SO_4^{2-}$ anions (>0.58 nm, in the hydrated form). Since smaller chloride ions can access a larger amount of SSA, this may eventually be the reason for higher capacitance.

More importantly, the effect of the cation size was investigated together with the impact of the electrolyte conductivity on the electrochemical performance. Almost perfectly rectangular shaped CVs were obtained by using the electrolyte concentrations at the maximum electrical conductivity, *i.e.* 6 M for LiCl (170 mS $cm^{-1}$), 5 M for NaCl (220 mS $cm^{-1}$) and 2 M for KCl (205 mS $cm^{-1}$). Furthermore, the increase of electrolyte conductivity improved capacitance values, which were almost the same for the three tested salts. Moreover, both series and distributed resistance values were lowered, *i.e.* the resistance outside and inside the pores, correspondingly. In terms of capacitance values, the selection of cations did not have a significant influence.

By electrochemical impedance spectroscopy measurements, the equivalent series resistance (ESR) found at the intersection of the high frequency limit, was attributed to the electronic resistance of the

electrodes and the ionic resistance of the bulk electrolyte. These values were very low, ~0.50 Ω $cm^2$ for all the 1 M electrolyte solutions. However, increasing the concentration of the electrolyte decreased these values even more to ~0.20 Ω $cm^2$, which clearly indicated that the improvement of the conductivity of the electrolyte decreased the resistance values. The conductivity values of all the electrolytes were very similar as well as the resistance values. Furthermore, the medium frequency diagonal line, which is characteristic of ion transport in the porosity (the de Levie porous electrode factor), was smaller. Therefore, the electrolyte resistance inside the pores was in relationship with the electrolyte conductivity for bulk electrolyte, supposedly due to the high concentration of ions inside the pores as well. The lower in-pore resistance shortened the transport pathways under electrode polarisation.

With aqueous neutral salts electrolyte, the voltage window could be extended up to 1.8V, which in the case of LiCl and NaCl CVs kept a rectangular shape close to the idea capacitive profile, while the cell working in KCl presented a more distorted CV curve due to the water reduction. At the low current density, the capacitance value was higher for the cells using NaCl and KCl because of the faradaic contribution from the partial electrolyte decomposition. However, the capacitance retention at high current density was much higher for LiCl (63%) in comparison with NaCl (47%) and KCl (32%).

KCl cells lost 50% of capacitance after 4 hours at 1.8 V, NaCl cells lost 40% of capacitance after 100 hours, while LiCl cells had a capacitance retention higher than 60%. As the capacitance retention of at least 80% should be evidenced in order to consider that cells pass the endurance test, none of the cells met this criterion. Therefore, LiCl was tested at a lower voltage, 1.6 V, which showed much stable performance since it retained 80% of the initial capacitance after 100 hours. Therefore, 1.6 V can be considered as the operating voltage window in laboratory conditions.

The advantage of using small sized ions was further proved with this moderately activated carbon, which had most of the pores below 0.7-0.8 nm. The CVs of LiCl and $Li_2SO_4$ were compared, in this case, and the three of them showed typical supercapacitor rectangular shape with capacitance values ~150 F $g^{-1}$. $Li_2SO_4$ showed the worst rate capability within the three electrolytes, since at high current density it only retained 15% of the capacitance, in comparison with the LiCl, specially the 6 M solution, which had a 66% of retention at high current density. The role of the electrolyte concentration was a decisive parameter to ensure the high rate capacitive response. The performance of AC12 at 1.6V and the AC16 at 1.8 V had very similar overall performances. The former degraded due to the size match between the ions and the pores that prevents the high rate ion transport and the former due to more capacitance loss from the electrolyte composition at high voltage. So, the use of smaller sized anions, $Cl^-$ instead of $SO_4^{2-}$enhanced the rate capability at medium current density. Therefore, LiCl could be a good alternative to access higher surface area, so capacitance is not limited by the utilized AC, and improve the capacitance at high current density. Furthermore, the high rate capacitance could be related to the electric conductivity of the electrolyte, since the studied ACs showed very similar capacitance retention even though their electrical conductivity was different.

This series of ACs were lastly tested in in neat 1-ethyl-3-methylimidazolium bis(trifluoromethylsulfonyl)imide (EMITFSI) electrolyte, which is a room temperature ionic liquid (IL) Most of the CVs of the symmetric supercapacitor cells showed the typical rectangular shape, and in the case of medium-highly activated ACs (KOH/HC ratio 4 to 6) capacitance values were as high as 179 F $g^{-1}$. On the contrary, ACs with a low degree of activation (KOH/HC ratio 2 and 3) showed a distorted CV shape due to the poor accessibility of the ions to the small sized pores of these carbons. Therefore, when using neat EMITFSI, the AC prepared with a KOH/HC of 4 was considered to have a pore size distribution that provided sufficiently good accessibility to the electrolyte and also a strong ion confinement. This together with a high SSA made it possible to achieve the highest gravimetric capacitance of all the studied ACs. Moreover, the increase of the average pore size did not improve the

value of capacitance for the highly activated ACs. More importantly from the application viewpoint, the volumetric capacitance of all of these ACs was as high as 80 F $cm^{-3}$.

Regarding the rate capability, measurements showed that wider pores did not have an effect on this parameter, *i.e.* harder activation procedures were not needed to increase the capacitance retention at high current density. Thus, in this case the observed capacitance loss could be linked to the conductivity of the electrolyte, which for ionic liquid is lower (8.4 mS $cm^{-1}$) than the traditional acetonitrile-based organic electrolyte (60 mS $cm^{-1}$).

Overall, electrochemical impedance spectroscopy reflected the typical Nyquist plot for supercapacitors with a quasi-vertical line at the low frequency and a ~ 45° slope line in the medium frequency due to the porous electrode RC distribution. The series resistance was low for medium-highly activated ACs varying between 2.0 and 2.8 Ω $cm^2$, and the in-pore ionic resistance fluctuated between 3.8 and 7.0 Ω $cm^2$. Thus, the well adapted porosity of AC4 was confirmed because further pore enlargement was not needed to provide high power. Because these activated carbons lacked mesopores, it was demonstrated that in fact mesopores might not be always needed to ensure a fast transport of ions from room temperature ionic liquids deep down pores.

The AC that performed the best in organic electrolyte was used to develop a LIC and a NIC together with its HC precursor. The AC was used as active material in the positive electrode and the HC as active material in the negative electrode. The CVs of the half-cell made with the HC behave similarly between 0.002 and 2 V *vs* $Na/Na^+$ and $Li/Li^+$, with a reversible broad oxidation/reduction peak below 1 V, indicating that the majority of the capacity came at this low potential range. In comparison with the Li half-cell, the Na cell had a larger reduction/oxidation potential window, which could be due to the lower reversibility of Na insertion, because of its bigger ionic radius, preventing more the insertion/extraction of these ions.

Galvanostatic charge discharge profiles provided a total specific capacity of 360 and 375 mA h $g^{-1}$ for Na and Li cells, respectively. In both cases the SEI formation, as a result of the decomposition of the carbonate solvent, took place at ~ 0.8-1.0 V vs. the respective metal/meal ion couple, and the reductive decomposition of organic electrolyte kept on until ~ 0.25 V, where the ion insertion into nanopores became a major process. After the second charge significant differences between Na based and Li based electrolyte began to occur since the capacity was reduced to 243 and 290 mA h $g^{-1}$, correspondingly. In both cases, the reversible ion insertion at high potentials was quite similar. At low potentials though, Li based cell had a higher capacity value, 180 mA h $g^{-1}$ than the Na-based cell, 147 mA h $g^{-1}$, because Na ions have lower accessibility into the pores. The rate capability of Li-and Na-based cells were quite similar until medium rates, however, at high rates Na-based cell underwent quite a remarkable decrease in capacity. Electrochemical impedance spectroscopy showed the Na-based cell had a higher charge transfer resistance than the Li-based one.

The CVs obtained in 3-electrode cells using the AC as active material from 1.5 to 4.2 V showed a quasi-rectangular profile both in 1 M $LiPF_6$ EC:DMC and 1 M $NaPF_6$ EC:PC. The rate capability was very similar for the cells working in Li- and Na-based electrolytes, having both also very similar IR drop from the galvanostatic charge discharge profiles, as well as almost exactly the same electrochemical impedance spectroscopy print.

The LIC was built using a mass balance of 1/1 of the HC the AC as negative and positive electrodes, correspondingly, in 1 M $LiPF_6$ in EC/DMC. Both electrodes were preconditioned by cycling 5 times the HC between 0.002 and 2.0 V vs $Li/Li^+$ at C/10, so the SEI layer was formed, and setting a cut-off potential of 0.2 V in order to avoid Li platting. The AC was preconditioned by cycling it until 4.2 V vs $Li/Li^+$. The positive electrode underwent a potential change between 2.1 to 4.4 V and the negative

between 0.2 to 0.6 V at 0.01 A $g^{-1}$. When the current density was increased to 2 A $g^{-1}$, the positive electrode withstood a smaller potential charge, between 2.3 and 4.3 V, and the negative electrode a larger one, between 0.2 and 0.8 V. In terms of energy and power density, the LIC at a discharge time of 2 minutes was able to store/deliver three-times more energy than its EDLC counterpart. It also showed a very good cyclability result, being able to retain the 94% of the initial capacity after cycling it at 2 A $g^{-1}$ for 10000 cycles.

A NIC was also assembled following the same configuration HC/AC configuration but using 1 M $NaPF_6$ in EC/PC as electrolyte. After the precondition step, at 0.1 A $g^{-1}$ the negative electrode worked between 0.1 and 0.7 V while the positive electrode operated between 2.2 and 4.3 V. However, at 2 A $g^{-1}$, the positive electrode moved between 3.0 and 4.2 V and the negative electrode underwent a potential range between 0 and 1.5 V and. The shape of the galvanostatic profile deviated from the typical linear behaviour expected for a capacitive system. The potential of the negative electrode overpassed the potentials for Na insertion. In comparison with the LIC, the NIC had a stronger decay of the energy to power, which is related to the non-ideal supercapacitor performance that showed at high rates. In this case, after 10000 cycles of charge and discharge at 2 A $g^{-1}$, the NIC system only could retain 40% of its initial capacity.

In this doctoral thesis advanced microporous carbons (nanoporous) from olive pits have been developed for minimizing as much as possible the environmental impact of the production. Different porosity features have been studied in different electrolytes in order to pursue a deeper understanding on the influence of capacitance in relationship with SSA, $L_0$, and electrical permittivity, while several symmetric and asymmetric systems have been proposed with the use of olive pits derived activated carbons.

# 5 RESUMEN

Los huesos de aceitunas son subproductos de la industria del aceite de oliva que se convierten en un desecho para los productores. Se componen de un 25% de celulosa, un 35% de hemicelulosa y un 40% de lignina, de forma que tienen un 50,8% de carbono, un 42,7% de oxígeno, un 7,1% de hidrógeno, un 0,48% de nitrógeno y un 0,04% de azufre en su contenido.

Los carbones activados (ACs) de los huesos de aceitunas que se utilizaron en este estudio se prepararon mediante un proceso que consta de dos etapas. Para ello se utilizó un horno tubular para calentar bajo un flujo de Ar de 100 ml $min^{-1}$ con una rampa de temperatura de 5 °C $min^{-1}$ hasta una temperatura predefinida durante 2 h. El primer paso del proceso fue la carbonización de la materia prima. En este paso se eliminaron la mayor parte de los elementos que no son carbono, principalmente el hidrógeno, oxígeno y nitrógeno, formando gases y alquitranes. El rendimiento fue del 25% para las temperaturas de entre 600 y 800 °C y al producto carbonoso resultante se le denomina carbono duro (HC). Aunque el HC tenía algunos dominios grafíticos, también constaba de capas de grafeno apiladas no grafíticas, que impiden su completa grafitización. El segundo paso fue la activación química con KOH, para el cual se mezcló físicamente el HC obtenido previamente con diferentes proporciones de KOH. A continuación, la mezcla de carbón y KOH se sometió al tratamiento de temperatura. En todos los casos, las temperaturas de carbonización y activación fueron elegidas para que fuesen las mismas. Después de la activación, los carbones activados se lavaron, en primer lugar, con una solución diluida de ácido clorhídrico durante 2 h, y después, con agua, hasta que el pH fuese neutro. Finalmente, se secaron a 120 °C en un horno a vacío. En esta parte del proceso, el rendimiento se vio reducido a medida que se aumentaba la relación KOH/C. Mediante el proceso de activación se formaron grietas distribuidas al azar y se introdujeron microporos dentro de las capas de grafeno.

En primer lugar, se analizaron las propiedades texturales de las muestras activadas con una relación KOH/carbono de 2,6 a temperaturas entre 700 y 1000 °C. Por un lado, se logró una distribución del tamaño de poro estrecho a 700 a 800 °C, con un tamaño de poro promedio por debajo de 1 nm y una diferencia en el área de superficie específica de ~ 100 $m^2$ $g^{-1}$. Por otro lado, cuando la temperatura se aumentó hasta 1000 °C, la distribución del tamaño de poro aumentó significativamente, obteniendo un tamaño de poro promedio mayor a 1 nm.

Obviamente, la capacitancia gravimétrica cambió en concordancia a las diferentes propiedades texturales de los carbones activados. En el electrolito acuoso, 6 M de KOH, la capacitancia aumentó de 176 a 218 F $g^{-1}$ al aumentar la temperatura de activación de 700 °C a 800 °C y disminuyó a 150 F $g^{-1}$ para los ACs de 1000 °C. La disminución de la capacitancia de 800 °C a 1000 °C está directamente relacionada con el hecho de que el área de superficie específica disminuyó en el mismo porcentaje. Sin embargo, el aumento de la capacitancia de 700 °C a 800 °C no corresponde al porcentaje de aumento del área de superficie, lo que sugirió que era necesario un análisis detallado teniendo en cuenta el SSA, el tamaño medio de poro y la permitividad dieléctrica.

En segundo lugar, se estudió la variación de las propiedades texturales en función de la relación de KOH/carbono utilizada en la activación. En general, la superficie especifica de área aumentó linealmente hasta un valor máximo de 2400 $m^2$ $g^{-1}$ para la relación de KOH/carbono 6.6, y disminuyó para proporciones de KOH/carbono mayores, debido a una combustión excesiva de carbono que destruyó algunas de las paredes de los poros. A la misma vez, el tamaño medio de poro aumentó linealmente, permaneciendo por debajo de 1 nm hasta la relación KOH/carbón de 6. Para mayores proporciones de KOH/carbón la tendencia lineal aumentó, lo que reflejaba la mayor variación del tamaño medio de poro con relación a KOH/carbón. La distribución del tamaño de poro mostró que, en efecto, la cantidad de agente activante amplía progresivamente el tamaño de poro hacia 2 nm. El cambio gradual del tamaño de poro permite usar la relación KOH/carbón como parámetro para controlar el diseño de la porosidad.

La  muestra la evolución de la capacitancia a diferentes relaciones de KOH/C. Cuando se testearon esta series de carbones activados como materiales activos para supercondensadores en electrolito acuoso 6 M KOH, los voltamogramas cíclicos mostraron que el valor de capacitancia gravimétrico aumentó hasta 260 F $g^{-1}$ para la relación de KOH/C de 6,6, en correlación con el aumento del área superficial específica, mientras que la capacitancia volumétrica alcanzó su valor más alto, de 135 F $cm^{-3}$, para la relación de KOH/C 2, cuando el carbón activado tenía menos porosidad, es decir, siendo este más denso. Desde el punto de vista práctico, el hecho de que la capacitancia volumétrica, el parámetro más demandado industrialmente, tenía un alto valor con un bajo burn-off es una ventaja, ya que requeriría menos cantidad de agente activante y presumiblemente menos agua para el paso de lavado, reduciendo el coste total del proceso. De forma similar al efecto de la temperatura en las propiedades texturales, la capacitancia específica no se vió afectada únicamente por la superficie especifica de área del carbón activado. Por lo cual hay una fluctuación en la dependencia de la capacitancia con la relación de KOH/C, el tamaño de poro promedio y la solvatación iónica que debería ser tomada en un cuenta.

La capacitancia de los condensadores eléctricos de doble capa se puede describir mediante el modelo de capacidad en sándwich para los microporos con forma de hendidura.

La fórmula se puede aplicar individualmente para la capacitancia del electrodo positivo y negativo individualmente. Las superficies de área accesibles a los iones de potasio e hidroxilo se calcularon a partir de datos de DFT, restando el área inferior al tamaño de cada ion a la superficie especifica total.

Asimismo, la anchura de poro media accesible para cada ion se calculó teniendo en cuenta el volumen correspondiente a los poros mayores al tamaño de los iones. Se consideró que el tamaño de $K^+$ era 0,42 nm, en forma hidratada, y el tamaño de $OH^-$0,63 nm.

Por un lado, la capacitancia por electrodo se calculó utilizando los datos de las adsorción de gas y el valor de la permitividad dieléctrica en vacío, en función a la permitividad dieléctrica relativa para cada uno de los iones. Mientras que, por otro lado, la capacitancia experimental de cada electrodo dentro de una celda simétrica se midió introduciendo un electrodo de referencia. Por lo tanto, se compararon la capacitancia calculada y la experimental.

Cuando la capacitancia calculada se representó frente a la capacitancia experimental para cada uno de los electrodes, no se encontró ninguna correlación entre puntos para diferentes  carbones microporosos, lo que implica que la permitividad dieléctrica efectiva no es un valor constante. Sin embargo, cuando al representar la permitividad efectiva frente al tamaño de poro promedio, se halló una correlación lineal, lo que sugiere que el ensanchamiento de los poros permite que más moléculas de agua rodeen a los iones. Al mismo tiempo, los valores de permitividad efectiva se vieron incrementados progresivamente en medida que la desolvatación de iones disminuía. Además, dependiendo del ion,  se observó un cambio más pronunciado de la permitividad cuando aumentaba el tamaño del catión para el electrodo negativo, lo que sugiere que los iones $K^+$ están más solvatados que los iones $OH^-$.

Como parte de la evaluación de los carbones activados a partir de los huesos de aceitunas para su utilización en supercondensadores, se analizó la respuesta capacitativa y se la relacionó con sus características porosas. Estos dispositivos deben tener alta potencia, por lo que la pérdida de capacitancia debe evitarse a altas densidades de corriente. La retención de capacitancia aumentó hasta una relación KOH/C de 6, es decir, para el carbón activados con mayor surpercifie especifica de area y tamaño medio de poro de ~ 1 nm. Además, a medida que se incrementó el tamaño de poro promedio de los carbonos activados, se mejoró la retención, de tal manera que al desbloquear la electrosorción de los iones solvatados se mejoró el transporte de iones a altas velocidades de corriente. En este sentido, los carbonos activados a partir de las relaciones KOH/C entre 2.6 y 6 ya tenían un tamaño un 25% mayor que los iones solvatados. La dependencia de la capacitancia con el tiempo de descarga mostró que los valores más altos de capacitancia para un tiempo de descarga bajo se obtuvieron con carbones con poros ligeramente más amplios que el tamaño de ión solvatado.

Por el contrario, cuando el tamaño de poro era significativamente más ancho que el tamaño del ion, la capacidad disminuyó.

El carbón activado a partir de la relación KOH/C de 6 se usó como ejemplo para mostrar que cada electrodo experimenta un rango de potencial diferente. En ese caso, el electrodo negativo usó una ventana de potencial más baja a baja densidad de corriente, lo que implicaba que la capacitancia de ese electrodo era más alta en comparación con la positiva. Sin embargo, cuando la densidad de corriente era alta, este comportamiento se invirtió y el electrodo positivo pasó a tener mayor capacitancia.

Teniendo esto en cuenta, la relación entre la capacitancia del electrodo positivo y el negativo se utilizó para tener una idea más clara del efecto del tamaño de poro sobre la capacitancia a diferentes densidades de corriente. Por lo que utilizando el concepto de la equivalencia de cargas almacenadas, se calculó la relación de capacitancia entre los dos electrodos.

Se observó que la capacitancia del electrodo positivo y del negativo y su relación cambiaron a medida que aumentaba la densidad de corriente. A baja densidad de corriente, el electrodo negativo mostró la capacitancia más alta para todas las propiedades porosas y a alta densidad de corriente, el positivo se convirtió en el más alto en capacitancia. Por lo tanto, la electrosorción de iones $OH^-$ se vio favorecidad a alta densidad de corriente en comparacio a la de los iones de $K^+$. Teniendo en cuenta los resultados obtenido del analysis de permitividad dieléctrica, la movilidad se vio más reducida en los iones e $K^+$ debido a su mayor solvatación.

En conclusión, respuesta de la capacidad en función de la densidad de corriente se relacionó con el tamaño del ion, la superficie específica, el tamaño medio de poro y la solvatación. Por un lado, los iones más pequeños pudieron acceder a una mayor superficie específica de área, proporcionando una mayor capacitancia gravimétrica. Además, un tamaño de poro desproporcionadamente amplio aumentó la solvatación de los iones, lo que dio lugar a la disminución del transporte de iones a altas densidades de corriente. Por otro lado, una menor contribución pseudocapacitiva que sólo ocurre en el electrodo negativo podría deteriorar la retención de capacitancia a alta densidad de corriente, por una mayor resistividad en el proceso de transferencia de carga faradáica. En cualquier caso, el electrodo negativo fue identificado como la causa de la pérdida de capacitancia a alta densidad de corriente para esta serie de carbones activados.

Como se hizo para el electrolito acuoso, también se llevó a cabo el estudio para relacionar las características porosas de los carbones activados para su uso en supercapacioters de base orgánica. En este caso se evaluaron la superficie especifica de área y el tamaño de poro promedio accesible para cada uno de los iones para los diferentes carbonos activados con relación KOH/C. Para ello, se consideraron únicamente los poros con un tamaño más grande al del tamaño de iones utilizando los cálculos obtenidos mediante el modelo DFT de los experimentos de adsorción de $N_2$ gas. El tamaño tomado para $Et_4N^+$ fue 0,68 nm y para $BF_4^-$ 0,48 nm, considerando que estaban parcialmente desolvatados. Por lo tanto, el área de superficie accesible es:

La superficie especifica de área fue aumentando hasta que alcanzó un valor máximo alrededor de la relación KOH/C 6. Se encontró que la superficie accesible para $BF_4^-$ tenía valores muy similares a los de la superficie específica total, debido a que la molecula de prueba, $N_2$, y el anión, $BF_4^-$ tienen tamaños similares. Sin embargo, se descubrió que la superficie accesible al $Et_4N^+$ es aproximadamente 3 a 5 veces inferior porque su tamaño es significativamente mayor al del $N^2$. Evidentemente, la superficie específica determinada por la adsorción de $N_2$ gas no se pudo tomar como la superficie accesible para el electrolito, especialmente cuando el tamaño de los iones era mayor que el tamaño de la molécula de prueba. De forma similar, el tamaño de poro accesible se calculó teniendo en cuenta los poros más grandes a los tamaños de cada ion.

De manera similar que con el área superficial, cuando se tuvo en cuenta la porosidad accesible para calcular el tamaño de poro promedio, el tamaño de poro accesible para BF4 no difirió mucho del

calculado a partir de la adsorción de gas N2, mientras que el tamaño de poro accesible para $Et_4N^+$ varió mucho más (~ 0,35 nm).

Por un lado, para los carbones activados con un tamaño de poro promedio menor a 1 nm, los voltamogramas cíclicos mostraron una disminución de la capacitancia al aproximarse a altos voltajes debido al efecto de tamizado de iones o la saturación de la superficie. Por lo que los poros con tamaños inferiores al nanómetro se vieron desfavorecidos para el almacenamiento capacitivo de carga, especialmente en el electrodo negativo, debido quelos cationes tuvieron poca accesibilidad. Por el contrario, los carbones activados con un tamaño medio de poro mayor a 1 nm, recuperaron la forma rectangular típica de los supercondensadores. Dado que el tamaño de poro promedio y el tamaño de poro accesible para el catión fueron diferentes, usar el primero para describir el rendimiento electroquímico podría conducir a interpretaciones erróneas. También se pudo observar que la disminución de capacitancia ocurrió para un tamaño de poro accesible mayor que el $Et_4N^+$ parcialmente desolvatado (0,68 nm), lo que indica que la eliminación de la capa de solvatación dificulta las mediciones de voltametría.

La capacitancia normalizada por la superficie accesible para $Et_4N^+$ indicó que la capacitancia tenía valores mayores a ~ 10 µF $cm^{-2}$ para tamaños de poro promedio superiores a 1 nm. En el caso de carbones activados que tuvieron el efecto de tamizado o saturación superficial, la capacitancia superficial superó 10 µF $cm^{-2}$. Sin embargo, este efecto se observó cosiderando la capacitancia promedio por electrodo, que se asumió ser la misma capacitancia para los electrodos positivos y negativos.

Sin embargo, podría haber una diferencia significativa en la capacitancia dependiendo de la compatibilidad carbono/ion, por ejemplo, debido a las restricciones de tamaño de poro. Por lo tanto, fue necesario analizar este efecto midiendo la capacitancia de los electrodos positivos y negativos por separado mediante el uso de un electrodo de referencia. Por lo tanto, la capacitancia superficial de cada electrodo se calculó dividiendo la capacitancia gravimétrica experimental de cada uno de los electrodos por los valores de la superficial accesible al contraión correspondiente, es decir, $C_{exp-}/S_{Et4N+}$ y $C_{exp+}/S_{BF4-}$.

La capacitancia del electrodo positivo fue casi constante, ~ 5 µF $cm^{-2}$, independientemente del tamaño de poro accesible. Por el contrario, la capacitancia del electrodo negativo se incrementó con los tamaños de poro accesibles más pequeños, teniendo en cuenta el valor de capacitancia extraído de la parte lineal del perfil de galvanostático de descarga.

En el caso del electrodo positivo, la $\varepsilon_{r+}$ cambió linealmente a medida que aumentaba el tamaño de poro, en acuerdo con la capacitancia del electrodo positivo. En el caso del electrodo negativo, la $\varepsilon_{r-}$ también cambió linealmente para los tamaños de poro que no mostraron restricciones para el transporte de iones. Sin embargo, para los tamaños de poro que mostraron una mayor saturación de poro o un efecto de tamizado de iones mayor, la $\varepsilon_{r+}$ se quedó fuera de la tendencia lineal debido a un confinamiento superior supuestamente de las moléculas de acetonitrilo entre los iones $Et_4N^+$. Este aumento anormal de la capacitancia puede ser causado porque la disminución en la separación de carga no se anuló por la disminución correspondiente en $\varepsilon_r$, antes de alcanzar el potencial de descomposición del electrolito. Sin embargo, esto afectó negativamente el rendimiento del supercondensador, ya que la ventana de voltaje completo no pudo utilizarse para el almacenamiento de carga. Desde la perspectiva práctica, la capacitancia gravimétrica máxima alcanzada con los carbones activados a partir de hueso de aceituna fue 140-150 F $g^{-1}$ y volumétrica 60 F $g^{-1}$, valores comparables a los comerciales.

Los perfiles galvanostáticos de carga/descarga tanto de las celdas simétricas como de los electrodos por separado variaron dependiendo de las características porosas de los carbones activados debido al confinamiento o la no restricción del electrolito. La **¡Error! No se encuentra el origen de la referencia.** muestra los perfiles galvanostáticos de carga/descarga de los supercondensadores simétricos para carbonos con diferente relación KOH/C en la activación. Los tamaños de poro con accesibilidades

restringidas sufrieron el fallo de la capacitancia en el electrodo negativo a altas densidades de corriente. Por el contrario, los tamaños de poro sin restricciones mostraron valores de capacitancia iguales para ambos electrodos a baja densidad de corriente, en este caso la disminución de capacitancia fue a causa del electrodo positivo, que también experimentó una ventana de potencial mayor, cerca del límite de descomposición del electrolito.

Por lo tanto, para diferentes tamaños de poro, la relación entre la capacitancia del electrodo positivo y el negativo cambió en función de la densidad de corriente. Para tamaños de poro de accesibilidad restringida, la capacitancia del electrodo positivo fue más alta que la del electrodo negativo a alta densidad de corriente, para tamaños de poro adaptados al tamaño de los iones, ambas capacitancias fueron similares y para los poros extensamente más amplios la capacitancia del electrodo negativo fue mayor a alta densidad de corriente. Es decir, $C_-/C_+$ aumentó gradualmente a medida que el tamaño de poro se hizo más ancho.

Teniendo en cuenta la retención de la capacitancia a altas corrientes, se pudo estimar qué tamaño de poro es óptimo. Este carbón activado tubo un tamaño de poro accesible de 1.2 y 1.04 nm para el $EtN_4^+$ y $BF_4^-$, respectivamente, que curiosamente se acerca al tamaño de los iones solvatados. Para este carbono activado, el valor de $C_-/C_+$ sobre la densidad de corriente no se desvió de la unidad, por lo que el electrolito era estable dentro de la ventana potencial del electrodo negativo y positivo. Por el contrario, con carbones activados que tienen tamaños de poros más amplios, la retención de la capacitancia fue menor al mismo tiempo que el valor $C_-/C_+$ aumentó, por lo que la ventana potencial que el electrodo positivo tuvo que abarcar se hizo más grande, más cercana al límite de descomposición del electrodo/electrolito.

La conductividad eléctrica de estos carbones activados fluctuó con valores muy parecidos entre todos ellos. Por lo tanto, no se pudo establecer una correlación significativa entre los valores de conductividad y la retención de la capacitancia a altas densidades de corriente.

Se seleccionó un carbón activado con accesibilidad de poro relativamente amplio, KOH/C 6, para estudiar los diferentes tipos de electrolitos basados en sales neutras, para los cuales se variaron los cationes y los aniones. En primer lugar, se investigó el efecto del anión, por lo que se prepararon soluciones de cloruro de litio, nitrato de litio y sulfato de litio en 1 M y se testaron con una ventana de voltaje estable de 1 V. Los voltamogramas cíclicos tuvieron la forma típica rectangular de supercondensadores para todas las soluciones de electrolitos, proporcionando valores de capacitancia entre 87 F $g^{-1}$ y 111 F $g^{-1}$ para $Li_2SO_4$ y LiCl, respectivamente.

La capacitancia del LiCl fue ligeramente más alta a la del $Li_2SO_4$, que podría atribuirse al tamaño de aniones más pequeño $Cl^-$ (0.36 nm, en estado no hidratado) en comparación con los aniones de $SO_4^{2-}$ (> 0.58 nm, en forma hidratada). Con iones de tamaños más pequeños se pudo acceder a mayor cantidad de la superficie, por lo que se aumentó el valor de la capacitancia.

En segundo lugar, se investigó el efecto del catión junto con el impacto de la conductividad del electrolito, la cual se optimizó aumentando la concentración de los electrolitos hasta 6 M para LiCl (170 mS $cm^{-1}$), 5 M para NaCl (220 mS $cm^{-1}$) y 2 M para KCl (205 mS $cm^{-1}$). Se obtuvieron CVs de forma rectangular casi perfecta mediante el aumento de la concentración de los electrolitos acuosos de KCl, NaCl y LiCl. Además, el aumento de la conductividad del electrolito mejoró los valores de capacitancia, ~ 150 F $g^{-1}$, que fueron muy similares para las tres sales probadas, y también se disminuyó la resistencia. Por lo que en términos de valores de capacitancia, la selección de cationes no tuvo una influencia significativa.

Por espectroscopia de impedancia electroquímica, exhibieron el comportamiento típico de un supercondensador, es decir, mostraron una línea a baja frecuencia casi vertical que pasa a una línea en un ángulo de ~ 45° a frecuencia media y finalmente intercepta el eje real. La resistencia equivalente en serie (ESR) se extrajo de la intersección del límite de alta frecuencia y se atribuyó a la resistencia electrónica de los electrodos y a la resistencia iónica del electrolito. Los valores obtenidos

fueron muy bajos, ~ 0,50 Ω $cm^2$ para todas las soluciones electrolíticas de 1 M. Sin embargo, el aumento de la concentración del electrolito disminuyó estos valores aún más, a ~ 0,20 Ω $cm^2$, lo que indica claramente que la mejora de la conductividad del electrolito ayudó a disminuir los valores de resistencia. Los valores de conductividad de todos los electrolitos fueron muy similares al igual que los valores de resistencia. Además, la línea diagonal de frecuencia media, que es característica del transporte de iones en la porosidad, era más pequeña. Por lo tanto, la resistencia del electrolito dentro de los poros se pudo relacionar con la conductividad del electrolito, posiblemente debido a que la superficie de este carbón activado era lo sufrientemente alta para que los iones accediesen a ella. La menor resistencia dentro de los poros acortó las vías de transporte cuando se polarizaron los electrodos.

Con electrolitos de sales neutras, la ventana de voltaje se pudo extender hasta 1.8V, mientras que los CVs de LiCl y NaCl mantuvieron una forma muy rectangular, aunque el CV de KCl presentó una forma bastante distorsionada debido a la reducción de agua. La retención de la capacitancia a altas densidades de corriente también fue menor para el electrolito de KCl. A baja densidad de corriente, el valor de capacitancia mayor se obtuvo con las celdas de NaCl y KCl debido a la contribución faradáica de la descomposición parcial de los electrolitos. Sin embargo, la retención de capacitancia a alta densidad de corriente fue mucho mayor para LiCl (63%) en comparación con NaCl (47%) y KCl (32%).

Cargar las celdas hasta 1,8 V implica superar la ventana de potencial estable del agua, lo cual también se puede observar para cada uno de los electrodos, es decir que superan los límites teóricos de la evolución del hidrógeno y el oxígeno. Por un lado, en la celda de tres electrodos se observa que el electrodo negativo se puede cargar hasta límites superiores a la evolución de hidrógeno. Por lo tanto, el uso de soluciones neutras acuosas concentradas evita que dos protones se absorban cerca el uno de otro en la superficie del electrodo para reaccionar entre sí y formar hidrogeno gas, al menos a potenciales donde comúnmente ocurre esta reacción. Esto podría deberse a la escasez de protones en la superficie del electrodo negativo, en comparación con el catión correspondiente. Por otro lado, los electrodos positivos también van más allá del límite de evolución de oxígeno pero en un menor grado, por lo que se mantendrían dentro de la ventana de potencial estable si se cargaran hasta 1,6 V solamente. La celda basada en NaCl está significativamente por encima del límite del electrodo porsitivo, lo que resulta en un peor desempeño bajo la floating test. La celda basada en KCl tiene un potencial de circuito abierto (OCP) desplazado hacia potenciales más negativos, lo que hace que el electrodo negativo se acerque más rápidamente a la degradación del electrodo negativo y probablemente cause un rendimiento de flotación extremadamente pobre. La comparación entre tres y dos celdas de electrodo muestra que una configuración simétrica no aprovecha la ventana de voltaje operacional completa para electrolitos de cloruro neutros. Por lo tanto, se podría realizar una mayor optimización balanceando la masa de las celdas.

Después del Floating test, las celdas de KCl perdieron el 50% de la capacitancia después de 4 horas a 1,8 V. Las celdas de NaCl perdieron un 40% de capacitancia después de 100 horas, mientras que las celdas de LiCl obtuvieron una retención de la capacitancia superior al 60%. Puesto que se debe considerar el 80% de la retención de capacitancia para pasar con éxito la prueba, ninguna de las celdas cumplió este criterio. Por lo tanto, la celda de LiCl se probó a un voltaje más bajo, 1,6 V, que mostró un rendimiento mucho más estable ya que retuvo el 80% de la capacitancia inicial después de 100 horas. Por lo tanto, 1.6 V debe considerarse como la ventana de voltaje de operación.

La ventaja de usar tamaños de iones pequeños se vio demostrada mediante este carbón moderadamente activado, que tenía la mayoría de los poros por debajo de 0,7-0,8 nm. Se compararon los CV de LiCl y $Li_2SO_4$, y los ambos mostraron una forma rectangular de supercondensador típica con valores de capacitancia ~ 150 F $g^{-1}$. $Li_2SO_4$ en 1M mostró una peor retención de la capacitancia a altas densidades de corriente reteniendo sólo el 15% de la capacitancia, en comparación con el LiCl, especialmente en la disolución de 6 M, que obtuvo una retención del 66%. El papel de la concentración de electrolitos fue un parámetro decisivo para garantizar una respuesta capacitiva a altas velocidades de carga y descarga. El carbón activado en una relación de KOH/C de 2 y el de KOH/C de 6 mostraron un comportamiento similar a 1,6 V y 1,8 V respectivamente. El primero se

degradó debido a la coincidencia de tamaño entre los iones y de los poros que impide el transporte de iones de alta velocidad y el segundo debido a una mayor pérdida de capacitancia por la descomposición del electrolito. Por lo tanto, el uso de aniones de menor tamaño como el $Cl^-$ en lugar de $SO_4^{2-}$ mejoró la retención de la capacitancia. Por lo tanto, el LiCl podría ser una buena alternativa para acceder a una mayor superficie de los carbones activados, por lo que la capacitancia no está limitada por el carbón activado que se utilice, al tiempo que mejora la capacitancia a una alta densidad de corriente. Además, la capacitancia a altas densidades de corriente podría estar relacionada con la conductividad eléctrica del electrolito, ya que los carbones activados en la relación KOH/C de 2 y 6 mostraron una retención de la capacitancia muy similar, a pesar de que su conductividad eléctrica fuese diferente.

Esta serie de carbones activados se testearon finalmente en electrolito de líquido iónico. La mayoría de los CVs de las celdas de supercondensadores simétricas mostraron una forma rectangular típica, que para carbones activados con relaciones de KOH/C de 4, 5, y 6 proporcionaron, 179, 163 y 171 F $g^{-1}$, respectivamente, siendo estos valores de capacitancia muy altos para carbones activados puramente microporosos en líquido iónico a temperatura ambiente. Por el contrario, los carbones activados con una relación de KOH/C de 2 y 3 mostraron una forma distorsionada de los CV, debido al escaso acceso de los iones a los pequeños poros. Por lo tanto, la relación de 4 tuvo una distribución de tamaño de poro que proporcionaba un buen acceso al electrolito y también un fuerte confinamiento de iones, esto junto con un área de superficie específica alta permitió alcanzar la capacitancia gravimétrica más alta de todos los carbonos activados estudiados. Al contrario, el aumento del tamaño medio de poro no mejoró el valor de la capacitancia para un mayor grado de activación. Además, la capacitancia volumétrica de estos carbones activados también fue alta, 80, 75 y 63 F $cm^{-3}$, respectivamente, para las relaciones KOHC de 4, 5 y 6.

La retención para los carbones menos activados, relaciones KOH/C de 2 y 3, fue muy baja, debido a que los poros no fueron accesibles. Para la relaciones de KOH/C de 4 a 6 se obtuvieron mejores retenciones, con valores similares para los tres, lo que demostró que las características porosas no tenían un efecto sobre este parámetro De esta forma, no se necesitaron procedimientos de activación más exhaustos para aumentar la retención de capacitancia a alta densidad de corriente. En este caso, la pérdida de capacitancia observada podría vincularse a la conductividad del electrolito, que para el líquido iónico es menor, 8,4 mS $cm^1$, cuando el electrolito orgánico tradicional tiene 60 mS $cm^{-1}$.

La espectroscopia de impedancia electroquímica mostró el diagrama típico de Nyquist para supercondensadores con una línea cuasi vertical a baja frecuencia (excepto para KOH/C de 2), y una línea de inclinación de ~ 45 ° en la frecuencia media debido a la distribución RC de electrodos porosos. La resistencia en serie fue baja para las relaciones entre KOH/C de 4 y 6, variando entre 2.0 y 2.8 Ω cm2, y la resistencia iónica en el poro fluctuó entre 3.8 y 7.0 Ω cm2. Por lo tanto, se confirmó que la porosidad estaba bien adaptada para KOH/C de 4, puesto que no fue necesaria una mayor ampliación de los poros para proporcionar una gran potencia. Debido a que estos carbones activados carecían de mesoporos, se demostró que no se necesitaban para garantizar una propagación rápida de líquidos iónicos a temperatura ambiente.

Uno de los mejores carbón activados para electrolito orgánico y líquido iónico se utilizó para desarrollar el LIC y NIC junto con su precursor de carbon duro (HC). Los CVs de la semicelda de HC tuvieron un comportamiento similar entre 0.002 y 2 V frente a $Na/Na^+$ y $Li/Li^+$, con un pico reversible de oxidación/reducción amplio por debajo de 1 V, lo que indica que la mayor parte de la capacidad se obtuvo a este bajo potencial, y también hubo un pico de oxidación por debajo de 0.25 V. En comparación con la celda Li, la celda Na tenía una ventana de reducción/oxidación más grande, lo que podría deberse a una menor reversibilidad de la inserción del sodio, debido a su mayor radio, evitando la extracción e inserción de estos iones.

Los perfiles de carga y descarga galvanostática proporcionaron una capacidad específica total de 360 y 375 mA h $g^{-1}$ para las celdas Na y Li, respectivamente. En ambos casos, la formación SEI tuvo lugar

a ~ 0.8-1.0 V como resultado de la descomposición del disolvente de carbonato y la descomposición reductiva del electrolito orgánico se mantuvo hasta ~ 0.25 V, donde comenzó la inserción de iones en los nanoporos. Después de la segunda carga, comenzaron a producirse diferencias significativas entre el electrolito basado en Na y el de Li, ya que la capacidad se redujo a 243 y 290 mA h $g^{-1}$, correspondientemente, es decir con valores notablemente inferiores para el de Na. Usando el modelo de "la casa de naipes" en la región donde los iones se intercalan entre láminas de grafeno (entre 1.0 y 0.2 V) para determinar la capacidad, a 0.5 V Na tenía 54 mA h $g^{-1}$ y Li 61 mA h $g^{-1}$ y los valores permanecieron similares hasta 0.25 V, 93 y 109 mA h $g^{-1}$, respectivamente. En ambos casos, la inserción reversible de iones a altos potenciales fue bastante similar. Sin embargo, a bajos potenciales, la celda basada en Li tenía un valor de capacidad mayor, 180 mA h $g^{-1}$, que la celda basada en Na, 147 mA h $g^{-1}$, porque los iones de Na tuvieron menos accesibilidad a los poros. La capacidad con respecto a la densidad de corriente de las celdas fue bastante similar hasta velocidades medias, aunque el sistema basado en Li siempre obtuvo valores ligeramente mejores. Sin embargo, a corrientes altas la diferencia entre ambos se hizo más pronunciada, ya que la celda del Na experimentó una disminución notable en la capacidad. Como la espectroscopia de impedancia electroquímica mostró la celda basada en Na tuvo una mayor resistencia a la transferencia de carga que la basada en Li.

Los CVs del carbon activado con una relación de KOH/C de 6 tuvo un comportamiento capacitivo de 1.5 a 4.2 V así como cierto aumento de la corriente en los extremos. El potencial de circuito abierto del AC fue de 2.9 y 3.3 V frente a $Na/Na^+$ y $Li/Li^+$, respectivamente. La retención de la capacidad fue muy similar para ambas celdas de los electrolitos basados en Li y Na, teniendo una caída de óhmica muy similar en los perfiles de carga/descarga galvanostática y con una huella de espectroscopia de impedancia electroquímica prácticamente idéntica.

Se construyó un condensador de iones de litio utilizando un balance de masa de 1/1 del HC y AC para electrodo negativo y positivo, correspondientemente, en 1 M $LiPF_6$ en EC/DMC. Ambos electrodos se precondicionaron, ciclando 5 veces el HC entre 0,002 y 2,0 V frente a $Li/Li^+$ a una tasa de C10, por lo que se formó la capa de SEI, y estableciendo un potencial de corte de 0,2 V para evitar la deposición de Li. El AC se precondicionó ciclando hasta 4,2 V frente a $Li/Li^+$. El perfil galvanostático de carga y descarga fue el típico de los supercondensadores, con un aumento/disminución constante de voltaje a lo largo del tiempo. El electrodo positivo sufrió un cambio de potencial entre 2.1 a 4.4 V y el negativo entre 0.2 a 0.6 V a 0.01 A $g^{-1}$. Cuando la densidad de corriente se aumentó a 2 A $g^{-1}$, el electrodo positivo resistió una carga de potencial más pequeña, entre 2,3 y 4,3 V, que el electrodo negativo, entre 0,2 y 0,8 V.

En términos de densidad de energía y potencia, el LIC obtuvo valores tres veces más altos que el EDLC para un tiempo de descarga de 2 minutos- Además, mostró un muy buen resultado de ciclabilidad, pudiendo retener el 94% de la capacidad inicial después de 10000 ciclos a 2 A $g^{-1}$.

Un condensador de iones de sodio se ensambló también siguiendo la misma configuración, es decir, un balance de masas de 1/1 con un electrodo positivo de AC y un electrodo negativo de HC, en $NaPF_6$ 1 M en EC/PC. El precondicionamiento del HC se llevó a cabo ciclando 5 veces de 0,002 V a 2 V frente a $Na/Na^+$ a una velocidad de C10 y cortando a 0,2 V. El AC se cargó a 4,2 V frente a $Na/Na^+$. El rango de potencial al que se sometió el electrodo negativo fue entre 0,1 y 0,7 V a 0,1 A g-1 y el electrodo positivo funcionó entre 2,2 y 4,3 V. Sin embargo, a 2 A $g^{-1}$, el electrodo positivo se movió entre 3.0 y 4.2 V y el electrodo negativo experimentó un rango potencial entre 0 y 1.5 V. Debido a este rango de potencial más extenso que experimento el electrodo negativo, se superó el potencial de inserción de Na, la forma del perfil galvanostático se desvio de la típica para supercondensadores. Porque primero tuvo una región de carga rápida y luego una región de carga lenta, lo que significa que solo la segunda fue impulsada por el AC. En comparación con el LIC, el NIC tuvo una disminución mayor de la energía en función de la potencia, lo que podría estar relacionado con la respuesta no ideal de supercondensador que se mostró a altas velocidades. De todos modos, ambos sistemas obtuvieron

altas densidades de energía mientras alcanzaban altas densidades de potencia. Después de 10000 ciclos de prueba a 2 A $g^{-1}$, sin embargo, este sistema solo pudo retener el 40% de su capacidad inicial

# 6 CONCLUSIONS

The following can be concluded from mutually adapting electrolytes and nanoporous carbons for enhanced supercapacitors:

- Hard carbons and activated carbons can be prepared by the pyrolysis and the chemical activation of olive pits, correspondingly.

- The porous features of the carbon materials, such as SSA and PSD can be fine-tuned by modifying the temperature and the amount of activating agent of the synthesis.

- These hard carbon and activated carbons from olive pits are efficient supercapacitor electrode materials in various electrolytes.

- Aqueous 6 M KOH electrolyte only requires of an activated carbon produced with a low amount of activating agent to provide high volumetric capacitance value that can even be retained at very high current density or, with another words, at low discharge time.

- Capacitive rate performance is related to the pore width, in such a way that if slightly solvated ions can provide a faster response in pores that slightly exceed solvated ion size the pore size slightly surpases the when pores are significantly wider than ions, there is an excessive solvation that worsens the ion transport as well as the capacitance at high current density, in 6 M KOH aqueous electrolyte.

- Organic 1.5M $(C_2H_5)_4NBF_4$ electrolyte requires of an activated carbon produced with a higher amount of activating agent than that for aqueous electrolyte to provide a high capacitance.

- The areal capacitance in the negative electrode increases for extreme confinement conditions, which underuses the electrolyte stability window and provides poor rate capability, implicating overall poor electrochemical performance of the supercapacitors.

- The relationship between the capacitance of the negative electrode and that of the positive, $C_-/C_+$, increases as the accessible pore size increases, for organic electrolyte. This has been calculated taking into account the relationship between average pore size and rate capability of separate electrodes.

- The maximum rate capability is achieved when capacitance values of the positive and negative electrodes are similar, i.e. $C_-/C_+ \sim 1$. This is the case when the accessible pore size at each electrode is close to the respective solvated ion size.

- When the accessibility of the electrolyte is unhindered, the capacitance of the negative electrode is higher than that of the positive electrode.

- Chloride salts have their highest capacitance retention and the lowest cell resistance when their concentration is increased to their maximum electrical conductivity.

- The bulk electrolyte conductivity reduces both, the ESR and the in-pore transport resistance, based on a high ionic mobility of the ions and a high degree of dissociation of the free ions .

- Aqueous 6M LiCl electrolyte only requires of an activated carbon produced with a low amount of activating agent to provide high capacitance value. Therefore, a more affordable ultramicroporous carbon can be used in electrochemical capacitors, while providing a great rate response with an extended voltage in aqueous electrolyte.

- Microporous carbons from olive pits can deliver high capacitance value and a low resistance at room temperature in neat EMI-TFSI.

- Strictly microporous carbons also enable high volumetric capacitance, for an adapted pore to ion size.

- High energy density and high power density lithium ion and sodium ion capacitors can be fabricated using carbons derived from olive pits. The positive electrode can be made by an activated carbon and the negative by a hard carbon.

- LIC and NIC overcome the energy density and power density of the EDLCs, while still having a comparable cyclability.

# 6 CONCLUSIONES

Se puede concluir lo siguiente a partir de la mutua adaptación de electrolitos y carbones nanoporosos para supercondensadores avanzados:

- Los carbones duros y los carbones activados pueden prepararse mediante la pirólisis y la activación química de los huesos de olivo, respectivamente.

- Las características de la porosidad de los materiales de carbón, tales como SSA y PSD se pueden ajustar modificando la temperatura y la cantidad de agente activador de la síntesis.

- Estos carbonos duros y carbones activados de las aceitunas son materiales de electrodos supercapacitadores eficientes en varios electrolitos.

- El electrolito acuoso 6 M de KOH sólo requiere de un carbón activado producido con una baja cantidad de agente activador para proporcionar un valor alto de capacitancia volumétrica el cual puede retenerse incluso a una densidad de corriente muy alta o, es decir, a un tiempo de descarga bajo.

- El rendimiento de la capacitancia a altas densidades de corriente está relacionado con el ancho de los poros, de tal manera que si los iones están ligeramente solvatados pueden proporcionar una respuesta más rápida en los poros que exceden ligeramente el tamaño de los iones solvatados, el tamaño de los poros aumenta ligeramente cuando los poros son significativamente más anchos que los iones. Cuando la solvatación es excesiva, el transporte de iones empeora, así como la capacitancia a alta densidad de corriente.

- El electrolito orgánico 1.5M de $(C_2H_5)_4NBF_4$ requiere de un carbón activado producido con una mayor cantidad de agente activador que el electrolito acuoso para proporcionar una alta capacitancia.

- La capacitancia del área en el electrodo negativo aumenta en condiciones de confinamiento extremas, lo que subutiliza la ventana de estabilidad del electrolito y proporciona una capacidad pobre a altas densidades de corriente, lo cual se convierte en un rendimiento electroquímico deficiente de los supercondensadores.

- La relación entre la capacitancia del electrodo negativo y la del positivo, $C_-/C_+$, aumenta a medida que aumenta el tamaño de poro accesible, para electrolito orgánico. Esto se ha calculado teniendo en cuenta la relación entre el tamaño de poro promedio y la capacidad de velocidad de electrodos separados.

- La capacidad de velocidad máxima se alcanza cuando los valores de capacitancia de los electrodos positivo y negativo son similares, es decir, $C_-/C_+ \sim 1$. Este es el caso cuando el tamaño de poro accesible en cada electrodo está cerca del tamaño de ion solvatado respectivo.

- Cuando la accesibilidad del electrolito no está impedida, la capacitancia del electrodo negativo es mayor que la del electrodo positivo.

- Las sales de cloruro tienen su mayor retención de capacitancia y la menor resistencia de las celdas cuando su concentración aumenta a su máxima conductividad eléctrica.

- La conductividad del electrolito reduce tanto la resistencia eléctrica en serie (ESR) como la resistencia al transporte en los poros, basándose en una movilidad iónica alta de los iones y en un grado de disociación alto de los iones libres.

- El electrolito acuoso 6M de LiCl solo requiere de un carbón activado producido con una baja cantidad de agente de activación para proporcionar un valor alto de capacitancia. Por lo tanto, se puede usar un carbón ultramicroporoso que sea más asequible en los condensadores electroquímicos, mientras se puede proporcionar una respuesta a gran velocidad con un voltaje extendido en electrolito acuoso.

- Los carbones microporosos de los huesos de olivo pueden ofrecer un alto valor de capacitancia y una baja resistencia utilizando EMI-TFSI puro a temperatura ambiente.

- Los carbonos estrictamente microporosos también permiten una alta capacitancia volumétrica, cuando el tamaño de poro está adaptado al tamaño de los iones.

- Los condensadores de iones de litio e iones de sodio de alta densidad de energía y densidad de alta potencia pueden ser fabricados utilizando carbones derivados de huesos de aceituna. El electrodo positivo puede hacerse con un carbón activado y el negativo con un carbón duro.

- Los LICs y NICs superan la densidad de energía y la densidad de potencia de los EDLC, a la vez que tienen una ciclabilidad comparable.